# OPTIMISED SOLDER INTERCONNECTIONS IN CRYSTALLINE SILICON (c-Si) PHOTOVOLTAIC MODULES FOR IMPROVED PERFORMANCE IN ELEVATED TEMPERATURE CLIMATE

**OSARUMEN OSAGUONA OGBOMO**

**DOCTOR OF PHILOSOPHY**

**FEBRUARY 2020**

# OPTIMISED SOLDER INTERCONNECTIONS IN CRYSTALLINE SILICON (C-SI) PHOTOVOLTAIC MODULES FOR IMPROVED PERFORMANCE IN ELEVATED TEMPERATURE CLIMATE

**Osarumen Osaguona Ogbomo**

BEng (Honours) FHEA

School of Engineering,

Faculty of Science and Engineering,

University of Wolverhampton,

WV1 1LY, UK

ogbomoosarumen@yahoo.com

A thesis submitted in partial fulfilment of the requirements for the award of Doctor of Philosophy of University of Wolverhampton

**February 2020**

# DECLARATION

This research has not been submitted in any form for any degree nor is it being submitted simultaneously for any degree other than the Doctor of Philosophy (PhD) being studied at the University of Wolverhampton. Also, I declare that this thesis is a product of my own investigations except otherwise stated and clearly acknowledged with references hence, I have not plagiarised the work of others.

---------- ----------

Osarumen Osaguona Ogbomo Date

(Student)

---------- ----------

Professor N.N. Ekere Date

(Director of Studies)

# DEDICATION

This research is dedicated to the Almighty God who granted me the grace, knowledge, wisdom, understanding, fortitude and diligence to embark on this journey and has guided me to its successful completion.

# ACKNOWLEDGEMENTS

This research was fully funded by the Schlumberger Faculty for the Future Foundation (FFTF). FFTF also provided a community of likeminded researchers who provide support for one another and share resources.

I wish to thank my supervisors Prof. N.N. Ekere and Dr Emeka H. Amalu for their invaluable suggestions, directions and support throughout my study. I appreciate their expert efforts to enhance the standard of my research. I specially wish to thank Dr Peter O. Olagbegi of the University of Benin, Nigeria, for his guidance, encouragement and insightful contributions.

I acknowledge the support of the University of Wolverhampton staff; academic, administrative and IT services. I am especially grateful to Mr. Pierre Parson, my excellent research administrator.

Special thanks go to my parents Mr. Daniel N. Ogbomo and Mrs. Eunice Ogbomo for being my ever present emotional and spiritual fortress. My siblings Engr. Efosa Uyi-Ufumwen, Mrs. Iyobosa Uyi-Ufumwen, Engr. Archibong Bob, Barr. Osato Bob, Mr. Osaze Ogbomo, Pharm. Ijeoma Ogbomo, and Miss Osayamen Ogbomo. I also extend appreciation to my friends and colleagues, most especially Dr Mandu Stephen Ekpenyong for making my stay at the University of Wolverhampton enjoyable.

# ABSTRACT

The operations of c-Si PV modules in elevated temperature climates like Africa and the Middle East are plagued with poor thermo-mechanical reliability and short fatigue lives. There is the need to improve the performance of the system operating in such regions to solve the grave energy poverty and power shortages. Solder interconnection failure due to accelerated thermo-mechanical degradation is identified as the most dominant degradation mode and responsible for over 40% of c-Si PV module failures. Hence the optimisation of c-Si PV module solder interconnections for improved performance in elevated temperature climate is the focus of this research. The effects of relevant reliability influencing factors (RIFs) on the performance (thermo-mechanical degradation and fatigue life) of c-Si PV module solder interconnections are investigated utilising a combination of ANSYS finite element modelling (FEM), Taguchi L25 orthogonal array and analytical techniques. The investigated RIFs are operating temperature, material combination and interconnection geometry. Garofalo creep relations and temperature dependent Young's Modulus of Elasticity are used to model solder properties, EVA layer is modelled as viscoelastic while the other component layers are modelled using appropriate constitutive material models.

Results show that fatigue life decays with increases in ambient temperature loads. A power function model $L = 721.48T^{-1.343}$, was derived to predict the fatigue life (years) of c-Si PV modules in any climatic region. Of the various ribbon-contact material combination models investigated, Silver-Silver, Aluminium-Aluminium, Silver-Aluminium and Aluminium-Silver are the top four best performing solder interconnection models with low deformation ratios, $\delta_R$, normalised degradation values, $N_{d_i} < 1$, and normalised fatigue life $N_{f_i} > 1$. Further findings indicate that only the solder layer demonstrates good miniaturisation properties while the standard

dimensions for ribbon and contact layers remain the best performing geometry settings. Additionally, from the Taguchi robust optimisation, the Aluminium-Silver ribbon-contact material combination model (ribbon = 180μm, solder = 56μm, contact = 50μm) demonstrated the best performance in elevated temperature climate, reduced solder degradation by 95.1% and is the most suitable substitute to the conventional c-Si PV module solder interconnection in elevated temperature climate conditions – in terms of thermo-mechanical degradation.

These findings presented provide more insight into the design and development of c-Si PV modules operating in elevated temperature climates by providing a fatigue life prediction model in various ambient conditions, identifying material combinations and geometry which demonstrate improved thermo-mechanical reliability and elongated fatigue life.

# TABLE OF CONTENTS

Contents

# LIST OF FIGURES

# LIST OF TABLES

# ABBREVIATIONS

| | |
|---|---|
| AM | Air mass |
| ANOM | Analysis of means |
| ANOVA | Analysis of variance |
| ANSYS | Analysis system |
| A-Si | Amorphous silicon |
| ATC | Accelerated thermal cycling |
| BGA | Ball grid array |
| CAD | Computer aided design |
| CdTe | Cadmium telluride |
| CIGS | Copper indium gallium selenide |
| C-Si | Crystalline silicon |
| CT | Central tendency |
| CTE | Coefficient of thermal expansion |
| DC | Direct current |
| DMA | Dynamic mechanical analysis |
| DOF | Degree of freedom |
| EL | Electroluminescence |
| EPBT | Energy payback time |
| EVA | Ethylene vinyl acetate |
| FEM | Finite element modelling |
| FF | Fill factor |
| FMEA | Failure modes and effects analysis |
| FMECA | Failure modes effects and criticality analysis |

| | |
|---|---|
| FTA | Fault tree analysis |
| GaAs | Gallium arsenide |
| HAc | Acetic acid |
| HPC | High performance computation |
| IEC | International electrotechnical Commission |
| IMC | Intermetallic compound |
| IR | Infrared |
| IV | Current voltage |
| LID | Light induced degradation |
| MPP | Maximum power point |
| MSE | Mean square error |
| NASA | National Aeronautics and Space Administration |
| NISE | National Institute of Solar Energy |
| NREL | National Renewable Energy Laboratory |
| PCB | Printed circuit board |
| PCE | Power conversion efficiency |
| PID | Potential induced degradation |
| PO | Polyolefin |
| PR | Performance ratio |
| PV | Photovoltaic |
| QE | Quantum efficiency |
| RBD | Reliability block diagram |
| RIF | Reliability influencing factor |

| | |
|---|---|
| RMSE | Root-mean square error |
| RPN | Risk priority number |
| SD | Standard dimension |
| SEM | Scanning electron microscope |
| SMT | Surface mount technology |
| SN | Signal to noise |
| SnAgCu (SAC) | Tin-silver-copper |
| STC | Standard test condition |
| TPT | Tedlar polyester tedlar |
| UV | Ultraviolet |

# CHAPTER 1

# INTRODUCTION

## 1.1 BACKGROUND

Over the last century, the awareness of climate change and global warming has grown and so hydrocarbon energy sources are criticised for their established adverse effects on the environment. Efforts are being made to change the energy supply paradigm by introducing renewable and sustainable energy sources into the mix. Renewable energy sources include solar, hydropower, geothermal, wind, wave power, biomass and biofuel. Photovoltaic (PV) modules are the leading solar energy emergent technologies. Sunlight is converted to useful electricity when it is incident on a photovoltaic material. In the absence of moving parts and waste products, PV modules can generate electricity virtually out of thin air. The entire planet possesses immense solar energy potential and it has been postulated that if solar power is truly embraced by the whole world, it can generate sufficient power in just one hour to meet our annual electricity demands (Harrington, 2015). Despite the solar potential of the planet, the solar energy resource is yet to be fully harnessed and so various forms of energy poverty still abound. This study seeks to improve the reliability of PV modules operating in elevated temperature climates which will contribute to the amelioration of energy poverty especially in African and Middle Eastern regions that are most deprived.

### 1.1.1 World solar energy potential

The regions of the world possess various intensities of solar irradiation which amount to their respective potential to generate electricity from sunlight via PV modules. Figure 1.1 shows the annual world solar energy potential in $kW/m^2$. The darker hues in the

coloured key signify the regions with higher solar irradiation while the lighter hues signify the regions with lower solar irradiation. The whole continent of Africa can be seen to possess the highest intensities of annual solar irradiation, as high as 2500kW/$m^2$, while the north-eastern parts of Russia possess the lowest intensities of a maximum 500kW/$m^2$. It is most astonishing that it is the regions of the world with the highest solar potential that are laden with the greatest forms of energy poverty. Over 50% of the population of Africa do not have access to electricity and it is over 55% in Nigeria (Gujba, Mulugetta and Azapagic, 2011; Aliyu, Ramli and Saleh, 2013; Lindeman, 2015; Olaniyan *et al.*, 2018; World Bank, 2018). The lucky few with access to electricity are burdened with unreliable, unavailable and epileptic power supply.

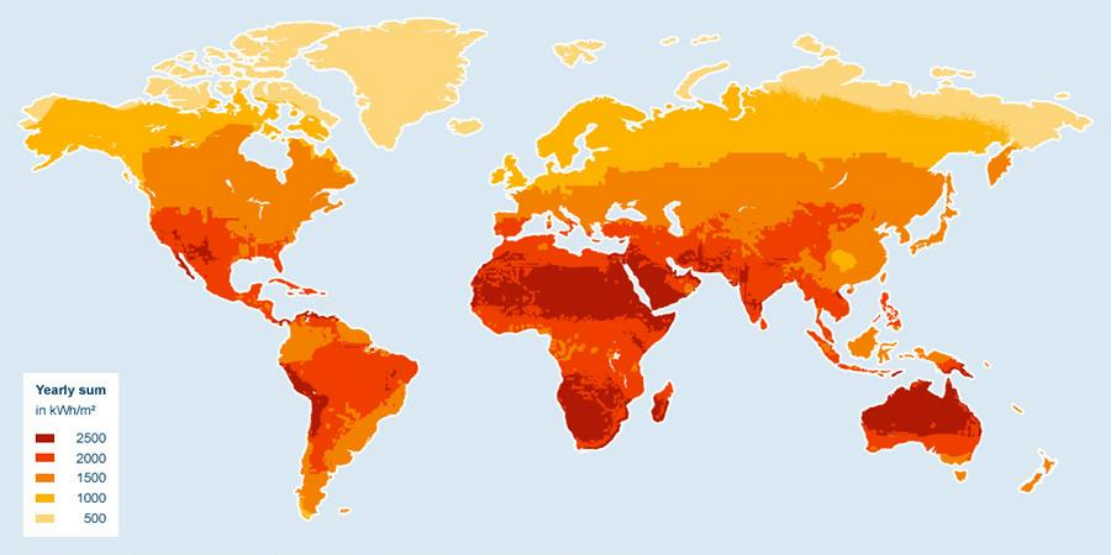


**Figure 1.1:** Annual world solar energy potential

Source: (World Energy Council, 2016)

The rural and remote communities particularly suffer power shortages and energy poverty. Owing to their sporadic settlement structure, inaccessible locations, and either too small or isolated power loads, they are often neglected by the national utility grid because supply to these regions makes little or no economic sense. In developing countries, the national utility grids struggle to supply reliable and affordable energy to

the major cities using the mainstream power supply technologies so supply to smaller more isolated areas is not quite in the cards.

PV modules; without requiring heavy and expensive machinery, maintenance, and distribution lines with inherent losses, provide a decentralised, sustainable and renewable solution to the problem of energy poverty in Africa and the developing world. PV modules are gradually creeping into the African energy mix, but hydrocarbon energy sources remain dominant in the market. People prefer to purchase a petrol/diesel generator that is relatively cheaper to acquire and install, but more expensive to fuel and maintain, and detrimental to their immediate environment, instead of a PV system. This is because more of their focus is on the very expensive initial acquisition and installation costs of the PV system with less consideration to its zero-emission technology, and negligible operation and maintenance costs. The insignificant running costs of the PV system are its major selling point because customers can reap juicy returns on investment over the typical long useful life (20-25 years) of the system. However, a lot of African customers are discouraged further from the PV system because its only seemingly great selling point, which is their ability to reap returns on investments over the long useful life, is at risk. In addition to the large initial investment required to install, PV module systems have been found to exhibit poor performance in the region. PV modules have been reported to fail within 7 years of installation in elevated temperature regions (Djordjevic, Parlevliet and Jennings, 2014; Kuitche, Pan and Tamizhmani, 2014; Tossa *et al.*, 2016; Petrana, Setiawan and Januardi, 2018). Presently, taking into consideration short useful life, energy payback time (EPBT) and return on investment, PV modules are not the most viable energy option in the region. Unfortunately, these are the same regions with the highest solar potential to generate electricity by PV modules but at the same time, suffer from grave energy poverty. By improving the performance and reliability of c-Si PV modules in elevated temperature

climates, this study will enhance their commercial viability in Africa and the developing world.

### 1.1.2 PV module challenges

Crystalline silicon (c-Si) PV modules are designed and manufactured to operate under certain conditions known as standard test conditions (STCs). These STCs are cell temperature of 25 °C, solar irradiation of 1000 W/m$^2$ and air mass of 1.5 (Köntges *et al.*, 2014, 2017). At these STCs, c-Si PV modules possess life expectancies of 20-25 years. However, actual field operating conditions differ significantly from the STCs and vary from one climatic region to another. PV modules are exposed to other climatic factors like actual ambient temperature, humidity and dust. Figure 1.2 shows a PV system exposed to ambient climatic conditions. Chapter 2 of this thesis discusses the operating conditions of c-Si PV modules further.

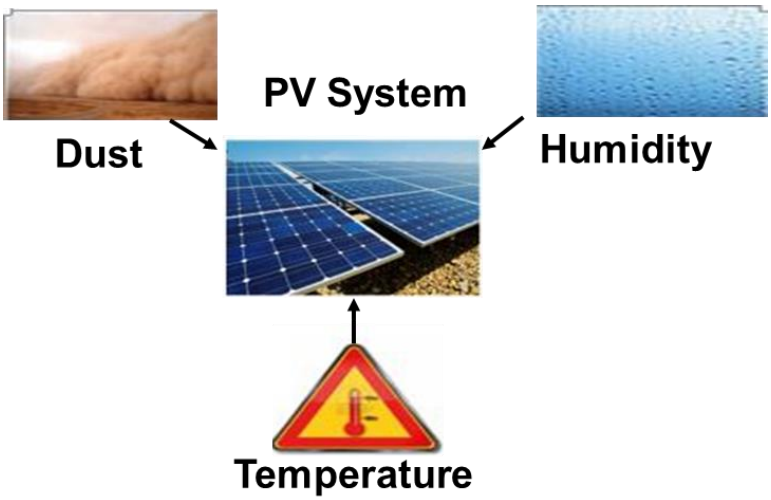


**Figure 1.2:** PV System exposed to ambient climatic conditions

Balato, Costanzo and Vitelli (2015), in their study on the optimization of both the power conversion efficiency and useful life of PV arrays by means of the dynamical reconfiguration of PV modules connections, state that PV module operations under non STCs like clouds, shadows, soiling, non-uniform ageing and orientation, strongly

compromise their power conversion efficiency and reliability. These effects are manifested as reduced Maximum Power Point (MPP), local overheating/hot spots, damaged bypass diodes, melting of solders, discoloration of encapsulant, cell and glass breakage. An experimental investigation on the effect of dust and weather conditions on the reduction of PV power output in Indonesia reports that certain changes in environmental conditions adversely affect the amount of incident solar radiation and hence impedes optical performance and efficiency. These factors; humidity, dust, rain, and partial cloud, can significantly decrease power output by more than 45% (Ramli *et al.,* 2016). Additionally, after two-weeks dust accumulation on the PV modules, they observed that the cloudy condition demonstrated the highest decrease in power output of more than 45%, followed closely by the rainy condition with a decrease of more than 40% and finally the dry condition with power output decrease of more than 10.8%. These findings provide evidence for the poor performance of PV modules in tropical African climates known to have dense cloud and rainy conditions.

Jiang and Lu (2015), in their study of dust accumulating process on solar photovoltaic modules with different surface temperatures, demonstrated that PV module performance is affected by many environmental factors including accumulated dust which is a significant parameter. Accumulated dust particles diminish sunlight intensity reaching the modules thereby decreasing the energy conversion output and efficiency of PV modules. In a study on the energy performance of different silicon photovoltaic technologies under hot and harsh climate, Tossa *et al.* (2016), exposed four PV modules with different technologies (monocrystalline, polycrystalline and tandem amorphous silicon) to the field operating conditions in the Sudan-Sahelian climate. They demonstrated that the actual performance and ageing of PV modules differ from data provided by manufacturers. They measured performance parameters using IV Bench outdoor monitoring test facility and established that the actual performance of PV

modules strongly depends on the climate and installation site environment. Measured PV module performance parameters include actual maximum power, average performance ratio, series resistance and maximum power temperature coefficient. The highest actual ambient temperatures recorded in their study were above 47 °C which drove the module temperature to as high as 75°C, and these harsh conditions led to thermally induced degradation.

It has been reported that the difference between the ambient and cell temperatures of a PV module can be as high as 22 °C depending on other factors like wind speed and direction, and humidity (Kurnik *et al.*, 2011). In the tropical climatic region with characteristic humid and elevated temperature operating conditions, cell temperatures can be as high as 90 °C. These non-STC operating conditions cause the accelerated thermo-mechanical degradation of PV modules which culminates in fatigue failure and reduced lifespan. It is therefore important to not solely rely on data provided by manufacturers because these data are measured at STCs but to consider the real field performances of PV module technologies. Elibol *et al.* (2016), statistically analysed the outdoor performance of different PV panel types under the hot and harsh climatic conditions of Turkey. They ascertained a relationship between power conversion efficiency and performance ratios, environmental temperature, PV module temperature and amount of irradiation. They observed that an ambient temperature increase of 1 °C decreased the efficiency of mono-crystalline panels by 0.084%. To improve the performance of c-Si PV modules in elevated temperature conditions, this study will determine the numerical relationship between solder interconnection degradation and operating temperature. Also, a power function model is derived to predict fatigue life (years) of c-Si PV modules in any climate. Further details are found in chapter 4 of this thesis.

### 1.1.3 PV module failure modes

Köntges (2014) described a defect in a PV module as anything that makes it different from a perfect PV module. A defect either leads to failure or remains a purely cosmetic issue. On the other hand, he reported a PV module failure as any effect that results in abnormal operations which are characterised by output power degradation, abnormal temperature profiles on the surface of modules, excessive thermal/mechanical stresses or, creates a safety issue. PV module failures are not reversed by normal operation and are relevant for warranty when they occur under expected operating conditions causing power loss. In accordance with International Electrotechnical Commission (IEC) standard [IEC 60904], a power loss failure has occurred only when the measured module power, $P_m$, plus the total uncertainty of the measurement, $\Delta P_m$, is less than the power printed on the module label, $P_i$, minus the tolerance stated on the module label, $\Delta P_i$ (Taylor, 2010). Equation 1.1 presents the condition for a power loss failure.

$$P_m + \Delta P_m < P_i - \Delta P_i \qquad \text{Equation 1.1}$$

PV module defects are easily detected by simple visual inspection, but failures require much more comprehensive tests which include Infrared thermography, electroluminescence imaging, UV fluorescence, ultrasonic inspection, and numerous performance tests like accelerated temperature and thermal cycling, accelerated structural degradation, accelerated reliability testing, mechanical, vibration and shock cycling (Djordjevic, Parlevliet and Jennings, 2014).

In the current study, only failure modes associated with operating conditions are considered so those caused by external factors are excluded. External factors include manufacturing errors, transportation and installation damages, vandalism, and acts of God. Catalogued PV module field failures modes include cell breakage, ethylene vinyl acetate (EVA) discoloration and delamination, burn marks, snail tracks/worm marks,

back-sheet adhesion loss, shattering and degradation of solder interconnection, module corrosion, potential induced degradation (PID), light induced power degradation (LID), glass abrasion, corrosion and breakage (Triki-Lahiani, Bennani-Ben Abdelghani and Slama-Belkhodja, 2017). PV module failures result in mechanical degradation, electrical degradation, or a combination of both, of the system which manifest as reduction in short-circuit current, voltage, power output, power conversion efficiency (PCE) and fatigue life. Table 1.1 presents the dominant c-Si PV module failure modes with their corresponding causes and effects. It can be observed from the table that the most common and dominant causes responsible for majority of the PV failures are high temperature, high humidity and UV light. It is also noticeable that one PV failure can become the cause for another. For instance, solder interconnection fatigue failure can cause hot spots and burn marks, encapsulant discoloration, cell cracking and snail tracks. The resulting effects of these PV failures range from increased series resistance and reduced power output to catastrophic safety hazards. Further details on the determination of dominant degradation modes of c-Si PV modules in elevated temperature climates is discussed in Chapter 2 of this thesis.

Jordan *et al.* (2015), studied the performance and aging of a 20-year-old monocrystalline silicon PV system in USA and found the electrical degradation to be about 0.8% per year. Utilising indoor experiments and outdoor continuous tests, they measured DC current, DC voltage, output power, module temperature, ambient temperature and irradiance levels. The researchers observed that short circuit current decrease, mostly caused by discoloration and soiling, resulted in electrical degradation of 0.5-0.6% per year. However, fill factor losses, primarily caused by increase in series resistance, resulted in a higher electrical degradation of 0.8% per year. Their findings deviate from most of literature which attribute higher electrical degradation to short circuit current losses rather than fill factor losses. Also, they observed that the overall

performance of the PV array was limited by the worst performing module. They noticed that the degradation rate of the entire array will match that of the worst performing module which is consistent with the theory that you are as strong as your weakest link. The solder interconnection has been reported as the most failure susceptible part of the PV module system, the dominant factor in PV module degradation and responsible for over 40% of recorded field PV module failures (Herrmann, 2010).

**Table 1.1:** Dominant c-Si PV module failure modes

Source: (Shrestha, 2014; Köntges, 2014)

| S/N | Failure Mode | Failure Cause | Effects |
|---|---|---|---|
| 1 | Back sheet adhesion loss | Movement of cells and solder interconnects, encapsulant gassing due to overheating, poor adhesion of cell metallisation, expansion and contraction of trapped air and moisture, unframed laminates | Exposure of active electrical components, Safety hazards on rainy days, power loss, overheating, corrosion |
| 2 | Burn marks, hot spots | Shading, solder bond failure, ribbon interconnect failure, bypass diode failure, faulty cell or string of cells | Back sheet burn, encapsulant burn, power loss, overheating, electrical arcing, fire hazard |
| 3 | Bypass diode failure | Poor heat dissipation, shading | Hot spots, junction box failure, electrical arcing, fire hazard |
| 4 | Cell cracks | Thermomechanical stress, solder interconnection failure | Power loss |

| S/N | Failure Mode | Failure Cause | Effects |
|---|---|---|---|
| 5 | Encapsulant delamination | UV light, high temperature, high humidity, tempering process caused by stress and weakened adhesion, contamination from the material | Transmission loss, reverse bias heating, power loss, optical reflection, optical decoupling of material |
| 6 | Encapsulant discoloration | High temperature, high humidity, thermal stress, UV light, hot solder joints, inappropriate encapsulant | Power loss, transmission losses, overheating, corrosion, embrittlement of EVA |
| 7 | Junction box failure | High humidity, high temperature, solder bond failure, bypass diode failure | Exposure of active electrical components, electrical arcing, fire hazard, power loss |
| 8 | Potential induced degradation | High temperature, high humidity, UV light, inappropriate encapsulant, back sheet and front cover materials | High leakage current, fraction of energy yield at low light conditions, power loss |
| 9 | Solder interconnection fatigue/failure | Thermal fatigue failure, coarsening of solder bonds, improper design and soldering process, less number of solder bonds | High series resistance, power loss, hot spots, back sheet burns |

| S/N | Failure Mode | Failure Cause | Effects |
|---|---|---|---|
| 10 | Snail tracks | High temperature, UV light, high humidity, thermal stress, inappropriate encapsulant and back sheet materials, hot solder joints | Reduced conductivity of silver contact layer, increases the visibility of cell cracks, power loss |

Hasselbrink *et al.* (2013), in their validation of the PV Life model using 3 million module-years of live site data, comprehensively reviewed the customer fleet returns sheets. They focused on the reasons for returns due to failure over an average deployment period of 5 years. They found that majority (circa 66%) of the returns were due to solder interconnection failures while encapsulant and back sheet failures accounted for about 22% of returns. Shrestha (2014), in the study to determine the dominant failure modes of field aged c-Si PV modules from three different plants, combined experimental and statistical methods, and selection of best method to calculate degradation rates under the hot and dry Arizona climate. It was determined that solder interconnection degradation was the most dominant failure mode in every power plant of the climatic region irrespective of construction material type, orientation, and mounting structure of the modules. On the metrics of risk priority number and defect occurrence, the solder interconnection fatigue failure was ranked the highest. The solder interconnection fatigue failure led to other safety failures like hotspots and back sheet burns, and an increase in series resistance of 20-40% even in the best performing PV modules in all sites. Hence, minimising the effects of solder interconnection degradation on the reliability of c-Si PV modules operating in elevated temperature conditions was the focus of the current study presented throughout this writeup.

## 1.2 RESEARCH PROBLEM / MOTIVATION

PV modules are described as composite structures built with bonded layers of various component materials. These component layers perform various roles ranging from electrical energy generation, to mechanical/structural support and protection from environmental conditions. As their functions differ, so do their material properties, and hence their impact on the reliability of PV modules, especially in harsh non-STCs, is of serious concern. From top to bottom without repetition, the component layers of the c-Si PV module are glass, EVA, copper ribbon interconnect, lead-free solder, silver contact, crystalline silicon PV cell, aluminium and Tedlar Polyester Tedlar (TPT) back sheet. The PV solder interconnection itself comprises of silver contact and copper ribbon interconnect with lead-free solder sandwiched in between joining the two layers.

During high temperature operations, the difference between ambient and cell temperatures is evident so this causes the component layers in the PV interconnection to expand and since they possess distinct material properties, they expand at different rates. During operation of the PV module, the ambient and cell temperatures fluctuate making the component layers expand and contract at different rates. This is attributed to the mismatch in their coefficients of thermal expansion (CTE) (Mallineni, 2013). This CTE mismatch is responsible for the accelerated thermo-mechanical degradation of the solder joint and fatigue failure of the PV system. Figure 1.3 is a schematic of the operation of a PV module in a hot climate.


**Figure 1.3:** Schematic showing the operation of PV Module in a hot climate

Source: (Ogbomo *et al.*, 2018)

During actual operation in hot climate, PV module is exposed to both the heat and light energies of the sun. The PV module was designed for only the light energy of the sun and so, it is therefore operating outside its designed parameters. Figure 1.3 shows that the PV module converts the light energy into useful electrical power, but the unwanted heat energy accelerates the solder interconnection degradation which leads to interconnection fatigue and eventual rupture. The effects of such operating conditions, which differ from the designed standard conditions, on the performance and reliability of PV solder interconnection is thus worthy of investigation.

Bosco, Silverman and Kurtz (2016), investigated the climate specific thermo-mechanical fatigue of flat plate photovoltaic module solder joints. They found that the rate of solder fatigue damage depends on three meteorological factors: mean daily maximum cell temperature, mean daily maximum cell temperature change and number of temperature reversals across a characteristic temperature. They employed an empirical formula which involved these three factors to accurately calculate the PV solder fatigue damage rates in seven cities and thereafter compared to finite element modelling (FEM) simulated results. Chantana, Kamei and Minemoto (2017), quantitatively investigated the influences of environmental factors on the performance ratio of Si-based PV modules after prolonged outdoor exposure using a multiple regression analysis. The environmental factors investigated in their study whose effects

on performance ratio were analysed quantitatively include irradiation intensity, average photon energy, module temperature and angle of incidence. These factors' influence on the crystalline PV modules manifest as degradation mechanisms: the decay of solder interconnection and discoloration of ethylene vinyl acetate film, and the corresponding decay of performance parameters are electrical loss, optical loss, blue-rich spectra, and open-circuit voltage loss.

Ndiaye *et al.* (2013), in their study of the degradation of silicon PV modules in the tropical climate of Senegal in West Africa, affirmed the economic importance of PV module fatigue life. They reported that customers are more critical in their choice of energy sources, with cost effectiveness and return on investment as primary selling points and so fatigue life and lifespan are determining factors. Also, temperature and humidity were identified are the most dominant factors responsible for all observed PV module failure modes, of which solder interconnection breakage topped the list. Additionally, they highlighted that the literature on PV module degradation does not specifically deal with one mode of degradation but rather deals with the degradation of the entire PV module. Hence, they recommended that for an in-depth and thorough study of PV module degradation, one mode of degradation should be investigated at a time.

Several researchers propose that the fatigue life of the solder interconnection can determine the reliability of the entire PV module (Sander *et al.*, 2010; Chandel et al., (2015); Bastidas-Rodriguez *et al.*, 2017; Jordan *et al.*, 2017). It is therefore important to research into the integrity and reliability of PV solder interconnections. Figure 1.4 presents a PV module showing the knee region of solder interconnection. The knee region of the PV solder interconnection is particularly vulnerable to fatigue failure (Ogbomo *et al.*, 2017).

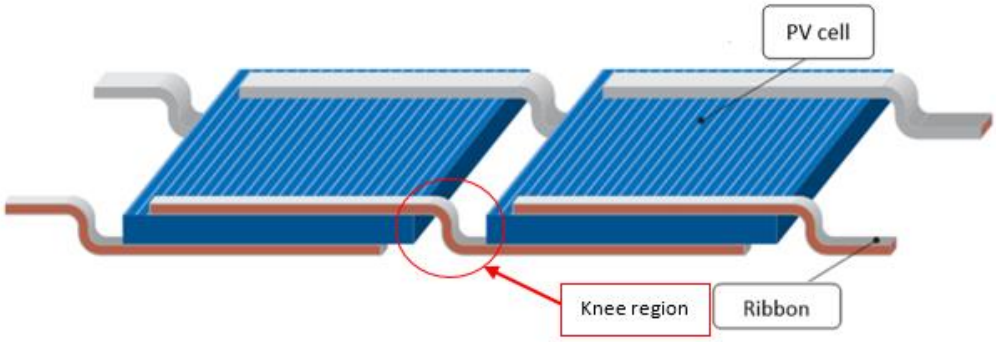


**Figure 1.4:** 2 PV cells connected in a module showing the knee region of solder interconnection

Source: (Ogbomo *et al.*, 2017)

The focus of the current research is to improve the thermo-mechanical reliability of c-Si PV solder interconnections operating at elevated temperatures which deviate significantly from the STC. This will be achieved firstly by investigating the effect of high temperature on the thermo-mechanical degradation of the solder interconnection to identify a numerical relationship between temperature rise from STC and solder interconnection degradation. Secondly, unlike previous research which predicted fatigue life of flip chip solder joints on ball grid arrays in various surface mount technologies at STC, this current study will predict the fatigue life of flat plate composite solder joints in PV modules under varying non-STC temperatures. Thirdly, identified reliability influencing factors will be designed and examined under high temperature conditions and thus, develop optimised c-Si PV solder interconnection model(s) which exhibit improved performance under these hot and harsh climatic conditions.

## 1.3 AIM AND OBJECTIVES

The aim of the study was to optimise reliability influencing factors (RIFs) of c-Si PV solder interconnections for improved performance in elevated temperature climates. The objectives are to:

1. Examine the numerical relationship between temperature rise and c-Si PV solder interconnection degradation and thus establish a fatigue life prediction model under varying non-STC temperatures.
2. Investigate the effect of material combination of bonded materials in c-Si PV solder interconnection on its degradation and thus, propose best material combination(s) for improved PV module performance in elevated temperature climates.
3. Investigate the effect of thickness of bonded materials in c-Si PV solder interconnection on its degradation in elevated temperature climates.
4. Optimise the RIFs (thickness of bonded materials and material combination) of c-Si PV solder interconnections to improve PV module performance in elevated temperature climates.

## 1.4 SCOPE OF RESEARCH

There are several technologies of PV modules and many more state-of-the-art technologies are yet to break into the markets and become commercial. PV module technologies include crystalline silicon, amorphous silicon (a-Si), copper indium gallium selenide (CIGS), cadmium telluride (CdTe), Gallium Arsenide (GaAs), concentrated PV modules, Nano-fibre, silicon germanium and tandem PV modules. In an earlier research published by the author (Ogbomo *et al.*, 2017), the performances of various PV module technologies under hot and harsh climatic conditions were critically

scrutinised. The PV modules were measured against performance parameters including energy payback time (EPBT), temperature coefficient of maximum power output (pMax), low irradiance effect on power output, high temperature effect on power conversion efficiency (PCE), contact recombination losses and thermo-mechanical reliability of solder interconnections. The crystalline silicon PV module was reported to have a pMax value of -0.5% / K which means that for every 1 °K temperature rise from STC, the maximum power output generated decreases by 0.5% (Aste, Pero and Leonforte, 2014). The c-Si PV module performed poorly in the elevated temperature climatic conditions while significantly contrasting with the PV module formed from cadmium telluride cell, back contacts and back-to-back solder interconnections whose maximum power output was unaffected by temperature rise (pMax = 0%). This cadmium telluride PV module was recommended to ensure improved performance in the hot and harsh climate. However, the crystalline silicon PV module possesses the greatest market share at about 84% while the cadmium telluride module has only about 6%. Figure 1.5 presents the market share of commercial PV modules while Fig. 1.6 shows the maximum PCE of the PV modules. GaAs possesses a PCE of 29 % which is currently the highest PCE of any non-concentrated PV cell system. However, due to high costs, GaAs PV modules struggle in the mainstream commercial scene with a market share of 1% and are therefore limited to specialty applications like space power generation.

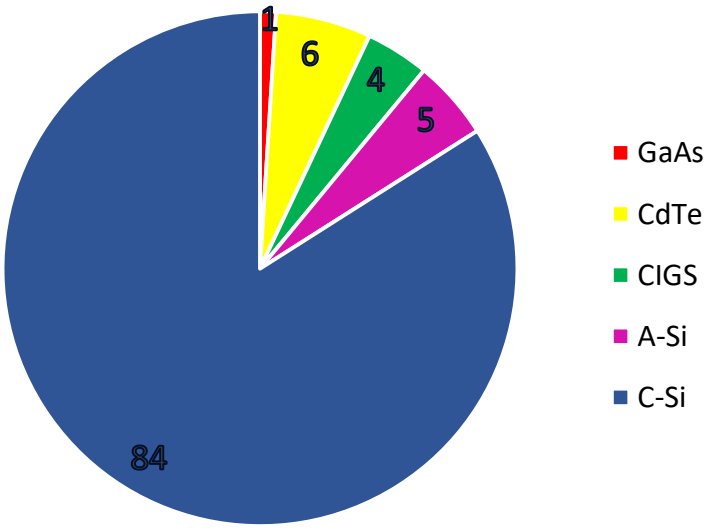


**Figure 1.5:** Market share of PV modules (%)

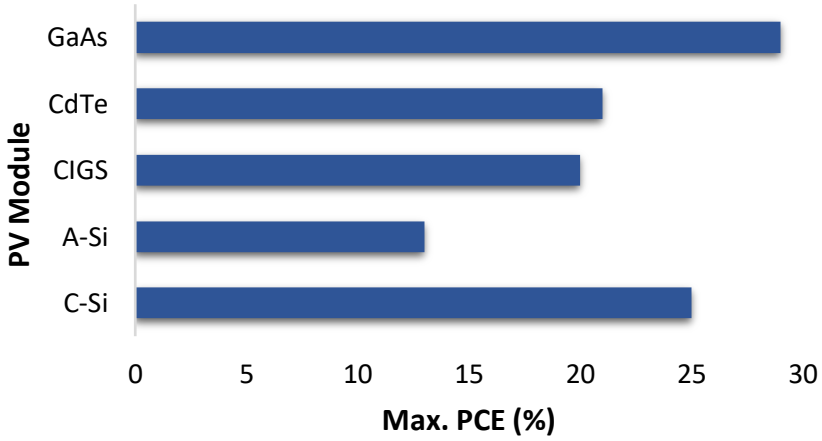


**Figure 1.6:** Maximum PCE of commercial PV modules (%)

There are several reasons for this market dominance of c-Si PV modules over CdTe PV modules which include highest PCE of any mainstream commercial PV module, more available referenceable data on reliability, performance and methodology, and generally they have been around longer hence they are ahead in research and development. Also, CdTe PV modules lose points because of the high cost of raw materials and toxicity of elemental cadmium. Crystalline silicon PV modules are thus still of utmost importance to research but more needs to be done to address their current poor performance in elevated temperature climates. Therefore, this current research focuses on optimising

the reliability influencing factors (RIFs) of c-Si PV solder interconnections to ensure improved performance in the hot and harsh climates.

Solder interconnection degradation has been highlighted as the most common and dominant of all the recorded c-Si PV module failure modes responsible for over 40% of field failures. This was extensively discussed in section 1.1.3 and presented clearly in Table 1.1. In terms of PV solder interconnection technologies, there are various types which include front-to-back and back-to-back solder interconnections. More detailed discussions on PV solder interconnection technologies will be presented in chapter 2. In the current research, the focus will be on the solder degradation failure mode only and the front-to-back interconnection technology will be examined. Also, only the factors causing failure in the normal operation of the c-Si PV module will be considered thus failure caused by manufacturing defects, transport, installation and vandalism will not be considered.

Some previous research (Skoplaki, Boudouvis and Palyvos, 2008; Jordan *et al.*, 2010; Kurnik *et al.*, 2011; Jordan and Kurtz, 2013; Ye *et al.*, 2014) have observed the electrical power degradation of c-Si PV modules due to the failures of their various component parts like glass, cell and encapsulant, but have neglected the contribution of solder interconnection failure. Other studies which have investigated the effects of solder interconnection failure on the performance of the c-Si PV module have done so with focus on electrical power degradation only (Sander *et al.*, 2010; Bastidas-Rodriguez *et al.*, 2017; Jordan *et al.*, 2017). Chandel *et al.* (2015), in their degradation analysis of 28-year field exposed c-Si PV modules in western Himalayan region of India, identified contact and interconnection degradation as the primary failure modes for the modules operating in the hot and harsh climatic conditions. They also reported that the solder interconnection degradation is responsible for increases in shunt and series resistances which lead to decrease in short circuit current and power output of the

c-Si PV module. PV module operations in non-STCs are critical as they affect performance and drives the high failure rates. The current study critically investigates the thermo-mechanical degradation of c-Si PV solder interconnections in elevated temperature climates. Thus, examines the numerical relationship between c-Si PV solder interconnection degradation and temperature rise, establishes fatigue life prediction models under the non-STCs, and proposes optimised combinations of RIFs to ensure improved PV module performance in elevated temperature climates. For the purpose of the current investigation, elevated temperature was defined as PV cell temperature (25 °C ≤ T ≤ 120 °C) and/or ambient temperature (25 °C ≤ T ≤ 45 °C). Chapter 4 of this thesis presents the investigation on the effect of operating temperature on photovoltaic interconnection degradation.

## 1.5 RESEARCH CONTRIBUTIONS

In this study, the RIFs of c-Si PV solder interconnection were optimised for improved performance in elevated temperature climates. The following are the significant research contributions.

1. In the finite element modelling (FEM) of the c-Si PV module, EVA and solder component layers were modelled with viscoelastic and temperature dependent material models instead of linear elastic models used by previous studies. This accounts for the sensitivity of their respective material properties to temperature changes and minimised inaccuracies in c-Si PV solder interconnection deformation results due to nonlinearities. Although, there have been some previous studies where nonlinear modelling of EVA and solder component layers were carried out, none has combined viscoelastic and temperature

dependent models to investigate the degradation of c-Si PV module solder interconnections in the manner presented in this research by the author.

2. In the investigation of c-Si PV solder interconnection degradation due to cell temperature rise from STC, three damage regions were identified with distinct numerical relationships between cell temperature rise and solder interconnection degradation, cell temperature ranges and degradation rates. Region 2, with the highest solder interconnection degradation rate, was identified as critical. The ambient temperatures which fall into this critical region (25°C to 45 °C) were used to investigate the effect of ambient temperature rise on c-Si PV solder interconnection degradation.
3. A fatigue life power function prediction model, $L = 721.48T^{-1.343}$ with a correlation coefficient of 0.9025, was derived. This model is a handy toolkit that can be applied easily and quickly by consumers to predict the lifespan (L), in years, of c-Si PV modules operating in their climatic region at various ambient temperatures (T).
4. To improve the reliability of c-Si PV solder interconnections in elevated temperatures, thirty-six (36) ribbon-contact material combination models from six (6) different materials (Aluminium, Brass, Copper, Silver, Tin and Zinc) were designed and their performances investigated in the ANSYS FEM environment. Four (4) models (Aluminium-Silver, Aluminium-Aluminium, Silver-Silver and Silver-Aluminium) were identified to significantly outperform the commercially conventional c-Si PV solder interconnection and reduce solder degradation by more than 90 % in the region.
5. Taguchi L25 orthogonal array was employed for the robust optimisation of solder interconnection parameter settings (material combination and geometry). From the four (4) proposed ribbon-contact material combination models (in 4

above), one hundred (100) c-Si PV solder interconnection FE models were designed and investigated. The Aluminium-Silver ribbon-contact material combination model (ribbon = 180μm, solder = 56μm, contact = 50μm) demonstrated best performance in elevated temperature climate and reduced solder degradation by 95.1% when compared to the conventional c-Si PV module design.

### 1.5.1 Publications from the research

Parts of this research have been published in high impact international journals and presented at international conferences.

1. **O.O. Ogbomo**, E.H. Amalu, N.N. Ekere and P.O. Olagbegi (2018), Effect of operating temperature on degradation of solder joints in crystalline silicon photovoltaic modules for improved reliability in hot climates. Solar Energy, 170, pp.682-693.
2. **O.O. Ogbomo**, E.H. Amalu, N.N. Ekere, (2017), Reliability influencing factors of PV module interconnections in hot climate. In: proc. of the Faculty for the Future Fellows & Alumnae Forum, Cambridge, United Kingdom, 5-8 November.
3. **O.O. Ogbomo**, E.H. Amalu, N.N. Ekere and P.O. Olagbegi (2017), Effect of coefficient of thermal expansion (CTE) mismatch of solder joint materials in photovoltaic (PV) modules operating in elevated temperature climate on the joint's damage. Procedia Manufacturing, 11, pp.1145-1152.
4. **O.O. Ogbomo**, E.H. Amalu, N.N. Ekere and P.O. Olagbegi (2017), A review of photovoltaic module technologies for increased performance in tropical climate. Renewable and Sustainable Energy Reviews, 75, pp.1225-1238.

5. **O.O. Ogbomo**, E.H. Amalu, N.N. Ekere, (2016), Numerical study on effect of high temperature on degradation of solder joints in photovoltaic module for improved reliability in hot climate. In: proc. Of the 26th International Conference on Flexible Automation and Intelligent Manufacturing (FAIM 2016), KSTC, Seoul, Republic of Korea, 27-30 June.
6. **O.O. Ogbomo**, E.H. Amalu, N.N. Ekere, (2016), Robust solar panel for improved performance in elevated temperature climate. In: proc. of the 4th Annual Research Conference, University of Wolverhampton, United Kingdom, 21st June, pp 26.
7. **O.O. Ogbomo**, E.H. Amalu, N.N. Ekere, (2016), Operation of Solar Energy Systems in Hot Climate. In: proc. of the 4th Annual Research Conference, University of Wolverhampton, United Kingdom, 21st June. This poster won the prize for importance to society.

## 1.6 RESEARCH STRUCTURE

The research structure gives an overview of the research plan carried out throughout the study. It is presented in Fig. 1.7.

## 1.7 THESIS OUTLINE

This study is presented in eight (8) chapters. Chapter 1 presents an overview of the research carried out in this study as the research structure. The background, research problem, aims and objectives, and research contributions are presented in chapter 1. Chapter 2 presents a review of the operations of c-Si PV modules under various climatic conditions, the resulting degradation modes and mechanisms, and the determination of dominant degradation modes in elevated temperature climates. Methodology, design of experiments and modelling procedures are presented in chapter 3. Chapter 4 presents

the investigation of effects of non STC operating temperatures (cell temperatures & ambient temperatures) on c-Si PV solder interconnections degradation. In chapters 5 and 6, the effects of material combination and thickness of bonded materials in the solder interconnection on its degradation are investigated. Chapter 7 employs robust Taguchi L25 orthogonal array to optimise the design points of reliability influencing factors (RIFs) and proposes optimal c-Si PV module solder interconnection model(s) that demonstrate improved performance in elevated temperature climates. Chapter 8 presents conclusions from the research, limitations of the research and recommendations for future work.

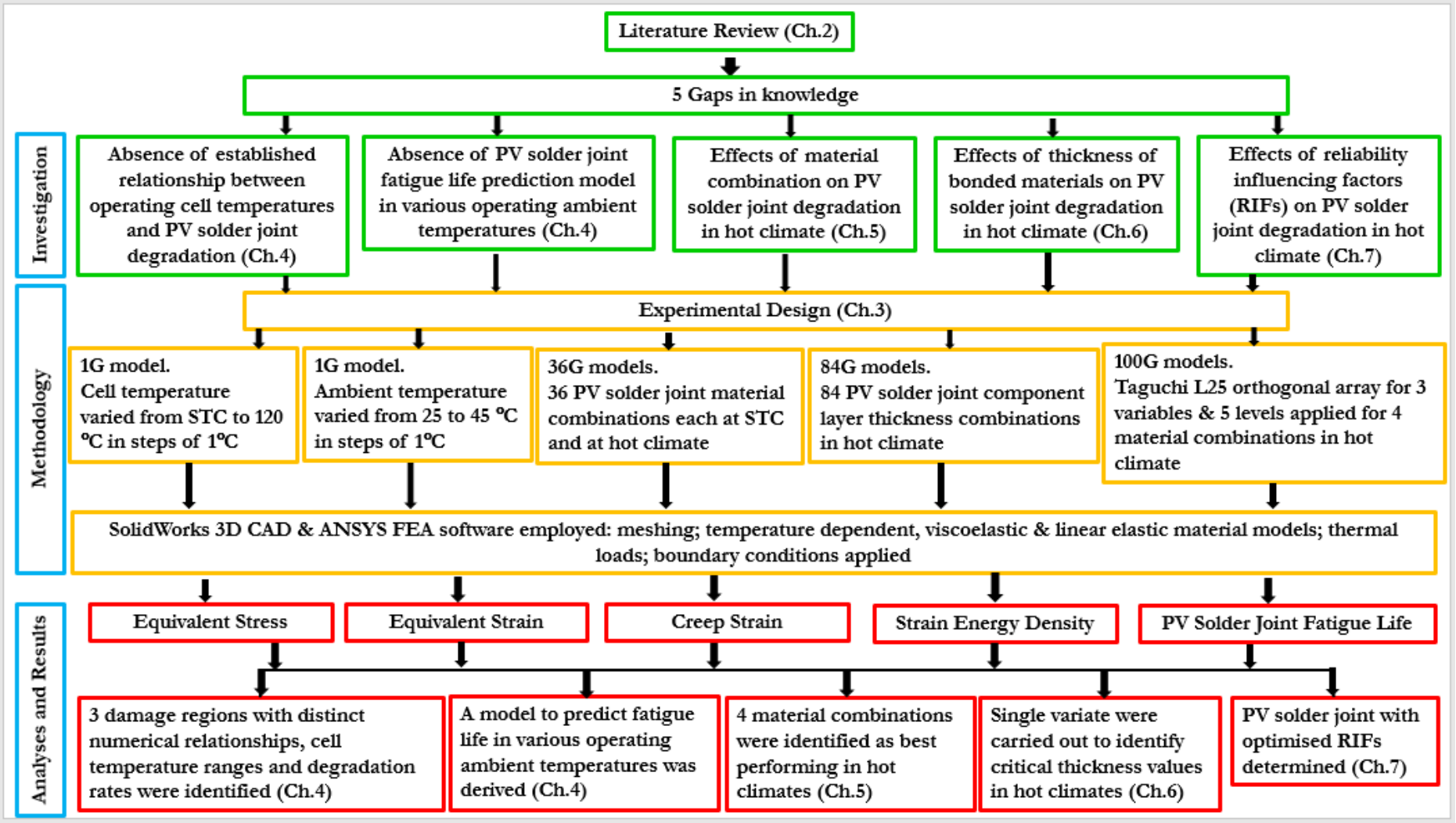


**Figure 1.7:** Research Structure

# CHAPTER 2

# LITERATURE REVIEW

## 2.1 INTRODUCTION

This chapter presents a comprehensive review of relevant research on the operations of c-Si PV modules under various climatic conditions, the resulting degradation modes and mechanisms, and the determination of dominant degradation modes in elevated temperature climates. The common PV module failure modes have been introduced in chapter 1 and presented clearly in Table 1.1. In this chapter, however, the dominant degradation modes of c-Si PV modules operating in elevated temperature climates will be determined using established methods which have been studied previously by several researchers. Methods include visual inspection, Infrared thermography, Electroluminescence imaging, performance parameter tracing, failure modes effects and criticality analysis (FMECA), reliability block diagram (RBD) and fault tree analysis (FTA). After the dominant degradation modes of c-Si PV modules are discussed in detail and their respective mechanisms identified, desired properties for the reliability design of c-Si PV module solder interconnections are considered.

The PV module operating conditions are presented in section 2.2, whilst the PV module dominant degradation modes in hot climate is presented in 2.3, the PV solder interconnection design considerations is presented in 2.4, and section 2.5 summarises the chapter.

## 2.2 PV MODULE OPERATING CONDITIONS

In the service life of c-Si PV modules, performance is dependent on several factors which include design parameters, material properties and operating conditions. The

operating conditions include a large range of parameters which relate to the climate, environment, and/or system configurations.

Working under these operating conditions, PV modules are susceptible to degradation. PV module degradation can be described as the gradual decay of its characteristics which may affect its ability to perform the intended function over a specified interval under stated conditions. When one or more components of the PV module experiences degradation, the entire module is affected. Although it is expected that PV modules, like other similar systems, will exhibit performance degradation over time, customers and other stakeholders are interested in the life expectancy of PV modules. Hence manufacturers have specified the 20/20 and/or 20/25 product warranty for their modules. This means that over their 20-25 years of operation, PV modules will only exhibit a maximum power output degradation of 20% which is a maximum annual degradation of 1% (Belmont, 2013; Smith, 2016). This warranty, printed on the PV module nameplates, can be misleading because the accompanying reliability tests are carried out under Standard Test Conditions (STC) which significantly differ from field operating conditions. There have been recorded values of annual degradation rates as high as 5.6% which is significantly higher than the maximum of 1% promised by manufacturers (Carr and Pryor, 2004).

The c-Si PV modules rely strongly on their attractive long-term return-on-investment to make them viable substitutes to the carbon-based energy sources with less expensive initial costs. Such attributes are considered by investors, developers and general customers in determining appropriate financing, selection and decommissioning of energy sources. When any uncertainty in the longevity and reliability of PV modules is present, the argument for the system as a standalone energy source against the carbon-based sources is significantly weakened. Surmounting the challenge faced by the PV

industry which is to make PV generated electricity cost effective, depends greatly on long-term performance and reliability of c-Si PV modules.

The power output of PV systems depends on stochastic environmental factors like solar irradiance, ambient temperature, wind speed, humidity and cloud cover. These environmental factors vary with weather, climate and region. Thus, the actual PV module power output in field operation varies from the output power rating quoted by the manufacturers which was measured under STCs. Also, PV modules experience different failure modes and mechanisms depending on their operating field conditions (Zaoui *et al.*, 2015). The disparity between the electrical characteristics of PV modules under STCs and those of various field operating conditions, exposes the nameplate data as insufficient in determining the actual performance of the system (Janakeeraman, 2013). In addition to module design, size, cost and energy payback period, it is important to examine the performance and reliability of PV modules under various field operating conditions to ascertain their viability as an off-grid, sustainable and renewable energy source.

This section presents a comparative study of the performance of PV modules operating under cold and hot climatic conditions, and how these operating conditions differ from the standard test conditions (STCs). STCs are discussed in sub section 2.2.1, cold climate applications in 2.2.2 and hot climate applications in 2.2.3.

### 2.2.1 Standard test conditions (STCs)

The Standard Test Conditions (STC) are the set industry standards under which PV modules are tested, compared and rated against one another. The conditions are solar radiation of 1000 W/m², cell temperature of 25 °C, wind speed of 1 m/s and air mass (AM) of 1.5. STCs are laboratory conditions which translate to a combination of the

solar irradiance intensity of a clear summer day, the module temperature of a clear winter day and the solar spectrum of a clear spring day (Zaoui *et al.*, 2015). They are ideal operating conditions for PV modules but are impossible to attain during actual field operations. C-Si PV modules are exposed to a series of tests according to the International Electrotechnical Commission (IEC) 61215 performance standards. There are bespoke performance standards for other PV module technologies, for instance, IEC 61646 is used to test amorphous silicon (a-Si) PV modules. These tests decide which c-Si PV modules meet up with the design qualifications set by manufacturers but since they are carried out under standard conditions, they do not paint the accurate picture and hence do not define nor cover reliability (Arndt and Puto, 2010). The 20/20 and/or 20/25 product warranty given by PV module manufacturers which promise a maximum annual power output degradation of 1% are authorised by the IEC standard tests but are misleading because they are not performed under the actual field operating conditions. For optimum design of PV modules, there is a need to test their performance under field installation conditions to ensure reliability; a major concern for customers and investors. Sections 2.2.2 and 2.2.3 discuss the performance of c-Si PV modules under the non STC conditions of the cold and hot climatic regions respectively. The investigation into the relationship between non STC operating temperatures and c-Si PV module reliability considering fatigue life is presented in Chapter 4 of this thesis.

One of the IEC standard tests used for c-Si PV modules include performance parameter tests. Performance parameters used for the tests include amongst others, the short circuit current ($I_{SC}$), open circuit voltage ($V_{OC}$), maximum power output ($P_{MAX}$) and temperature coefficient (FSEC, 2010). Figure 2.1 presents performance parameters on a current versus voltage (I-V) curve. The red line signifies the output current values against voltage while the values of output power against voltage are plotted on the blue line. $I_{SC}$ is the maximum current value, it occurs when there is no or very low

impedance in the system, and it is measured when $V_{OC}$ = 0. $V_{OC}$, on the other hand, is the maximum voltage and occurs when $I_{SC}$ = 0. At both short circuit and open circuit situations, there is no power output. The maximum power point, $P_{MP}$, of the system is at coordinates ($V_{MP}$, $I_{MP}$).

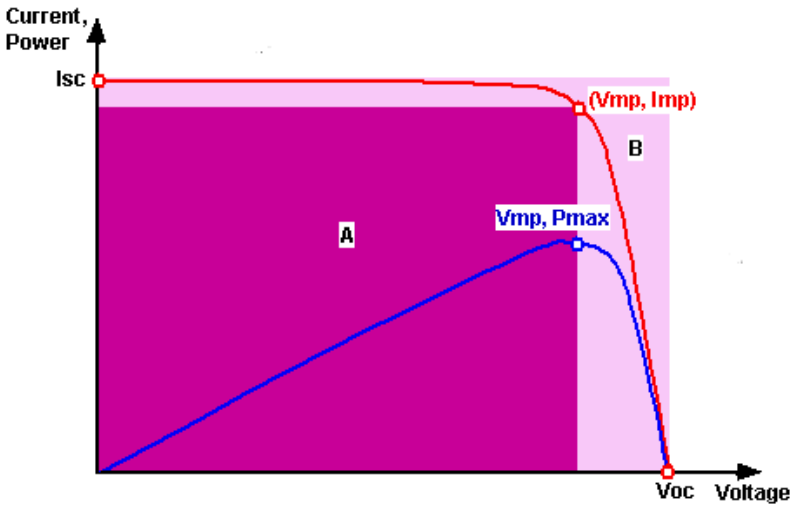


**Figure 2.1:** Performance parameters displayed on I-V curve

Source: (Green, 1981)

There is a measure of PV cell quality known as fill factor (FF) which is a ratio of maximum point power to theoretical power. Theoretical power, $P_T$, is the power output when both $V_{OC}$ and $I_{SC}$ are considered together. FF is different for various PV cells and it is affected by operating conditions. Section 2.3 presents the discussion on the modes, mechanisms and effects of c-Si PV module degradation in elevated temperature climates.

As shown schematically in Fig. 2.1, FF, is the ratio of the largest rectangle to fit under the I-V curve, Area A, to the area bordered by the theoretical power coordinates, Area B. Fill factor is defined in Eqns. 2.1-2.3.

$$FF = \frac{Area\ A}{Area\ B} \qquad \text{Equation 2.1}$$

Inputting the power terms into Eqn. 2.1,

$$FF = \frac{P_{MP}}{P_T}$$ Equation 2.2

Inputting the corresponding current and voltage terms into Eqn. 2.2,

$$FF = \frac{I_{MP} \times V_{MP}}{I_{SC} \times V_{OC}}$$ Equation 2.3

The power conversion efficiency (PCE) is another performance parameter printed on c-Si PV module name plates whose values are based on those measured at STC. PCE is the ratio of the electrical power output, $P_{OUT}$, generated by the PV module to the solar power input, $P_{IN}$. PCE is sensitive to operating condition and this will be discussed in detail in sections 2.2.2 and 2.2.3 under cold and hot climate applications of c-Si PV modules.

The power conversion efficiency is given by:

$$\eta = \frac{P_{OUT}}{P_{IN}}$$ Equation 2.4

And at the maximum power point,

$$\eta_{max} = \frac{I_{MP} \times V_{MP}}{G \times A}$$ Equation 2.5

Where G = solar irradiation at STC 1000 W/m² and A = surface area of PV module (m²).

### 2.2.2 Cold climate applications

For the purpose of this study, the cold climate is defined to include regions outside the latitude lines of the Tropic of Cancer (23° 26´ N) and the Tropic of Capricorn (23° 26´ S). These include regions in the Arctic Circle (66° 34´ N), Antarctic Circle (66° 34´ S) and the Poles (North and South). This region covers Europe, most of Asia except for some countries in South East Asia like India and Singapore, most of North America except some countries in the far south of the continent like Guatemala and Panama, the

extreme south of South America, and the southern half of Australia. Figure 2.2 shows an example of c-Si PV modules installed in a cold climate region.

Unlike the designed operating conditions of c-Si PV modules, discussed in section 2.2.1 under STCs, the cold climatic region is characterised by below zero temperatures especially during winter, shorter days and often murky conditions, low incident sunlight for approximately six months of the year, distinct seasons and seasonal temperatures (Mussard, 2017). In addition to freezing temperatures, PV modules operating in cold climates are exposed to hail impact and snow loading, and their power output is lower than STC projections because of lower annual solar energy potential. However, the average recorded annual degradation rates of c-Si PV modules in this region is 0.5% which is better than the 1% promised by manufacturers. This implies that the lifespan and reliability of the PV module is enhanced in the cold climate region. The increased PCE of c-Si PV modules operating in low temperatures has been reported by several researchers and they have indicated that higher efficiencies at these low temperatures can partially compensate for the shorter and murkier days in the region. Dubey, Sarvaiya and Seshadri (2013), reviewed the temperature dependency of PCE and its effect on PV production in the world. They attributed the increase in conversion efficiency and power output as temperature dropped to decreased electron-hole pair recombination rates and carrier concentrations. Pantic *et al*. (2016), proposed five different models to predict solar module temperature, output power and efficiency in Nis, Serbia. They compared statistical values obtained from their models to experimental values from the field tests in the temperate climate. They determined that the PCE was higher in winter months than in summer months and power conversion efficiency can increase by 12% with a temperature drop of 20 °C. However, power output generated was higher in the summer months than in the winter months due to longer daylight hours and higher solar irradiation.

Although power output generated by c-Si PV modules operating in the predominantly murky cold climates is relatively lower than other operating conditions primarily because of low incident sunlight and irradiation, their power conversion efficiency, fatigue life and reliability flourish under cold (i.e. below STC) temperature conditions. Premature failures are absent, degradation is mostly due to long term field exposure and ageing and hence the PV modules are able to match the 20/20, and/or 20/25 manufacturers design promise.


**Figure 2.2:** c-Si PV module installations in hot climate (a) and cold climate (b) regions

Source: (Packard *et al.*, 2012)

### 2.2.3 Hot climate applications

The hot climate is defined, for the purpose of this study, to include regions within the latitude lines of the Tropic of Cancer which is north of the equator (23° 26´ N) and the Tropic of Capricorn is which south of the equator (23° 26´ S). This region covers most of Africa and Middle East except for countries in the far north and south of the continent like Tunisia and South Africa, most of South America, South East Asia, few

countries in North America, and the northern half of Australia. Figure 2.2 shows an example of c-Si PV modules installed in a hot climate region.

This hot climatic zone includes regions that experience, on average, high temperatures and long sunlight days for most of the year. Hot climates encompass several operating conditions which could be hot and humid or hot and dry. They could be tropical or arid regions. Tropical regions are characterised by dense forests and vegetation, high humidity (35% to 85%), heavy cloud cover, high rates of precipitation, slow wind speeds (0.2 m/s and lower) and high ambient temperatures (18 °C to 40 °C) which can drive c-Si PV module temperatures to as high as 90 °C (Carr and Pryor, 2004; Ogbomo *et al.*, 2017a). Arid regions are known for sparse vegetation if any, low humidity (average of 20%), low rates of precipitation, fast winds leading to sand storms at certain times of the year, and extreme temperatures for day and night as well as summer and winter seasons (as high as 50 °C in summer) (Mohammed, Boumediene and Miloud, 2016). These non STC operating conditions in hot climates significantly affect the performance of c-Si PV modules in the regions. The impact of high temperature operations on the electrical performance parameters of c-Si PV modules has been investigated and reported by several researchers. They have highlighted the low power output, poor power conversation efficiency, and significant temperature coefficient of power output (pMax = -0.5%) of the system under hot climatic conditions. The dominant failure modes observed in the region include discolouration of EVA, delamination of EVA, PV cell damage, solder interconnection degradation and cracking. These non STC operating conditions culminate in higher failure rates and shorter fatigue lives of c-Si PV modules in hot climates. There is the need to mitigate the adverse effects of elevated temperature operating conditions on c-Si PV modules. Hence, the focus of the present research is on improving the thermo-mechanical reliability of the system in elevated temperature climate operating conditions.

Zaoui *et al.* (2015), in their combined experimental and simulation study on the effects of irradiance and temperature on photovoltaic modules, reported that at a constant value of solar irradiation, the power output and power conversion efficiency decrease as cell temperature increases. In their study, they reported that there is a power output decrease of about 54.54 % when they varied cell temperature from 25 °C STC to 100 °C. One of the objectives of the current study seeks to numerically describe the effect of temperature rise from STC on the thermo-mechanical reliability and fatigue life of c-Si PV modules. Chapter 4 of this thesis presents the investigation on the sensitivity of c-Si PV module fatigue life and reliability to temperature rise, and the determination of the numerical relationships between temperature rise and c-Si PV module reliability in form of a power function for predicting the fatigue life in any operating temperature. This power function will provide a toolkit that can be easily used by everyday PV module users as well as the experts involved in the design of c-Si PV modules.

Walsh *et al.* (2012), researched into the performance of commercial PV modules in the Singapore tropical climate and proposed an optimised PV model for the region. Their parameters for PV module performance included short circuit current, normalised module efficiency and a few visual defects like glass corrosion. Similar to other previous studies (Skoplaki, Boudouvis and Palyvos, 2008; Jordan *et al.*, 2010; Kurnik *et al.*, 2011; Jordan and Kurtz, 2013; Ye *et al.*, 2014) where the electrical power degradation of c-Si PV modules due to the damage of component parts like glass, cell and encapsulant, was observed, Walsh *et al.* (2012) have neglected the contribution of solder interconnection failure. They have not considered the thermo-mechanical degradation of solder interconnections, crack initiation, propagation and fracture in the solder layer, and overall fatigue life of the PV module. Also, they neglected the interaction between the component layers of the composite flat plate c-Si PV module especially the solder interconnection which has been reported as the most susceptible

part and responsible for over 40% of PV modules field failures under elevated temperature operating conditions. The focus of this current study is the c-Si PV module performance with emphasis on solder interconnection degradation under elevated temperature conditions in order to improve thermo-mechanical reliability and elongate fatigue life. The interaction between component layers of the c-Si PV module is of interest to the present study especially how their behaviours under elevated temperature operating conditions influence the degradation of the solder interconnection. Chapter 3 provides more details on the design and modelling of the component layers of the c-Si PV module with their respective temperature dependent, viscoelastic and creep properties. Section 2.3 discusses how dominant PV module degradation modes are defined and determined which informs on the decision to place the highest value and attention on solder interconnection degradation rather than other reported field failure modes.

## 2.3 PV MODULE DOMINANT DEGRADATION MODES IN ELEVATED TEMPERATURE CLIMATE

The c-Si PV module is a composite of several component layers which have distinct characteristic functions and material properties. During the operations of c-Si PV modules, these component layers interact with one another and although there are no actual moving parts within the module, degradation and ultimate failure occur. Taking such material interactions and eventual degradation into account, manufacturers' warranty set useful lives at 20-25 years. However, these lifetime figures are arrived at after accelerated tests under STCs which do not reflect actual field conditions. The typical operating conditions of the c-Si PV modules were discussed in section 2.2. Hot climate operating conditions are of utmost importance to the current study because they

have been reported to significantly diminish the performance and reliability of the system. Under elevated temperature climates, the performance of c-Si PV modules degrades significantly that means they are unable to carry out the designed function which is to generate electrical power. Hence, c-Si PV modules experience premature failures, shorter lifespans and are unable to meet the specified manufacturers' warranty. This can be attributed to defects and degradation modes that are at variance to those experienced under STCs.

Section 1.1.3 introduced recorded PV module failure modes and Table 1.1 presented the PV module field failure modes, causes and effects. From Table 1.1, it can be observed that one degradation mode can become the cause of another. In this section, the dominant c-Si PV module degradation modes in elevated temperature climate will be discussed. Section 2.3.1 focuses on the robust methods of determining the dominant c-Si PV module degradation modes and section 2.3.2 discusses the identified dominant degradation modes and their effects on the performance and reliability of the system in hot climate.

### 2.3.1 Determination of dominant degradation modes

The composite nature of c-Si PV modules implies that if one of the components has a problem, the entire system may be at risk. Like the saying goes: "You are only as strong as your weakest link". Over the years, several methodologies have sprung up to determine failure modes and mechanisms of c-Si PV modules. These methodologies are based on historical trends, engineering judgments, and/or qualitative assessments and tests. In the determination of dominant failure modes, it is not enough to monitor defects with highest frequency, but we also need to determine if and how these defects significantly affect the performance output and reliability of the system. Some failure

modes have a greater effect on the performance and degradation rate of the c-Si PV modules hence, they are more detrimental to long term reliability.

Shrestha (2014), in his study to determine the dominant failure modes of 5900 different c-Si PV modules operating in the hot and dry climate of Arizona, differentiated between various forms of degradation which are cosmetic defects, safety failures, durability loss and reliability failure. He applied both experimental and statistical methods to determine dominant failure modes and selected best method to calculate degradation rates. Safety failures exceed mere cosmetic defects because they cause safety issues to the consumer, lead to hazardous operations and do not comply to government regulations for safe operations. Durability loss was described as a "soft" degradation of PV modules that still meet their warranty limit and so do not qualify for warranty claims while reliability failure is a "hard" degradation of the PV modules before their warranty limit and so qualify for warranty claims. Reliability failures include safety failures and exhibit degradation rates greater than 1% per annum. Degradation rates of c-Si PV modules in elevated temperature climates have been reported to be as high as 5.6% per annum (Carr and Pryor, 2004). Figure 2.3 presents the metric definitions of safety failure, reliability failure, and durability loss.

It is known that defects, degradation and eventual failure of PV modules can be dictated by manufacturing errors in design and packaging, transportation and/or operating conditions. For the current study, the focus is on c-Si PV degradation due to effects of operating condition only and more particularly, elevated temperature climate operating condition. All other causes of defects and degradation of c-Si PV modules are considered as negligible.

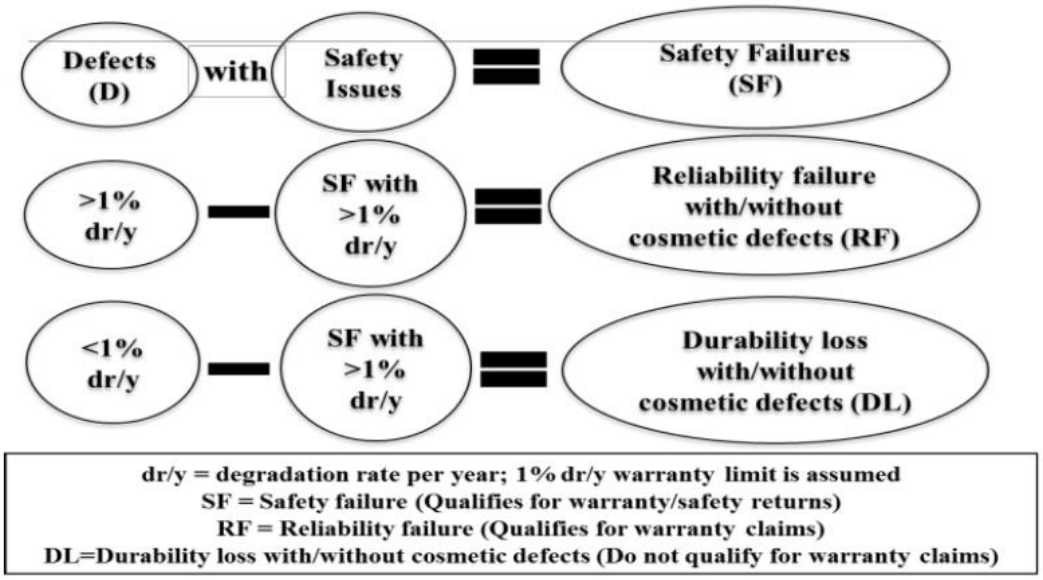


**Figure 2.3:** Metric definitions for safety failure, reliability failure, and durability loss

Source: (Shrestha, 2014)

In the robust determination of the dominant degradation modes of c-Si PV modules operating in hot climates, there are crucial elements to be considered. First, the key degradation mechanisms are identified. It is important to separate the failure mechanisms of c-Si PV modules along the line of significance. This is to avoid spending resources on those failure mechanisms that have no serious effects on the performance of the system. There are several techniques for identification of degradation and some of which are discussed in section 2.3.1.1. The second element to be considered is establishing the effects that the degradation mechanisms have on the reliability goals of the system. This entails defining the economic penalty of the identified degradation mechanisms, frequency of occurrence and severity, and target degradation locations. Mechanisms of degradation can either be localised to component failures, overall module failures or life limiting wear out. In the field of Quality Engineering, robust designs are defined as those that provide the lowest cost solution to desired specifications based on consumer needs (Fowlkes and Creveling, 1995). Costs have been defined to not only include those of materials and manufacturing but also,

losses to society as a result of the deficiency of the product. Quality Engineering and robust designs are discussed further in chapter 3 of this thesis. Failure modes effects and criticality analysis (FMCEA) addresses this second element of the determination of dominant degradation modes. FMCEA is further discussed in section 2.3.1.2.

The quantification of the effects of the degradation mechanisms on performance parameters forms the third element to be considered. The performance parameters are measured under STCs and compared with those obtained under the elevated temperature climate operating conditions. Performance parameters include power output, short circuit current, open circuit voltage, series and shunt resistance, and fatigue life. Performance index and ratio can be derived for adequate comparison. Also, contained in this third element, is defining what physical parameters each degradation mechanism depends on. Some physical parameters include maximum stresses, strain, thermal cycling, component material and geometry, and coefficient of thermal expansion. In chapter 5 of this thesis, five (5) modes performance comparison are derived to relate the reliability of the conventional c-Si PV solder interconnections to that of the proposed material combinations of solder interconnections.

The fourth and final puzzle piece for consideration is developing methods to predict the degradation. After the parameter dependencies are defined, degradation prediction models can be developed. This is done by manipulating aforementioned physical parameters with the aim of accurate useful life prediction and elongation. It is not enough to only highlight the problems i.e. degradation modes without trying to provide solutions. This feeds into the focus of the current study which is to improve the reliability of c-Si PV module interconnections in elevated temperature climate by optimising reliability influencing factors (RIFs). Useful life prediction models not only improve reliability but also increase cost effectiveness of the system and ensures good return on investment. Further discussion on useful life prediction models are presented

in chapter 3 of this thesis while chapter 7 discusses optimisation of RIFs. Reliability block diagram (RBD) and fault tree analysis (FTA) address this fourth element in the determination of dominant c-Si PV module degradation modes under elevated temperature climate operating conditions. RBD and FTA are further discussed in sections 2.3.1.3 and 2.3.1.4 respectively.

#### 2.3.1.1 Degradation mode inspection

The first step in the determination of the dominant degradation modes of c-Si PV modules operating in elevated temperature climates is inspection. In the inspection stage, the normal functions of the system and its component layers are described, degradation modes of each component are identified, the causes and effects of the individual degradation modes on the performance of the system are defined and quantified. There are several methods used for inspecting degradation in c-Si PV modules however, only the key methods namely: visual inspection, Infrared thermography, electroluminescence, and I-V tracer are discussed in this thesis.

Visual inspection is usually the first method applied in the determination of dominant degradation modes of c-Si PV modules. It evaluates and catalogues visually observable defects. It can be said that visual inspection emphasises the symptoms of the degradation modes such as material discoloration and texture changes, rather than diagnosing the root causes such as hot spots and electrochemical migration. Packard, Wohlgemuth and Kurtz (2012), of the National Renewable Energy Laboratory (NREL) developed a visual inspection sheet. This sheet is a clear, concise and easy to use data collection tool which formalises the process for field defects data collection. This visual inspection sheet was developed by evaluating more than sixty (60) PV modules of different technologies and field exposures. The sheet contains fourteen (14) sections

which focus on different components as well as the entire module. A sample of the visual inspection sheet is found in the appendix of this thesis. Recorded defects include scratches, cracks and chips on the glass layer, delamination and discoloration of EVA, cracks and discoloration of solder interconnection, burn marks and bubbles on the back sheet. This visual inspection sheet, often accompanied by photographic evidence, provides consistency, objectivity and is an established toolkit in the detailed data collection of the physical state of PV modules. The visual inspection sheet is tried, tested and used in numerous NREL studies and other mainstream researchers like (Chattopadhyay *et al.*, 2015; Smith, 2016).

C-Si PV modules are sensitive to temperature fluctuations and possess temperature coefficient of power output of -0.5% / K. Visual inspection only, cannot detect such temperature changes. These temperature fluctuations originate from the operating environment which then influences and leads to spikes in cell and module temperatures. In chapter 4 of this thesis, the effect of temperature changes on the reliability of c-Si PV modules operating in various ambient temperatures is discussed further. Infrared (IR) thermography method can be used to detect temperature changes and to locate hot spots in PV modules. IR thermography operates in the electromagnetic radiation wavelength range which is longer than visible light thus generally invisible to the human eye, so they are captured by sensitive IR cameras. The process involves taking an IR image from the backside of the module with the module terminals short-circuited. The IR image is taken at solar irradiation >500 $W/m^2$ to enable proper detection of hotspots. Figure 2.4 presents an IR camera and image. Hotspots have been reported by several researchers as detrimental to the performance of c-Si PV modules and their effects are aggravated in elevated temperature climate operating conditions.

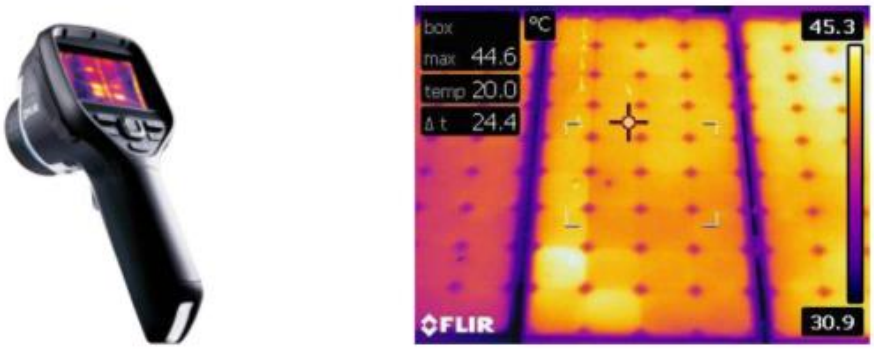


**Figure 2.4:** Infrared camera (left) and Infrared image (right)

Source: (Chattopadhyay *et al.*, 2015)

The third method that is widely used is Electroluminescence (EL) imaging. The EL imaging utilised in the determination of dominant degradation modes of c-Si PV modules in elevated temperature climates exceeds visual inspection and IR imaging in its functionality. EL imaging works based on both optical and electrical phenomena in which light is emitted in a material as a result of electric current passing through it. EL imaging can detect the extent and nature of cracks and breaks in PV cells and solder interconnections. Figure 2.5 shows EL imaging using the image difference technique. The image difference technique extracts an EL image by taking pixel by pixel differences between two (2) EL images (Chattopadhyay *et al.*, 2015). One image is taken with the module terminals in forward-bias and the other in open-circuit. Light regions represent active areas in the c-Si PV module while dark regions signify inactive, cracked and broken areas.

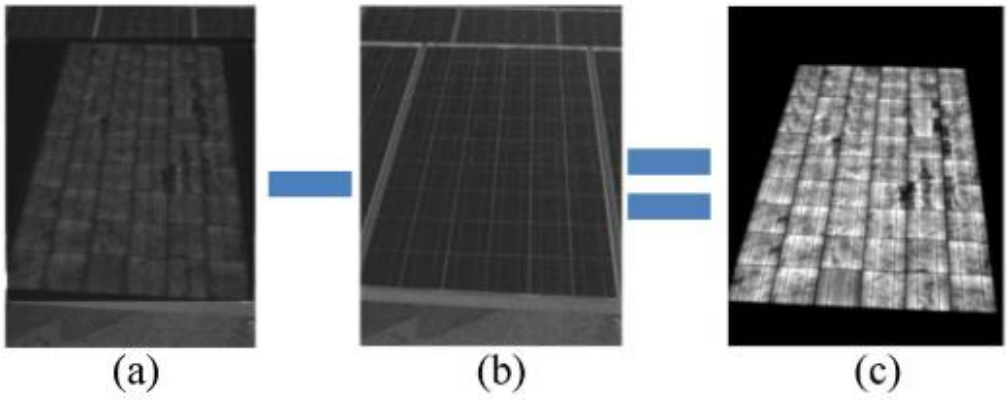


**Figure 2.5:** EL image with module in forward bias (a) EL image with the module in open circuit (b) EL image extracted by image difference technique (c)

Source: (Chattopadhyay *et al.*, 2015)

After cataloguing the c-Si PV module defects through visual inspection, IR thermography and/or EL imaging, it is important to correlate the identified degradation modes with electrical performance parameters using the I-V Tracer method. This correlation provides information to determine if a degradation mode significantly affects the ability of the c-Si PV module to generate electrical power reliably. Degradation modes can be termed benign or dominant depending on significant effects on performance parameters. Current-Voltage (I-V) measurements are done to record performance parameters including short circuit current, open circuit voltage, and power output.

Paggi *et al.* (2014), employed EL imaging to study the fatigue degradation and electric recovery in silicon solar cells embedded in photovoltaic modules. They reported that cracks in PV cells led to increase in series resistance and power output losses of up to 10%. The location of the cracks, nature and direction of crack propagation in the c-Si PV cells can significantly increase their effects on performance parameters. Power output decreases of up to 25 % have been recorded when cracks cross contacts and busbars of c-Si PV solder interconnections. In another study employing EL imaging together with algorithms, differential equations and laboratory experiments, the cracks

in c-Si PV cells were found to increase moisture diffusion. High moisture diffusion leads to inactive PV cells and increased electrical degradation (Lenarda and Paggi, 2016).

Insulation resistance is another important performance parameter that requires measurement. It measures the quality of encapsulant and back sheet materials which provide needed insulation (earthing / grounding) of the PV module. Low levels of insulation resistance raise safety concerns for the personnel handling such modules because they lead to high leakage current which also cause potential induced degradation and performance degradation (Chattopadhyay *et al.*, 2015). Hotspots and snail trail discoloration defects in c-Si PV modules have been found to decrease insulation resistance. Snail trails have also been correlated to micro-cracks and increased moisture diffusion through encapsulants and back sheets. These degradation modes have been linked to a decrease in maximum power output of about 40% from STC reference values (Sitthiphol *et al.*, 2016).

Smith (2016), in his study on the degradation effects in PV modules, described performance degradation of PV modules as a reduction or loss in their ability to attain their designed function which is to generate electrical power over their useful life. He attributed performance degradation to one or more degradation modes of the system. He employed a combination of visual inspections and performance parameter measurement approaches to ascertain and quantify the effects of these degradation modes on the PV modules in the hot climate of Perth, Australia. He used an adapted version of the visual inspection sheet developed by NREL (Packard, Wohlgemuth and Kurtz, 2012). The test subject data were obtained from actual field PV module installations. The Spire 5600SLP Solar Simulator laboratory equipment, located in the Engineering and Energy Department of the Murdoch University, was used to measure performance parameters; $P_{MAX}$, $V_{OC}$, $I_{SC}$, Fill Factor and power conversion efficiency, of the PV modules at STC

and then compared to the performance parameter data obtained over 20 years of field data collection in the hot climate operating conditions. The Spire 5600SLP Solar Simulator has high levels of accuracy and repeatability with maximum repeatability error of 0.15% and maximum measurement error of ±3%. This comparison provided more understanding of the effects that specific degradation modes have on the PV module performance.

Shrestha (2014), applied visual inspection, IR thermography, I-V Tracer and diode tester in his determination of dominant degradations in the hot Arizona climate. He identified degradations at the component layer interfaces of cell-contact, cell-ribbon interconnect and solder interconnection as the most dominant degradation modes. Thermal cycling loads and stresses were found to induce these degradation modes. In the hot climate condition, the primary cause of thermal cycling stress was mismatch between the coefficients of thermal expansion of the component layer materials. As a result, an increase in series resistance and thus decrease in power output of the c-Si PV module were recorded. The series resistance of the module was estimated using the expression in Eqn. 2.6.

$$R_S = CS \times \frac{V_{OC} - V_{MP}}{I_{MP}} \qquad \text{Equation 2.6}$$

Where $R_S$ = series resistance, CS = capacitor amplifier at 0.32 for mono c-Si PV modules and 0.34 for poly c-Si PV modules.

Herrmann (2010), studied how temperature cycling degraded PV modules from seven (7) different manufacturers. He used various tests including visual inspection, EL imaging, I-V measurement, series resistance and insulation resistance. Under day and night temperature change, $\Delta T = 70$ °C, PV cell connector breakage was highlighted as the dominant degradation mode for all the c-Si PV modules from the different

manufacturers. The cell connectors undergo cyclic motion within the encapsulation material causing thermal stresses and eventual breakage due to material fatigue.

#### 2.3.1.2 Failure modes effects and criticality analysis (FMECA)

FMECA is a statistical reliability tool used to methodically identify, analyse and catalogue degradation modes within a system and quantify the effects of such degradation modes on the performance and safe operation of the system. The FMCEA is an extension of its precursor; the failure modes and effects analysis (FMEA). The FMEA does not incorporate the criticality (or risk) element of degradation modes which is a product of severity, occurrence and detection factors. FMEA is one of the earliest and widely used reliability techniques for systematic failure analysis, and it combines qualitative and quantitative methods. It was first used by the United States Military in 1949, then by the National Aeronautics and Space Administration (NASA) in the early 1960s, by the late 1960s, it had been used in the automotive industry, then in the 1980s, it was applied in electronics and semiconductor manufacturing. The IEC 60812 standard, also known as Analysis Techniques for System Reliability, was then introduced for FMCEA procedures in the electronics industry. Today, FMECA is applied to numerous industries including PV systems, food service, software and healthcare (IMCA, 2002; IEC, 2006b; Catelani *et al.*, 2011; Kuitche, Tamizhmani and Pan, 2011).

There are two approaches adopted in FMCEA. They are the bottom up and top down approaches. In its early days, FMCEA was described as a bottom up approach in which every component was scrutinised for any anomalies before then going ahead to determine what effects such degradation modes may have on the performance levels of the system. The bottom up approach can be said to stem from Murphy's Law which

states that everything that can go wrong will go wrong if given the chance to. There have been numerous versions of Murphy's Law over the years and when applied to FMECA, it states that everything that can fail, shall fail and will usually fail at the worst possible moment. Therefore, the bottom up approach of FMCEA considers all component parts of the c-Si PV module as prospective failure points and aims to eliminate their effects on the system or at the very least, minimise them. This bottom up approach is effective by leaving no stone unturned but can be tedious and expensive. Some recent practical applications of FMCEA tend towards a top down approach. For the top down approach to FMCEA, the performance of the c-Si PV module system is observed at a reference point i.e. STC, and then any deviations in performance parameters are noted. Identified degradation modes are then linked to defects in component layers. There are applications in which a combination of the bottom up and top down approaches is used. For the current study, a combination of the approaches to FMCEA is applied to determine the dominant degradation modes of c-Si PV modules operating in hot climates. The objectives of FMCEA are to identify degradation modes, develop models to predict degradation, identify physical parameters for accelerated life tests, highlight costs of degradation modes to the system performance, rank degradation modes according to perceived risk, propose design changes and/or alternatives to operational procedure to minimise degradation modes (Quintana and Kurtz, 2008; Kuitche, 2014; Kuitche, Pan and Tamizhmani, 2014; Shrestha, 2014). The identification of degradation modes from field data has been discussed in section 2.3.1.1. Identification methods discussed include visual inspection, IR thermography, EL imaging, I-V measurement and insulation resistance. The current study is rooted deeply in FMCEA. The aim of the study was to optimise reliability influencing factors (RIFs) of c-Si PV solder interconnections for improved performance in elevated temperature climates. Chapters 4, 5, 6, and 7 of thesis presents proposed changes to the design of

c-Si PV module solder interconnections with the aim of minimising degradation modes aggravated in elevated temperature climate operating conditions and improving the reliability of the c-Si PV module solder interconnection system.

The major focus of FMECA is the determination of risk and risk priority number. Risk (or criticality) is a measure of the consequence of a degradation mode and its probability of occurrence on the system. Risk priority number (RPN) is a metric assigned to each field degradation mode. RPN ranks the degradation modes and it indicates which components are less reliable and prone to failure. The dominant degradation modes can then be determined based on highest RPN. Equations 2.7 and 2.8 present the equations for risk and RPN respectively. With respect to the ranking degradation modes by RPN, their risks to the overall system can be minimised by redesigning elements of the system or changing the operating conditions. The field operating conditions vary from environment to environment, they are different from STC and are difficult to control. The focus of this study is to reduce the risks posed by dominant degradation modes by redesigning the component layers of the c-Si PV module and thereby improve their reliability in hot climates.

$$Risk = severity \times probability\ of\ occurrence \quad \text{Equation 2.7}$$

$$RPN = S \times O \times D \quad \text{Equation 2.8}$$

Where S = rank of severity of the degradation mode, O = rank of the occurrence of the degradation mode and D = rank of the likelihood of detecting the degradation mode.

Severity indicates how the degradation mode affects the performance and safe operation of the system. The rank of severity (S) is a qualitative classification of severity. S is a dimensionless number given to degradation modes according to how serious their effects are on the normal operation of the system. S is high for critical effects and low for non-critical effects. Table 2.1 presents the rank of severity.

**Table 2.1:** Rank of severity

Source: (IEC, 2006b; Catelani *et al.*, 2011; Kuitche, Pan and Tamizhmani, 2014; Shrestha, 2014; OpenAIS, 2015)

| Rank of Severity (S) | Description | Severity |
|---|---|---|
| 1 | No discernible effect | None |
| 2 | Insignificant | Very Minor |
| 3 | Minor cosmetic effect | Minor |
| 4 | Cosmetic effect | Very Low |
| 5 | Slight deterioration of component parts. Reduced performance. | Low |
| 6 | Deterioration of component parts. Reduced performance. | Moderate |
| 7 | Significant degradation of the system. System is operable but at low performance | High |
| 8 | Remote safety concerns. The system is inoperable with loss of primary function | Very High |
| 9 | Safety concerns. Affects safe operation of the system and prevents compliance to government regulations | Hazardous with warning |
| 10 | Safety hazard. Catastrophic with no system operation or noncompliance with government regulations | Hazardous without warning |

Occurrence corresponds to the estimated number of failures that could occur as a result of a degradation mode over a predetermined or stated period which is usually the operational life of the system. The rank of occurrence (O) places degradation modes in levels according to their probability of occurrence over the period. The highest rank is given to the degradation mode with the greatest failure probability and vice versa for the lowest failure probability. The frequency of failure occurrence is calculated using the

cumulative number of module failures per thousand units per year (CNF). Table 2.2 presents the rank of occurrence.

**Table 2.2:** Rank of occurrence

Source: (IEC, 2006b; Catelani *et al.*, 2011; Kuitche, Pan and Tamizhmani, 2014; Shrestha, 2014; OpenAIS, 2015)

| **Rank of Occurrence (O)** | **Frequency CNF/1000** | **Failure Occurrence** |
|---|---|---|
| 1 | ≤ 0.01 module per thousand per year | Remote. Failure is unlikely |
| 2 | 0.1 module per thousand per year | |
| 3 | 0.5 module per thousand per year | Low. Relatively few failures |
| 4 | 1 module per thousand per year | |
| 5 | 2 modules per thousand per year | Moderate. Occasional failures |
| 6 | 5 modules per thousand per year | |
| 7 | 10 modules per thousand per year | High. Repeated failures |
| 8 | 20 modules per thousand per year | |
| 9 | 50 modules per thousand per year | Very High. Failure is almost inevitable |
| 10 | ≥ 100 modules per thousand per year | |

Detection is the likelihood that a degradation mode will be diagnosed, and its resulting effect prevented before it can affect the performance of the system. The rank of detection (D) places dimensionless values on degradation modes based on the possibility of their detection. D is in reverse order to the rank of severity (S) and rank of occurrence (O). The higher the possibility of detection, the lower the value of D and vice versa. Table 2.3 presents the rank of detection.

**Table 2.3:** Rank of detection

Source: (Catelani *et al.*, 2011; Kuitche, Pan and Tamizhmani, 2014; Shrestha, 2014)

| Rank of Detection (D) | Description | Detection |
|---|---|---|
| 1 | Monitoring system itself will most certainly detect | Almost certain |
| 2 | Very high probability (most likely) of detection using visual inspection | Very high |
| 3 | Moderate probability (less likely) of detection using visual inspection | High |
| 4 | Very probability (most likely) of detection using conventional handheld inspection equipment like IR thermography | Moderately high |
| 5 | Moderate probability (less likely) of detection using conventional handheld inspection equipment like IR thermography | Moderate |
| 6 | Very high probability (most likely) of detection using non-conventional handheld inspection equipment like cell line checker | Low |
| 7 | Moderate probability (less likely) of detection using non-conventional handheld inspection equipment like cell line checker | Very low |
| 8 | Very high probability (most likely) of detection using performance parameter measurement equipment like I-V tracer | Extremely low |
| 9 | Moderate probability (less likely) of detection using performance parameter measurement equipment like I-V tracer | Remote |
| 10 | Detection impossible in the field | Almost uncertain |

The FMCEA combines quantitative computation methods of the RPN ranking metric and the qualitative inspection and description of the field operational data. FMCEA has been tried and tested by several researchers. The values for S, O, and D are assigned

based on qualitative analyses and engineering judgements. This can lead to some variation from one study to another. However, the range of reported values is small. Table 2.4 presents the FMCEA of c-Si PV module degradation modes in elevated temperature climate. The degradation modes identified are broken / chipped PV cells, encapsulant delamination, encapsulant discoloration, back sheet warping, solder interconnection damage, PV cell / metallisation discoloration, and burn marks / hotspots. The degradation modes with the top three (3) highest mean RPNs are solder interconnection damage with RPN = 256, encapsulant discoloration with RPN = 143 and PV cell / metallisation discoloration with RPN = 133. These three (3) degradation modes are ascertained as dominant and have the most effect on the performance of c-Si PV modules in hot climates. Section 2.3.2 discusses each of these degradation modes in more detail.

**Table 2.4:** FMCEA of c-Si PV module degradation modes in hot climate

| Degradation Mode | Broken / Chipped PV Cells | | | | Encapsulant Delamination | | | | Encapsulant Discoloration | | | | Back sheet Warping | | | | Solder Interconnection Damage | | | | PV Cell / Metallisation Discoloration | | | | Burn marks / Hot spots | | | |
|---|---|---|---|---|---|---|---|---|---|---|---|---|---|---|---|---|---|---|---|---|---|---|---|---|---|---|---|---|
| | S | O | D | RPN | S | O | D | RPN | S | O | D | RPN | S | O | D | RPN | S | O | D | RPN | S | O | D | RPN | S | O | D | RPN |
| (Sarr *et al.*, 2017) | 5 | 8 | 7 | 280 | 7 | 4 | 6 | 168 | 7 | 8 | 7 | 392 | 8 | 4 | 4 | 128 | 7 | 6 | 8 | 336 | 9 | 8 | 5 | 360 | 9 | 6 | 3 | 162 |
| (Gallardo-Saavedra *et al.*, 2017) | NA | NA | NA | NA | 4 | 4 | 8 | 128 | 4 | 4 | 10 | 160 | NA | NA | NA | NA | 5 | 5 | 10 | 250 | 6 | 4 | 4 | 96 | 4 | 4 | 10 | 160 |
| (Basu, 2015) | NA | NA | NA | NA | 9 | 4 | 2 | 72 | 9 | 10 | 2 | 180 | 8 | 8 | 4 | 256 | 9 | 8 | 4 | 288 | 9 | 8 | 3 | 216 | 9 | 8 | 4 | 288 |
| (Kuitche, Pan and Tamizhmani, 2014) | 1 | 6 | 1 | 6 | 1 | 6 | 1 | 6 | 3 | 10 | 5 | 150 | 3 | 8 | 5 | 120 | 5 | 10 | 4 | 200 | 3 | 6 | 3 | 54 | 2 | 6 | 3 | 36 |
| (Shrestha, 2014) Site 1 | NA | NA | NA | NA | 3 | 7 | 2 | 42 | 3 | 6 | 2 | 36 | 8 | 3 | 2 | 48 | 10 | 6 | 6 | 360 | 3 | 8 | 2 | 48 | 9 | 5 | 4 | 180 |
| (Shrestha, 2014) Site 2 | NA | NA | NA | NA | NA | NA | NA | NA | 6 | 9 | 2 | 108 | 8 | 3 | 2 | 48 | 5 | 9 | 8 | 360 | NA | NA | NA | NA | 2 | 2 | 4 | 16 |

| Degradation Mode | Broken / Chipped PV Cells | | | | Encapsulant Delamination | | | | Encapsulant Discoloration | | | | Back sheet Warping | | | | Solder Interconnection Damage | | | | PV Cell / Metallisation Discoloration | | | | Burn marks / Hot spots | | | |
|---|---|---|---|---|---|---|---|---|---|---|---|---|---|---|---|---|---|---|---|---|---|---|---|---|---|---|---|---|
| | S | O | D | RPN | S | O | D | RPN | S | O | D | RPN | S | O | D | RPN | S | O | D | RPN | S | O | D | RPN | S | O | D | RPN |
| (Shrestha, 2014) Site 3 | NA | NA | NA | NA | 9 | 3 | 2 | 54 | 3 | 10 | 2 | 60 | 8 | 3 | 2 | 48 | 5 | 10 | 8 | 400 | NA | NA | NA | NA | 8 | 4 | 4 | 128 |
| (Kuitche, 2014) | 1 | 6 | 1 | 6 | 1 | 6 | 1 | 6 | 3 | 10 | 5 | 150 | 3 | 8 | 5 | 120 | 5 | 10 | 4 | 200 | 3 | 6 | 3 | 54 | 2 | 6 | 3 | 36 |
| (Francis and Colli, 2014) | 10 | 2 | 4 | 80 | 4 | 4 | 10 | 160 | 8 | 2 | 8 | 128 | NA | NA | NA | NA | 10 | 4 | 6 | 240 | 8 | 4 | 8 | 256 | 10 | 2 | 6 | 120 |
| (Catelani *et al.*, 2011) | 5 | 4 | 5 | 100 | 5 | 3 | 6 | 90 | NA | NA | NA | NA | NA | NA | NA | NA | 6 | 4 | 6 | 144 | 4 | 4 | 5 | 80 | 5 | 3 | 6 | 90 |
| (Kuitche, Tamizhmani and Pan, 2011) | 7 | 2 | 4 | 56 | 7 | 2 | 3 | 42 | 7 | 9 | 1 | 63 | 7 | 5 | 1 | 35 | 6 | 2 | 3 | 36 | 6 | 2 | 3 | 36 | 9 | 2 | 2 | 36 |
| **Mean** | 4.8 | 4.7 | 3.7 | 88 | 5 | 4.3 | 4.1 | 76.8 | 5.3 | 7.8 | 4.4 | 143 | 6.6 | 5.3 | 3.1 | 100 | 6.6 | 6.7 | 6.1 | 256 | 5.7 | 5.6 | 4 | 133 | 6.3 | 4.4 | 4.5 | 114 |
| **Max** | 10 | 10 | 10 | 1000 | 10 | 10 | 10 | 1000 | 10 | 10 | 10 | 1000 | 10 | 10 | 10 | 1000 | 10 | 10 | 10 | 1000 | 10 | 10 | 10 | 1000 | 10 | 10 | 10 | 1000 |

#### 2.3.1.3 Reliability block diagram (RBD)

Reliability block diagram (RBD) is a methodical diagrammatic representation of all the functions of component subsystems required for the successful operation of the system. The system success mode for c-Si PV modules can be set as the 20/20 or 20/25 manufacturers' warranty which implies a maximum annual degradation of 1%, or desired performance parameters like maximum output power obtained at STCs. The RBD method can recognise weak links among component parts, quantify system level reliability for a specified period, identify major contributors to performance degradation, highlight trade-offs between costs and unreliability, and point out where design changes need to be made to ensure improved reliability (Quintana and Kurtz, 2008).

RBD applies Boolean logic to link functioning components needed for the desired performance of the system. One of the fundamental assumptions of the technique is that components (blocks) can only exist in two (2) states: functional (or up) state and failed (or down) state. Another important assumption is that individual events are statistically independent. This means that the failure of one component does not affect the functioning of any other component within the modelled system. RBD technique has been developed according to the IEC 61078 standard and it is primarily applied to systems without repair and where the order in which failures occur does not matter (IEC, 2006a). The assumptions associated with the reliability block diagram limits its application to determine the dominant degradation modes of c-Si PV modules in elevated temperature climate. The limitations of RBD for the current study include firstly, the component layers of c-Si PV modules do not exist only in either functional or failed states as mentioned in the RBD assumptions. The component layers have been reported to deteriorate and result in the performance degradation of the system. Hence performance degradation does not always lead to

total system failure. Secondly, there have been reported cases of one degradation mode being to cause of another which contradicts the statistical independence assumption of the RBD method. In comparison to the FMCEA, the RBD technique lacks the advanced analysis required to address the unique characteristics and degradation modes of c-Si PV modules in elevated temperature conditions.

#### 2.3.1.4 Fault tree analysis (FTA)

Fault tree analysis (FTA) is a top down deduction method that identifies all potential root causes of a system failure. FTA applies Boolean logic to combine series of lower level events which cause higher level events. FTA assumes a functionality failure of the system which is the top event and attempts to highlight all the associated components that could cause such an event to occur. FTA procedure has evolved from the IEC 61025 standard and has been applied to different systems (IEC, 2006c). In the case of c-Si PV modules, the top fault events could be no power output, high performance degradation rate or short fatigue life. In fault tree analysis, events and basic elements may need to occur simultaneously, in place of one another, or in tandem to one another in order to cause the top fault event. In some instances, certain events and basic events may trigger others that are higher up on the tree (IMCA, 2002). FTAs are performed graphically in the form of fault tree modes. Events and fault modes are represented by symbols and logical gate operators. Table 2.5 presents some fault tree symbols and their respective descriptions.

Unlike the FMCEA which is applied for performance and reliability prediction, the FTA is better as a retrospective tool. FTA is more suited to systems requiring repair and thus, may be limited in its application to determine the dominant degradation modes of c-Si PV modules in elevated temperature climates. FTA seeks to

understand how systems fail in order to reduce the risk of a system functional failure. The application of FTA involves using FMCEA as a complementary method (Quintana and Kurtz, 2008).

**Table 2.5:** Fault tree symbols and descriptions

Source: (IMCA, 2002; IEC, 2006c; Quintana and Kurtz, 2008)

| Fault Tree Symbol | Description |
|---|---|
|  | Fault in a box: Fault is as a result of previous faults which appear lower on the tree. Examples of a c-Si PV module faults are no power output, high performance degradation, short lifespan, etc |
| 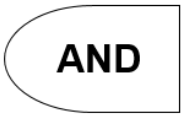 | AND gate: Connects two or more faults that must occur simultaneously to cause the preceding fault which appears higher on the tree. |
| 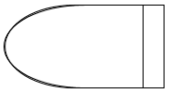 | Priority AND gate: Connects two or more faults that must occur simultaneously and in a certain order to cause the preceding fault which appears higher on the tree |
| 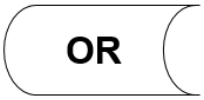 | OR gate: Connects subsequent faults that could cause the preceding fault which appears higher on the tree |
|  | Exclusive OR gate: Fault occurs if only one of the input faults occur |
| 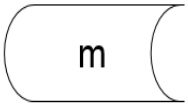 | Voting OR gate: Fault occurs if “m” or more out of “n” input faults occur |
| 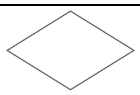 | Fault to be analysed further with more time and/or information |
| 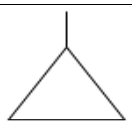 | Transfer in events. Example is ambient temperature |
| 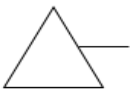 | Transfer out events. |
|  | Root cause of the top fault event. Example of root causes for c-Si PV modules are solder interconnection degradation, encapsulant discoloration and PV cell/metallisation discoloration. |

### 2.3.2 Dominant degradation modes in hot climate

Section 2.3.1 discussed various methods of identifying dominant degradation modes of c-Si PV modules in elevated temperature climate based on their respective effects on performance and cost to the consumer. Amongst other methods, the applications of FMCEA, RBD and FTA as techniques of determining dominant degradation modes were reviewed. Solder interconnection degradation, encapsulant discoloration and PV cell / metallisation discoloration were highlighted as the dominant degradation modes of c-Si PV modules in elevated temperature climates. These identified dominant degradation modes possessed the top three (3) highest risk priority numbers (RPNs) compared to the other recorded field failure modes. Solder interconnection degradation topped the list with the highest RPN. See Table 2.4 for further details. Figure 2.6 presents dominant degradation modes of c-Si PV modules in an elevated temperature climate.

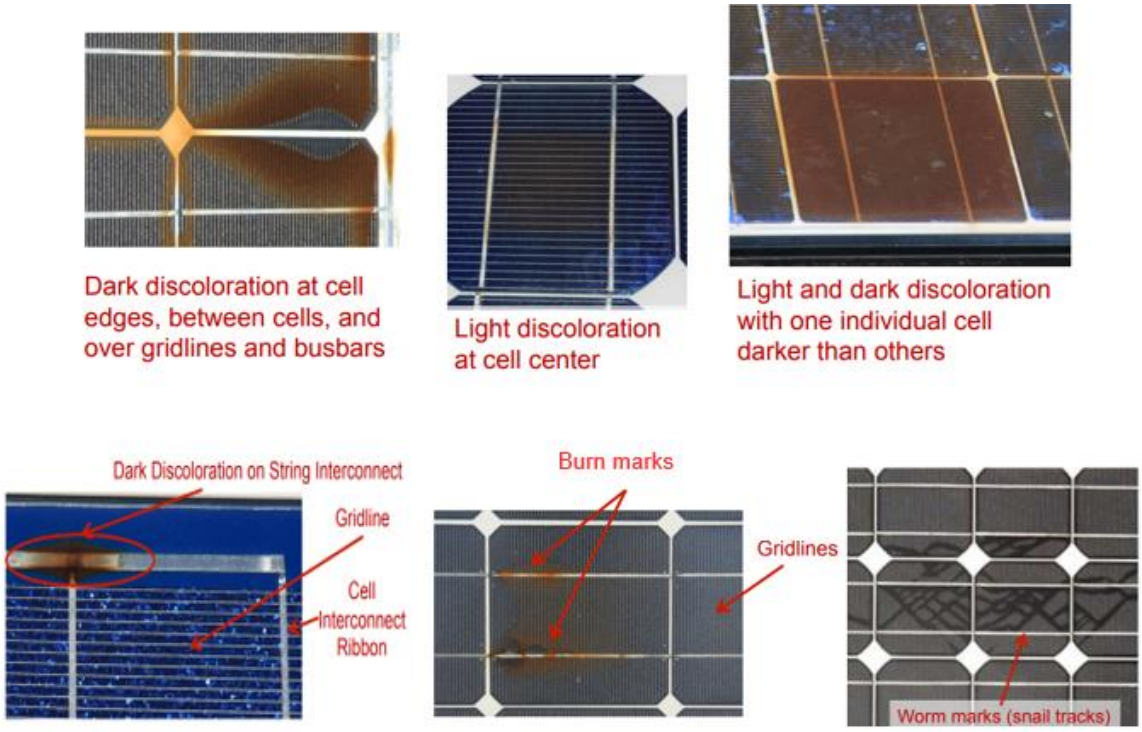


**Figure 2.6:** Dominant degradation modes of c-Si PV modules in elevated temperature climate

Source: (Packard, Wohlgemuth and Kurtz, 2012)

This section discusses the functions of these vulnerable component layers of the c-Si PV module and how their degradation influence system performance in elevated temperature climate operations. PV cell / metallisation discoloration is presented in section 2.3.2.1, encapsulant discoloration in 2.3.2.2 and solder interconnection degradation in 2.3.2.3.

#### 2.3.2.1 PV cell / metallisation discoloration

The PV cell and its metallisation form the basic unit of an electricity generating c-Si PV module. The PV cell is made of electrically neutral semiconductor material which in this case is crystalline silicon. The semiconductor material remains neutral until it is excited by solar energy. The PV cell material absorbs photons in sunlight to create free electrons and their accompanying holes thus, electron-hole pairs are created in the semiconductor material. A contact (i.e. metallisation) is an electrical conductor attached to the PV cell to collect the freed electrons and holes. Positively charged contacts attract electrons and negatively charged contacts attract holes. The contacts form a complete electric circuit with PV cells and enable electric current to flow from the PV cells to a load thereby generating electrical power (Ogbomo *et al.*, 2017). Figure 2.7 presents the components of a typical PV cell. In order to amplify the electric power generated by PV cells, they are connected in strings to form c-Si PV modules. See section 2.3.2.3 under solder interconnection degradation for more details.

The absorption capacity of PV cells determines the power conversion efficiency (PCE) of the c-Si PV module. Not all the incident solar irradiation is converted into useful electric power by PV modules. The PCE of single junction nonconcentrated c-Si PV modules is presently limited to 30% due to several factors including

variation in band gap energy of the incident photons and PV cell material, reflection, heat generation and spaces in the c-Si PV module where the incident photons pass through without meeting any PV cell material (Smith, 2016). Refer to Eqns. 2.4 and 2.5 for PCE relations. PCE is further reduced under high temperature conditions. At high temperatures, the internal resistance of the PV cell material increases hence power output and power conversion efficiency decrease. This can be attributed to an increase in entropy (i.e. degree of disorderliness). Thermal energy infused into the system excites the free electrons which collide with one another and produce even more heat. In this more excited state, free electrons can recombine with holes before they can be collected by positive contacts. This is known as recombination losses.

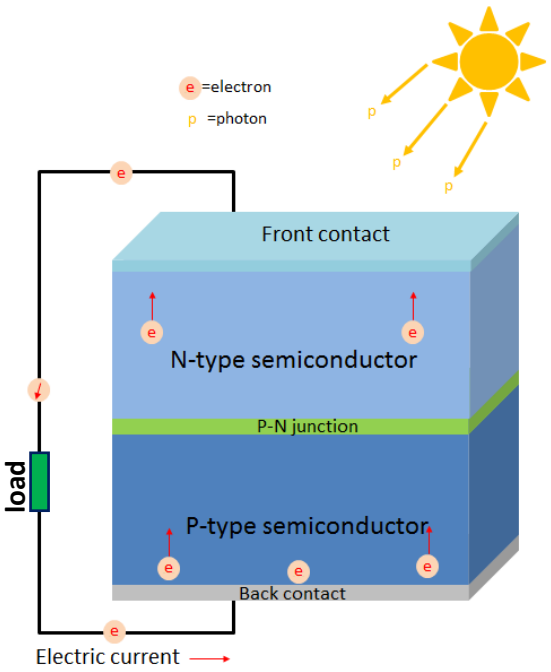


**Figure 2.7:** Components of a typical PV cell

Source: (Ogbomo *et al.*, 2017)

The degradation of c-Si PV cells has been reported as responsible for over 10% of field failures. The inability of an individual PV cell to convert solar irradiation into useful electrical power output can significantly affect other cells and the entire module (Paggi *et al.*, 2014). Therefore, it is justified that PV cell / metallisation

discoloration has been highlighted in this study as a dominant degradation mode of c-Si PV modules operating in elevated temperature climates with the third highest average RPN from the failure modes effects and criticality analysis (FMECA) carried out in section 2.3.1.2. This degradation mode poses a major challenge to the basic function of the system which is to generate electrical power.

Snail tracks (snail trails / worm marks) are a form of discolouration of the PV cell and its metallisation. The name was coined from their appearance and they occur at the front side metallisation of c-Si PV cells. This discolouration influences the ability of the cells to absorb incident solar irradiation and inhibits generation of useful electrical power (Köntges *et al.*, 2017). Some studies have shown that the type of encapsulant used can determine the susceptibility of PV cells to develop snail tracks (Kim *et al.*, 2016). Section 2.3.2.2 discusses further the effect of encapsulant degradation on the other component layers of the c-Si PV module.

PV cell discoloration can force the system into reverse bias. PV cell shading can also cause reverse bias. In reverse bias, the negative region of the cell is connected to the positive terminal and vice versa for the positive region. A high resistance path is created in the circuit which prevents the flow of electric current. In reverse bias, c-Si PV cells fail to convert incident photons to useful electrical power and instead, heat is generated (Van Dyk and Meyer, 2004; Chandel *et al.*, 2015). As heat is produced from a reverse biased PV cell, which is exaggerated under elevated temperature conditions, hot spots and burn marks can occur. Ensuing overheating due to reverse bias leads to premature aging and degradation of other component layers of the c-Si PV module like the encapsulant and solder interconnections. Resulting power output loss can be as high as 33% (Meyer and Van Dyk, 2004; SUNPOWER, 2013; Balato, Costanzo and Vitelli, 2015).

#### 2.3.2.2 EVA encapsulant discoloration

The encapsulant component layer of c-Si PV modules is a polymeric thermoset material that embeds the PV cells and solder interconnections between the glass front sheet layer and the back-sheet layer. The functions of the encapsulant layer can be broadly divided into mechanical, electrical and optical properties. Its mechanical properties include providing structural support, positioning and shock absorbance to protect the brittle PV cells from shocks to the glass and / or back-sheet. Electrically, the encapsulant layer maintains the insulation resistance of the module by isolating the c-Si PV module circuit elements from the environment and avoids short circuits which ensures safe operations. It is also required that the encapsulant attains and sustains low absorbance and high transmittance of the incident solar irradiation in the active spectrum of the PV cells. This optical property of the encapsulant allows the PV cells to generate the maximum possible photocurrent. Recommended initial transmittance of encapsulant have been reported as $\geq 90\%$ with a loss of $< 5\%$ after 20 years (Czanderna and Pern, 1996). It should be noted that these values were arrived at under STCs and the transmittance level is expected to decrease as temperature increases.

Encapsulant materials used in PV modules include Ethylene Vinyl Acetate (EVA), Polyolefin (PO) elastomers and several silicones. EVA is the leading encapsulant used in c-Si PV modules. This is because of its ability to conserve and balance the required mechanical, electrical and optical properties under UV and high temperature exposure, and ensure reliable performance of the c-Si PV module (Köntges *et al.*, 2017). Although, there is growing research interest in PO elastomers, EVA remains the main encapsulant and is used for the design of the c-Si PV models investigated in this study. The degradation of EVA begins with the formation of acetic acid (HAc) followed by photooxidation and breakage of main polymer chains. The degradation

of the optical properties of EVA is manifested as discoloration (yellowing or browning) of the polymeric material (Pern, 1996). Under standard test conditions, EVA discoloration is expected to occur towards the end of the 20-25-year service life. Referring to the reliability bathtub curve of c-Si PV modules, EVA discoloration effects ought to manifest after the warranty and into the wear out failure region. However, under hot climate operations, EVA discoloration is experienced mostly in the midlife failure region and sometimes in the infant failure region which are both well before the warranty line (Meydbray and Dross, 2016). EVA discoloration was determined as a dominant degradation mode of c-Si PV modules operating in hot climates with the second highest average RPN from the FMECA carried out in section 2.3.1.2. This degradation mode is detrimental to the basic purposes of EVA which means there is an increase in solar incident light absorbance by EVA and a corresponding decrease in sunlight transmittance to the PV cells. This situation poses a major challenge to the primary function of the system which is to generate electrical power.

Köntges *et al.* (2017), in their assessment of photovoltaic module failures in the field, quantified the effect of EVA discoloration on power output using a performance parameter known as short circuit current density. They ascertained that the power output loss caused by EVA discoloration also depends on the quantum efficiency (QE) of the PV cell in the same spectral range as the absorption of the chromophores. Chromophores are the parts of a material responsible for its colour. A linear correlation was established between the generated electric current at a given spectral wavelength and the absorbance of the EVA at this wavelength. An increase in absorbance of EVA decreases the short circuit current density and power output. Equations 2.9 and 2.10 respectively, present the short circuit current density of the

c-Si PV module before and after external losses like absorbance of EVA are considered.

$$J_{SC} = q \int_0^{\infty} [I(\lambda)\, EQE(\lambda)\, dI\,] \qquad \text{Equation 2.9}$$

Where $J_{SC}$ = short circuit current density, q = elementary charge, I = incident light spectral intensity, λ = wavelength and EQE = external quantum efficiency.

$$J_{SC} = q \int_0^{\infty} [I(\lambda)\, \big(1 - R(\lambda) - A(\lambda)\big)\, EQE(\lambda)\, dI] \qquad \text{Equation 2.10}$$

Considering external losses, A = absorbance of EVA and R = reflection of the incident light on the front sheet of the module.

The losses in short circuit current and power output induced by EVA discoloration start out at a constant rate and then the degradation rate increases as absorbance of EVA increases. There have been reported cases of short circuit current losses of 10% per year in high temperature climates. EVA degradation is aggravated in high temperatures and has detrimental effects on PV cells and solder interconnections.

In this study, EVA component layer is modelled as viscoelastic with temperature dependent material properties. This model of EVA considers how its behaviour affects other component layers of the c-Si PV module and produces results that are closely related to field failure data (Paggi, Kajari-Schröder and Eitner, 2011). Previous researches have modelled EVA as linear elastic which ignores any effects on PV cells and solder interconnections (Jordan *et al.*, 2017). Chapter 3 of this thesis discusses the material models of c-Si PV module component layers.

#### 2.3.2.3 Solder interconnection degradation

C-Si PV cells are connected in series to form strings of cells and then these strings are connected in parallel to form PV modules. This is achieved using solder

interconnections to sum up power output generation from individual cells. The conventional c-Si PV module interconnection consists of copper ribbons and silver contacts with solder alloy sandwiched in between. The front-to-back orientation of solder interconnections is considered in this study. This means that c-Si PV cells are connected from the front of one cell to the back of the adjoining cell and so on throughout the module. Figure 2.8 presents c-Si PV cells interconnected in a module. Figure 2.9 presents the front-to-back orientation of c-Si PV module interconnections.

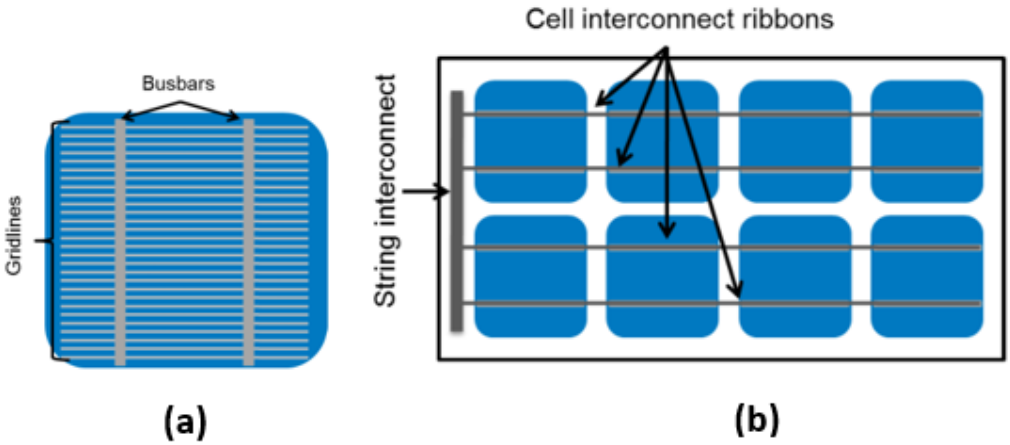


**Figure 2.8:** c-Si PV cell showing gridlines and busbars (a) c-Si PV cells connected in a module (b)

Source: (Köntges *et al.*, 2014)

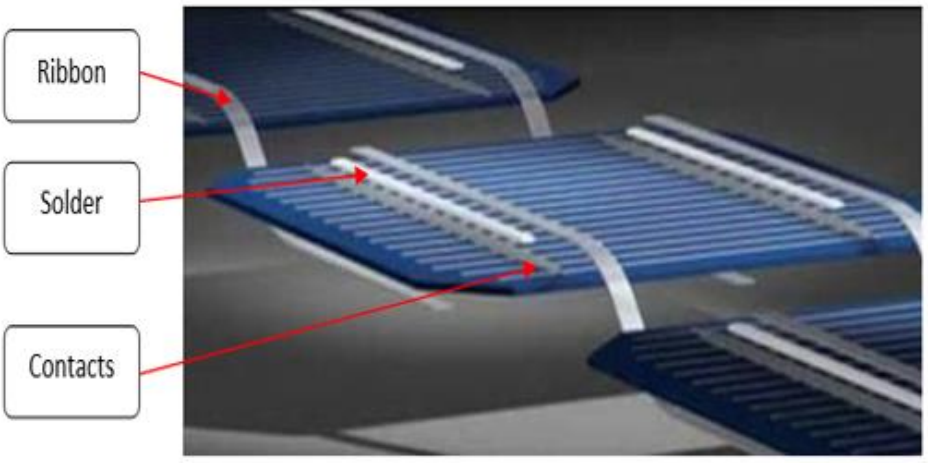


**Figure 2.9:** Front-to-back c-Si PV module interconnection

Source: (Adcock and Henckens, 2011)

PV solder interconnection degradation has been reported as responsible for over 40% of recorded field failures of c-Si PV modules and failure rates are thought to be higher in elevated temperature climates (Ogbomo *et al.*, 2017). Solder interconnection degradation was highlighted as a dominant degradation mode of c-Si PV modules operating in elevated temperature climates with the highest average RPN from the FMECA discussed in section 2.3.1.2. As solder interconnection degradation has been found to be the most dominant of the degradation modes of c-Si PV modules operating in elevated temperature climates, it has been selected as the primary focus of this study. Chapters 4, 5, 6 and 7 will present the results of the study on the design and optimisation of key factors that influence thermomechanical reliability of c-Si PV module solder interconnections in elevated temperature climates and the recommendations for enhancing their fatigue life.

Solder interconnection degradation has been attributed to the mismatch between the coefficients of thermal expansion (CTE) of its bonded component layer materials (copper ribbon, solder alloy and silver contacts). Expansion and contraction of bonded component materials induce degradation in the solder interconnection (Hui *et al.*, 2013; Zarmai *et al.*, 2015). Figure 2.10 illustrates the solder interconnection under flexural loading due to CTE mismatch of the bonded materials. The silver contact layer with higher CTE will expand more than the copper ribbon with lower CTE (Ogbomo *et al.*, 2017). This CTE mismatch leads to thermo mechanical induced cyclic stresses and strains in the solder joint. What follows is crack initiation, crack propagation, and fatigue failure which cause premature aging and limits useful life. Under elevated temperature operating conditions, this degradation mode of c-Si PV modules is aggravated and can manifest in various forms. They include thermomechanical fatigue of solder bond, and ribbon breakage (Mallineni, 2013). One disconnection of solder interconnections can result in high series resistance and

power output losses of up to 35% (Köntges *et al.*, 2014). The current study aims to design reliability into c-Si PV modules by limiting the effects of CTE mismatch between bonded materials of solder interconnections. Section 2.4 discusses some design considerations of c-Si PV module interconnections and chapter 5 of this thesis presents the investigation on the effect of material combination on solder interconnection degradation in elevated temperature climate.

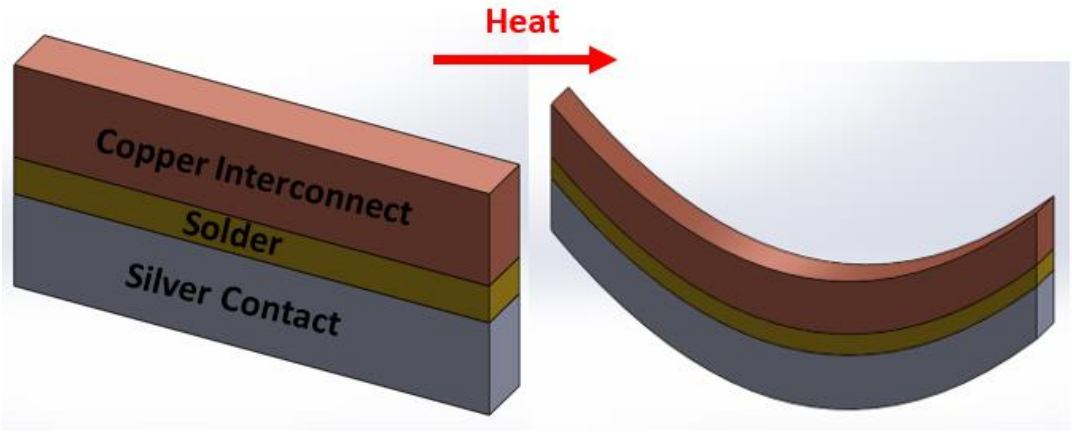


**Figure 2.10:** Solder interconnection showing effect of differential material expansion rate

Source: (Ogbomo *et al.*, 2017)

Rajput *et al.* (2016), performed a comprehensive analysis of the degradation mechanisms of ninety (90) c-Si PV modules exposed to the hot climate of Gurgaon, India. Visual inspection, thermal imaging, I-V parameters, insulation resistance and degradation rate were some of the methods applied to quantify c-Si PV module degradation in their investigation. Of all observed defects, those that occurred in busbars, cell ribbon interconnects and string ribbon interconnections were highlighted as most frequent. These degradation modes caused significant power output degradation. Average power output degradation = 1.9% / year and maximum power degradation = 4.1% / year. Both values are higher than the manufacturers' warranty of a maximum 1% / year power output degradation.

Belmont (2013), employed visual inspection method, IR thermography and electrical performance parameter monitoring in his study to evaluate the degradation and reliability of one hundred (100) c-Si PV modules operating in the hot climatic region of Arizona, USA. Amongst the different degradation modes identified, solder bond fatigue and ribbon interconnect breakage were determined to be the most serious mode with the most detrimental impact on generated electrical power. The ribbon interconnects broke away from the connecting busbar as a result of thermal expansion and contraction. Thermomechanical fatigue ensued in ribbons due to this thermal cyclic load. As the ribbons broke, the pathways for current flow reduced hence a power output loss of 40% was observed.

Ghani *et al.* (2015), studied how cell temperature affects electrical performance parameters of c-Si PV modules using experimental and numerical methods. They determined the electrical behaviour of the modules under ten (10) cell temperature loads (T = 25 °C, 30 °C, 35 °C, 40 °C, 45 °C, 50 °C, 55 °C, 60 °C, 65 °C, 70 °C) using a single diode five (5) parameter model. The performance parameters observed were photogenerated current, reverse saturation current, series resistance, shunt resistance and diode ideality factor. These parameters were experimentally measured, and their obtained values compared to those obtained from the model. Applying Kirchhoff's laws, they obtained the single-diode-five-parameter characteristic model. Equation 2.11 presents the characteristic model. A program using MATLAB software was used to solve the partial differential equations required to assemble to Jacobian matrix and numerically solve the parameter model using the Newton–Raphson method.

$$I = I_{PH} - \frac{V+IR_S}{R_{SH}} - I_0\left[e^{\left(\frac{V+IR_S}{n\,V_{TH}}\right)} - 1\right] \qquad \text{Equation 2.11}$$

Where I = current, $I_{PH}$ = photogenerated current, V = voltage, $R_S$ = series resistance, $R_{SH}$ = shunt resistance, $I_O$ = reverse saturation current, n = diode ideality factor and $V_{TH}$ = thermal voltage.

The root-mean square error analysis (RMSE) was utilised to quantify the accuracy of the applied method by comparing values obtained from experiments ('exp') and those from the characteristic model ('model'). Equations 2.12 - 2.13 were applied in the RMSE analyses. The lower the RMSE value, the greater the accuracy of results. RMSE values in this case were below 0.006 which is highly accurate.

$$MSE(i_{exp}, i_{model}) = \frac{1}{N}\sum_{i=1}^{N}(i_{exp} - i_{model})^2 \quad \text{Equation 2.12}$$

$$RMSE = \sqrt{MSE} \quad \text{Equation 2.13}$$

Their findings showed that as temperature increased from T = 25 °C to T = 70 °C, the serious degradation occurred in cell solder bonds, interconnection ribbons, and cell metallisation. As a result, series resistance greatly increased by 65%, photogenerated current increased moderately by 5.87%, reverse bias current significantly increased by 2700% and power output decreased by more than 25%.

The degradation of electrical performance parameters of c-Si PV modules has been studied and reported by numerous researchers. However, the bespoke thermomechanical degradation of c-Si PV module solder interconnections due to high temperature operating conditions remains to be thoroughly investigated. There have been some strides to ascertain the high temperature performance of solder joints, but these are limited to ball grid arrays in printed circuit boards and other surface mount electronics technologies (Ghaffarian, 2000; Amalu *et al.*, 2011; Otiaba *et al.*, 2013; Qin *et al.*, 2015). The ball grid array has a different solder alloy (mostly lead based solder), solder shape, size and orientation from the composite c-Si PV module solder interconnections (Guyenot *et al.*, 2011). However, Zarmai (2016),

modelled the performance of c-Si PV module solder interconnections to predict their reliability using finite element modelling (FEM). He sought to design the solder joints against fatigue failure. He designed nine (9) different models with different combinations of chosen solder joint geometrical parameters. Designed solder joint parameters were solder joint thickness, solder joint width and intermetallic compound (IMC) thickness. The number of cycles to failure of each model was predicted and thermomechanical stresses and strains at the solder joints were considered. His reported optimised model demonstrated an 18% improvement in cycles to failure when compared to the experimental value.

This study advances the work carried out by Zarmai (2016), and other researches in several ways. It reports on studies focused on providing understanding on the degradation of flat plate composite solder interconnections and the approaches for improving the thermomechanical reliability of c-Si PV modules operating in hot climate conditions. To this end, first, a numerical relationship will be established between operating temperature (PV cell and ambient temperatures) and the fatigue life of c-Si PV module interconnections. Unlike Zarmai (2016) where the investigation was carried out under standard test conditions, chapter 4 of this thesis considers actual elevated temperature climate field temperatures and their resulting effects on the reliability of the system. Secondly, material combination as well as geometry has been included as reliability influencing factors which determine the performance of c-Si PV module interconnections in elevated temperature climate. Mismatch between the physical properties of component layer materials has been highlighted as a major cause of thermal cycle stresses responsible for the thermomechanical degradation of c-Si PV module interconnections most especially in elevated temperature climates. The effect of material combination on the reliability of c-Si PV modules in elevated temperatures is addressed in chapter 5 of

this thesis. Thirdly, a robust Taguchi L25 orthogonal array is applied to optimise reliability influencing factors and determine optimal model(s) which improve performance of c-Si PV modules in elevated temperature climates. Zarmai (2016), applied a less robust Taguchi L9 array in his study. More details on the design of experiment is presented in chapter 3 of this thesis. Fourthly, unlike previous studies on the thermo-mechanical reliability of c-Si PV modules, a combination of viscoelastic and temperature dependent material models are applied in the finite element modelling (FEM) of c-Si PV module interconnections. Applying viscoelastic and temperature dependent material models in the FEM investigations of c-Si PV modules have been reported to produce results which are closely related to laboratory experimental results and minimise simulation errors due to nonlinearities (Eitner *et al.*, 2011; Paggi, Kajari-Schröder and Eitner, 2011).

## 2.4 PV SOLDER INTERCONNECTION DESIGN CONSIDERATIONS IN ELEVATED TEMPERATURE CLIMATES

The functions of c-Si PV solder interconnections can be broadly divided into electrical, thermal and mechanical functions (Chung, 2001; Wohlgemuth and Kempe, 2013; Kraemer and Wiese, 2014). The electrical power generated by individual c-Si PV cells is summed up when they are connected by solder interconnections to form strings and modules. Also, solder interconnections provide structural and mechanical support to the c-Si PV cells by keeping the arrangement in place within the module. Additionally, the solder interconnections dissipate heat from working c-Si PV cells during operation. To perform expected functions, solder interconnections require certain qualities.

The performance of c-Si PV modules in elevated temperature climates has been reported as poor with higher failure rates and shorter useful life. Solder interconnection degradation has been reported as the most dominant degradation mode of the system in the region. In order to design reliability into c-Si PV modules which is the aim of this study, novel combinations of bonded materials in the solder interconnection will be proposed. The performance of these proposed material combinations will be compared to that of the conventional c-Si PV module solder interconnection in elevated temperature climates. Chapter 5 discusses the investigation on the effect of bonded materials in the solder interconnection on its degradation. However, before getting into more details of the proposed material combinations, it is important to understand what desired properties of solder interconnections are considered in its design especially for elevated temperature operations (Nadimpalli and Spelt, 2010; Liu, Johnston and Snaith, 2013; Kraemer and Wiese, 2014; Zarmai *et al.*, 2015).

The mismatch between the coefficients of thermal expansion of bonded materials in solder interconnection has been repeatedly attributed to its degradation especially in elevated temperature climates. The author previously recommended that materials with closer CTE values are to be used to minimise thermomechanical stress and strain, and improve reliability (Ogbomo *et al.*, 2017). Temperature rise increases deformation and strain in a material. Equations 2.14 – 2.17 relate temperature rise to deformation, strain and stress in a material.

$$\delta = \alpha L \Delta T \qquad \text{Equation 2.14}$$

$$\varepsilon = \frac{\delta}{L} \qquad \text{Equation 2.15}$$

Where δ = deformation, $\alpha$ = CTE, L = initial length, ΔT = temperature rise, and ε = strain.

Combining Equations 2.14 and 2.15,

$$\varepsilon = \alpha \Delta T \qquad \text{Equation 2.16}$$

It is known that stress is directly proportional to strain. This implies that stress also increases as temperature rises.

$$\sigma = E\varepsilon \qquad \text{Equation 2.17}$$

Where σ = stress and E = Young's Modulus

Heat accumulation in c-Si PV modules is responsible for majority of its degradation modes and is detrimental to electrical power output, power conversion efficiency, thermomechanical reliability and performance. Elevated temperature condition impacts the quantity of heat accumulated in the bonded materials of solder interconnections. Equation 2.18 relates temperature rise to quantity of heat accumulated in a material.

$$Q = mc\Delta T \qquad \text{Equation 2.18}$$

Where Q = quantity of heat, m = mass of the material and c = specific heat capacity. For each degree temperature rise, there is a corresponding increase in quantity of heat accumulated. High thermal conductivity is a desired property of bonded materials in solder interconnections to achieve good heat management and efficient heat dissipation.

High temperatures are known to increase the resistivity (i.e. internal resistance of a material to the flow of electric current) and decrease conductivity. At elevated temperatures, the freed electrons in the material are thermally energised so they vibrate and collide with one another. The electrons' resistance to the flow of electric current increases and electrical conductivity is impeded.

$$\rho = \rho_0 \left[1 + t_\rho(\Delta T)\right] \qquad \text{Equation 2.19}$$

Where $\rho$ = final resistivity, $\rho_0$ = initial resistivity and $t_\rho$ = temperature coefficient of resistivity. Resistivity is directly proportional to electrical resistance.

$$R \propto \rho \qquad \text{Equation 2.20}$$

$$R = R_0\,[1 + t_\rho(\Delta T)] \qquad \text{Equation 2.21}$$

Where $R_0$ = initial resistance and $R$ = final resistance. Equation 2.19 – 2.21 imply that as temperature rises, resistivity and electrical resistance increase. In turn, electrical resistance influences generated electric current and power output. Equations 2.22 and 2.23 relate electrical resistance to electric current and power output.

$$I = \frac{V}{R} \qquad \text{Equation 2.22}$$

$$P = I^2R \qquad \text{Equation 2.23}$$

Where I = electric current, V = voltage and P = electrical power output. At constant voltage, increase in electrical resistance leads to decrease in electric current and consequently decrease in power output.

Electrical resistance is also related to cross-sectional area (A) of a material. Equation 2.24 presents this relation. As the cross-sectional area (A) decreases, the electrical resistance increases.

$$R = \frac{\rho L}{A} \qquad \text{Equation 2.24}$$

Increase in series resistance has been attributed to various modes of degradations in c-Si PV modules. Series resistance is an established obstacle to electric current and power output generation. It is important to minimise resistance to the flow of electric current as much as possible. (Van Dyk and Meyer, 2004). High resistivity is not desired in solder interconnections instead high electrical conductivity is. Chapter 6 of this thesis presents the investigation on the effect of thickness of bonded materials in

solder interconnection on the degradation of c-Si PV module solder interconnections and proposes geometrical dimensions that will achieve improved reliability in elevated temperature climates.

## 2.5 SUMMARY

An in-depth review of the operations of c-Si PV modules under various climatic conditions and resulting degradation modes and mechanisms has been presented in this chapter. Standard test condition (STC), cold and hot climate operations were considered. Performance parameters including electric current, generated power output, power conversion efficiency (PCE) and maximum power output degradation rate per annum were observed under different operating conditions. Manufacturers' warranty of maximum power output degradation of 1% per year was achieved by c-Si PV modules under STC and cold climate but not in elevated temperature where power degradation was as high as 5.6% per year. Elevated temperature climate was highlighted as the critical operating condition resulting in poor performance, higher failure rates and shorter useful life of c-Si PV modules.

Visual inspection, Infrared (IR) thermography, Electroluminescence (EL) imaging, performance parameter tracing, failure modes effects and criticality analysis (FMECA), reliability block diagram (RBD) and fault tree analysis (FTA) are among the methods whose applications to determine the dominant degradation modes of c-Si PV modules operating in elevated temperature climates were reviewed. Several recorded field degradation modes were scrutinised and three (3) modes were highlighted as dominant and possessed the highest mean risk priority numbers (RPNs). Solder interconnection damage with RPN = 256, encapsulant discoloration with RPN = 143 and PV cell / metallisation discoloration with RPN = 133.

Solder interconnection degradation, the most dominant degradation mode, was found to be responsible for hotspots, increase heat accumulation, increase series resistance, reduce PCE, reduce electric current, reduce generated electrical power, thermomechanical fatigue failure and limited useful life. Desired properties of solder interconnections which depend on material and geometrical parameters were considered. Some of which include high thermal conductivity, high electrical conductivity, low resistivity and electrical resistance as well as minimised coefficient of thermal expansion (CTE) mismatch between bonded materials. This study aims to redesign c-Si PV module solder interconnections and thereby improve their reliability in elevated temperature climates. The next, chapter 3, presents the methodology, design of experiments and modelling procedure employed in this study.

# CHAPTER 3

# METHODOLOGY

## 3.1 INTRODUCTION

In the previous chapter, solder interconnection degradation was identified as the most dominant failure mode of c-Si PV modules operating in elevated temperature climates. In order to perform a robust investigation of the thermo-mechanical degradation of c-Si PV module solder interconnections and improve the reliability of the system in the operating condition, a research methodology was designed and presented in this chapter. This study employs a combination of finite element modelling (FEM) employing ANSYS software package, design of experiment utilising Taguchi orthogonal array and analytical techniques. Due to the size and complex nature of c-Si PV modules, the number of test vehicles to be investigated which is in excess of five (5) hundred models in the current study, the need to isolate degradation modes, the minimisation of experimental errors, cost and time savings amongst other reasons, FEM method is chosen.

By applying different loads, boundary conditions and material models, the effects of the reliability influencing factors (RIFs) on the performance of c-Si PV module solder interconnections in elevated temperature climates are investigated through FEM discussed in section 3.2. Taguchi orthogonal array, discussed in section 3.3, is employed for the robust optimisation of RIFs.

## 3.2 FINITE ELEMENT MODELLING (FEM)

Historically, laboratory experiments have been the primary tools for performing most types of investigations. However systematic they may be, laboratory experiments

involve a lot of trial and error which consume loads of time and effort and employ destructive methods of testing. To obtain field data and perform laboratory experiments on the performance of c-Si PV modules can take several years and a great deal of money. In recent years, finite element modelling (FEM) has been utilised to investigate such parameters that would otherwise be too expensive and time consuming to investigate using only laboratory experiments. FEM retains the intricacies of laboratory experiments but eliminates destructive test methods, minimises running cost implications and reduces experiment run times from years to hours and minutes. In the current study, FEM is applied to perform accelerated testing of c-Si PV solder interconnections and predict fatigue lifetime in elevated temperature climates.

The FEM procedure applied in this study broadly involves designing three dimensional (3D) models of c-Si PV modules using SolidWorks CAD software and simulating the response of the FE model to applied loads in the ANSYS Mechanical Research Package version 18.2 environment. The general ANSYS FEM procedure is presented in Figure 3.1. The FEM investigation required High Performance Computation (HPC) which was carried out on a bespoke computer workstation in the University of Wolverhampton School of Engineering. Specifications of the workstation include 64-bit Operating System, Inter(R) 2.10 GHz Processor, 64 GB RAM and 3.5 TB hard drive storage.

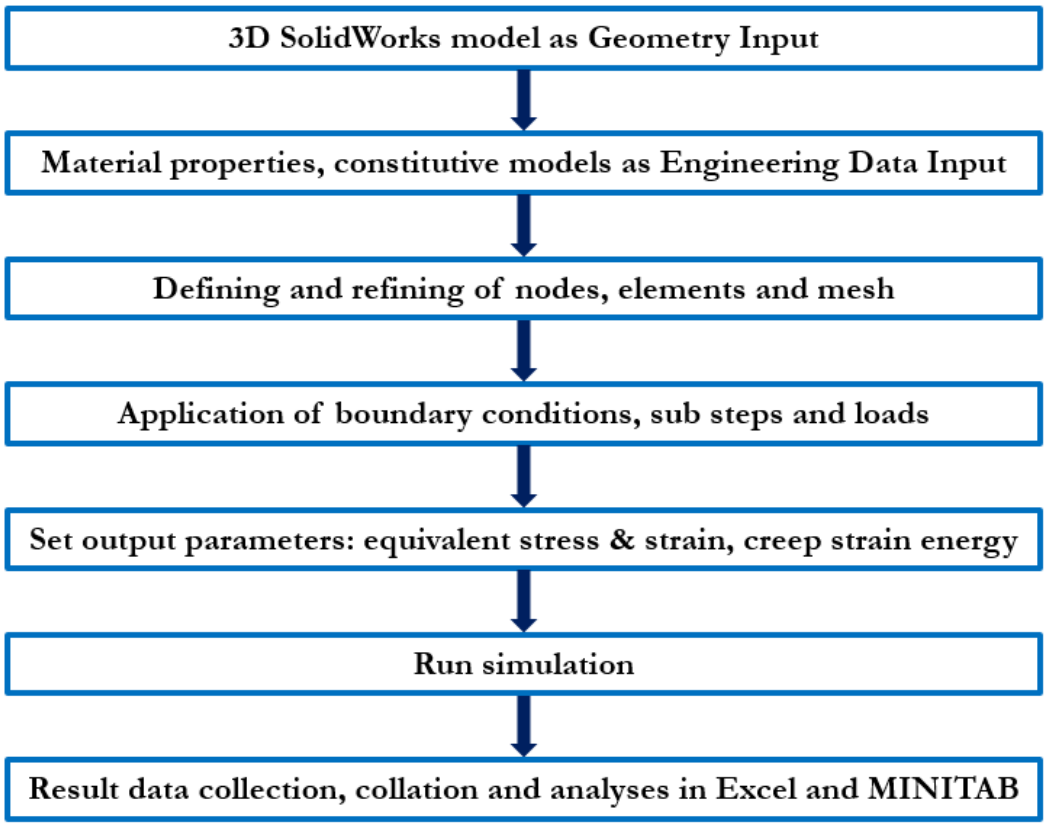


**Figure 3.1:** ANSYS FEM general procedure

Standard sized 156 mm by 156 mm PV cells are interconnected by solder joints to from c-Si PV modules. Taking advantage of the symmetry of the c-Si PV module architecture, a 1mm by 1mm section of the system is modelled. Using this section model lessened modelling time and maximised available hard drive and RAM disc space. In the SolidWorks environment, each component layer of the c-Si PV module is first sketched in 2D before extrusion is done to arrive at the solid 3D unit. Each 3D unit is then assembled using the required mating type ensuring all interfaces are perfectly bonded. The component materials of conventional c-Si PV modules from top-to-bottom without repetition are glass, EVA encapsulant, copper ribbon, Sn3.5Ag0.5Cu (SAC) solder, silver front contact, crystalline silicon wafer, aluminium back contact and Tedlar back sheet. The materials and their respective mechanical properties are presented in Table 3.1 while Table 3.2 presents component layer dimensions.

**Table 3.1:** C-Si PV module component materials and respective mechanical properties

Source: (Smith and Madeni, 2002)

| **Material** | **CTE ($10^{-6}/K^{-1}$)** | **Young's Modulus (MPa)** | **Poisson Ratio** | **Thermal conductivity (W/mK)** | **Shear Modulus (MPa)** |
|---|---|---|---|---|---|
| Silver | 10.4 | 7 | 0.37 | 429 | 2.5547 |
| Copper | 17 | 85.7 | 0.34 | 399 | 31.978 |
| Solder | 23.2 | See Eqn.3.1 | 0.30 | 60 | See Eqn.3.1 |
| Aluminium | 11.9 | 6 | 0.33 | 237 | 2.2556 |
| Silicon | 3.5 | 130 | 0.22 | 148 | 53.279 |
| Glass | 8.5 | 73.3 | 0.21 | 1.8 | 30.289 |
| EVA | 270 | See Fig. 3.5 | 0.4999 | 0.35 | See Fig. 3.5 |
| Tedlar | 30 | 1.4 | 0.4 | 0.2 | 0.5 |
| IMC | 16.3 | 85.56 | 0.309 | 34.1 | 32.681 |
| Zinc | 30 | 108 | 0.25 | 115 | 43.2 |
| Brass | 19 | 125 | 0.31 | 109 | 47.71 |
| Tin | 23.4 | 50 | 0.36 | 66 | 18.382 |

**Table 3.2:** c-Si PV module component layer dimensions

Source: (Hren, 2011; SEAI, 2014)

| **Component layer** | **Height (μm)** | **No of layers** |
|---|---|---|
| Silver front contact | 50 | 1 |
| Copper ribbon | 200 | 2 |
| Solder | 46 | 2 |
| Aluminium back contact | 25 | 1 |
| c-Si Wafer | 200 | 1 |
| Glass | 3000 | 1 |
| Top EVA encapsulant | 160 | 1 |
| Bottom EVA encapsulant | 210 | 1 |
| Tedlar back sheet (TPT) | 190 | 1 |
| IMC | 4 | 2 |

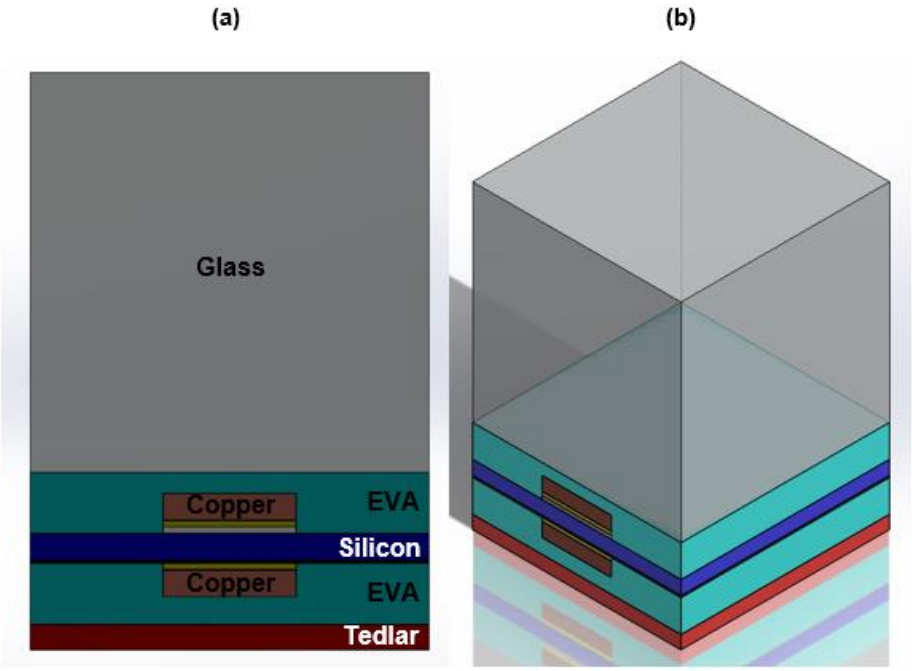


**Figure 3.2:** C-Si PV module architecture end view (a) 3D view (b)

The different views of the c-Si PV module architecture from the SolidWorks software environment are presented in Fig. 3.2. The PV module architecture from SolidWorks is converted to the acceptable Parasolid (.x_t) format which forms the Geometry Input for ANSYS FEM environment. More details on simulation and modelling are found in section 3.2.3.

### 3.2.1 Loads and boundary conditions

The IEC 61215 standard thermal cycle used by the manufacturers of c-Si PV modules for fatigue life and reliability tests is applied as the thermal cycle load. This ensures that actual field operating conditions where temperatures continually rise and fall over the lifetime of the module are modelled (Arndt and Puto, 2010). Figure 3.3 shows a plot of the IEC 61215 temperature profile against time. The profile commences at 25 °C with low (or cold) dwell at -40 °C ± 2°C and high (or hot) dwell at 85 °C ± 2°C. The ramp up and ramp down rates are 1.667 °C/min, and both upper and lower dwell times are 10 minutes each for the 200 cycles applied. There are

some other thermal load profiles available in literature, but they are not suitable to the current investigation because they are intended for ball grid arrays (BGA) and flip chip solder joints in printed circuit boards (PCBs) and other surface mount technologies (SMTs) which function under different operating conditions to c-Si PV modules. These SMT thermal cycle profiles possess hot dwell as high as 157 °C and cold dwell of -38 °C with ramp rate of 15 °C/min (Amalu and Ekere, 2012b, 2012a). In the case of the flat composite solder interconnections in c-Si PV modules, variations of the IEC 61215 standard have been applied by several researchers. Zarmai (2016), applied a thermal cycle load between temperature limits of -40 °C and 85 °C for six (6) cycles. The profile commenced at 25 °C, ramped up at 3 °C/min, ramped down at 6 °C/min and both dwell times were 20 minutes each. Jeong, Park and Han (2012), employed a thermal cycle with cold and hot dwells of -40 °C and 85 °C respectively for one hundred (100) cycles, ramp rate of 8 °C/min and dwell times of 20 minutes. In the current study, a steady ramp rate of 1.667 °C/min was used which demonstrates closer real-life operating conditions, allows gradual stress accumulation and minimises thermal shock.

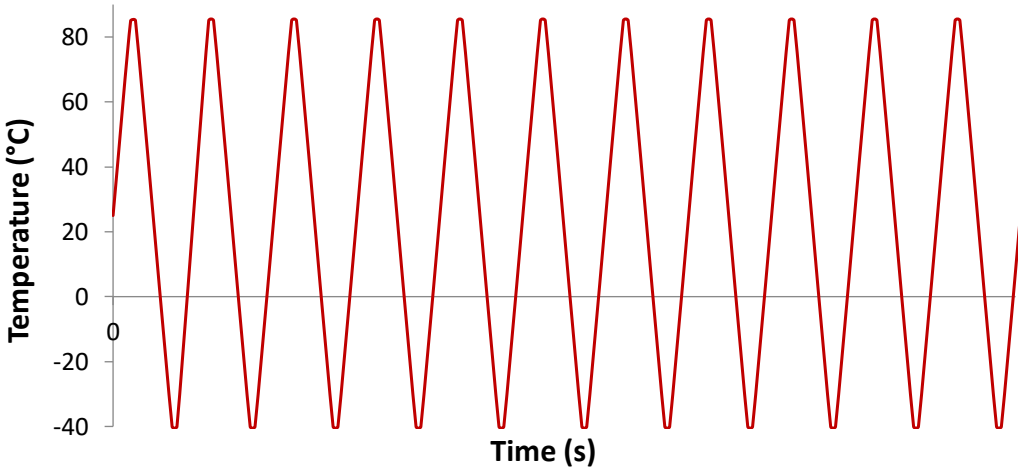


**Figure 3.3:** IEC 61215 temperature profile showing temperature (°C) against time (s)

Source: (Arndt and Puto, 2010)

Over the years, c-Si PV modules tested under the IEC 61215 standard tests have gone into field operations and produced a wide range of lifespans with some modules meeting their 20/20 or 20/25 manufacturers' power warranty while others fail or degrade more than their designed and predicted levels (Sastry *et al.*, 2010; Polverini *et al.*, 2013). This difference in performance has been attributed to the ambient operating conditions of the modules. Thus, the IEC 61215 standard has been criticised because its ambient conditions are those of standard test conditions (STCs). STCs were discussed in detail in Chapter 2 of this thesis. Rajput *et al.* (2016), in their study of the degradation of mono-crystalline photovoltaic modules after 22 years of outdoor exposure in the composite climate of India, identified the shortcomings of the IEC standard test. They carried out a comprehensive analysis of the degradation mechanisms of ninety (90) c-Si PV modules installed at the National Institute of Solar Energy (NISE) in Gurgaon, utilising visual inspection, thermal imaging, I-V characteristics, rate of degradation and insulation resistance measurement. They further proposed that in order to fully understand the field performance of PV modules and ensure long term reliability, their generation and growth of defects, as well as their degradation mechanisms ought to be studied under actual outdoor operating conditions. In this study, the application of the IEC 61215 standard was taken a step further by employing the thermal cycle at non-STC ambient conditions. Therefore, the performance of c-Si PV solder interconnections under actual elevated temperature climate thermal loads is accurately investigated. Further discussions on the effect of operating temperature on PV interconnection degradation are discussed in chapter 4 of this thesis.

The assumptions and boundary conditions applied for the simplification of the PV solder interconnection model are presented in Fig. 3.4. They include:

- All materials are isotropic and homogenous.

- All component layers are perfectly bonded.
- Static conditions are applied and so displacement of the model = 0 in all directions.
- Models have uniform temperature field and are perfectly insulated so temperature gradient = 0, and heat loss = 0.
- Residual stresses (from soldering process) = 0

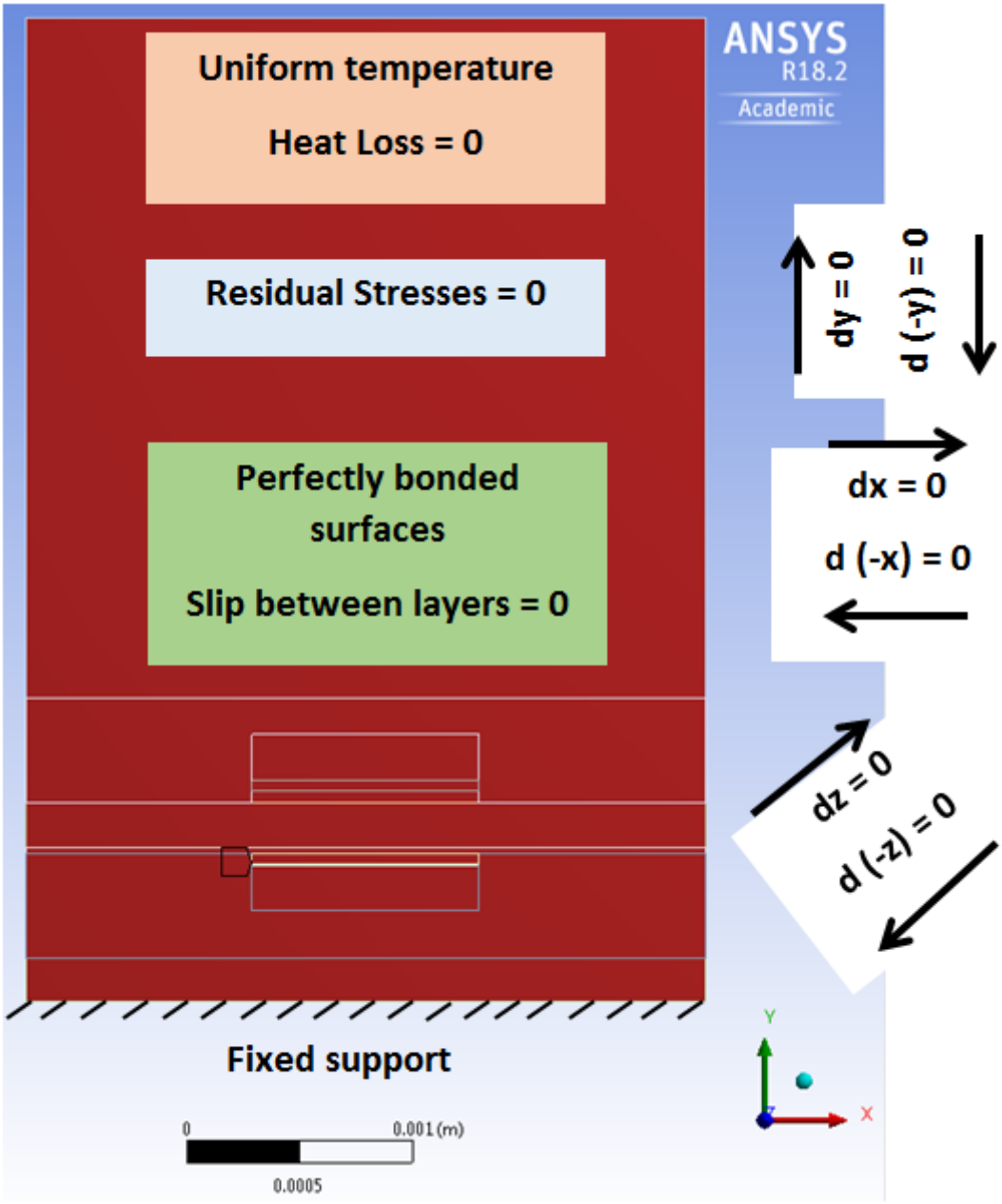


**Figure 3.4:** Boundary condition diagram

### 3.2.2 Constitutive material models

In addition to the mechanical properties presented in Table 3.1, constitutive material models are included in the Engineering Data Input to the ANSYS FEM environment. Except for solder and EVA encapsulant layers, all other component materials of c-Si PV module are modelled as linear elastic. Solder is modelled according to its creep properties as well as temperature dependent Young's Modulus. The Young's Modulus and CTE of SnAgCu (SAC) solders have been found to show significant nonlinear temperature dependence (Schubert *et al.*, 2001; Wiese *et al.*, 2001). This relationship between Young's Modulus of Sn3.5Ag0.5Cu solder, Y, and absolute temperature, T, is expressed in Eqn. 3.1.

$$Y = 62348 - 54.6T \qquad \text{Equation 3.1}$$

In the determination of degradation in SAC solder joints under thermal cycling loads, creep deformation is considered as the primary degradation mode. Creep deformation has been reported to be responsible for the formation of cracks, propagation of cracks and eventual fracture of solder joints (Miller *et al.*, 2010). Creep testing is important to determine the rate of deformation at a certain load and stress level below its yield strength. C-Si PV solder interconnection models can be designed to operate under elevated temperature conditions by predicting number of cycles-to-failure. Creep deformation is used to understand material behaviour and forms the basis for fatigue life prediction models.

Syed (2004) derived a life prediction model for SAC solder joints by combining the Monkmann-Grant equation for creep rupture, and the time-fraction rule. Equation 3.2 presents the Monkmann-Grant equation for creep rupture which states that steady state creep strain rate, $\dot{\varepsilon}_{cr}$, is inversely related to rupture time, $t_r$. $\varepsilon_f$, is creep ductility or strain at the commencement of failure.

$$t_r = \frac{\varepsilon_f}{\dot{\varepsilon}_{cr}}$$ Equation 3.2

Equation 3.3 presents the time-fraction rule. Here number of cycles to failure, $N_f$, is expressed as a function of rupture time. $n$, is the number of steps within a cycle, $\Delta t_i$, is time spent at each stress level within a cycle and $t_{ri}$, is the rupture time at each stress level.

$$N_f = \left(\sum_{i=1}^{n} \frac{\Delta t_i}{t_{ri}}\right)^{-1}$$ Equation 3.3

Combining Eqns. 3.2 and 3.3,

$$N_f = \left(\sum_{i=1}^{n} \frac{\Delta t_i \dot{\varepsilon}_{cri}}{\varepsilon_f}\right)^{-1}$$ Equation 3.4

The accumulated creep strain, $\varepsilon_{acc}$, is the summation of the creep strain for all steps within the whole cycles. Equation 3.4 can be simplified to become Eqn. 3.5. $C$, is the inverse of creep ductility.

$$N_f = (C\varepsilon_{acc})^{-1}$$ Equation 3.5

Equation 3.5 can be converted to an energy-based fatigue life prediction model to become Eqn. 3.6. Where, $W$, is the creep energy density for failure and $\omega_{acc}$, is accumulated creep strain energy density.

$$N_f = (W\omega_{acc})^{-1}$$ Equation 3.6

Syed (2004) derived values for constants of fatigue life prediction (C and W) of SAC solders after performing linear multiple regression analysis of the hyperbolic sine and double power law creep constitutive models. C = 0.0405 and W = 0.0014. Equations 3.5 and 3.6 are applied in the current study to predict fatigue life of each c-Si PV module solder interconnection model under the elevated temperature conditions.

Describing the creep behaviour of solder can be a complex task and the findings of several published reports vary due to experimental loads and boundary conditions.

The temperature and stress dependency of steady state creep strain rate founds majority of solder creep constitutive models. Wong *et al.*, (2016), critically reviewed the robustness of eight (8) different creep fatigue models. Some of the examined models applied approaches where either pure creep or pure fatigue were the dominant damage mechanisms. The authors however argued that a good strain life model should be capable of capturing the full spectrum of creep-fatigue from pure fatigue to pure creep rupture. This condition was satisfied by the unified strain life equation which integrated creep functions into fatigue equation and revealed superior performance in the benchmarking exercise.

Table 3.3 presents some of the frequently referenced creep constitutive models of SAC solders. After creep strain rate is derived using one of these constitutive models, it is inputted in Eqns. 3.5 and 3.6 for fatigue life prediction. Zhang, Dasgupta and Haswell (2003) proposed an analytical viscoplastic constitutive and energy-partitioning model for the Sn3.9Ag0.6Cu solder alloy under high homologous temperature and high stress conditions and compared model findings to those obtained from laboratory experiments using thermo-mechanical-microstructural test (TMMT) system. Schubert *et al.* (2001) studied the thermo-mechanical properties and creep deformation of lead-containing and lead-free solders in order to estimate their creep resistance. They employed thermo-mechanical analysis (TMA Netzsch model 202), DMA, tensile test and creep tests on bulk specimens. Microstructural appearance of the solders was observed with transmission electron microscope (TEM) and SEM. The 95.5Sn3.8Ag0.7Cu solder alloy was found to demonstrate enhanced mechanical strength and better high temperature creep resistance than the other lead-free solder alloys. Also, SAC solders were found to possess lower activation energy and hence thermal-mechanical fatigue resistance compared to Sn-Ag solders.

**Table 3.3:** Creep constitutive models of SAC solders

| Reference | Constitutive Model | Parameter Values |
|---|---|---|
| (Zhang, Dasgupta and Haswell, 2003) | Hyperbolic sine law converted to tensile form $\dot{\varepsilon}_{cr} = A_1[\sinh \alpha\sigma]^n exp\frac{-H_1}{kT}$ | $A_1 = 143.4s^{-1}$,$\alpha = 0.108MPa^{-1}$, $n = 3.7884$, $^{H}/_{k} = 7567$, $E(MPa) = 24224 - O.O206T\ (°K)$ |
| (Schubert *et al.*, 2001) | Hyperbolic sine law $\dot{\varepsilon}_{cr} = A_1[\sinh \alpha\sigma]^n exp\frac{-H_1}{kT}$ | $A_1 = 277984s^{-1}$, $\alpha = 0.02447MPa^{-1}$, $n = 6.41$, $^{H}/_{k} = 6500$, $E(MPa) = 61251 - 58.5T\ (°K)$, $CTE = 20.0\ ppm/K$, $Poisson's\ ratio = 0.36$ |
| (Schubert *et al.*, 2003) | Garofalo creep model $\dot{\varepsilon}_{cr} = C_1[\sinh(C_2\sigma)^{C_3}]\exp\left(-\frac{C_4}{T}\right)$ | $C_1 = 277984s^{-1}$, $C_2 = 0.02447MPa^{-1}$, $C_3 = 6.41$, $C_4 = 6500$ |
| (Wiese, *et al.*, 2001) | Double power law $\dot{\varepsilon}_{cr} = A_1 exp\left(\frac{-H_1}{kT}\right)\left(\frac{\sigma}{\sigma_n}\right)^{n_1} + A_2 exp\left(\frac{-H_2}{kT}\right)\left(\frac{\sigma}{\sigma_n}\right)^{n_2}$ | $A_1 = 4 \times 10^{-7}s^{-1}$, $^{H_1}/_{k} = 3223$, $n_1 = 3.0$, $A_2 = 1 \times 10^{-12}s^{-1}$, $^{H_2}/_{k} = 7348$, $n_2 = 12.0$, $\sigma_n = 1MPa$, $E(MPa) = 59533 - 66.667T(°K)$ |
| (Morris, Song and Hua, 2003) | Dorn equation $\dot{\gamma} = \frac{AGb}{kT}\left(\frac{\tau}{G}\right)^n exp\left(\frac{-Q}{kT}\right)$ | $A = preexponential\ factor$, $G = shear\ modulus$, $kT = Boltzmann\ temperature$, $b = Burger's\ vector$, $\tau = shear\ stress\ n = 6.6\ for\ low\ stress\ regime; n = 10.7\ for\ high\ stress\ regime$, $Q; activation\ energy = 95\ kJ/mole\ for\ low\ stress\ regime, 75\ kJ/mole\ for\ high\ stress\ regime$ |

In their later study (Schubert *et al.*, 2003), they presented the Garofalo creep model for predicting the fatigue life of the Sn3.5Ag0.5Cu solder alloy. Fatigue behaviour of the solders was described based on empirical power-law relationships and creep data

by the Garofalo model. They ascertained that accumulated creep strain was inversely related to fatigue life of the solder. In the current study, Garofalo creep model is employed because it had been applied successfully in predicting the number of cycles to failure of the same Sn3.5Ag0.5Cu solder alloy used in the c-Si PV solder interconnection model under investigation. However, in (Schubert *et al.*, 2003), the test vehicles were flip chip, ball grid array (BGA) and printed circuit boards (PCBs) but the present research introduces a new dimension by focusing on the thermo-mechanical performance of composite solder joints in c-Si PV modules under elevated temperature conditions. Wiese *et al.* (2001), applied the double power law to describe the steady state creep behaviour of lead-free solders and lead-based solders using experiments on bulk specimens and flip-chip joints. Morris, Song and Hua (2003), in their study on the creep properties of Sn-rich solder joint, performed high temperature creep tests on nine pad single shear creep specimens which had copper metallisation on one side, Sn3.0Ag0.5Cu solder in between and electroless nickel on the other. They observed the steady state creep rates separated into two regimes (i.e. low stress and high stress) with distinct stress exponents (n). Also, the Sn3.0Ag0.5Cu solder demonstrated anomalous temperature dependence at temperatures slightly above room temperature.

EVA material is known to possess unique thermo-viscoelastic rheological properties which enable the material provide flexibility and support required of a good PV module encapsulant. The degradation of EVA under non-STC operating conditions significantly increases the degradation of c-Si PV solder interconnections and affects the performance of other component layers (Matsunaga *et al.*, 2011; Sinha, Sastry and Gupta, 2016; Gagliardi, Lenarda and Paggi, 2017; Rajput, Sastry and Tiwari, 2017). In chapter 2 of this thesis, EVA encapsulant discoloration was discussed as one of the dominant degradation modes of c-Si PV modules operating in elevated

temperature climates. Paggi and Sapora (2015), in their study to assess the deformation of PV modules applied fractional calculus to derive a thermo-viscoelastic model of EVA. Their findings showed that the rheological behaviour of EVA causes variation of gaps between PV cells leading to solder interconnection fracture, increases PV cell deformation, and its degradation results to power output loss.

The accurate modelling of EVA is of utmost importance to the current study because there have been reports that modelling EVA as viscoelastic instead of linear elastic produces FEM results with values close to laboratory experimental results and minimise simulation errors associated with nonlinearities (Eitner *et al.*, 2011; Paggi, Kajari-Schröder and Eitner, 2011). In addition to modelling EVA as viscoelastic, its Young's Modulus is temperature dependent. Figure 3.5 presents a chart of Young's Modulus of EVA against temperature for different relaxation times. In the current study, the Young's Modulus values of EVA at each temperature point on the IEC 61215 thermal cycle load, shown in Fig. 3.3, are derived. These values are then fed into the ANSYS FEM environment as part of the Engineering Data Input.

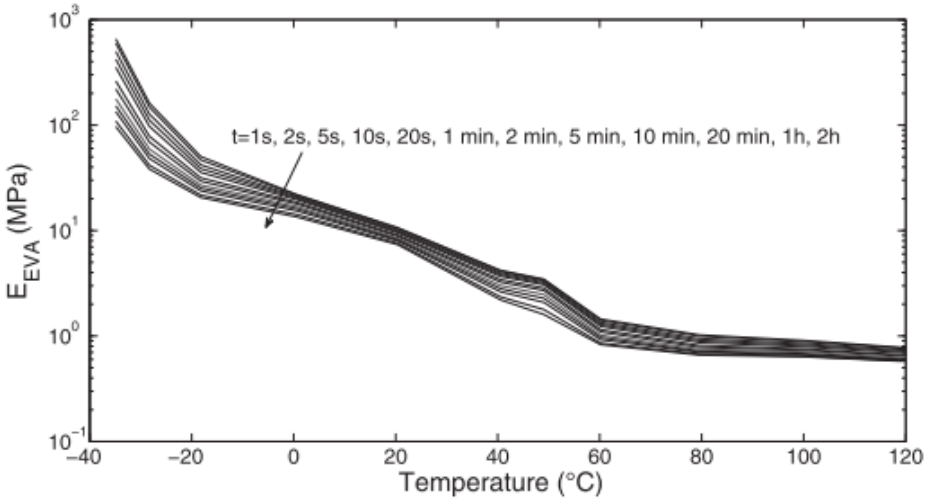


**Figure 3.5:** Young's modulus (MPa) of EVA versus temperature (°C), for different relaxation times

Source: (Paggi, Kajari-Schröder and Eitner, 2011)

### 3.2.3 Simulation and modelling

Referring to the ANSYS FEM general procedure in Fig. 3.1, the next steps after entering the Geometry Input and Engineering Input make up the simulation and modelling. The c-Si PV model now in the acceptable Parasolid (.x_t) format, is the Geometry input into Static Structural analysis system to simulate the solder interconnection degradation response. Static Structural, the chosen Analysis System, was appropriate for the current investigation for several reasons some of which are now discussed. Firstly, mass, inertia and damping effects of the model are not important to the investigation. Hence, Static Structural Analysis System is adequate for the simulation of c-Si PV solder interconnection degradation under the temperature load conditions. Secondly, the c-Si PV model is assumed to be static (i.e. displacement in x, y, and z directions = 0) and all component layer perfectly bonded without slip between layers. Since there is no consideration of relative motion between component layers, Static Structural Analysis system is adequate for the current investigation. Thirdly, applied loads and output parameters are dependent on temperature rather than time. Hence no dynamic responses such as time-history analysis under the action of time-dependent loads are required. Lastly, all component layers of the c-Si PV model have uniform temperature field and are perfectly insulated (i.e. temperature gradient = 0, and heat loss = 0). Taking these reasons and other boundary conditions into account, the Static Structural Analysis System was chosen over Transient Structural and Transient Thermal Analysis Systems for the current study (Rust and Schweizerhof, 2003; Giurgiu, Ciortan and Pupaza, 2013).

After the analysis system is chosen, the loads and boundary conditions are defined. All the component layer interfaces are perfectly bonded, the fixed support is set at the TPT back sheet making the deformation shear free and in 1D, analysis settings are set at the required sub steps, the Creep control is TURNED ON with Creep Limit

Ratio set at 8, and the IEC 61215 from Fig. 3.3 is the applied thermal load at various non STC ambient temperatures depending on the investigation being carried out.

Neglecting nonlinearities and utilising a less advanced model, a fine mesh model is used for the solder interconnection components, but a relatively coarser mesh is used for the other non-focus layers. A mesh convergence study was carried out to determine the element size used in the FEM simulations. This enabled the author to check the accuracy of the FEM solutions. The mesh element size refinement was done according to the element size reduction factor. Table 3.4 presents the Mesh convergence study. Figure 3.6 is a plot of the Critical Parameters against Element Size Reduction Factor. It can be observed that as element size reduces, Accumulated Creep Strain Energy Density (i.e. measure of solder interconnection degradation) values converge while the simulation runtime continues to increase. A point is reached where any further mesh refinement makes no difference in solder degradation but results in further increase in simulation runtime (Patil and Jeyakarthikeyan, 2018). In the current study, this critical point occurred at element size reduction factor 2 and was used for all FEM simulations presented in this thesis.

**Table 3.4:** Mesh Convergence Study

| **Element Size Reduction Factor** | **Element Thickness (E-06 m)** | **Accumulated Creep Strain Energy Density (E-02 Pa)** | **Simulation runtime (hours)** |
|---|---|---|---|
| 1 | 46.00 | 1.1152 | 1.25 |
| 2 | 23.00 | 1.8023 | 4.50 |
| 3 | 15.33 | 1.7954 | 10.40 |
| 4 | 11.50 | 1.7873 | 15.10 |
| 5 | 9.20 | 1.7823 | 18.30 |

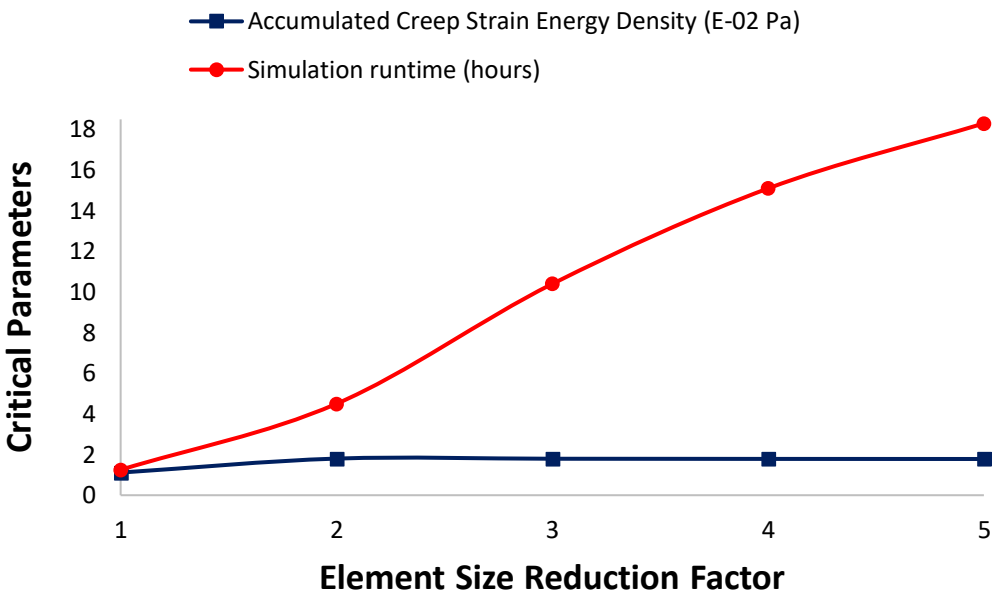


**Figure 3.6:** Critical Parameters vs Element Size Reduction Factor

Figures 3.7 and 3.8 present different views of the c-Si PV module showing applied meshes. The ANSYS FEM model of the c-Si PV module comprised of 9344 solid elements, 25992 contact elements, 35336 total elements, 54201 nodes and 1000 maximum sub steps. For further details of the ANSYS FEM codes, see Appendices.

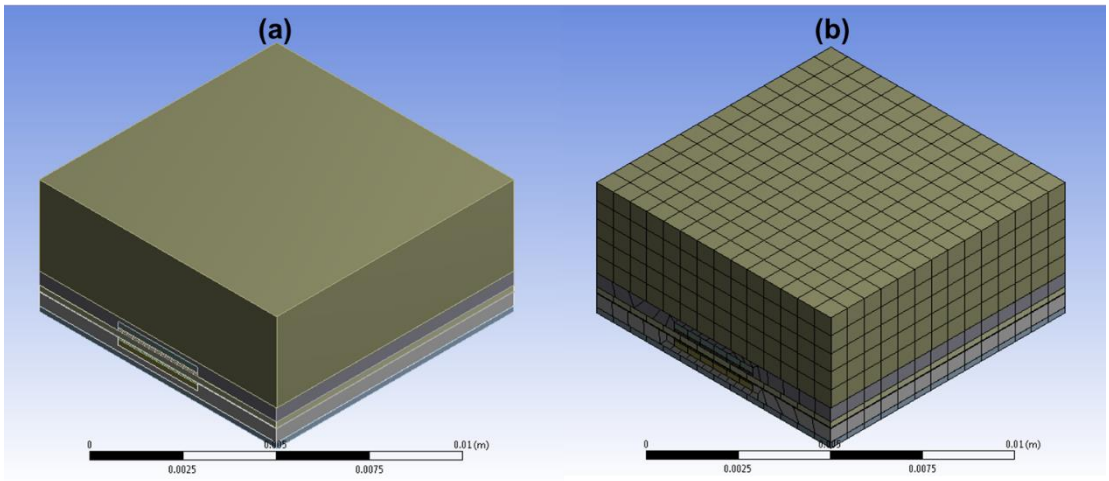


**Figure 3.7:** c-Si PV module 3D view (a) showing mesh (b)

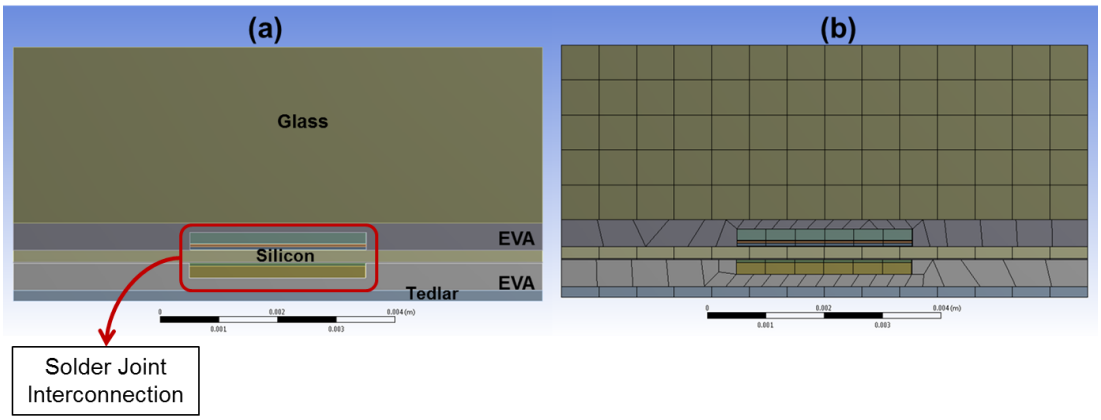


**Figure 3.8:** c-Si PV module end view (a) showing mesh (b)

A few previous researches have considered the accumulation of residual stresses in PV modules during and after encapsulation. Mean compressive stresses between 40 MPa and 65 MPa at the PV cell edges and 140 MPa at the PV cell centre have been reported (Ojo and Paggi, 2016a, 2016b). However, in the current study, the degradation of c-Si PV solder interconnections under non STC operating conditions is investigated and compared to the initial configuration (i.e. STC operating conditions). This means that only variations in stress and strains from the initial configuration are considered and not the absolute values of stress and strain, so the residual stresses are taken as negligible. Details of other applied boundary conditions are found in section 3.2.1

The output parameters of the ANSYS FEM simulation include Equivalent Stress, Equivalent Strain, Equivalent Creep Strain and Creep Strain Energy. The measure of c-Si PV solder interconnection degradation is the accelerated creep strain energy density, $\omega_{acc}$. In Eqn. 3.6, $\omega_{acc}$ is required to predict the fatigue life of solder interconnections. This parameter is not a direct output parameter from the ANSYS environment, but it is derived from the creep strain energy values. Equations 3.7-3.10 lay out the steps to derive accumulated creep strain energy density from creep strain energy.

$$E = \frac{E_c}{V}$$ Equation 3.7

Where $E$ is the maximum creep strain energy density (Pa), $E_c$ is the maximum creep strain energy per cycle (Joule) and $V$ is the solder layer volume ($m^3$).

$$E_A = \sum_{i=1}^{n} |E_i - E_{i+1}|$$ Equation 3.8

$$\sum_{i=1}^{n} |E_i - E_{i+1}| = |E_1 - E_2| + |E_2 - E_3| + \cdots + |E_{n-1} - E_n|$$ Equation 3.9

$$E_A = \omega_{acc}$$ Equation 3.10

$E_A$, is the same as the accumulated creep strain energy density, $\omega_{acc}$. It is calculated as the sum of the absolute difference between the maximum creep strain energy density value in one cycle and the successive cycle. n is the number of cycles.

## 3.3 TAGUCHI ORTHOGONAL ARRAY

The current investigation into the performance of c-Si PV solder interconnections in elevated temperature climates takes on different facets. Each one of the RIFs of c-PV solder interconnections is first considered individually and then the combinations of multiple RIFs are considered. Single variate designed experiments are employed when individual RIFs are considered while Taguchi orthogonal array is used to design the experiments investigating multiple RIFs. Taguchi's design of experiments was first used to improve the quality of products in Japan but has now gone on to be applied in several fields. Prior to Taguchi, quality assurance depended on inspecting the products at the end of the manufacturing line. Products were either accepted or rejected based on whether they fell within the design tolerance range. Taguchi exposed the limitations of previous methods by pointing out that quality cannot be improved by inspection but must be designed into the system from the start (Tsui,

1996; Ryan and Morgan, 2007; Ryan, 2011). There have been other designs of experiment methods applied in studies on optimisation, such as the Full Factorial and Fractional Factorial. Taguchi provides a more efficient and robust DOE for several reasons; some of which are discussed. Firstly, the elimination of unnecessary design points and experimental runs thereby saving cost. Unlike in the full factorial DOE method, Taguchi only includes the set of factor and level combinations suggested in the orthogonal array. Take an instance of an investigation involving optimisation of three (3) factors at three (3) levels, the number of Taguchi experimental runs is nine (9) while it is twenty-seven (27) for the full factorial DOE (Pignatiello and Ramberg, 1991; Wysk *et al.*, 2000; Ryan, 2011). Secondly, Taguchi includes the effects of noise factors. Most of other fractional factorial DOEs, although involving fewer experimental runs compared to the full factorial, do not consider the effect of noise factors on the investigation. Noise factors are those that are usually external to the system but significantly influence the performance of the system. Noise factors are either too expensive or difficult to control. Elevated temperature is a noteworthy noise factor as is the case in the current investigation on c-Si PV solder interconnection degradation (Phadke, 1989; Ahmad Dar and Anuradha, 2018). Lastly, Taguchi offers a more robust DOE by embedding a verification step in its procedure. This ensures that the performance of optimal design(s) identified by the DOE can be further tested (Ramberg *et al.*, 1991; Athreya and Venkatesh, 2012).

Applying Taguchi's orthogonal array design provides an off-manufacturing-line Quality Engineering method which brings about what is known as Robust Design. Robust design is an engineering methodology used in the research and design (R&D) stage of product development to ensure productivity improvement by manufacturing high quality products quickly and at low cost. Robust design aims to achieve products with minimum sensitivity to variations in uncontrollable environmental

factors (Ramberg *et al.*, 1991; McEwan, Belavendram and Abou-Ali, 1992; Fowlkes and Creveling, 1995). These uncontrollable factors are called “noise factors” and they either too difficult or expensive to control. In the case of the current study, the noise factor is the ambient temperature of the elevated temperature climates. The flow chart of the parameter design process is presented in Fig. 3.9.

### 3.3.1 Parametric design approach

To proceed with the Taguchi orthogonal array design, variables must be defined as either independent or dependent. The independent variables are the parameters whose dimensions can be changed to produce a “performance response” which is the dependent variable. The independent variables are also called “control factors” and they are designed to optimal levels to improve quality and minimise sensitivity to noise factors. Control factors that reduce the variability in the system caused by noise factors are identified. Also, control factors are categorised according to the influence they have on the performance parameter. Those control factors with no influence on the performance parameter can be designed with more relaxed tolerance. In the present study, the control factors are the RIFs of c-Si PV solder interconnections while the performance response is the accumulated creep strain energy density (the measure of c-Si PV solder interconnection degradation).

An example design problem will be used to describe the Taguchi robust design. In this scenario, there are three (3) control factors (X, Y, Z) at three (3) design levels (1, 2, 3) and one (1) performance response (P). The Taguchi L9 orthogonal array, shown in Table 3.5, is the best array to be utilised for this design problem. MINITAB statistics software is employed for the data analyses.

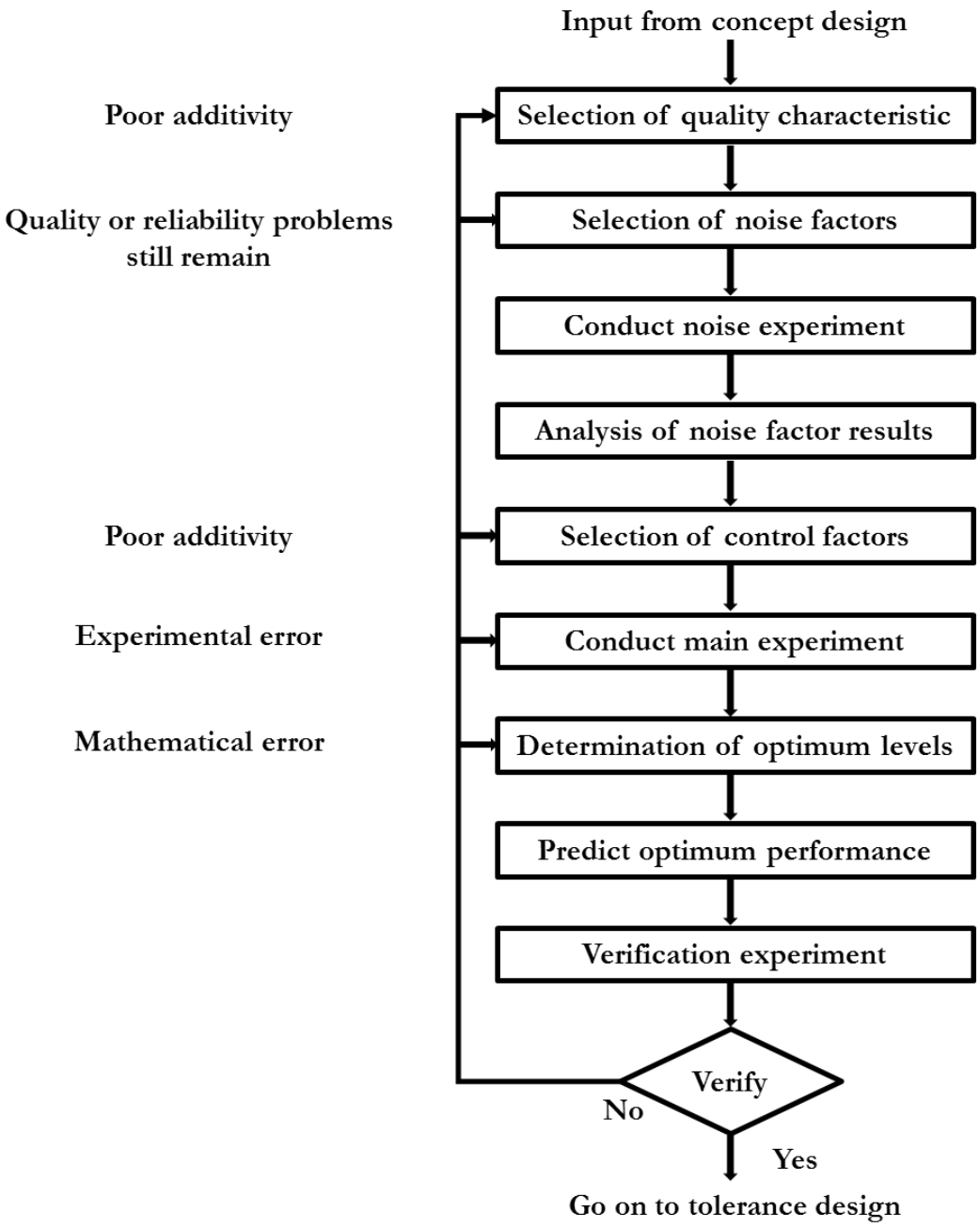


**Figure 3.9:** Flow chart of the parameter design process

Source: (Fowlkes and Creveling, 1995)

### 3.3.2 Optimal parameter design

Taguchi's robust design method is based on statistical tools applied to achieve Quality Engineering goals. The mean performance response and standard deviation can be calculated using Eqn. 3.11 and Eqn. 3.12 respectively.

$$\bar{y} = \frac{1}{N}\sum_{i=1}^{N} y_i \qquad \text{Equation 3.11}$$

$$S = \sqrt{\sum_{i=1}^{N} \frac{(y_i - \bar{y})^2}{N-1}} \qquad \text{Equation 3.12}$$

Where $\bar{y}$ is the mean performance response, $N$, is the experimental run, $y_i$, is the performance response for an experimental run, and $S$, is the standard deviation.

**Table 3.5:** Taguchi L9 orthogonal array

| **Experiment No.** | **Control Factors** | | | **Mean Response Parameter** | **Signal to Noise Ratio** |
|---|---|---|---|---|---|
| | **X** | **Y** | **Z** | **P** | **SN** |
| 1 | 1 | 1 | 1 | $P_1$ | $SN_1$ |
| 2 | 1 | 2 | 2 | $P_2$ | $SN_2$ |
| 3 | 1 | 3 | 3 | $P_3$ | $SN_3$ |
| 4 | 2 | 1 | 2 | $P_4$ | $SN_4$ |
| 5 | 2 | 2 | 3 | $P_5$ | $SN_5$ |
| 6 | 2 | 3 | 1 | $P_6$ | $SN_6$ |
| 7 | 3 | 1 | 3 | $P_7$ | $SN_7$ |
| 8 | 3 | 2 | 1 | $P_8$ | $SN_8$ |
| 9 | 3 | 3 | 2 | $P_9$ | $SN_9$ |

For product improvement, Taguchi uses signal to noise (SN) ratios. SN ratios are derived from the quadratic quality loss function and are calculated for each experimental run (Phadke, 1989; Fowlkes and Creveling, 1995; Steinberg and Bursztyn, 1998). SN ratios and performance response parameter values for each independent variable at its designed levels are derived. Taguchi's method uses a graphical approach to analyse data. The graphs are analysed to pick the parameter level which maximises the SN ratio and meets the performance response parameter target. The response parameter may either require minimisation or maximisation.

Analysing the graphs for SN ratios and performance response parameters, the control factors can be categorised according to if they affect the performance response only, the variation only, both the performance response and variation or neither the performance response nor variance. Based on these categories, control factors can be designed to reduce variation, make the product more robust, meet the target performance response or achieve best cost savings.

Depending on the nature of the target performance response parameter, SN ratios can either be for minimisation, normalisation or maximisation. For minimisation, the smaller the target performance response the better, larger is better for maximisation while closest to nominal value is better for normalisation. Equations 3.13 – 3.15 present the SN ratio relations. Where, $SN_S$, is for minimisation, $SN_N$, is for normalisation and $SN_L$, is for maximisation.

$$SN_S = -10\log\left(\frac{1}{N}\sum_{i=1}^{N} y_i^2\right) \quad \text{Equation 3.13}$$

$$SN_N = -10\log\left(\frac{\bar{y}^2}{S^2}\right) \quad \text{Equation 3.14}$$

$$SN_L = -10\log\left(\frac{1}{N}\sum_{i=1}^{N} \frac{1}{y_i^2}\right) \quad \text{Equation 3.15}$$

The current study utilises the minimisation SN ratio (i.e. smaller the better). This is because the aim is to improve the reliability of c-Si PV modules in elevated climates and so the performance response, c-Si PV solder interconnection degradation, must be minimised. More details on the application of Taguchi's robust design are discussed in chapter 7 of this thesis. Referring to Table 3.5, the worst design levels will have the lowest SN while the highest SN will be at the best design levels. Confirmation experiments are then carried out at the optimal design level settings to verify that the predicted performance is actualised.

Another useful tool of the Taguchi robust design method is the parameter interaction plot. Parameter interaction plots indicate any relationship between individual independent variables at their level settings (Ahmad Dar and Anuradha, 2018). Parallel lines indicate no relationship while intersecting lines indicate strong interaction between independent variables. Figure 3.10 presents the Taguchi L9 interaction plot from MINITAB software environment.

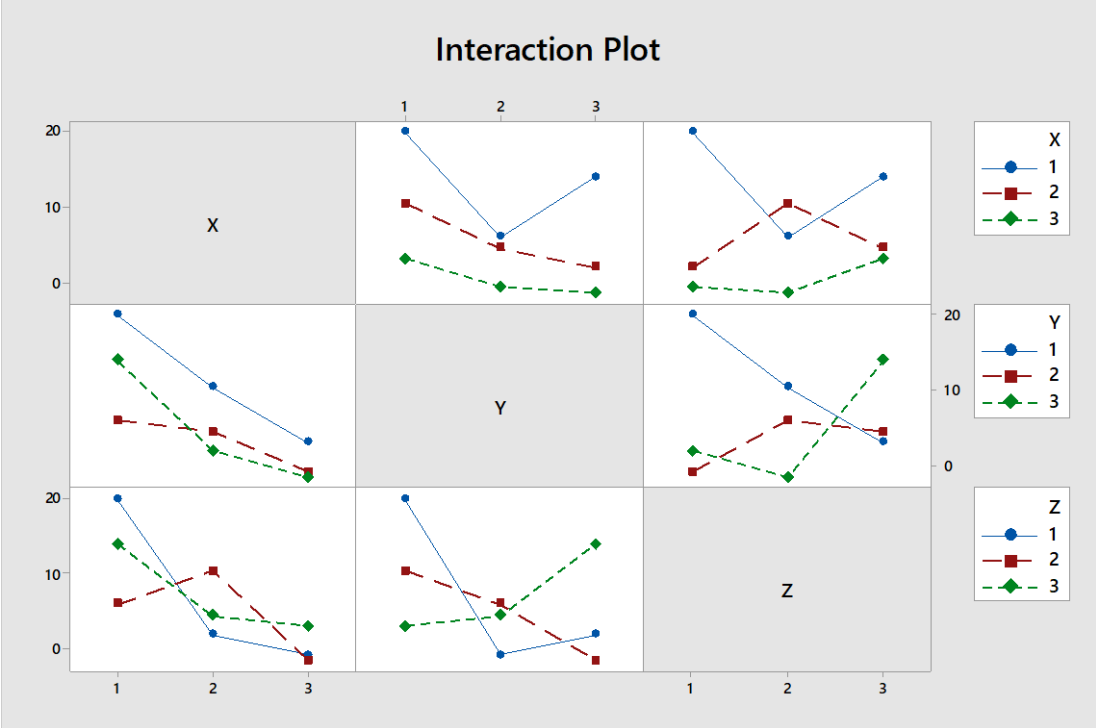


**Figure 3.10:** Taguchi L9 array interaction plot

The number of two-way interactions from Taguchi orthogonal array can be derived from Eqn. 3.16. The degree of freedom (DOF) for each two-way interaction is calculated using Eqn. 3.17 Where, ♯ = number of two-way interactions, $p$ = number of control factors, and $m$ = number of levels.

$$♯ = \frac{p!}{2(p-2)!} \qquad \text{Equation 3.16}$$

$$DOF = (m-1)(m-1) \qquad \text{Equation 3.17}$$

## 3.4 SUMMARY

This chapter presented the employed research methods for the current investigation which entail finite element modelling (FEM) and Taguchi orthogonal array supported by analytical approaches. C-Si PV solder interconnection model design and simulation were carried out using SolidWorks 3D CAD software and ANSYS Mechanical Research Package v18.2 on a bespoke HPC workstation in the University of Wolverhampton School of Engineering. The ANSYS FEM process involved the application of the IEC 61215 standard thermal cycle load, meshes, elements, nodes, sub steps and boundary conditions.

To determine solder interconnection degradation and predict fatigue life, appropriate material properties and constitutive models were applied. These constitutive material models include creep deformation, linear elasticity, viscoelasticity and temperature dependent Young's Modulus of elasticity. Taguchi orthogonal array and accompanying analytical approaches are applied for the robust optimisation of reliability influencing factors (RIFs) of c-Si PV solder interconnections.

The various research methods discussed are employed to determine the effects of elevated temperature conditions on the reliability influencing factors (RIFs) of c-Si PV solder interconnections and propose optimised model(s) with improved reliability in the operating climate. Chapters 4 – 7 present the detailed discussions of these investigations.

# CHAPTER 4

# EFFECT OF OPERATING TEMPERATURE ON PHOTOVOLTAIC (C-Si PV) INTERCONNECTION DEGRADATION

## 4.1 INTRODUCTION

This chapter presents a study on the effects of operating temperature on c-Si PV solder interconnection degradation using ANSYS FEM software package. The effect of operating temperature is one of the defined reliability influencing factors (RIFs) of the PV solder interconnection. More details are presented in chapter 1. The standard lifetime of c-Si PV modules is within the range of 20-25 years but for these modules to attain such life expectancies, they must operate under standard test conditions (STCs). Chapter 2 of this thesis discussed STCs in detail. The actual field operating conditions of c-Si PV modules significantly differ from STCs and change from one climate to another with reported cases of cell temperatures as high as 90 °C in elevated temperature climates. The reported deviation of PV module operating temperatures (cell and ambient) from STCs in elevated temperature climates calls for research aimed at providing more information to predict the performance and fatigue life of modules in the climatic zone accurately (King, Boyson and Kratochvil, 2002; Hussein, Ahmad and El-Ghetany, 2004; Pacca, Sivaraman and Keoleian, 2007; Huld *et al.*, 2010; Obinata *et al.*, 2010; Woyte *et al.*, 2013). This chapter presents the study on the effect of operating temperature of the c-Si PV modules and how it affects their reliability and fatigue life. Solder interconnection which has been identified as the most failure susceptible component layer of PV modules is the focus of the current investigation.

There are literature on the electrical power degradation of c-Si PV modules (Sander *et al.*, 2010; Bastidas-Rodriguez *et al.*, 2017; Jordan *et al.*, 2017), however the current study focuses on the thermo-mechanical degradation of c-Si PV solder interconnections due to high temperature operating conditions. In addition, a numerical relationship between c-Si PV cell temperature rise from STC and solder joint degradation is established. Also, fatigue life prediction is carried out under various non-STC ambient operating temperatures.

The finite element modelling employed is presented in section 4.2. The investigations on the effects of non-STC cell temperatures and ambient temperatures on c-Si PV solder joint degradation are presented in sections 4.3 and 4.4 respectively. Section 4.5 concludes the chapter.

## 4.2 FINITE ELEMENT MODELLING

In the investigation of the effect of non-STC cell temperatures and ambient temperatures on the degradation of c-Si PV solder interconnections, finite element modelling is employed. A 1mm by 1mm c-Si PV cell assembly is designed using the SolidWorks 3D modelling software package. The designed model is then converted to the acceptable Parasolid (*.x_t) format which forms the Geometry input to the ANSYS FEM Academic Research Mechanical software environment where its response to the applied thermal loads and boundary conditions are simulated. Accumulated creep strain energy density quantifies the solder joint degradation. Equations 3.7 – 3.10 describe in detail how to calculate accumulated creep strain energy density.

The Engineering Data input to the ANSYS FEM package includes coefficient of thermal expansion (CTE), Young's Modulus, Poisson Ratio and other mechanical

properties of the c-Si PV module component layer materials. Refer to Table 3.1 for the complete properties of the c-Si PV module component layers. The material components are modelled using several thermo-mechanical models including linear elastic, viscoelastic, creep and temperature dependent material models. The Garofalo creep model, was utilised to simulate the maximum creep strain energy which is the degradation response of the solder layer. Constitutive material models are included in the Engineering Data. When all inputs are complete, coordinate systems, mesh size, fixed support and boundary conditions are set. The analysis settings and thermal condition are set at 26 steps. The Creep control was TURNED ON with Creep Limit Ratio set at 8 and the simulation proceeded. Further details of the model design procedure and constitutive material models can be found in chapter 3 of this thesis.

## 4.3 EFFECT OF CELL TEMPERATURE

This section presents the investigation on the effect of cell temperature on c-Si PV solder interconnection degradation. For each 1 °C step rise from 25°C STC, the corresponding solder joint degradation is generated from the ANSYS FEM simulation output. The applied PV cell temperature load range is 25 °C ≤ T ≤ 120 °C. To fully understand and quantify the effect of high temperature on PV solder joint degradation, the relationship between solder joint degradation and each 1 °C rise in c-Si PV cell temperature from STC is described numerically.

Previous researchers have examined the effect of cell temperature rise on the electrical power output degradation of c-Si PV modules. Dubey *et al.* (2013) and Kato (2012) reported that the temperature coefficient pMax of c-Si PV modules is -0.5%. This implies that for every 1 °K PV cell temperature rise from the STC, the power conversion efficiency (PCE) of the PV module decreases by 0.5%. However,

there is no recorded numerical relationship between PV cell temperature and the thermo-mechanical degradation of PV solder joints. This current study establishes this numerical relationship which provides information to improve the performance and reliability of c-Si PV modules in elevated temperature climates.

### 4.3.1 Solder interconnection degradation due to cell temperature rise

The degradation of c-Si PV solder interconnection is determined at every 1 °C temperature rise from 25 °C STC in the ANSYS FEM environment. At each temperature load step, the creep strain energy (solder interconnection damage) is generated. Applying Equation 3.7, the creep strain energy density is calculated. Results show that for each 1 °C rise in PV cell temperature, there is a corresponding increase in the maximum creep strain energy density. Figure 4.1 presents the creep strain energy distribution in the ANSYS FEM environment. The coloured key represents the solder interconnection damage graduation with greatest damage indicated as red and least damage indicated as dark blue.

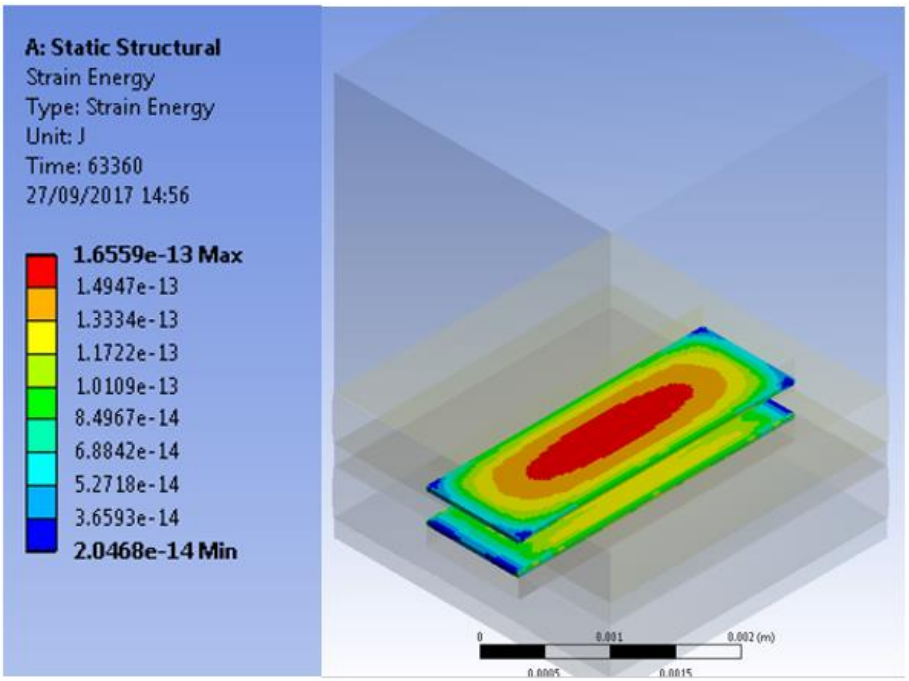


**Figure 4.1:** Creep strain energy (solder damage) in ANSYS FEM environment

### 4.3.2 Numerical relationship between solder interconnection degradation and cell temperature rise

In section 4.3.1, it was discussed that solder interconnection degradation increased with each 1 °C rise in cell temperature however, the correlation of the two entities cannot be simply described as linear. Figure 4.2 presents the plot of maximum strain energy density (solder interconnection damage) versus cell temperature. It can be observed that there are three (3) distinct damage regions. These damage regions signify three distinct cell temperature ranges, numerical relationship between cell temperature and solder interconnection degradation, and solder interconnection degradation rate. The characteristics of the damage regions manifest in the change of shape of the plot as it progresses from one region to the next.

Region 1 falls within the cell temperatures of 25 °C and 42 °C. The relationship between cell temperature and solder interconnection degradation is quadratic and the solder degradation rate increased steadily from 1.53 Pa/°C to 10.03 Pa/°C. Region 2 is between cell temperatures 43 °C and 63 °C and demonstrates the highest solder degradation with the constant rate of 12.06 Pa/°C. The relationship between cell temperature and solder interconnection degradation is linear which leaves the solder degradation rate constant throughout the region. In region 3 (64 °C to 120 °C), a logarithmic relationship is observed between cell temperature and solder interconnection degradation. The solder degradation rate decreases from 5.47 Pa/°C to 2.25 Pa/°C and this reduction in accumulated creep strain energy density can be attributed to operation at high homologous temperatures. Unlike in regions 1 and 2, the increase in cell temperature resulted in decrease in accumulated creep strain energy density due to decreased solder hardness (Amalu and Ekere, 2012a).

Region 2 is identified as the critical region. This is because solder degradation rate is highest and constant at 12.06 Pa/°C. It is of significance to understand the way c-Si

PV modules operating within this damage region behave in order to improve their reliability and fatigue life. The cell temperatures observed in this region align with reported elevated temperature climate operating conditions hence, they will be used for the ambient operating temperature experiments discussed in section 4.4.

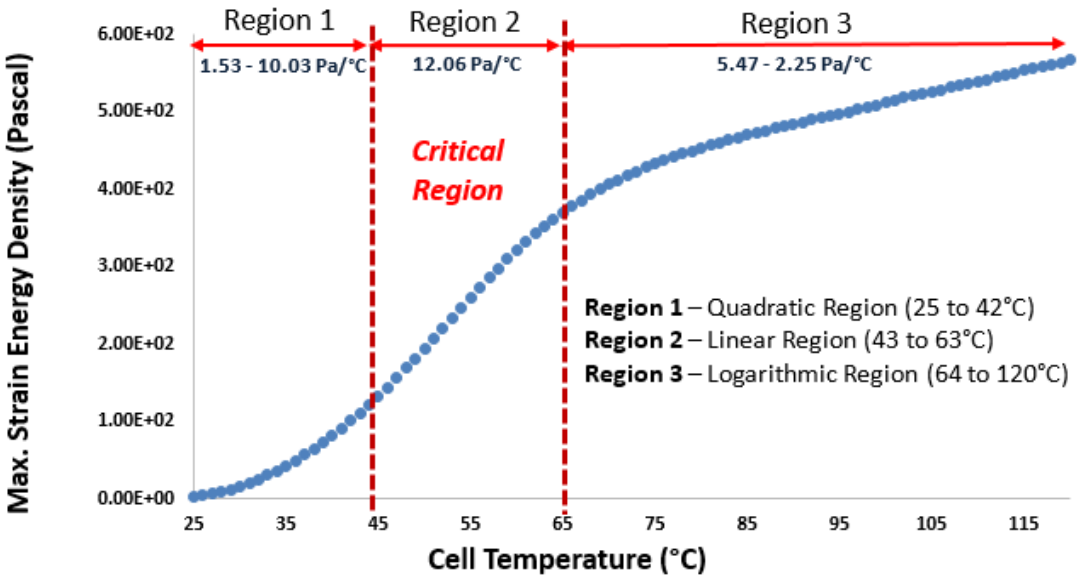


**Figure 4.2:** Max. strain energy density against cell temperature showing three damage regions

## 4.4 EFFECT OF AMBIENT TEMPERATURE

This section presents the investigation on the effect of ambient temperature on c-Si PV solder interconnection degradation utilising the ANSYS FEM software environment. The field operating temperature condition of c-Si PV modules are better described by thermal cycles because temperatures rise and fall over the lifetime of the system. The IEC 61215 standard thermal cycle load is applied to describe the temperature load in this study (Arndt and Puto, 2010). Refer to chapter 3 for more discussions on loads and boundary conditions.

In section 4.3, region 2 was identified as the critical solder damage region. Operating temperatures that belong to this solder damage region are used to investigate the

effect of ambient temperature on solder interconnection degradation. These temperature values are within the range reported by previous researches on the typical field operating temperatures of c-Si PV modules (Ghani *et al.*, 2015) in elevated temperature climates. The difference between c-Si PV cell temperature and ambient temperature has been reported to be as high as 22 °C (Kurnik *et al.*, 2011). Equation 4.1 presents the relation between these two temperature parameters.

$$T_{cell} - 22\ °C \approx T_{ambient} \quad \text{Equation 4.1}$$

$$T_{elevated} = \frac{T_{upper\ limit} + T_{lower\ limit}}{2} \quad \text{Equation 4.2}$$

For this study, the ambient temperature loads varied within the range 25 °C ≤ T ≤ 45 °C. The degradation of c-Si PV solder interconnections at these ambient temperatures is investigated and fatigue life predicted. Inputting $T_{upper\ limit}$ = 45 °C and $T_{lower\ limit}$ = 25 °C into Eq. 4.2, the elevated temperature, $T_{elevated}$ = 35 °C. This elevated temperature value will be used as the ambient operating temperature load for the other investigations on RIFs of c-Si PV module discussed in chapters 5, 6 and 7.

### 4.4.1 Solder interconnection degradation due to ambient temperature rise

The degradation of the c-Si PV solder interconnection is determined at each ambient temperature load and thermal cycling load. Maximum creep strain energy data values are recorded off the ANSYS FEM software environment. Equations 3.7 - 3.10 are applied to calculate accumulated creep strain energy density which quantifies solder interconnection degradation. Solder degradation is observed to increase as ambient temperature increases. Table 4.1 presents accumulated creep strain energy density (Pa) at corresponding ambient temperature values. The lowest solder degradation of 0.01203 Pa was recorded at 25 °C while the highest degradation of 0.05207 Pa was

at 45 °C. Figure 4.3 presents hysteresis loops at ambient temperatures 25 °C and 45 °C. A hysteresis loop is a plot of equivalent stress (Pa) versus equivalent strain. The area under a hysteresis loop signifies the creep strain energy accumulated and dissipated in the c-Si PV solder interconnection. The area under the hysteresis loop at ambient temperature 45 °C is larger than that of 25 °C. This means that solder degradation is greatest at 45 °C and least at 25 °C. Findings agree with researches on the relationship between hysteresis loop size and temperature rise (Mustafa *et al.*, 2011; Vandevelde *et al.*, 2007).

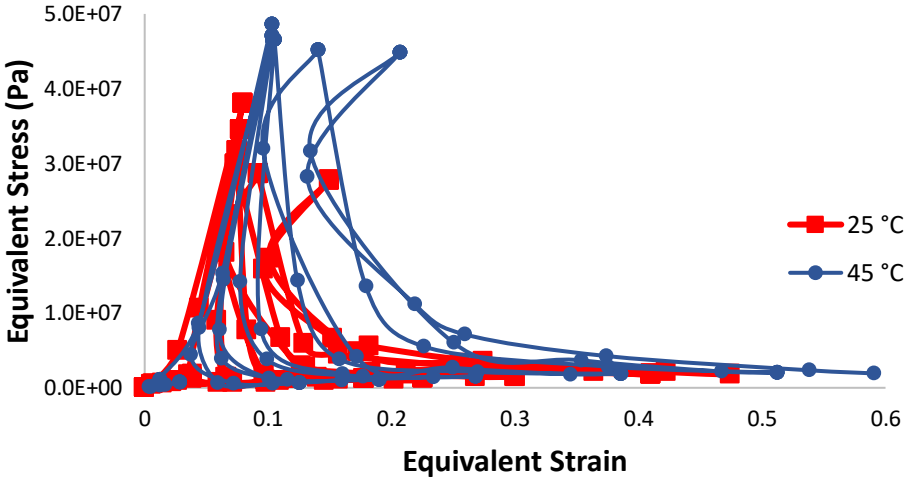


**Figure 4.3:** Equivalent stress (Pa) versus equivalent strain at ambient temperatures 25 °C and 45 °C

### 4.4.2 Fatigue life prediction under varying ambient temperatures

Accumulated creep strain energy density has been used to quantify solder interconnection degradation in sub section 4.4.1 but in this sub section, it is used to predict fatigue life of the c-Si PV module. Equation 3.6 is applied to determine the mean fatigue life (cycles), $N_f$, of the system at each ambient temperature load.

$$L = \left(\frac{t_c}{y}\right) N_f \qquad \text{Equation 4.3}$$

Equation 4.3 presents the relation between mean fatigue life, L (in years) and mean fatigue life, $N_f$ (in cycles), where, $t_c$ is the time per cycle (in seconds), and $y$ is one year (in seconds). Equation 4.3 was derived to calculate the lifetime of c-Si PV modules in years. Converting fatigue life from cycles to years will make life expectancy values easier to understand and use by real life consumers in the field.

$N_f$ and L values are presented in Table 4.1, and Fig. 4.4 presents the variation of mean fatigue life with ambient temperature. There is an inverse relationship between solder degradation and fatigue life. Also, fatigue life is observed to decay as ambient temperature increases. The longest fatigue life of 59355 cycles to failure (9.6 years) was recorded at ambient temperature of 25 °C while at 45 °C, the shortest of 13718 cycles to failure (4.3 years) was recorded.

Equation 4.4 was derived by the author to predict the fatigue life (years) of c-Si PV modules within the ambient temperature range 25 °C ≤ T ≤ 45 °C. Where: L is the mean fatigue life (years) and T is the ambient temperature (°C). This function provides a projection of mean fatigue life with a correlation coefficient of 0.9025. The power function presented in Eqn. 4.4 is a handy relation that can be easily applied by consumers to predict the lifespan (in years) of c-Si PV modules operating in their climatic region.

$$L = 721.48T^{-1.343} \qquad \text{Equation 4.4}$$

Qin *et al.* (2014) proposed damage mechanics method which revealed that strain energy density performs a power function correlation with the cycle numbers of crack initiation and propagation. Section 4.4.3 discusses further the effect of cycle number on the accurate determination of solder interconnection degradation. Figure 4.5 is a plot of mean fatigue life (years) and ambient temperature (°C). The thick continuous red line represents the fatigue life values obtained by applying Eqn. 4.3

and measured data from the ANSYS FEM experiment while the broken blue line represents fatigue life values obtained by applying the derived power function model from Eqn. 4.4.

**Table 4.1:** Solder joint degradation and mean fatigue lives at corresponding ambient temperatures

| **Ambient Temperature (°C)** | **Accumulated Max. Creep Strain Energy Density ($10^{-2}$Pa)** | **$N_f$ ($10^4$cycles)** | **L (Years)** |
|---|---|---|---|
| 25 | 1.20 | 5.90 | 9.6 |
| 27.5 | 2.23 | 3.20 | 8.4 |
| 30 | 2.84 | 2.50 | 7.5 |
| 32.5 | 3.57 | 2.00 | 6.7 |
| 35 | 4.37 | 1.60 | 6.1 |
| 37.5 | 4.32 | 1.70 | 5.6 |
| 40 | 4.54 | 1.60 | 5.1 |
| 42.5 | 4.74 | 1.50 | 4.7 |
| 45 | 5.21 | 1.40 | 4.3 |

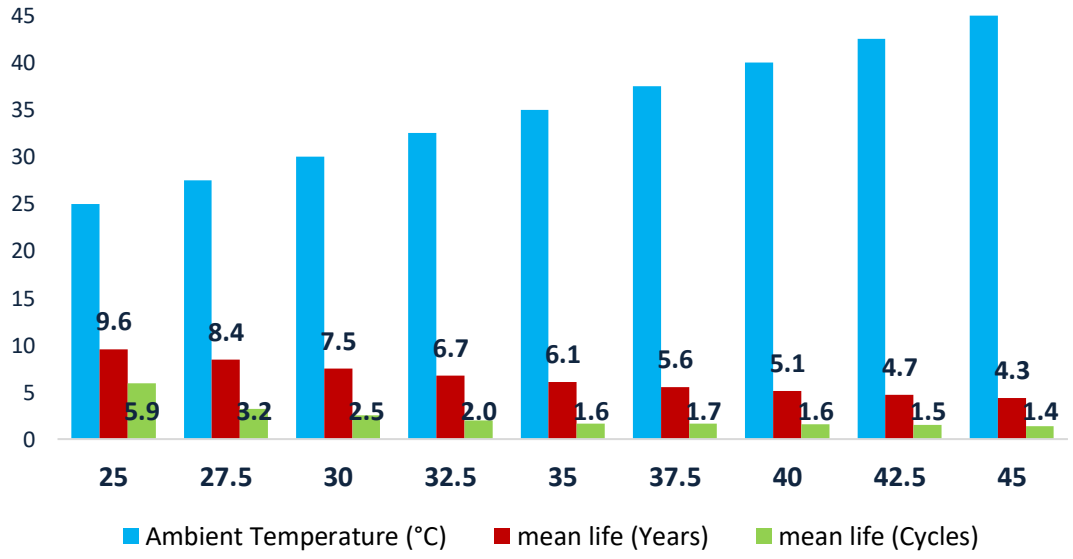


**Figure 4.4:** Mean fatigue life variation with ambient temperature (°C)

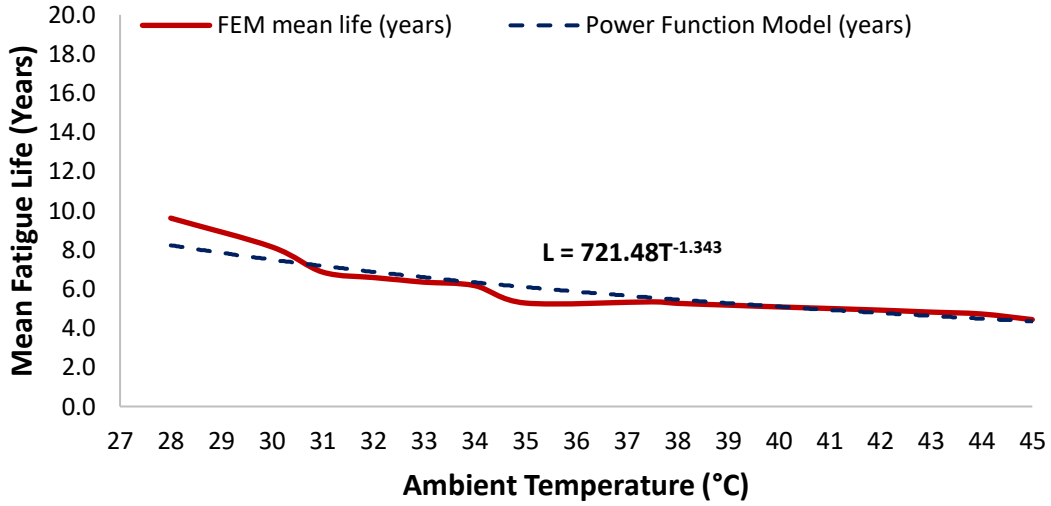


**Figure 4.5:** Plot of mean fatigue life (Years) from FEM and power function model against ambient temperatures (°C)

### 4.4.3 Effect of cycle number on the accurate determination of solder interconnection degradation

In this section, the effect of thermal cycle number on the determination of c-Si PV solder interconnection degradation is discussed under the headings of equivalent stress, equivalent strain, cyclic deformation and IMC deformation. The analysed data is obtained from the ANSYS FEM software environment.

#### 4.4.3.1 Equivalent stress

The c-Si PV solder interconnection model is simulated under the IEC 61215 thermal cycle at each ambient temperature load. Equivalent stress values of the solder component layer are recorded off the ANSYS FEM software environment. Figure 4.6 presents the plot of equivalent stress (Pa) over cycle number at the different ambient temperature loads. It is observed that from the beginning of cycling up to cycle number 2, the equivalent stress values are highest on the 25 °C curve and lowest on the 45 °C curve. As the cycling continues, a turning point is reached at cycle number

3. At the turning point, all the ambient temperature curves converge, and all their equivalent stress values are equal. Initial cycle instability is surpassed and beyond the turning point, a transition region can be seen from cycle number 4. Further cycling shows the divergence of the curves with 45 °C demonstrating highest equivalent stress values while the lowest values on the 25 °C curve. Henceforth and throughout the rest of the thermal cycles, the plot follows the same trend as discussed in previous sections where solder degradation increased with operating temperature. These observations have been reported in earlier published research by the author (Ogbomo *et al.*, 2018) and aligns with other studies which state that equivalent stress values are highest from cycle number 3 onwards, and at least six (6) thermal cycles are required to accurately qualify solder degradation thereby avoiding errors caused by initial cycle instability (Amalu and Ekere, 2012; Chao *et al.*, 2016).

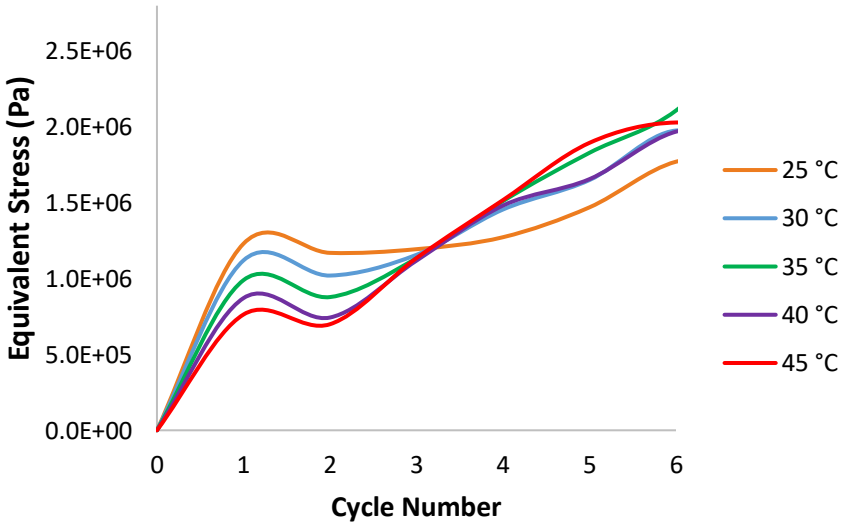


**Figure 4.6:** Equivalent stress (Pa) over cycle number at various ambient temperatures

### 4.4.3.2 Equivalent strain

As in section 4.4.3.1, the c-Si PV solder interconnection model is simulated under the thermal cycles and at each ambient temperature load. Equivalent strain values of

the solder component layer are recorded from the ANSYS FEM software environment. Figure 4.7 is the plot of equivalent strain over cycle time at the various ambient temperature loads. The beginning of cycling up to cycle number 2 shows little difference between the equivalent strain curves at the ambient temperatures. This occurrence in the solder can be attributed to its temperature dependent Young's Modulus of expansion as described in Eqn. 3.1 and nature of the IEC 61215 test standard thermal cycle load. The slow ramp rate, 1.667 °C/min, of the IEC 61215 minimises thermal shock and causes the strain to be accumulated gradually in the solder interconnection. Right after cycle number 2, there is a turning point at cycle number 3 similar to that observed in Fig. 4.6. The curves begin to display divergence, and this is sustained throughout the rest of the thermal cycles. It is worthy to note that accelerated thermal cycling (ATC) performed in FEM environments should not be carried out with less than three (3) cycle numbers to avoid errors and misleading results.

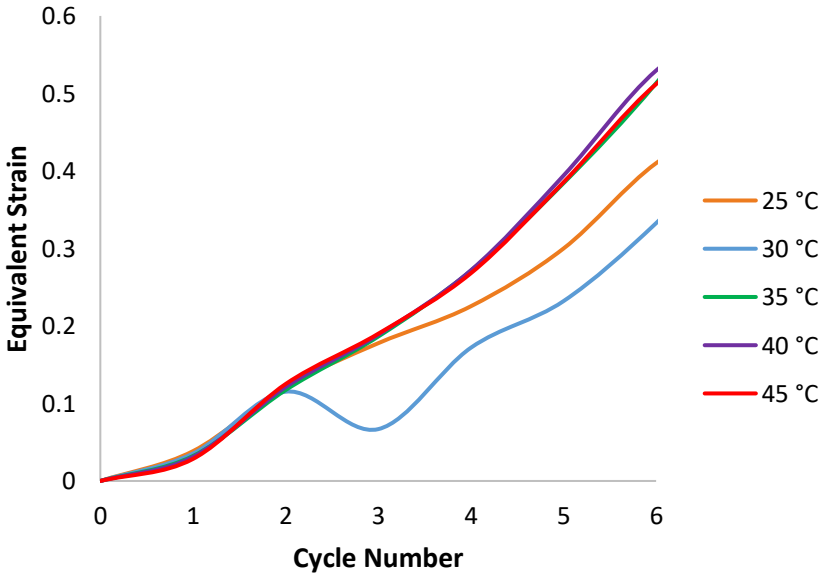


**Figure 4.7:** Equivalent strain over cycle number at various ambient temperatures

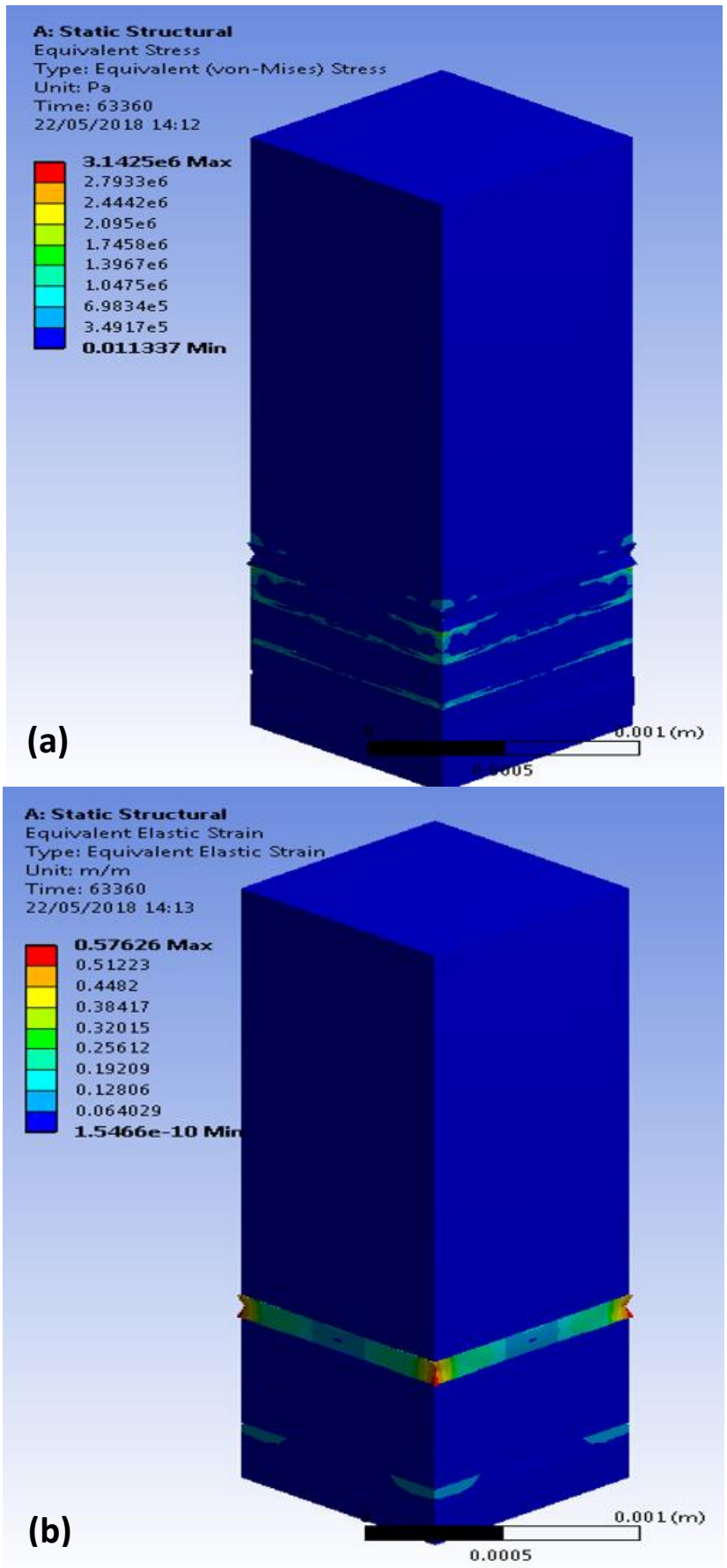


**Figure 4.8:** Equivalent stress (a) and equivalent strain (b) at 45 °C ambient temperature

#### 4.4.3.3 Material degradation due to cyclic deformation

The solder interconnection layers remain the focus of the current investigation, but it is noteworthy to pan out focus to the entire c-Si PV module. From the findings, other component layers of the c-Si PV module are observed to possess higher stress and strain levels than the solder layer and thus can influence the degradation of the solder interconnection. Results indicate that EVA is the component layer with the greatest stress and strain accumulation in the c-Si PV module. EVA demonstrated these high degradation levels at all the investigated ambient temperature loads. Figure 4.8 (a) and (b) show the equivalent stress and equivalent strain distribution on the c-Si PV module under 45 °C ambient load in the ANSYS FEM software environment. The coloured key displays the graduation of the component layer material degradation. Red represents the highest material degradation observed in the EVA layer while the lowest material degradation is represented by the dark blue hue.

As earlier discussed, the material properties of solder were modelled as temperature dependent. Also, EVA layer was modelled as viscoelastic as opposed to linear elastic models used by some other researchers. Applying viscoelastic and temperature dependent material models enables a better description of EVA properties and reduces inaccuracy related to nonlinearities in the FEM simulations. Figure 3.5 shows the plot of Young's Modulus (MPa) of EVA versus temperature (°C) for different relaxation times. Further details on constitutive material models can be found in chapter 3 of this thesis. Several researchers (Paggi, Corrado and Rodriguez, 2013; Paggi *et al.*, 2014; Phinikarides *et al.*, 2014; Borri, Gagliardi and Paggi, 2018) have experimentally characterised the material degradation of c-Si PV modules due to cyclic deformation and have reported EVA encapsulant layer to significantly influence the behaviour of the solder interconnection, increase gaps between cells and aggravate solder interconnection degradation.

#### 4.4.3.4 Material degradation due to IMC deformation

In this section, the effect of including IMC layer in the modelling of c-Si PV solder interconnection degradation is investigated. Two sets of c-Si PV solder interconnection models are simulated under the IEC 61215 thermal cycle at each ambient temperature load. One set of the models includes the IMC layer while the other does not. The IMC layer material used for this current study is $Cu_6Sn_5$. This IMC material is consistent with solder interconnections formed by SAC305 solders and copper which have been used in the c-Si PV solder interconnection models (Qin *et al.*, 2014). Accumulated creep strain energy density values, which quantify solder interconnection degradation, are calculated from the ANSYS FEM data.

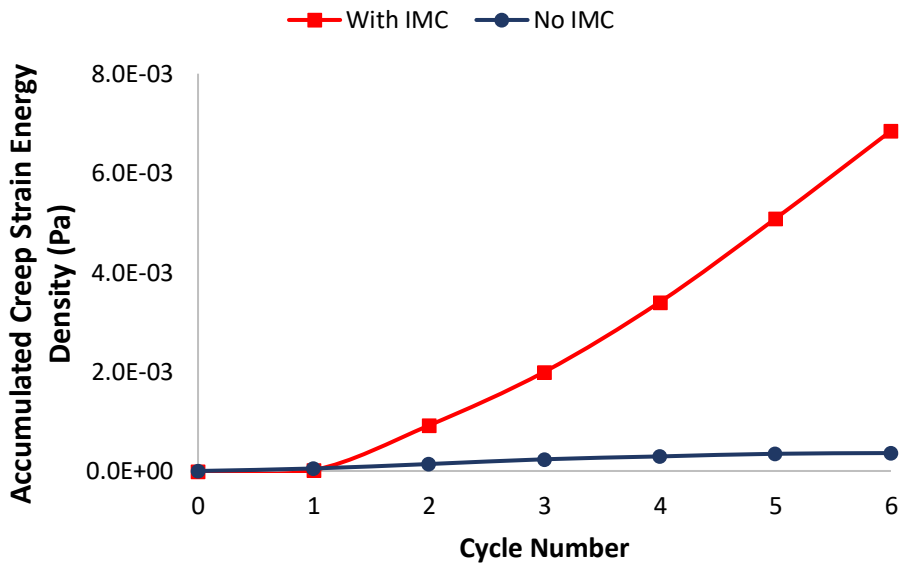


**Figure 4.9:** Solder degradation versus cycle number at 25 °C ambient temperature

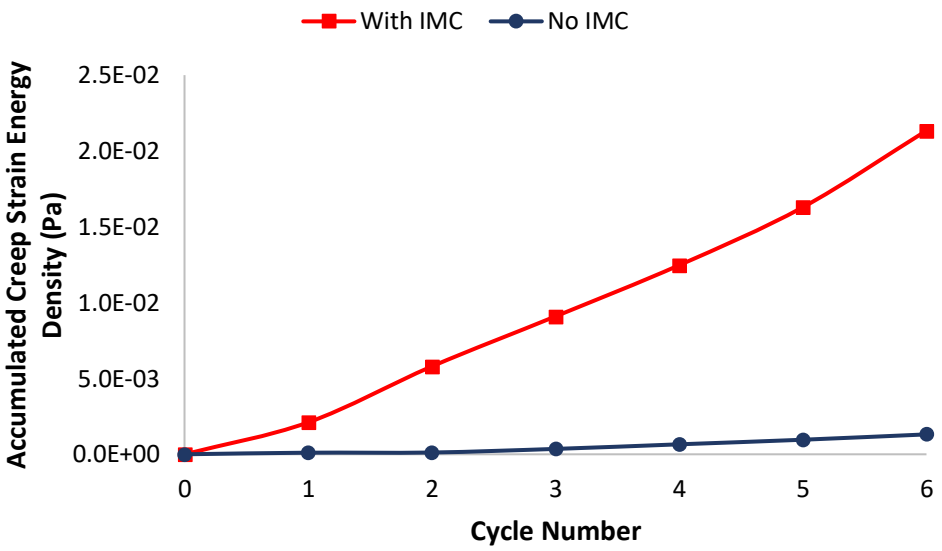


**Figure 4.10:** Solder degradation versus cycle number at 45 °C ambient temperature

Figures 4.9 and 4.10 present the degradation of the two sets of c-Si PV solder interconnection models (with IMC & no IMC) versus cycle number at 25 °C and 45 °C ambient temperatures respectively. It can be observed that the models with no IMC demonstrate less solder interconnection degradation than those with IMC. As the thermal cycling progresses, the creep strain energy density continues to accumulate and rise steeply in the model with IMC while in the model with no IMC, a plateauing is observed. This trend continues for the rest of the thermal cycles and at all the investigated ambient temperature loads. This implies that the inclusion of the IMC layer significantly influences the solder interconnection degradation irrespective of ambient temperature load. Also, this effect accumulates as thermal cycling progresses. Including IMC in the FE models produces more realistic results than models without IMC. Crack initiation in solder joints has been reported to begin at the IMC layer due to higher brittleness in the layer (George, 2010; Amalu *et al.*, 2011; Nadimpalli and Spelt, 2011; Amalu and Ekere, 2012; Amalu and Ekere, 2012; Xiao *et al.*, 2013; Chao *et al.*, 2016). Figure 4.11 shows SEM micrographs of c-Si PV solder interconnection model showing the IMC phases and crack location. Cracks

lead to increase in series resistance, reduced electrical insulation and power output loss in c-Si PV modules (Paggi *et al.*, 2014).

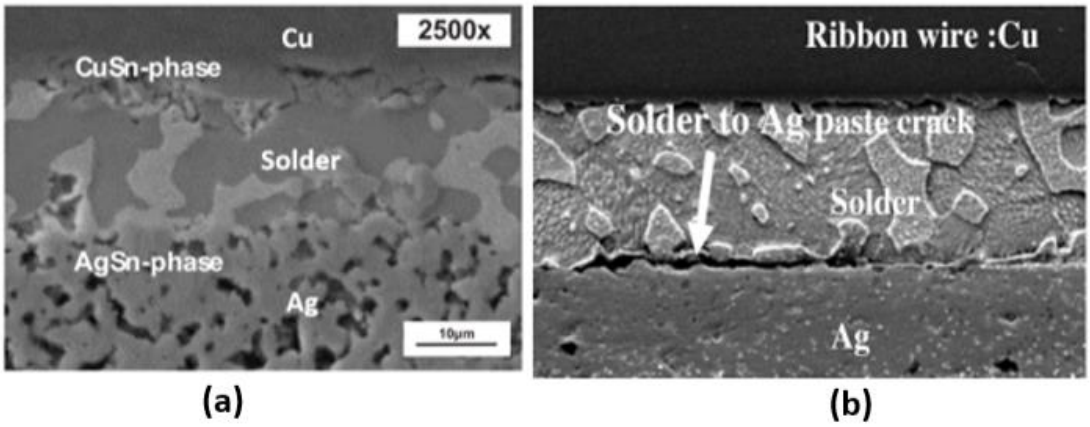


**Figure 4.11:** SEM micrographs of c-Si PV solder interconnection model showing CuSn (a) and AgSn (b) IMC phases in SAC solder-to-silver layer crack

Sources: (a) Schmitt *et al.*, 2012 and (b) Jeong, Park and Han, 2012

Several researchers have investigated the effect of IMC layer on the reliability of solder joints in printed circuits boards (PCBs) and other surface mount technologies (SMTs) but there is a dearth of studies in c-Si PV module solder interconnections (George, 2010; Amalu *et al.*, 2011; Nadimpalli and Spelt, 2011; Amalu and Ekere, 2012; Amalu and Ekere, 2012; Xiao *et al.*, 2013; Chao *et al.*, 2016). Chao *et al.* (2016), in their study of the low cycle fatigue behaviour of SAC solder joints, described the fracture morphologies of solder under different frequencies and strain ranges. They observed fatigue cracks initiated around the edges of the joint at the boundary between the IMC and solder layers. The cracks then propagate with the solder layer along the IMC/solder layer interfaces. With increasing frequency, intergranular fracture transformed to trans-granular fracture which leads to final fracture. Amalu and Ekere (2012) simulated 3D flip chip models in ANSYS 13 to predict the damage and fatigue life of bonded material assemblies in high temperature operations. They determined the IMC layer between the copper die and

solder is most susceptible to crack initiation and propagation. In a later study (Amalu and Ekere, 2012a), they varied the thickness of the IMC layer in five (5) flip ship models to evaluate its effect on solder joint reliability. They observed that the models with the thickest and thinnest IMC layers influenced the reliability of solder joints.

The previous published studies have been focused on the effect of IMC layer on the degradation of ball solder joints and flip chips in PCBs and other surface mount electronics but there is none on composite solder joints in c-Si PV modules especially under various non-standard ambient and cell temperatures. Therefore, this current research presents findings which contribute to knowledge on the effects of IMC layer on the degradation of c-Si PV solder interconnection at various ambient temperature loads.

## 4.5 CONCLUSIONS

This chapter presented an investigation on the effects of non STC operating temperatures (cell temperatures & ambient temperatures) on c-Si PV solder interconnections degradation using ANSYS FEM software environment. The accumulated creep strain energy density values for each of the applied loads were calculated to quantify solder interconnection degradation.

Results show that solder interconnection degradation increases with each 1°C cell temperature rise from the STC. Three damage regions were observed over the cell temperature range with distinct numerical relationships between solder interconnection degradation and cell temperature, and degradation rates (Pa/°C). Region 1 (25 °C to 42 °C) is characterised by degradation rate increasing quadratically from 1.53 Pa/°C to 10.03 Pa/°C. Region 2 (43 °C to 63 °C), with a constant degradation rate of 12.06 Pa/°C, demonstrates a linear relationship between

solder interconnection degradation and cell temperature. Region 3 (64 °C to 120°C) shows a declining degradation rate from 5.47 Pa/°C at the beginning of the region to 2.25 Pa/°C at the end of the region, and a logarithmic numerical relationship. Region 2 showed the highest degradation rate and was identified as the critical damage region. The cell temperature range in region 2 are characteristic of elevated temperature climates which induce maximum damage in the solder joint and account for the high failure rate of the c-Si PV module observed in the region.

The fatigue life of the c-Si PV module was found to decay under the applied ambient temperature loads. A power function model $L = 721.48T^{-1.343}$, was derived by the author to predict the fatigue life (years) of the system within the ambient temperature range 25 °C ≤ T ≤ 45 °C. This model is a handy toolkit for consumers to determine the lifetime of their c-Si PV modules in any climatic region. The model predicts c-Si PV module average life in London and elevated temperature climate to be 19 years and 6 years respectively. The London module fatigue life is within the 1.4 factor of safety range of the 25-year manufacturers' warranty, but the elevated temperature climate life is abysmal and buttresses the high failure rate observed in the region. Energy payback time (EPBT) and return on investment are significantly affected.

Further findings show that the inclusion of the IMC layer in the c-Si PV module influences the solder interconnection degradation. The set of c-Si PV models with IMC layer demonstrated greater accumulation of creep strain energy density in the solder joint which steeply accrued as thermal cycling progressed. On the other hand, the set of models with no IMC showed significantly lesser solder interconnection degradation and creep strain energy density accumulation plateaued as thermal cycling continued. This implies that IMC layer is important for the accurate modelling of c-Si PV modules in ANSYS FEM environment. Additionally, cycle number influences the accuracy of FEM results. Equivalent stress and equivalent

strain values displayed turning points after cycle number 3 and then conformed to expected trends.

As the presented findings have shown the poor performance of the c-Si PV modules in non STC operating conditions, the next chapters 5, 6 and 7 will aim to redesign the conventional system to improve thermo-mechanical reliability, ensure longevity of fatigue life and attractive return on investment in elevated temperature climates.

# CHAPTER 5

# EFFECT OF MATERIAL COMBINATION OF BONDED MATERIALS IN THE SOLDER JOINT ON PHOTOVOLTAIC (PV) INTERCONNECTION DEGRADATION

## 5.1 INTRODUCTION

This chapter presents an investigation on the effects of material combination on the degradation of c-Si PV solder interconnections for improved reliability in elevated temperature climate using ANSYS FEM. The effect of material combination is one of the defined reliability influencing factors (RIFs) of the PV solder interconnection. Refer to chapter 1 for more details. In chapter 4, the conventional c-Si PV solder interconnection was described to comprise of copper ribbon and silver contact with Sn3.5Ag0.5Cu solder alloy sandwiched in between. Judging by the findings presented in sections 4.3 and 4.4 of the chapter on the effect of operating temperature on c-Si PV solder interconnections, and the subsequent establishment of a power function model to predict fatigue life under any ambient operating temperature, it is expected that the conventional solder interconnection will perform poorly under elevated temperature climate conditions. Section 5.3 will present the findings on the performance of the conventional c-Si PV interconnection under STC and elevated temperature climate conditions. Section 5.4 discusses the performance of various ribbon-contact material combinations hence ascertain their suitability to replace the conventional c-Si PV solder interconnection for improved reliability in elevated temperature climates.

## 5.2 FINITE ELEMENT MODELLING

In the investigation of the material combination on the degradation of c-Si PV solder interconnections for improved reliability in elevated temperature climate, finite element modelling was employed. A 1mm by 1mm c-Si PV cell assembly was designed using the Solid Works 3D modelling software package. The completed 3D model was then converted to the acceptable Parasolid (*.x_t) format which forms the Geometry input to the ANSYS FEM environment. The designed model was the input to ANSYS Academic Research Mechanical software package to simulate the c-Si PV model response to the applied thermal loads and boundary conditions. The chosen materials for the material combination experiments are Aluminium, Brass, Copper, Silver, Tin and Zinc. They have been selected because of characteristic qualities which include thermal conductivity, electrical conductivity and coefficient of thermal expansion (CTE). These material properties constitute part of the Engineering Data input to the ANSYS Academic Research Mechanical software package.

These six (6) materials will be joined to form thirty-six (36) different ribbon-contact combinations of the c-Si PV solder interconnection. Table 5.1 presents the ribbon-contact material combination grid. The material components are modelled using several thermo-mechanical models including linear elastic, viscoelastic, creep and temperature dependent material models. The Garofalo creep model is used to determine the maximum creep strain energy which is a measure of PV solder interconnection degradation. The material properties of solder and EVA layers demonstrate temperature dependence and viscoelasticity. Hence, they are modelled using the appropriate material models. Further details of the model design procedure, material properties and constitutive material models can be found in chapter 3 of this thesis.

**Table 5.1:** Ribbon-Contact material combination grid

| Material Combinations | | Ribbon | | | | | |
|---|---|---|---|---|---|---|---|
| | | Aluminium | Brass | Copper | Silver | Tin | Zinc |
| Contact | Aluminium | 1 | 2 | 3 | 4 | 5 | 6 |
| | Brass | 7 | 8 | 9 | 10 | 11 | 12 |
| | Copper | 13 | 14 | 15 | 16 | 17 | 18 |
| | Silver | 19 | 20 | 21 | 22 | 23 | 24 |
| | Tin | 25 | 26 | 27 | 28 | 29 | 30 |
| | Zinc | 31 | 32 | 33 | 34 | 35 | 36 |

Accumulated creep strain energy density (Pa), Equivalent Stress (Pa), Equivalent Strain and Creep Strain are utilised to quantify solder interconnection degradation. Also, applying Eqn. 3.6, the fatigue lives of all thirty-six ribbon-contact combinations are derived. The performances of all thirty-six ribbon-contact combinations are compared to the conventional c-Si PV interconnection under elevated temperature climate conditions. The combination(s) with best performance(s) under the elevated temperature operating condition will be identified and proposed to be used in the redesign of c-Si PV modules for improved reliability in the climate.

## 5.3 PERFORMANCE OF CONVENTIONAL PV SOLDER INTERCONNECTION

The performance of the conventional c-Si PV solder interconnection is investigated under STC and elevated temperature climate conditions. This performance comparison of the conventional c-Si PV solder interconnection is presented in section 5.3.1. Thereafter in section 5.3.2, the modes of comparing the performance of

the conventional c-Si PV solder interconnection to the other thirty-six (36) ribbon-contact material combinations under elevated temperature climate operating conditions are derived by the author.

### 5.3.1 Performance comparison of conventional PV solder interconnection at STC and elevated temperature climate

The performance of the conventional c-Si PV solder interconnection which comprises of copper ribbon joined to silver contact by the Sn3.5Ag0.5Cu solder alloy, is investigated under STC and elevated temperature climate conditions. As presented in Table 5.2 and Fig. 5.1, the degradation of the solder interconnection is measured by the accumulated maximum creep strain energy density. The degradation value in elevated temperature climate is 2.64 times that in STC. The fatigue life of the solder interconnection decreases from 19.2 years in STC to 5.28 years in elevated temperature climate which is a 72.5% decrease. This means that under elevated temperature climate conditions, the conventional c-Si PV module is operating at only 27.5% of its designed performance and fatigue life. It is therefore ostensible that there is an urgent need to proffer a solution.

**Table 5.2:** Performance of conventional c-Si PV solder interconnection at STC and elevated temperature climate

| Operating Condition | Accumulated Max. Creep Strain Energy Density (E-04 Pa) | Fatigue Life (E+03 Cycles) | Fatigue Life (years) |
|---|---|---|---|
| STC | 120 | 59.355 | 19.20 |
| Elevated temperature | 437 | 16.333 | 5.28 |

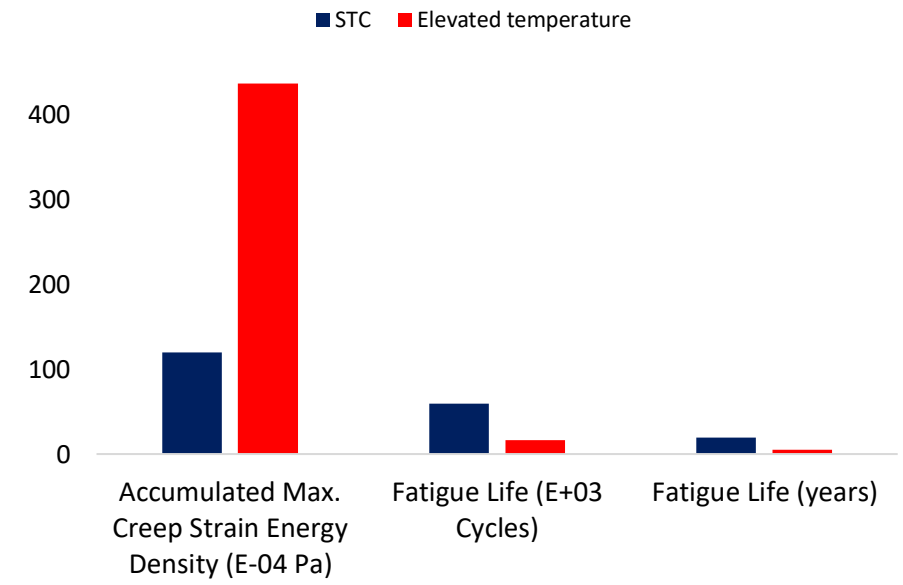


**Figure 5.1:** Performance comparison of conventional PV solder interconnection at STC and elevated temperature climate

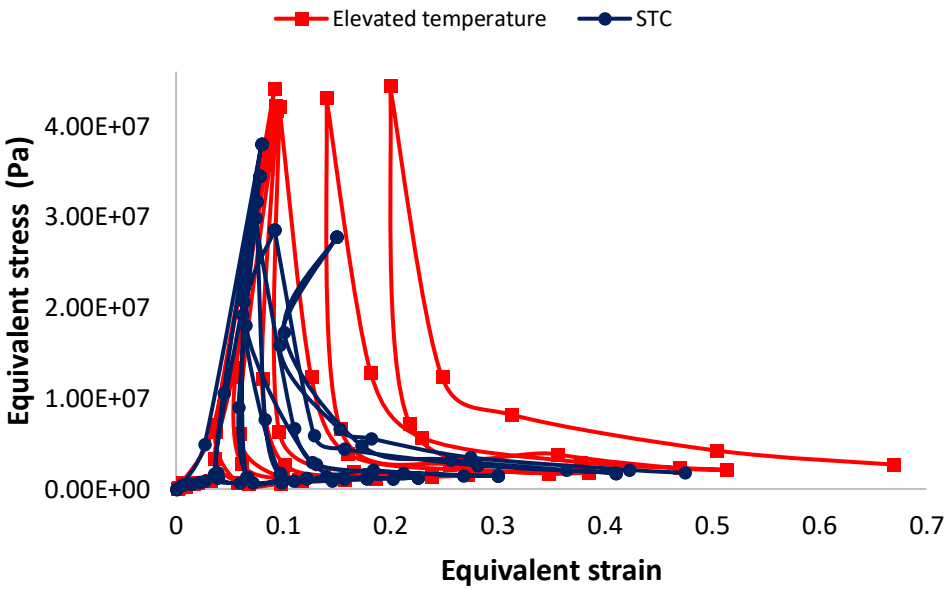


**Figure 5.2:** Equivalent stress against equivalent strain of conventional PV solder interconnection at STC and elevated temperature climate

Hysteresis loops, presented in Fig. 5.2, which are plots of equivalent stress (Pa) against equivalent strain, are also used to compare the performance of the conventional c-Si PV solder interconnection at STC and elevated temperature climate. The creep strain energy dissipated and accumulated in the solder

interconnections are represented by the area under the loops. The larger the area under the hysteresis loops, the greater the solder interconnection degradation. Therefore, the elevated temperature climate operating condition shown to have larger area under the hysteresis loops, creates greater solder interconnection than at STC with smaller area under the loops. This finding agrees with studies on the connection between hysteresis loop size and temperature rise (Vandevelde *et al.*, 2007; Mustafa *et al.*, 2011).

Figure 5.3 is the plot of equivalent stress against cycle number of the conventional c-Si PV solder interconnection at STC and elevated temperature climate. The STC curve demonstrates higher stress values than the elevated temperature climate curve from the beginning of cycling up to cycle number 2. Right after cycle number 2, the curves converge at a point (turning point) where the stress values on both curves are equal. Immediately beyond the turning point is cycle number 3 where the curves diverge with the elevated temperature climate curve demonstrating higher stress values than that of STC. Also, the STC curve is observed to begin to plateau and fall while the elevated temperature climate curve continues to climb from cycle number 5 onwards. This trend continues for the rest of the thermal cycles. This observation; equivalent stress values are highest from cycle number 3 onwards and at least six (6) thermal cycles are sufficient to qualify solder joint degradation, is in line with findings from section 4.4 of chapter four, a previously published research by the author (Ogbomo *et al.*, 2018) and reports from other researchers (Amalu and Ekere, 2012a).

Figure 5.4 is the plot of equivalent strain against cycle number of the conventional c-Si PV solder interconnection at STC and elevated temperature climate. Both STC and elevated temperature climate curves show little difference in strain values from the beginning of cycling up to cycle number 2. Similar to observations in Fig. 5.3,

Fig. 5.4 shows a turning point right after cycle number 2. The strain curves diverge and by cycle number 3, there is a clear difference in strain values with the elevated temperature climate curve demonstrating higher strain values than that of STC. This trend continues for the rest of the thermal cycles.

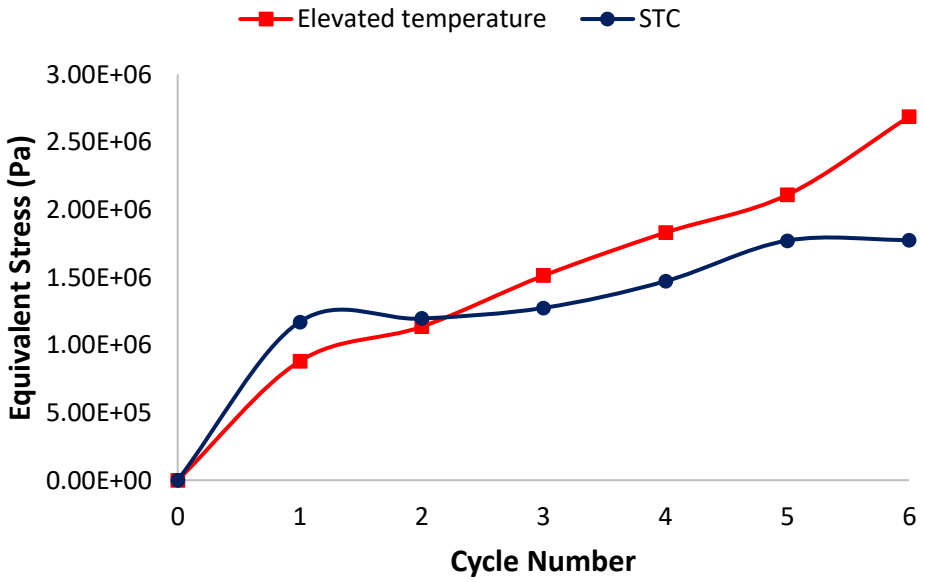


**Figure 5.3:** Equivalent stress against cycle number of conventional PV solder interconnection at STC and elevated temperature climate

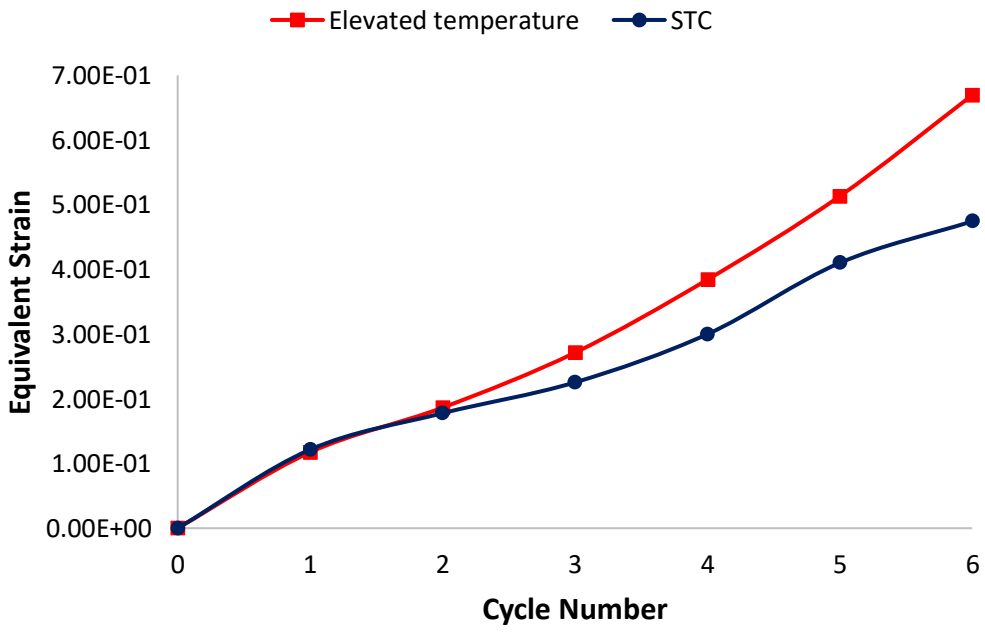


**Figure 5.4:** Equivalent strain against cycle number of conventional PV solder interconnection at STC and elevated temperature climate

Figure 5.5 shows the creep strain energy distribution on the solder layer under elevated temperature conditions in the ANSYS FEM environment. The coloured keys indicates the graduation of the solder degradation with red as greatest and royal blue as least. As shown in Fig. 5.5, the highest creep strain energy values are located at the centre of the solder layer. This is similarly observed in Fig. 5.7 and Fig. 5.9 which display the equivalent stress and equivalent strain distribution on the solder layer under elevated temperature climate conditions. The highest values for the equivalent stress and equivalent strain are located at the centre of the solder layer. Several researchers (Paggi, Corrado and Rodriguez, 2013; Borri, Gagliardi and Paggi, 2018) who have investigated solder deformation, crack initiation and crack propagation using laboratory experiments, FEM and numerical methods have reported that cracks initiate at the middle of the solder layer. This is in line with findings from this present study. Figures 5.6, 5.8 and 5.10 show the creep strain energy, equivalent stress and equivalent strain distributions respectively on the solder layer under STC. The highest values are observed at the corners of the solder layer.

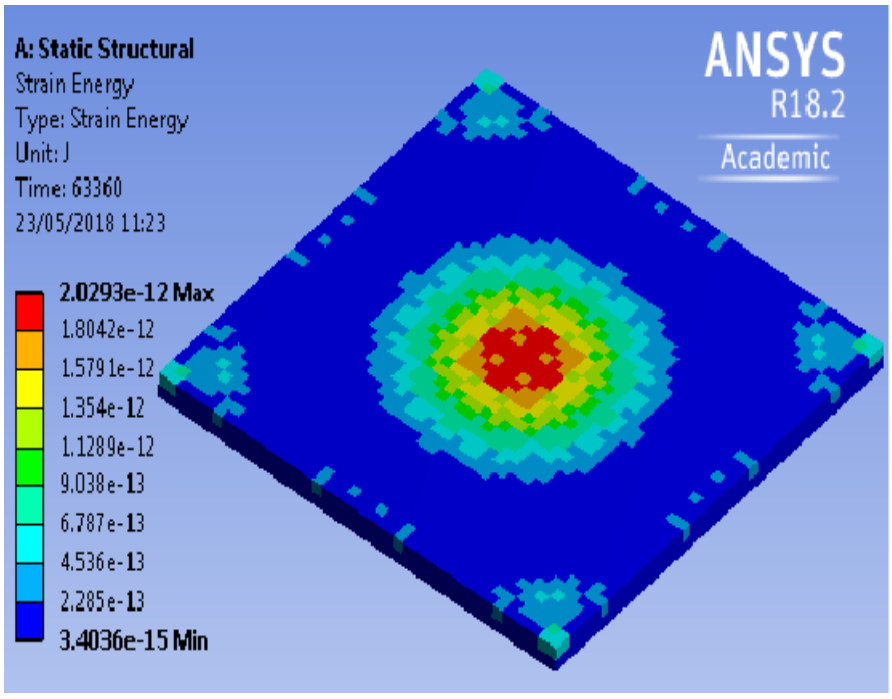


**Figure 5.5:** Creep strain energy in elevated temperature climate

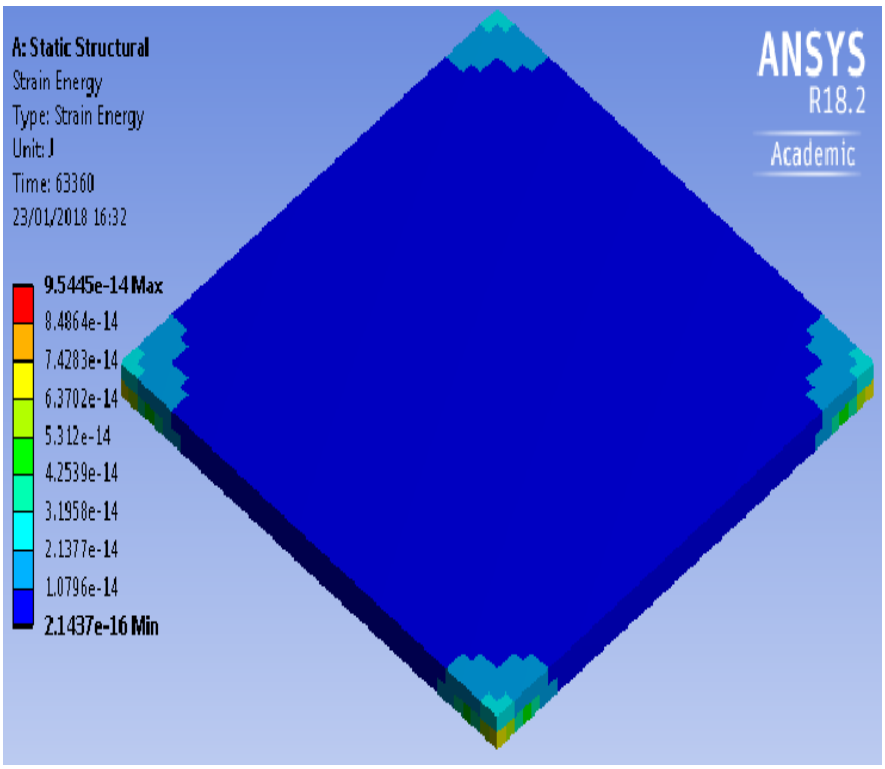


**Figure 5.6:** Creep strain energy at STC

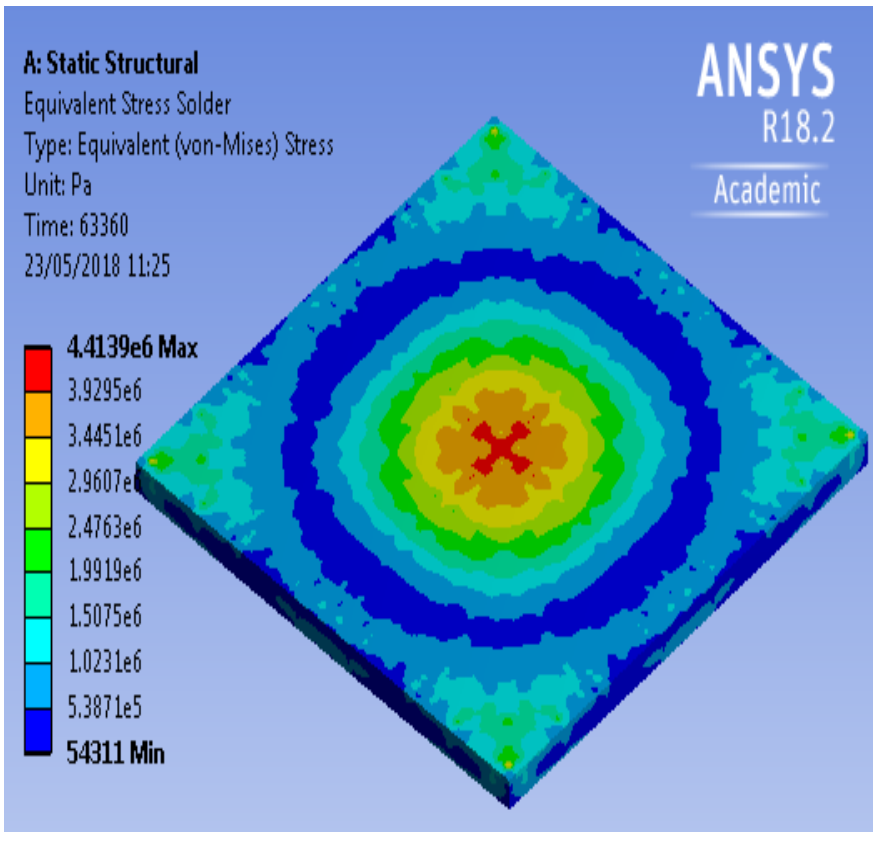


**Figure 5.7:** Equivalent stress in elevated temperature climate

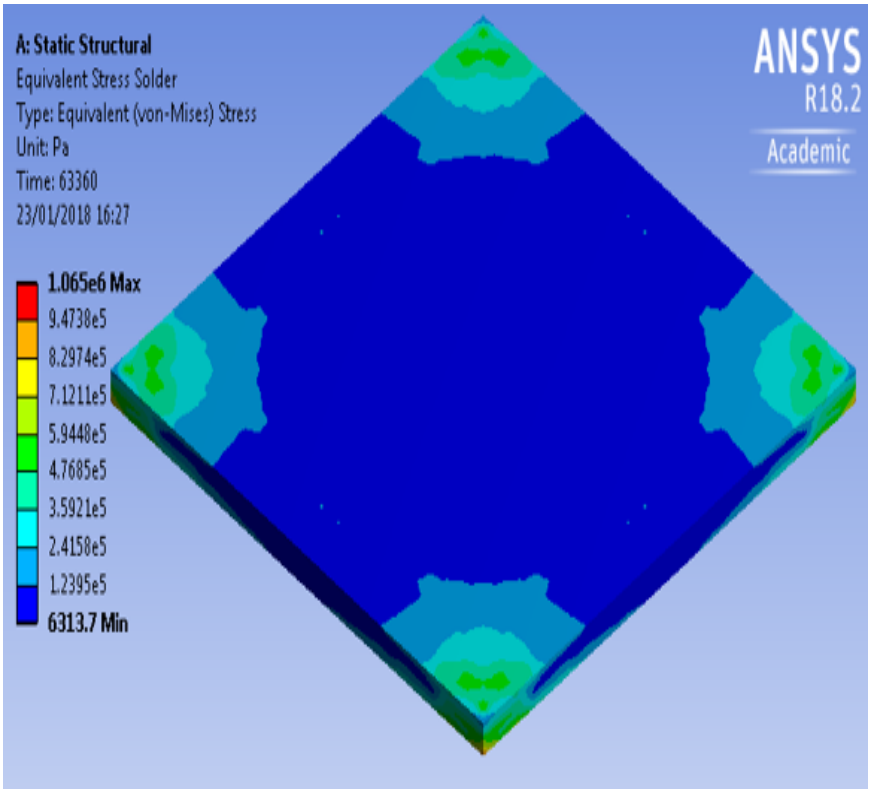


**Figure 5.8:** Equivalent stress at STC

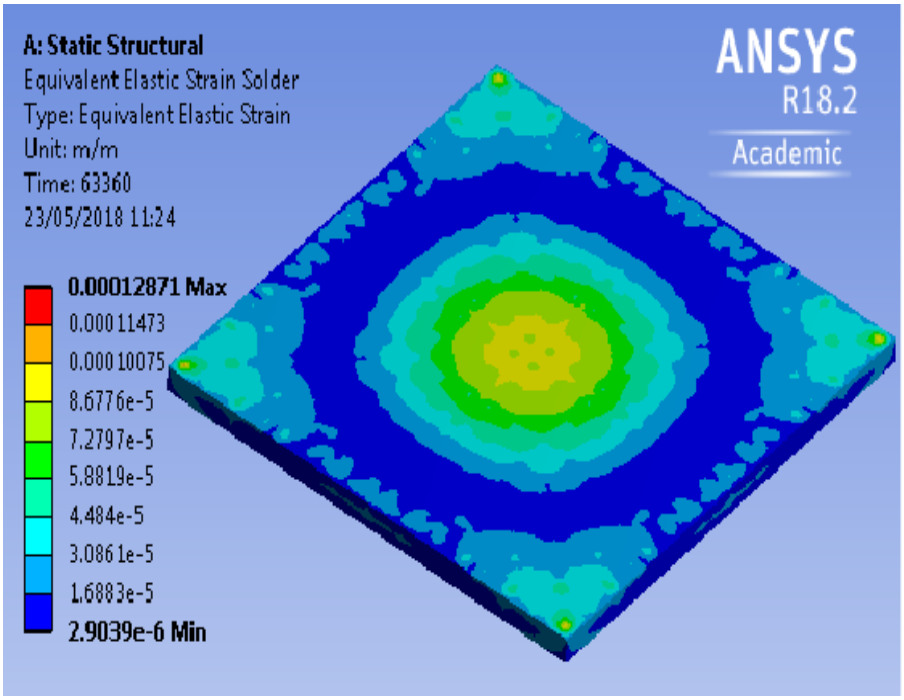


**Figure 5.9:** Equivalent strain in elevated temperature climate

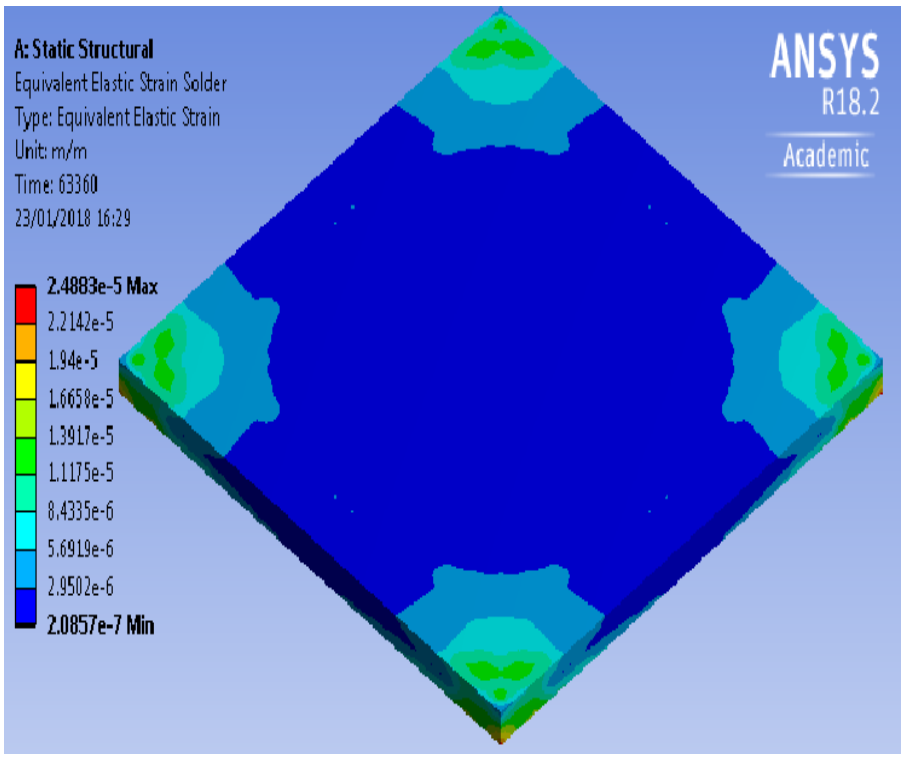


**Figure 5.10:** Equivalent strain at STC

### 5.3.2 Modes of performance comparison of conventional PV solder interconnection and proposed material combinations in elevated temperature climate

In section 5.2 and in Table 5.1, the six (6) chosen materials were joined to form thirty-six (36) different ribbon-contact combinations of the c-Si PV solder interconnection. In order to identify which of the thirty-six proposed ribbon-contact material combinations demonstrate best performance in elevated temperature climate, they will be compared to the performance of the conventional c-Si PV solder interconnection. The conventional solder interconnection under elevated temperature climate conditions will be assigned the role of central tendency (CT) and all other material combinations will either cluster or disperse around the CT. The best designs will disperse from the CT while the worst designs will cluster around the CT.

#### 5.3.2.1 Mode 1

The normalised degradation value, $N_{d_i}$, of each ribbon-contact material combination with combination number, $i$, is the ratio of the solder interconnection degradation of that combination to the solder interconnection degradation of the CT. $N_{d_i}$, as presented in Eqn. 5.1, expresses the solder interconnection degradation of each combination as a factor of the CT value.

$$N_{d_i} = \frac{Degradation\ of\ Combination}{Degradation\ of\ CT} \qquad \text{Equation 5.1}$$

Equation 5.2 is derived by inputting the degradation value of CT in Eqn. 5.1. Where $N_{d_{CT}}$= normalised degradation of CT, $N_{d_{BD}}$= normalised degradation of best design and $N_{d_{WD}}$= normalised degradation of worst design.

$$N_{d_{CT}} = 1, \left(N_{d_{BD}} \ll 1 \ll N_{d_{WD}}\right) \qquad \text{Equation 5.2}$$

#### 5.3.2.2 Mode 2

The normalised fatigue life, $N_{f_i}$, of each ribbon-contact material combination with combination number, $i$, is the ratio of the fatigue life of that combination to the fatigue life of the CT. $N_{f_i}$, as presented in Eqn. 5.3, expresses the fatigue life of each combination as a factor of the CT value.

$$N_{f_i} = \frac{fatigue\ life\ of\ Combination}{fatigue\ life\ \ of\ CT} \qquad \text{Equation 5.3}$$

Equation 5.4 is derived by inputting the fatigue life value of CT in Eqn. 5.3. Where $N_{f_{CT}}$= normalised fatigue life of CT, $N_{f_{BD}}$= normalised fatigue life of best design and $N_{f_{WD}}$= normalised fatigue life of worst design.

$$N_{f_{CT}} = 1, \left(N_{f_{BD}} \gg 1 \gg N_{f_{WD}}\right) \qquad \text{Equation 5.4}$$

#### 5.3.2.3 Mode 3

The normalised degradation deviation, $D_i$, of each ribbon-contact material combination with combination number, $i$, is the percentage deviation of the normalised degradation of that combination, $N_{d_i}$, from the normalised degradation of the CT, $N_{d_{CT}}$. $D_i$, as presented in Eqn. 5.5, expresses the normalised degradation of each combination as a percentage of the CT value.

$$D_i = \frac{N_{d_i} - N_{d_{CT}}}{N_{d_{CT}}} \times 100 \qquad \text{Equation 5.5}$$

Equation 5.6 is derived by inputting the normalised degradation value of CT in Eqn. 5.5. Where $D_{CT}$= normalised degradation deviation of CT, $D_{BD}$= normalised degradation deviation of best design and $D_{WD}$= normalised degradation deviation of worst design.

$$D_{CT} = 0\%, (D_{BD} \ll 0\% \ll D_{WD}) \qquad \text{Equation 5.6}$$

#### 5.3.2.4 Mode 4

The normalised fatigue life deviation, $F_i$, of each ribbon-contact material combination with combination number, $i$, is the percentage deviation of the normalised fatigue life of that combination, $N_{f_i}$ , from the normalised fatigue life of the CT, $N_{f_{CT}}$. $F_i$, as presented in Eqn. 5.7, expresses the normalised fatigue life of each combination as a percentage of the CT value.

$$F_i = \frac{N_{f_i} - N_{f_{CT}}}{N_{f_{CT}}} \times 100 \qquad \text{Equation 5.7}$$

Equation 5.8 is derived by inputting the normalised fatigue life value of CT in Eqn. 5.7. Where $F_{CT}$= normalised fatigue life deviation of CT, $F_{BD}$= normalised fatigue

life deviation of best design and $F_{WD}$= normalised fatigue life deviation of worst design.

$$F_{CT} = 0\%, (F_{BD} \gg 0\% \gg F_{WD}) \quad \text{Equation 5.8}$$

#### 5.3.2.5 Mode 5

The deformation ratio, $\delta_{R_i}$, of each ribbon-contact material combination with combination number, $i$, is the ratio of the solder deformation of that combination, $\delta_{solder_i}$, to the total deformation in the c-Si PV module, $\delta_{T_i}$. The higher the deformation ratio, the greater the solder interconnection degradation. In a study on the thermo-mechanical deformation degradation of c-Si PV modules in operation, (Amalu *et al.*, 2018), deformation ratio was one of the analytical methods provided to validate FEM simulation results. The deformation ratio values derived from the analytical method will be compared to those obtained from the ANSYS FEM environment. Applying fundamental mechanics theories and principles, $\delta_{R_i}$, is derived in Eqns. 5.9 - 5.13.

Recalling Eqns. 2.15 and 2.17,

$$\delta = \frac{\sigma}{E} L \quad \text{Equation 5.9}$$

$$\delta = \frac{PL}{AE} \quad \text{Equation 5.10}$$

Where δ = deformation, σ = stress, E = Young's Modulus of expansion, L = length, P = force and cross-sectional area, A = height (h) by width (w).

Deformation ratio,

$$\delta_{R_i} = \frac{\delta_{solder_i}}{\delta_{T_i}} \quad \text{Equation 5.11}$$

The c-Si PV module is assumed as a composite laminate beam with height = $h_T$ and Young's Modulus of expansion = $E_T$. Combining Eqns. 5.10 and 5.11,

$$\delta_{R_i} = \frac{PL}{wh_{solder_i}E_{solder}} \times \frac{h_T w E_T}{PL} \quad \text{Equation 5.12}$$

The force (P), width (w) and length (L) are the same for all the c-Si PV models. Equation 5.12 becomes,

$$\delta_{R_i} = \frac{h_T E_T}{h_{solder_i}E_{solder}} \quad \text{Equation 5.13}$$

$E_T$, was derived by (Amalu *et al.*, 2018) as:

$$E_T = \frac{\sum_{j=1}^{n} E_j h_j}{\sum_{j=1}^{n} h_j} \quad \text{Equation 5.14}$$

Where $E_j$, = Young's Modulus of expansion for each component layer material, h = height of component layer and n = number of layers.

$$h_T = \sum_{j=1}^{n} h_j \quad \text{Equation 5.15}$$

In the application of the deformation ratio analytical method, the key components included in the composite beam laminate are EVA, ribbon, SAC solder, contact, c-Si, and TPT. The temperature dependent Young's modulus of EVA and SAC solder are derived at elevated temperature from Fig. 3.5 and Eqn. 3.1 respectively while Table 3.1 presents the properties of the other component layers. The glass layer is excluded because its thickness is ≫ than the sum of thicknesses of the other layers. The effect of the expansions of the other layers on glass is negligible. By applying this assumption, the degree of freedom for a rational numerical analysis is reduced for simplification (Paggi, Kajari-Schröder and Eitner, 2011; Amalu *et al.*, 2018).

Modes 1 – 4 as derived by the author as well as mode 5 are applied to the FEM results data from the material combination experiments presented in section 5.4.

## 5.4 PERFORMANCE OF PROPOSED PV SOLDER INTERCONNECTIONS

In section 5.3, it was discussed that the conventional c-Si PV solder interconnection only operates at about 27.5% of its designed performance under elevated temperature climate conditions. In this section, several material combinations will be tested for their suitability to replace the conventional solder interconnection in the climatic region employing single variate experiments. To afford greater readability, the material combination investigations will be divided into contact modelling in section 5.4.1, ribbon modelling in 5.4.2 and zero CTE mismatch combinations in 5.4.3.

Each combination will be compared to the CT. Mode 1, presented in Eqns. 5.1 & 5.2, and Mode 3, presented in Eqns. 5.5 & 5.6 will be applied to derive the values for normalised degradation, $N_{d_i}$ and normalised degradation deviation, $D_i$ respectively. Mode 2, presented in Eqns. 5.3 & 5.4, and Mode 4, presented in Eqns. 5.7 & 5.8 will be applied to derive the values for normalised fatigue life, $N_{f_i}$ and normalised fatigue life deviation, $F_i$ respectively. Mode 5 is applied to validate FEM results with analytical methods. Refer to section 5.3.2 for more details on the modes of performance comparison of conventional PV solder interconnection and proposed material combinations in elevated temperature climate.

### 5.4.1 Contact modelling

The sole function of the c-Si PV cell is to generate useful electricity from exposure to sunlight. This function is made possible by the contact layer which conducts the electric charges generated by the system as useful electricity. Contact technology was discussed in chapter 2. This section presents the experiments which examine the thermo-mechanical behaviour of several ribbon-contact material combinations of the

solder interconnection by varying the contact layer material. The performance of each of these Combs. is then be compared to that of the CT, hence, identify the combination with least degradation, longest fatigue life and improved reliability of c-Si PV module solder interconnection in hot temperature climate. Silver contact is discussed in subsection 5.4.1 while Aluminium, Brass, Copper, Tin and Zinc contacts are presented in 5.4.1.2, 5.4.1.3, 5.4.1.4, 5.4.1.5, and 5.4.1.6 respectively.

#### 5.4.1.1 Silver Contact

For this set of material combination experiments, the contact and solder component layers are kept constant at Silver and Sn3.5Ag0.5Cu alloy respectively while the material for the ribbon layer is varied. Table 5.3 presents the solder interconnection degradation for the Silver contact experiments. The best design for the Silver contact set of experiments is the Aluminium-Silver material combination ($N_{d_{BD}}$= 0.02 & $D_{BD}$= -98%). This means that the solder degradation of this Al-Ag Combination is 0.02 times that of the CT and has decreased degradation by 98%. The worst design for the Silver contact set of experiments is the Brass-Silver material combination ($N_{d_{WD}}$= 3.04 & $D_{WD}$= 204%). This means that the solder degradation of this B-Ag Combination is 3.04 times that of the CT and has increased degradation by 204%.

Table 5.4 presents the fatigue life for the Silver contact experiment. The fatigue life values for the best design, Al-Ag Combination, are $N_{f_{BD}}$= 56.99 & $F_{BD}$= 5599%). This means that the fatigue life this Al-Ag Combination is 56.99 times that of the CT and has increased fatigue life by 5599%. The fatigue life values for the worst design, B-Ag Combination, are $N_{f_{WD}}$= 0.33 & $F_{WD}$= -67%). This means that the fatigue life of this B-Ag Combination is 0.33 times that of the CT and has decreased fatigue life by 67%.

**Table 5.3:** Solder interconnection degradation for Silver contact experiment

| **Ribbon Material** | **Accumulated Max. Creep Strain Energy Density (E-04 Pa)** | $N_{d_i}$ | $D_i$ **(%)** |
|---|---|---|---|
| Aluminium | 7.68 | 0.02 | -98 |
| Brass | 1330 | 3.04 | 204 |
| Copper | 437 | 1.00 | 0 |
| Tin | 395 | 0.90 | -10 |
| Zinc | 404 | 0.92 | -8 |

**Table 5.4:** Fatigue life for Silver contact experiment

| **Ribbon Material** | **Fatigue Life (E+03 Cycles)** | **Fatigue Life (years)** | $N_{f_i}$ | $F_i$ **(%)** |
|---|---|---|---|---|
| Aluminium | 930.358 | 300.91 | 56.99 | 5599 |
| Brass | 5.286 | 1.74 | 0.33 | -67 |
| Copper | 16.333 | 5.28 | 1.00 | 0 |
| Tin | 18.070 | 5.84 | 1.11 | 11 |
| Zinc | 17.660 | 5.71 | 1.08 | 8 |

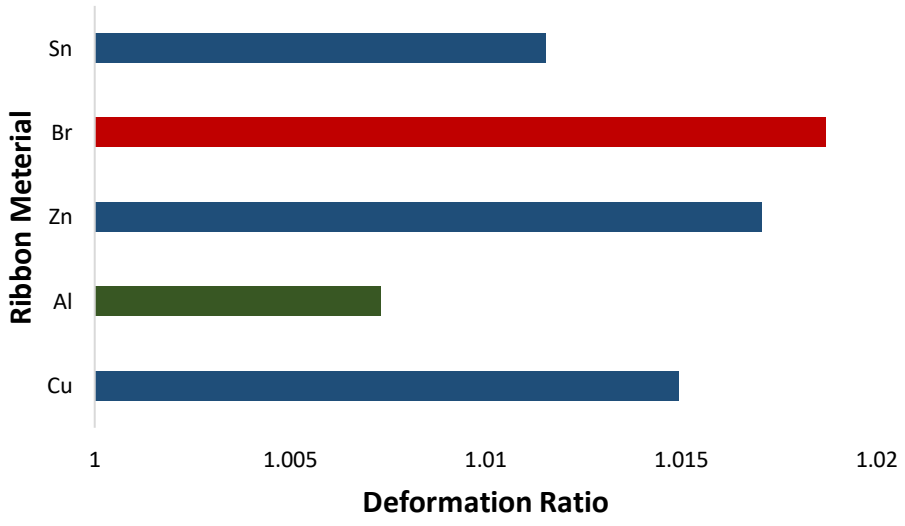


**Figure 5.11:** Deformation ratios for the Silver contact investigation

Figure 5.11 presents the deformation ratios for the Silver contact investigation. The B-Ag combination possesses the highest $\delta_R$ value (red bar) while the Al-Ag combination had the lowest $\delta_R$ value (green bar). These results derived from the analytical model follow the same trend of the solder degradation results obtained from the FEM simulations.

#### 5.4.1.2 Aluminium Contact

For this set of experiments the contact and solder component layers are kept constant at Aluminium and Sn3.5Ag0.5Cu alloy respectively while the material for the ribbon layer is varied. Table 5.5 presents the solder interconnection degradation for the Aluminium contact experiments. The degradation values for the best design, Silver-Aluminium, are $N_{d_{BD}}$= 0.01 & $D_{BD}$= -99%. This Ag-Al Combination has a solder degradation which is 0.01 times that of the CT and has decreased degradation by 99%. The worst design for the Aluminium contact set of experiments is the Brass-Aluminium material combination ($N_{d_{WD}}$= 2.95 & $D_{WD}$= 195%). This means that the solder degradation of this B-Al Combination is 2.95 times that of the CT and has increased degradation by 195%.

**Table 5.5:** Solder interconnection degradation for Aluminium contact experiment

| **Ribbon Material** | **Accumulated Max. Creep Strain Energy Density (E-04 Pa)** | $N_{d_i}$ | $D_i$ (%) |
|---|---|---|---|
| Brass | 1290 | 2.95 | 195 |
| Copper | 356 | 0.81 | -19 |
| Silver | 6.08 | 0.01 | -99 |
| Tin | 363 | 0.83 | -17 |
| Zinc | 1030 | 2.36 | 136 |

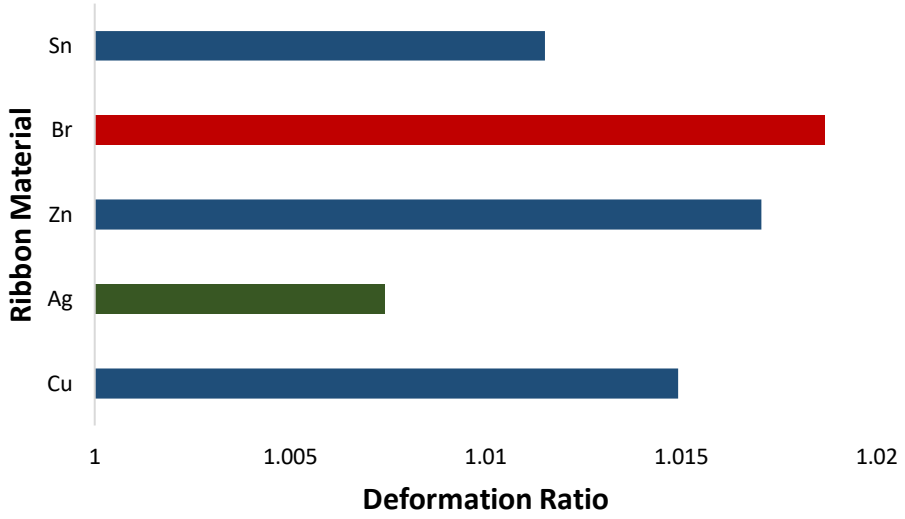


**Figure 5.12:** Deformation ratios for the Aluminium contact investigation

Figure 5.12 presents the deformation ratios for the Aluminium contact investigation. The results derived from the analytical model follow the same trend of the FEM simulation results for solder deformation. Table 5.6 presents the fatigue life for the Aluminium contact experiment. The fatigue life values for the best design, Ag-Al Combination, are $N_{f_{BD}}$= 72.01 & $F_{BD}$= 7101%). This means that the fatigue life this Ag-Al Combination is 72.01 times that of the CT and has increased fatigue life by 7101%. The fatigue life values for the worst design, B-Al Combination, are $N_{f_{WD}}$= 0.34 & $F_{WD}$= -66%). This means that the fatigue life of this B-Al Combination is 0.34 times that of the CT and has decreased fatigue life by 66%.

**Table 5.6:** Fatigue life for Aluminium contact experiment

| **Ribbon Material** | **Fatigue Life (E+03 Cycles)** | **Fatigue Life (years)** | $N_{f_i}$ | $F_i$ **(%)** |
|---|---|---|---|---|
| Brass | 5.531 | 1.79 | 0.34 | -66 |
| Copper | 20.078 | 6.49 | 1.23 | 23 |
| Silver | 1175.566 | 380.22 | 72.01 | 7101 |
| Tin | 19.693 | 6.37 | 1.21 | 21 |
| Zinc | 6.953 | 2.25 | 0.43 | -57 |

#### 5.4.1.3 Brass Contact

For this set of experiments the contact and solder component layers are kept constant at Brass and Sn3.5Ag0.5Cu alloy respectively while the material for the ribbon layer is varied. Table 5.7 presents the solder interconnection degradation for the Brass contact experiments. The best design for the Brass contact set of experiments is the Aluminium-Brass material combination ($N_{d_{BD}}$= 1.25 & $D_{BD}$= 25%). This means that this Al-B Combination performed worse than the CT with $N_{d_i} > 1$ and a positive $D_i$ value. It can be concluded that Brass as a contact material is not a suitable substitution to the CT. Figure 5.13 presents the deformation ratios for the Brass contact investigation. The results derived from the analytical model confirm the solder degradation results obtained from the FEM simulations.

**Table 5.7:** Solder interconnection degradation for Brass contact experiment

| **Ribbon Material** | **Accumulated Max. Creep Strain Energy Density (E-01 Pa)** | $N_{d_i}$ | $D_i$ **(%)** |
|---|---|---|---|
| Aluminium | 0.548 | 1.25 | 25 |
| Copper | 6.65 | 15.22 | 1422 |
| Silver | 0.611 | 1.40 | 40 |
| Tin | 2.46 | 5.63 | 463 |
| Zinc | 11.6 | 26.54 | 2554 |

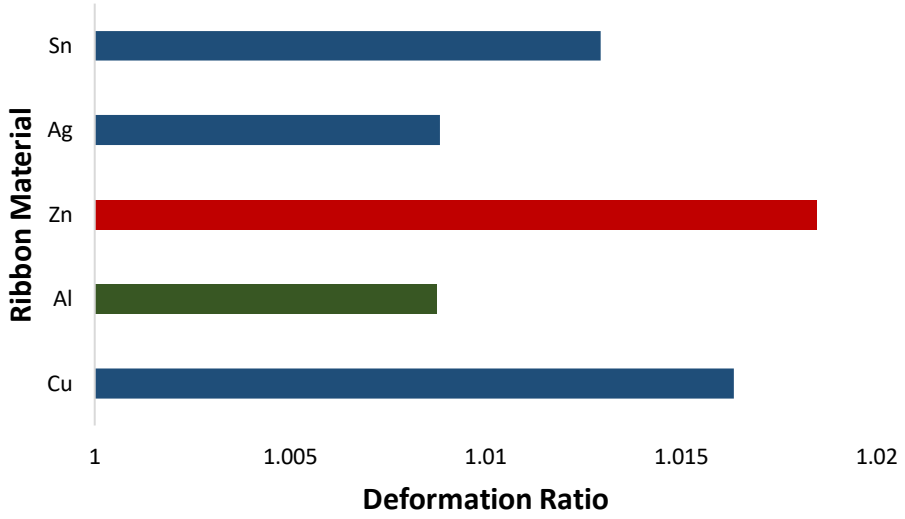


**Figure 5.13:** Deformation ratios for the Brass contact investigation

**Table 5.8:** Fatigue life for Brass contact experiment

| **Ribbon Material** | **Fatigue Life (E+03 Cycles)** | **Fatigue Life (years)** | $N_{f_i}$ | $F_i$ **(%)** |
|---|---|---|---|---|
| Aluminium | 13.033 | 4.22 | 0.80 | -20 |
| Copper | 1.074 | 0.35 | 0.07 | -93 |
| Silver | 11.692 | 3.78 | 0.72 | -28 |
| Tin | 2.909 | 0.94 | 0.18 | -82 |
| Zinc | 0.618 | 0.20 | 0.04 | -96 |

Table 5.8 presents the fatigue life for the brass contact experiment. The fatigue life values for the best design, Al-B Combination, are $N_{f_{BD}}$= 0.8 & $F_{BD}$= -20%. The unsuitability of the Brass contact material is buttressed by $N_{f_i} < 1$ and a negative $F_i$ value.

#### 5.4.1.4 Copper Contact

For this set of experiments the contact and solder component layers are kept constant at Copper and Sn3.5Ag0.5Cu alloy respectively while the material for the ribbon layer is varied. Table 5.9 presents the solder interconnection degradation for the Copper contact experiments. The best design for the Copper contact set of experiments is the Aluminium-Copper material combination ($N_{d_{BD}}$= 1.11 & $D_{BD}$= 11%). Solder degradation of this Al-Cu Combination is 1.11 times that of the CT and degradation is increased by 11%. This means that this Al-Cu Combination performed worse than the CT with $N_{d_i} > 1$ and possessed a positive $D_i$ value. It can be concluded that Copper as a contact material is not a suitable substitution to the CT. Figure 5.14 presents the deformation ratios for the Copper contact investigation.

**Table 5.9:** Solder interconnection degradation for Copper contact experiment

| **Ribbon Material** | **Accumulated Max. Creep Strain Energy Density (E-01 Pa)** | $N_{d_i}$ | $D_i$ **(%)** |
|---|---|---|---|
| Aluminium | 0.486 | 1.11 | 11 |
| Brass | 7.27 | 16.64 | 1564 |
| Silver | 0.545 | 1.25 | 25 |
| Tin | 2.15 | 4.92 | 392 |
| Zinc | 9.73 | 22.27 | 2127 |

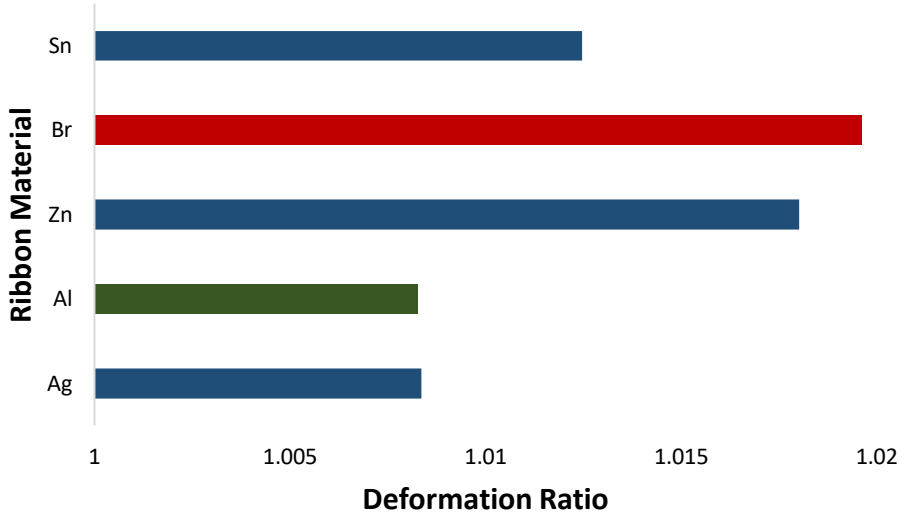


**Figure 5.14:** Deformation ratios for the Copper contact investigation

Table 5.10 presents the fatigue life for the Copper contact experiment. The fatigue life values for the best design, Al-Cu Combination, are $N_{f_{BD}}$ = 0.9 & $F_{BD}$= -10%. The unsuitability of the Copper contact material is buttressed by $N_{f_i} < 1$ and a negative $F_i$ value.

**Table 5.10:** Fatigue life for Copper contact experiment

| **Ribbon Material** | **Fatigue Life (E+03 Cycles)** | **Fatigue Life (years)** | $N_{f_i}$ | $F_i$ **(%)** |
|---|---|---|---|---|
| Aluminium | 14.687 | 4.75 | 0.90 | -10 |
| Brass | 0.982 | 0.32 | 0.06 | -94 |
| Silver | 13.111 | 4.24 | 0.80 | -20 |
| Tin | 3.320 | 1.07 | 0.20 | -80 |
| Zinc | 0.734 | 0.24 | 0.05 | -95 |

### 5.4.1.5 Tin Contact

For this set of experiments the contact and solder component layers are kept constant at Tin and Sn3.5Ag0.5Cu alloy respectively while the material for the ribbon layer is

varied. Table 5.11 presents the solder interconnection degradation for the Tin contact experiments. The degradation values for the best design, Aluminium-Tin, are $N_{d_{BD}}$= 0.81 & $D_{BD}$= -19%. This Al-Sn Combination has a solder degradation which is 0.81 times that of the CT and has decreased degradation by 19%. The worst design for the Tin contact set of experiments is the Zinc-Tin material combination ($N_{d_{WD}}$= 14.9 & $D_{WD}$= 1390%). This means that the solder degradation of this Zn-Sn Combination is 14.9 times that of the CT and has increased degradation by 1340%. The trend from the FEM solder degradation results is the same for the results derived from the analytical model. Figure 5.15 presents the deformation ratios for the Tin contact investigation.

**Table 5.11:** Solder interconnection degradation for Tin contact experiment

| **Ribbon Material** | **Accumulated Max. Creep Strain Energy Density (E-01 Pa)** | $N_{d_i}$ | $D_i$ **(%)** |
|---|---|---|---|
| Aluminium | 0.355 | 0.81 | -19 |
| Brass | 3.92 | 8.97 | 797 |
| Copper | 3.27 | 7.48 | 648 |
| Silver | 0.402 | 0.92 | -8 |
| Zinc | 6.51 | 14.90 | 1390 |

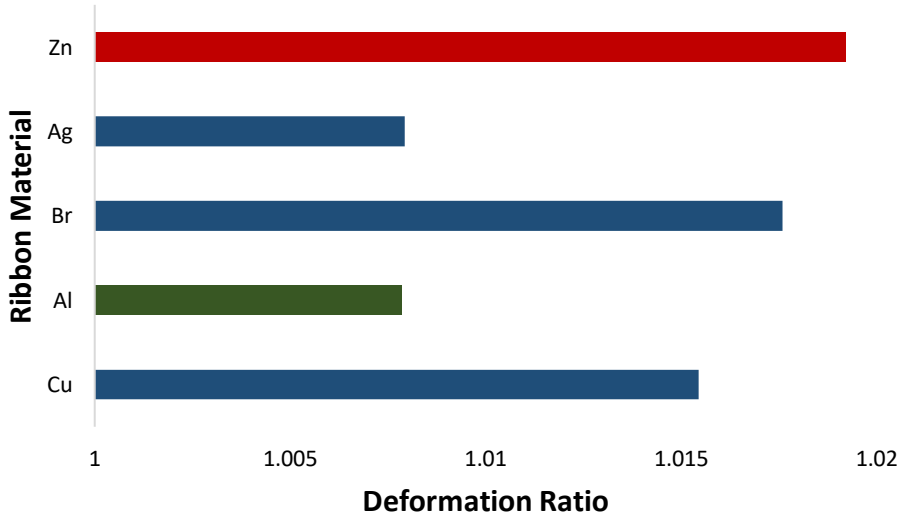


**Figure 5.15:** Deformation ratios for the Tin contact investigation

Table 5.12 presents the fatigue life for the Tin contact experiment. The fatigue life values for the best design, Al-Sn Combination, are $N_{f_{BD}}$= 1.23 & $F_{BD}$= 23%). This means that the fatigue life this Al-Sn Combination is 1.23 times that of the CT and has increased fatigue life by 23%. The fatigue life values for the worst design, Zn-Sn Combination, are $N_{f_{WD}}$= 0.07 & $F_{WD}$= -93%). This means that the fatigue life of this Zn-Sn Combination is 0.07 times that of the CT and has decreased fatigue life by 93%.

**Table 5.12:** Fatigue life for Tin contact experiment

| **Ribbon Material** | **Fatigue Life (E+04 Cycles)** | **Fatigue Life (years)** | $N_{f_i}$ | $F_i$ (%) |
|---|---|---|---|---|
| Aluminium | 2.0141 | 6.51 | 1.23 | 23 |
| Brass | 0.1822 | 0.59 | 0.11 | -89 |
| Copper | 0.2185 | 0.71 | 0.13 | -87 |
| Silver | 1.7863 | 5.78 | 1.09 | 11 |
| Zinc | 0.1097 | 0.35 | 0.07 | -93 |

#### 5.4.1.6 Zinc Contact.

For this set of experiments the contact and solder component layers are kept constant at Zinc and Sn3.5Ag0.5Cu alloy respectively while the material for the ribbon layer is varied. Table 5.13 presents the solder interconnection degradation for the Zinc contact experiments. The best design for the Zinc contact set of experiments is the Aluminium-Zinc material combination ($N_{d_{BD}}$= 1.16 & $D_{BD}$= 16%). This means that this Al-Zn Combination performed worse than the CT with $N_{d_i} > 1$ and a positive $D_i$ value. It can be concluded that Zinc as a contact material is not a suitable substitution to the CT.

**Table 5.13:** Solder interconnection degradation for Zinc contact experiment

| **Ribbon Material** | **Accumulated Max. Creep Strain Energy Density (E-01 Pa)** | $N_{d_i}$ | $D_i$ **(%)** |
|---|---|---|---|
| Aluminium | 0.509 | 1.16 | 16 |
| Brass | 9.49 | 21.72 | 2072 |
| Copper | 6.08 | 13.91 | 1291 |
| Silver | 0.567 | 1.30 | 30 |
| Tin | 2.24 | 5.13 | 413 |

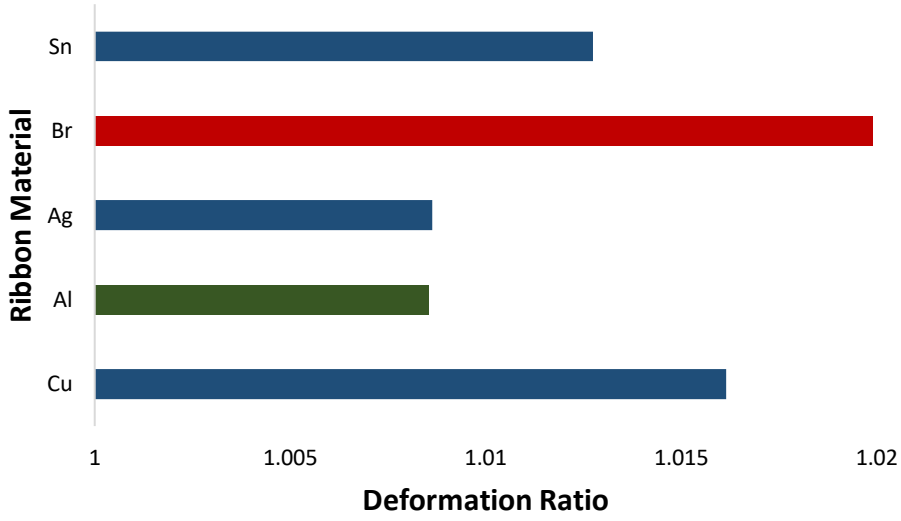


**Figure 5.16:** Deformation ratios for the Zinc contact investigation

**Table 5.14:** Fatigue life for Zinc contact experiment

| **Ribbon Material** | **Fatigue Life (E+03 Cycles)** | **Fatigue Life (years)** | $N_{f_i}$ | $F_i$ **(%)** |
|---|---|---|---|---|
| Aluminium | 14.020 | 4.53 | 0.86 | -14 |
| Brass | 0.752 | 0.24 | 0.05 | -95 |
| Copper | 1.175 | 0.38 | 0.07 | -93 |
| Silver | 12.588 | 4.07 | 0.77 | -23 |
| Tin | 3.187 | 1.03 | 0.20 | -80 |

Figure 5.16 presents the deformation ratios for the Zinc contact investigation. Table 5.14 presents the fatigue life for the Zinc contact experiment. The fatigue life values for the best design, Al-Zn Combination, are $N_{f_{BD}}$= 0.86 & $F_{BD}$= -14%. The unsuitability of the Zinc contact material is buttressed by $N_{f_i} < 1$ and a negative $F_i$ value.

### 5.4.2 Ribbon modelling

The electricity conducted from a single c-Si PV cell is minute and so several PV cells must be connected to form a string and then a module. This interconnection of PV cells sums up the electricity generated. Ribbon interconnects link one cell to another to form a module. Ribbon technology was discussed in chapter 2. This section presents the experiments which examine the thermo-mechanical behaviour of several ribbon-contact material combinations of the solder interconnection by varying the ribbon layer material. The performance of these Combs. is then be compared to that of the CT, hence, identify the combination with least degradation, longest fatigue life and improved reliability of c-Si PV module solder interconnection in elevated temperature climate. Copper ribbon is discussed in subsection 5.4.2.1 while Aluminium, Brass, Silver, Tin and Zinc ribbons are presented in 5.4.2.2, 5.4.2.3, 5.4.2.4, 5.4.2.5, and 5.4.2.6 respectively.

#### 5.4.2.1 Copper ribbon

For this set of experiments the ribbon interconnect and solder component layers are kept constant at Copper and Sn3.5Ag0.5Cu alloy respectively while the material for the contact layer is varied. Table 5.15 presents the solder interconnection degradation for the Copper ribbon experiments. The best design for the Copper ribbon set of

experiments is the Copper-Aluminium material combination ($N_{d_{BD}}$= 0.81 & $D_{BD}$= -19%). This means that the solder degradation of this Cu-Al Combination is 0.81 times that of the CT and has decreased degradation by 19%. The worst design for the Copper ribbon set of experiments is the Copper-Brass material combination ($N_{d_{WD}}$= 15.22 & $D_{WD}$= 1422%). This means that the solder degradation of this Cu-B Combination is 15.22 times that of the CT and has increased degradation by 1422%. The results derived from the deformation ratio analytical model confirms the trend of the FEM solder degradation results. Figure 5.17 presents the deformation ratios for the Copper ribbon investigation. Cu-Al combination has the highest $\delta_R$ value (red bar) while the Cu-Al combination has the lowest $\delta_R$ value (green bar).

**Table 5.15:** Solder interconnection degradation for Copper ribbon experiment

| **Contact Material** | **Accumulated Max. Creep Strain Energy Density (E-01 Pa)** | $N_{d_i}$ | $D_i$ **(%)** |
|---|---|---|---|
| Aluminium | 0.356 | 0.81 | -19 |
| Brass | 6.65 | 15.22 | 1422 |
| Silver | 0.437 | 1.00 | 0 |
| Tin | 3.27 | 7.48 | 648 |
| Zinc | 6.08 | 13.91 | 1291 |

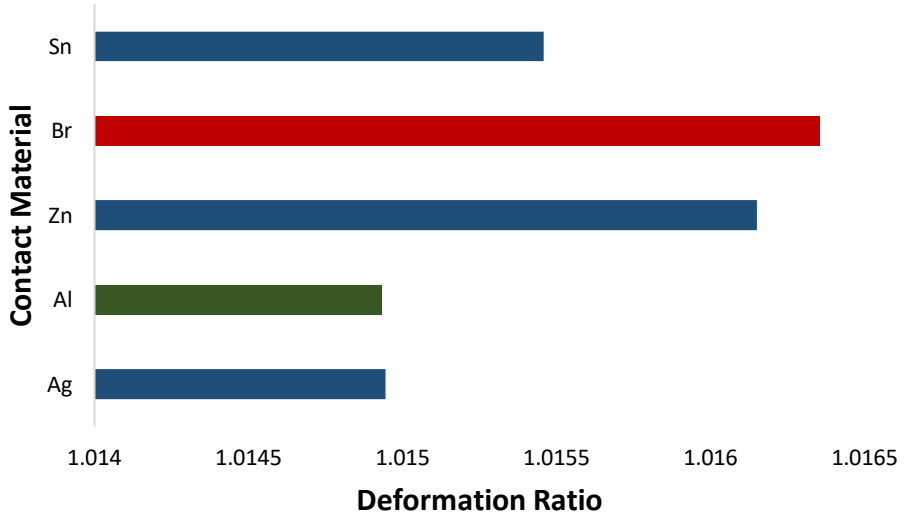


**Figure 5.17:** Deformation ratios for the Copper ribbon investigation

**Table 5.16:** Fatigue life for Copper ribbon experiment

| **Contact Material** | **Fatigue Life (E+04 Cycles)** | **Fatigue Life (years)** | $N_{f_i}$ | $F_i$ **(%)** |
|---|---|---|---|---|
| Aluminium | 2.0078 | 6.49 | 1.23 | 23 |
| Brass | 0.1074 | 0.35 | 0.07 | -93 |
| Silver | 1.6333 | 5.28 | 1.00 | 0 |
| Tin | 0.2185 | 0.71 | 0.13 | -87 |
| Zinc | 0.1175 | 0.38 | 0.07 | -93 |

Table 5.16 presents the fatigue life for the Copper ribbon experiment. The fatigue life values for the best design, Cu-Al Combination, are $N_{f_{BD}}$= 1.23 & $F_{BD}$= 23%). This means that the fatigue life this Cu-Al Combination is 1.23 times that of the CT and has increased fatigue life by 23%. The fatigue life values for the worst design, Cu-B Combination, are $N_{f_{WD}}$= 0.07 & $F_{WD}$= -93%). This means that the fatigue life of this Cu-B Combination is 0.07 times that of the CT and has decreased fatigue life by 93%.

#### 5.4.2.2 Aluminium ribbon

For this set of experiments the ribbon interconnect and solder component layers are kept constant at Aluminium and Sn3.5Ag0.5Cu alloy respectively while the material for the contact layer is varied. Table 5.17 presents the solder interconnection degradation for the Aluminium ribbon experiments. The degradation values for the best design, Aluminium-Silver, are $N_{d_{BD}}$= 0.02 & $D_{BD}$= -98%. This Al-Ag Combination has a solder degradation which is 0.02 times that of the CT and has decreased degradation by 98%. The worst design for the Aluminium contact set of experiments is the Aluminium-Brass material combination ($N_{d_{WD}}$= 1.25 & $D_{WD}$=

25%). This means that the solder degradation of this Al-B Combination is 1.25 times that of the CT and has increased degradation by 25%. Figure 5.18 presents the deformation ratios for the Aluminium ribbon investigation.

Table 5.18 presents the fatigue life for the Aluminium ribbon experiment. The fatigue life values for the best design, Al-Ag Combination, are $N_{f_{BD}}$= 56.99 & $F_{BD}$= 5599%). This means that the fatigue life this Al-Ag Combination is 56.99 times that of the CT and has increased fatigue life by 5599%. The fatigue life values for the worst design, Al-B Combination, are $N_{f_{WD}}$= 0.8 & $F_{WD}$= -20%). This means that the fatigue life of this Al-B Combination is 0.8 times that of the CT and has decreased fatigue life by 20%.

**Table 5.17:** Solder interconnection degradation for Aluminium ribbon experiment

| **Contact Material** | **Accumulated Max. Creep Strain Energy Density (E-05 Pa)** | $N_{d_i}$ | $D_i$ **(%)** |
|---|---|---|---|
| Brass | 5480 | 1.25 | 25 |
| Copper | 4860 | 1.11 | 11 |
| Silver | 76.8 | 0.02 | -98 |
| Tin | 3550 | 0.81 | -19 |
| Zinc | 5090 | 1.16 | 16 |

**Table 5.18:** Fatigue life for Aluminium ribbon experiment

| **Contact Material** | **Fatigue Life (E+03 Cycles)** | **Fatigue Life (years)** | $N_{f_i}$ | $F_i$ **(%)** |
|---|---|---|---|---|
| Brass | 13.033 | 4.22 | 0.80 | -20 |
| Copper | 14.687 | 4.75 | 0.90 | -10 |
| Silver | 930.358 | 300.91 | 56.99 | 5599 |
| Tin | 20.141 | 6.51 | 1.23 | 23 |
| Zinc | 14.020 | 4.53 | 0.86 | -14 |

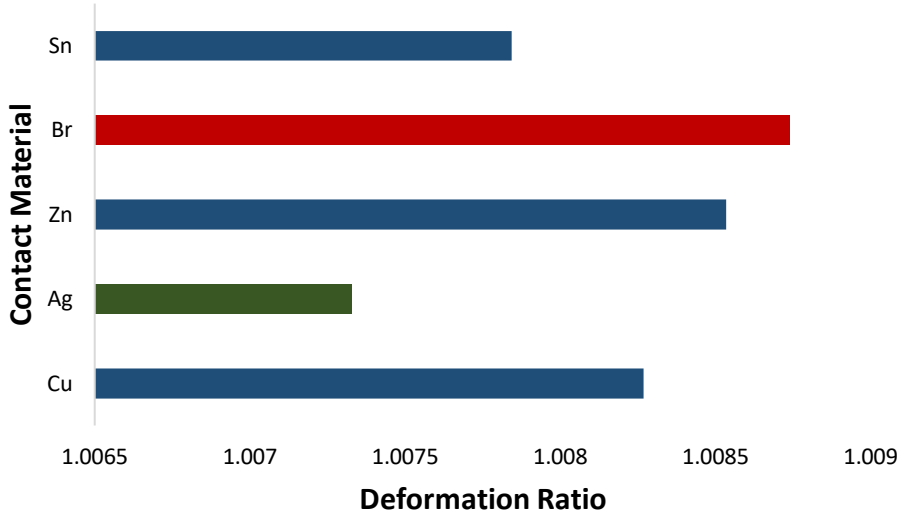


**Figure 5.18:** Deformation ratios for the Aluminium ribbon investigation

### 5.4.2.3 Brass ribbon

For this set of experiments the ribbon interconnect and solder component layers are kept constant at Brass and Sn3.5Ag0.5Cu alloy respectively while the material for the contact layer is varied. Table 5.19 presents the solder interconnection degradation for the Brass ribbon experiments. The best design for the Brass ribbon set of experiments is the Brass-Aluminium material combination ($N_{d_{BD}}$= 2.95 & $D_{BD}$= 195%). This means that this B-Al Combination performed worse than the CT with $N_{d_i} > 1$ and a positive $D_i$ value. It can be concluded that Brass as a ribbon material is not a suitable substitution to the CT.

**Table 5.19:** Solder interconnection degradation for Brass ribbon experiment

| **Contact Material** | **Accumulated Max. Creep Strain Energy Density (E-01 Pa)** | $N_{d_i}$ | $D_i$ (%) |
|---|---|---|---|
| Aluminium | 1.29 | 2.95 | 195 |
| Copper | 7.27 | 16.64 | 1564 |
| Silver | 1.33 | 3.04 | 204 |
| Tin | 3.92 | 8.97 | 797 |
| Zinc | 9.49 | 21.72 | 2072 |

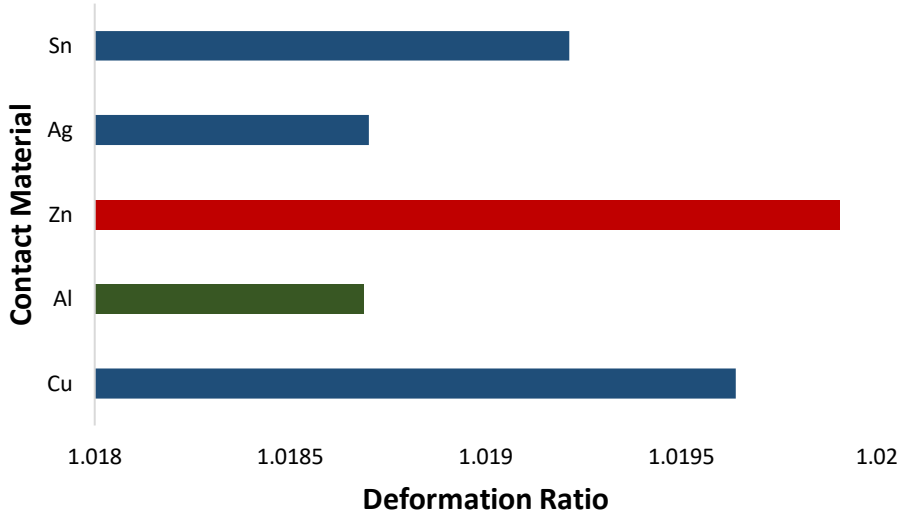


**Figure 5.19:** Deformation ratios for the Brass ribbon investigation

The deformation ratios for the Brass ribbon investigation is presented in Fig. 5.19. Table 5.20 presents the fatigue life for the Brass ribbon experiment. The fatigue life values for the best design, B-Al Combination, are $N_{f_{BD}}$= 0.34 & $F_{BD}$= -66%). The unsuitability of the Brass ribbon material is buttressed by $N_{f_i} < 1$ and a negative $F_i$ value.

**Table 5.20:** Fatigue life for Brass ribbon experiment

| **Contact Material** | **Fatigue Life (E+03 Cycles)** | **Fatigue Life (years)** | $N_{f_i}$ | $F_i$ **(%)** |
|---|---|---|---|---|
| Aluminium | 5.531 | 1.79 | 0.34 | -66 |
| Copper | 0.982 | 0.32 | 0.06 | -94 |
| Silver | 5.386 | 1.74 | 0.33 | -67 |
| Tin | 1.822 | 0.59 | 0.11 | -89 |
| Zinc | 0.752 | 0.24 | 0.05 | -95 |

#### 5.4.2.4 Silver ribbon

For this set of experiments the ribbon interconnect and solder component layers are kept constant at Silver and Sn3.5Ag0.5Cu alloy respectively the material for the contact layer is varied. Table 5.21 presents the solder interconnection degradation for the Silver ribbon experiments. The best design for the Silver ribbon set of experiments is the Silver-Aluminium material combination ($N_{d_{BD}}$= 0.01 & $D_{BD}$= -99%). This means that the solder degradation of this Ag-Al Combination is 0.01 times that of the CT and decreased degradation by 99%. The worst design for the Silver ribbon set of experiments is the Silver-Brass material combination ($N_{d_{WD}}$= 1.4 & $D_{WD}$= 40%). This means that the solder degradation of this Ag-B Combination is 1.4 times that of the CT and has increased degradation by 40%. The worst and best designs from the FEM results correspond to the same combinations with the highest and lowest $\delta_R$ values from the analytical model. The deformation ratios for the Silver ribbon investigations is presented in Fig. 5.20.

Table 5.22 presents the fatigue life for the Silver ribbon experiment. The fatigue life values for the best design, Ag-Al Combination, are $N_{f_{BD}}$= 72.01 & $F_{BD}$= 7101%). This means that the fatigue life this Ag-Al Combination is 72.01 times that of the CT and has increased fatigue life by 7101%. The fatigue life values for the worst design, Ag-B Combination, are $N_{f_{WD}}$= 0.72 & $F_{WD}$= -28%). This means that the fatigue life of this Ag-B Combination is 0.72 times that of the CT and has decreased fatigue life by 28%.

**Table 5.21:** Solder interconnection degradation for silver ribbon experiment

| Contact Material | Accumulated Max. Creep Strain Energy Density (E-04 Pa) | $N_{d_i}$ | $D_i$ (%) |
|---|---|---|---|
| Aluminium | 6.08 | 0.01 | -99 |
| Brass | 611 | 1.40 | 40 |
| Copper | 545 | 1.25 | 25 |
| Tin | 400 | 0.92 | -8 |
| Zinc | 567 | 1.30 | 30 |

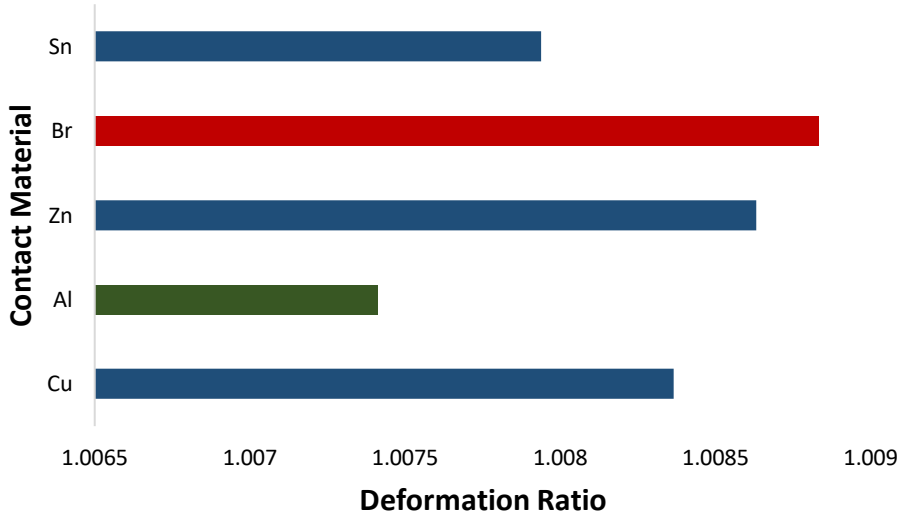


**Figure 5.20:** Deformation ratios for the Silver ribbon investigation

**Table 5.22:** Fatigue life for silver ribbon experiment

| Contact Material | Fatigue Life (E+04 Cycles) | Fatigue Life (years) | $N_{f_i}$ | $F_i$ (%) |
|---|---|---|---|---|
| Aluminium | 117.5566 | 380.22 | 72.01 | 7101 |
| Brass | 1.1692 | 3.78 | 0.72 | -28 |
| Copper | 1.3111 | 4.24 | 0.80 | -20 |
| Tin | 1.7863 | 5.78 | 1.09 | 9 |
| Zinc | 1.2588 | 4.07 | 0.77 | -23 |

### 5.4.2.5 Tin ribbon

For this set of experiments the ribbon interconnect and solder component layers are kept constant at Tin and Sn3.5Ag0.5Cu alloy respectively while the material for the contact layer is varied. Table 5.23 presents the solder interconnection degradation for the Tin ribbon experiments. The degradation values for the best design, Tin-Aluminium, are $N_{d_{BD}}$= 0.83 & $D_{BD}$= -17%. This Sn-Al Combination has a solder degradation which is 0.83 times that of the CT and has decreased degradation by 17%. The worst design for the Tin ribbon set of experiments is the Tin-Brass material combination ($N_{d_{WD}}$= 5.63 & $D_{WD}$= 463%). This means that the solder degradation of this Sn-B Combination is 5.63 times that of the CT and has increased degradation by 463%.

**Table 5.23:** Solder interconnection degradation for Tin ribbon experiment

| **Contact Material** | **Accumulated Max. Creep Strain Energy Density (E-01 Pa)** | $N_{d_i}$ | $D_i$ **(%)** |
|---|---|---|---|
| Aluminium | 0.363 | 0.83 | -17 |
| Brass | 2.46 | 5.63 | 463 |
| Copper | 2.15 | 4.92 | 392 |
| Silver | 0.395 | 0.90 | -10 |
| Zinc | 2.24 | 5.13 | 413 |

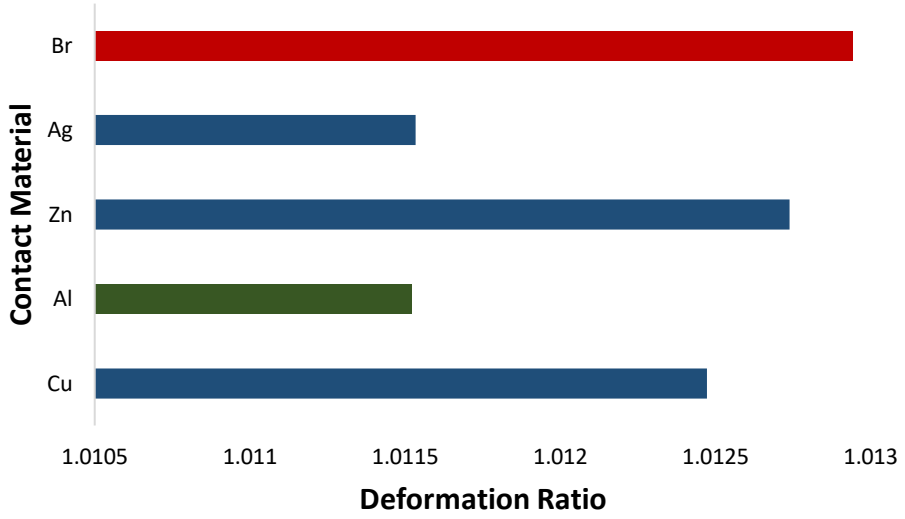


**Figure 5.21:** Deformation ratios for the Tin ribbon investigation

**Table 5.24:** Fatigue life for Tin ribbon experiment

| **Contact Material** | **Fatigue Life (E+04 Cycles)** | **Fatigue Life (years)** | $N_{f_i}$ | $F_i$ **(%)** |
|---|---|---|---|---|
| Aluminium | 1.9693 | 6.37 | 1.21 | 21 |
| Brass | 0.2909 | 0.94 | 0.18 | -82 |
| Copper | 0.3320 | 1.07 | 0.20 | -80 |
| Silver | 1.8070 | 5.84 | 1.11 | 11 |
| Zinc | 0.3187 | 1.03 | 0.20 | -80 |

Figure 5.21 presents the deformation ratios for the Tin ribbon investigation. The FEM solder degradation results are supported by the deformation ratio results derived from the analytical model. The best design from the FEM results corresponds to the same Sn-Al comb with the lowest $\delta_R$ value and the worst design is the Sn-B comb with the highest $\delta_R$ value. Table 5.24 presents the fatigue life for the Tin ribbon experiment. The fatigue life values for the best design, Sn-Al Combination, are $N_{f_{BD}}$= 1.21 & $F_{BD}$= 21%). This means that the fatigue life this Sn-Al Combination is 1.21 times that of the CT and has increased fatigue life by 21%. The fatigue life values for the worst design, Sn-B Combination, are $N_{f_{WD}}$= 0.18 & $F_{WD}$=

-82%). This means that the fatigue life of this Sn-B Combination is 0.18 times that of the CT and has decreased fatigue life by 82%.

#### 5.4.2.6 Zinc ribbon

For this set of experiments the ribbon interconnect and solder component layers are kept constant at Zinc and Sn3.5Ag0.5Cu alloy respectively while the material for the contact layer is varied. Table 5.25 presents the solder interconnection degradation for the Zinc ribbon experiment. The best design for the Zinc ribbon set of experiments is the Zinc-Silver material combination ($N_{d_{BD}}$= 0.92 & $D_{BD}$= -8%). This means that the solder degradation of this Zn-Ag Combination is 0.92 times that of the CT and has decreased degradation by 8%. The worst design for the Zinc ribbon set of experiments is the Zinc-Brass material combination ($N_{d_{WD}}$= 26.54 & $D_{WD}$= 2554%). This means that the solder degradation of this Zn-B Combination is 26.54 times that of the CT and has increased degradation by 2554%. Figure 5.22 presents the deformation ratios for the Zinc ribbon experiments. Results derived from the analytical model support the FEM solder degradation results. Zn-B which was identified as the worst design possessed the highest $\delta_R$ value while Zn-Ag with the lowest $\delta_R$ value is the best design.

**Table 5.25:** Solder interconnection degradation for Zinc ribbon experiment

| **Contact Material** | **Accumulated Max. Creep Strain Energy Density (E-01 Pa)** | $N_{d_i}$ | $D_i$ **(%)** |
|---|---|---|---|
| Aluminium | 1.03 | 2.36 | 136 |
| Brass | 11.6 | 26.54 | 2554 |
| Copper | 9.73 | 22.27 | 2127 |
| Silver | 0.404 | 0.92 | -8 |
| Tin | 6.51 | 14.90 | 1390 |

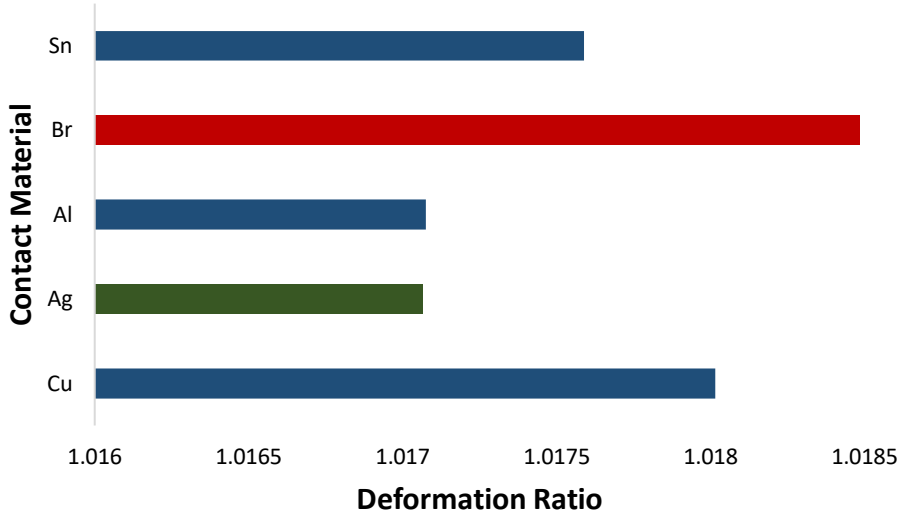


**Figure 5.22:** Deformation ratios for the Zinc ribbon investigation

Table 5.26 presents the fatigue life for the Zinc ribbon experiment. The fatigue life values for the best design, Zn-Ag Combination, are $N_{f_{BD}}$= 1.08 & $F_{BD}$= 8%). This means that the fatigue life this Zn-Ag Combination is 1.08 times that of the CT and has increased fatigue life by 8%. The fatigue life values for the worst design, Zn-B Combination, are $N_{f_{WD}}$= 0.04 & $F_{WD}$= -96%). This means that the fatigue life of this Zn-B Combination is 0.04 times that of the CT and has decreased fatigue life by 96%.

**Table 5.26:** Fatigue life for Zinc ribbon experiment

| **Contact Material** | **Fatigue Life (E+03 Cycles)** | **Fatigue Life (years)** | $N_{f_i}$ | $F_i$ **(%)** |
|---|---|---|---|---|
| Aluminium | 6.953 | 2.25 | 0.43 | -57 |
| Brass | 0.618 | 0.20 | 0.04 | -96 |
| Copper | 0.734 | 0.24 | 0.05 | -95 |
| Silver | 17.660 | 5.71 | 1.08 | 8 |
| Tin | 1.097 | 0.35 | 0.07 | -93 |

### 5.4.3 Zero CTE mismatch combinations

Several researches have reported the role CTE mismatch plays in the degradation of c-Si PV modules and the solder interconnections especially. Chapters 2 and 3 have discussed CTE mismatch contributions to c-Si PV module failure modes especially under elevated temperature conditions. During operation, the component layers of c-Si PV solder interconnections expand and contract at different rates. After numerous cycles of operation, the solder joint experiences fatigue and eventual failure. This thermo-mechanical degradation is aggravated under elevated temperature climates. It is of import to examine the effect of zero CTE mismatch on the performance of c-Si PV solder interconnection under elevated temperature climate conditions.

This section of this study investigates the thermo-mechanical behaviour of several ribbon-contact material combinations of the solder interconnection with zero CTE mismatch by keeping the materials of both the contact and ribbon component layers the same. The solder layer is kept constant at Sn3.5Ag0.5Cu alloy. The performance of these combinations will then be compared to that of the CT, hence, identify the combination with least degradation, longest fatigue life and improved reliability of c-Si PV module solder interconnection in elevated temperature climate. Section 5.4.3.1 will discuss the solder interconnection degradation of various ribbon-contact material combinations from the zero CTE experiments. Section 5.4.3.2 will discuss the fatigue life of various ribbon-contact material combinations from the zero CTE experiments. The ribbon-contact material combinations investigated in this set of experiments are Aluminium-Aluminium (Al-Al), Brass-Brass (B-B), Copper-Copper (Cu-Cu), Silver-Silver (Ag-Ag), Tin-Tin (Sn-Sn) and Zinc-Zinc (Zn-Zn).

#### 5.4.3.1 Zero CTE solder interconnection degradation

Table 5.27 presents the solder interconnection degradation for the zero CTE experiment. The best designs for this zero CTE set of experiments are the Aluminium-Aluminium ($N_{d_{BD1}}$= 0.01 & $D_{BD1}$= -99%) and Silver-Silver ($N_{d_{BD2}}$= 0.01 & $D_{BD2}$= -99%). This means that their solder interconnection degradation is 0.01 times that of the CT and decrease degradation by 99%. It can be observed from the table that these Al-Al and Ag-Ag Combs. are the only material combinations with $N_{d_i} < 1$ and negative $D_i$ values and are therefore suitable replacements to the CT in elevated temperature climate conditions. The other zero CTE material combinations (B-B, Cu-Cu, Sn-Sn and Zn-Zn) performed worse than the CT with $N_{d_i} > 1$ and possessed positive $D_i$ values. It can be concluded these Combs. are not suitable substitutions to the CT. Figure 5.23 presents the deformation ratios for the zero CTE investigations. Applying the analytical model, the Ag-Ag combination possessed the lowest $\delta_R$ value while the B-B comb had the highest $\delta_R$ value.

**Table 5.27:** Solder interconnection degradation for zero CTE experiment

| **Material Combination** | **Accumulated Max. Creep Strain Energy Density (E-03 Pa)** | $N_{d_i}$ | $D_i$ **(%)** |
|---|---|---|---|
| Al-Al | 0.604 | 0.01 | -99 |
| B-B | 1000 | 22.88 | 2188 |
| Cu-Cu | 542 | 12.40 | 1140 |
| Ag-Ag | 0.577 | 0.01 | -99 |
| Sn-Sn | 159 | 3.64 | 264 |
| Zn-Zn | 1110 | 25.40 | 2440 |

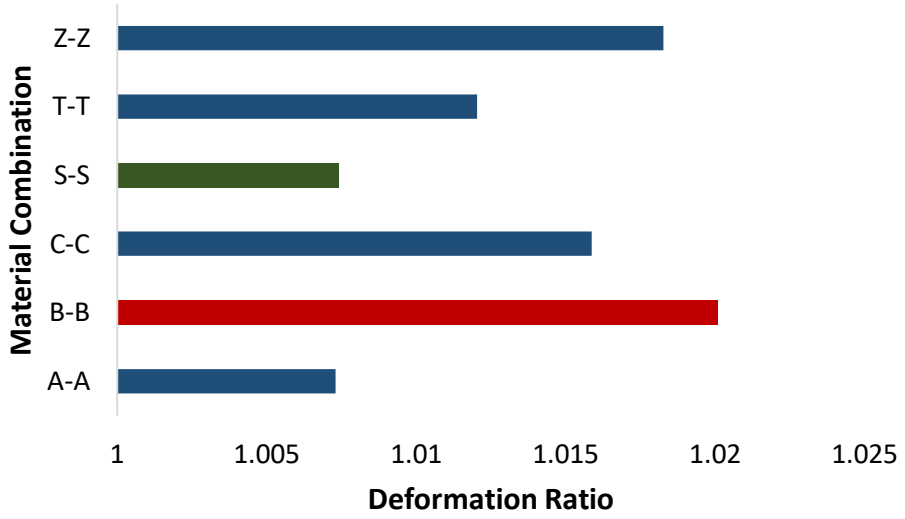


**Figure 5.23:** Deformation ratios for zero CTE investigation.

### 5.4.3.2 Zero CTE fatigue life

Table 5.28 presents the fatigue life for the zero CTE experiment. The fatigue life values for the best designs, Al-Al and Ag-Ag Combs., are $N_{f_{BD_1}}$= 72.4 & $F_{BD1}$= 7140%, and $N_{f_{BD_2}}$= 75.86 & $F_{BD2}$= 7486%, respectively. It can be observed from the table that these Al-Al and Ag-Ag Combs. are the only material combinations $N_{f_i} > 1$ and a positive $F_i$ values. The unsuitability of the other zero CTE material combinations (B-B, Cu-Cu, Sn-Sn and Zn-Zn) as substitutes to the CT are observed in Table 5.28 with $N_{f_i} < 1$ and negative $F_i$ values.

**Table 5.28:** Fatigue life for zero CTE experiment

| **Material Combination** | **Fatigue Life (E+03 cycles)** | **Fatigue Life (years)** | $N_{f_i}$ | $F_i$ **(%)** |
|---|---|---|---|---|
| Al-Al | 1181.914 | 382.28 | 72.40 | 7140 |
| B-B | 0.714 | 0.23 | 0.04 | -96 |
| Cu-Cu | 1.319 | 0.43 | 0.08 | -92 |
| Ag-Ag | 1238.4095 | 400.55 | 75.86 | 7486 |
| Sn-Sn | 4.504 | 1.46 | 0.28 | -72 |
| Zn-Zn | 0.643 | 0.21 | 0.04 | -96 |

## 5.5 CONCLUSIONS

This chapter presented an investigation on the effects of material combination on the degradation of c-Si PV solder interconnections for improved reliability in elevated temperature climate using ANSYS FEM environment. Six (6) materials were utilised to form thirty-six (36) different ribbon-contact model combinations of the c-Si PV solder interconnection. The performance of each of the thirty-six ribbon-contact material combinations was compared to that of the conventional c-Si PV solder interconnection to test their suitability to replace the latter in elevated temperature operating conditions.

The thirty-six (36) c-Si PV modules were modelled in the ANSYS FEM environment using several thermo-mechanical models including linear elastic, viscoelastic, creep and temperature dependent material models. The Garofalo creep model was used to determine the maximum creep strain energy which is a measure of PV solder interconnection degradation. Five (5) modes were derived and applied to compare the performance of the conventional c-Si PV solder interconnection with the thirty-six (36) proposed ribbon-contact material combinations. These modes are based on analytical models derived from fundamental mechanics principles and theories. For all sets of investigations, the deformation results derived from the analytical model demonstrated the same trends as the solder degradation results obtained from the FEM environment.

All combinations formed from Brass contacts (Al-B, Cu-B, Ag-B, Sn-B, Zn-B) and Brass ribbons (B-Al, B-Cu, B-Ag, B-Sn, B-Zn) materials were found to be unsuitable replacements to the conventional c-Si PV solder interconnection in elevated temperature climate conditions. This is because they performed worse than the conventional solder interconnection by increasing solder degradation with $N_{d_i} > 1$,

and positive $D_i$ values, as well as decreasing fatigue life with $N_{f_i} < 1$ and negative $F_i$ values. Other groups of material combinations found to be unsuitable substitutions to the conventional c-Si PV solder interconnection in elevated temperature climate conditions are those formed from Copper contacts (Al-Cu, B-Cu, Ag-Cu, Sn-Cu, Zn-Cu) and Zinc contacts (Al-Zn, B-Zn, Cu-Zn, Ag-Zn, Sn-Zn). The Brass, Zinc and Copper materials contributed majorly to the stiffness of the composite laminate beam model resulting in increased stress and degradation of the solder interconnection.

Results from the zero CTE mismatch experiments show that only the Al-Al and Ag-Ag ribbon-contact material combinations are suitable replacements for the conventional c-Si PV solder interconnection in elevated temperature climate conditions. They decreased degradation by 99% with solder deformation 0.01 times that of the CT. Also, these Al-Al and Ag-Ag combinations increased fatigue life with $N_{f_i} > 1$ and positive $F_i$ values. The other zero CTE mismatch ribbon-contact material combinations (B-B, Cu-Cu, Sn-Sn, Zn-Zn) were found to be unsuitable substitutions.

The chosen ribbon-contact material combinations ranked in order of performance are Silver-Silver, Aluminium-Aluminium, Silver-Aluminium, and Aluminium-Silver. They have been chosen because each combination possesses the four (4) most desirable performance indicators. Applying the modes of performance comparison, their individual performance values fall within a narrow margin of $N_{d_i}$= 0.01-0.02 & $D_i$= -99% to -98% hence any of the four could replace the conventional c-Si PV solder interconnection in elevated temperature climate conditions.

In the next chapter of this thesis, chapter six, each of these four (4) chosen ribbon-contact material combinations will be tested against another reliability

influencing factor which is the effect of thickness of bonded materials in c-Si PV solder interconnection on its degradation in elevated temperature climates. This would be another step in determining the optimal design of the c-Si PV solder interconnection for improved performance in elevated temperature climates.

# CHAPTER 6

# EFFECT OF THICKNESS OF BONDED MATERIALS IN THE SOLDER JOINT ON PHOTOVOLTAIC (PV) INTERCONNECTION DEGRADATION

## 6.1 INTRODUCTION

This chapter presents an investigation on the effects of thickness of bonded materials in the solder joint on the degradation of c-Si PV solder interconnections for improved reliability in elevated temperature climate using ANSYS FEM. The effect of thickness of bonded materials in the solder joint is one of the defined reliability influencing factors (RIFs) of the PV solder interconnection. Refer to chapter 1 for more details. In chapter 5 of this thesis, the effect of material combination on the performance of the c-Si PV solder interconnection in elevated temperature climate conditions was investigated. During the material combination experiments performed, the dimensions of the solder interconnection were fixed at those used in commercial PV modules. These dimensions, presented in Table 3.2, are referred to from here on out as the standard dimensions (SD). However, in this chapter, the focus will be placed on redesigning the solder interconnection of the c-Si PV module which comprises of the Sn3.5Ag0.5Cu solder alloy sandwiched in between the ribbon and contact component layers. By varying the thicknesses of the ribbon, solder and contact component layers, new models of the c-Si PV solder interconnection will be designed and tested for their suitability to replace the conventional solder interconnection of standard dimensions in the elevated temperature operating condition.

Section 6.2 will present the details of the finite element modelling procedure, material properties and models. To afford greater readability, the thickness variation investigations will be divided into solder layer thickness modelling, which is presented in section 6.3, contact layer thickness modelling in 6.4 and ribbon layer thickness modelling in 6.5.

## 6.2 FINITE ELEMENT MODELLING

ANSYS FEM is employed in the investigation of the effect of thickness of bonded materials in the solder joint on the c-Si PV interconnection degradation in elevated temperature climate. In chapter 5, four (4) ribbon-contact material combinations were chosen as the most suitable replacements for the conventional c-Si PV solder interconnection in elevated temperature climate conditions. The four chosen material combinations are Silver-Silver, Aluminium-Aluminium, Silver-Aluminium and Aluminium-Silver. These Combs. will be used to design eighty-four (84) c-Si PV solder interconnection models in which either the ribbon, solder or contact component layers have had their thicknesses varied from the standard. Single variate experiments will be carried out in the ANSYS FEM environment.

1mm by 1mm c-Si PV cell assemblies of the 84 models are designed using the Solid Works 3D modelling software package. The completed 3D models constitute the Geometry input to the ANSYS FEM environment but are first converted to the acceptable Parasolid (*.x_t) format. The standard dimensions of the component layers can be seen in Table 3.2. Further details of the model design procedure can be found in chapter 3 of this thesis. The designed models are inputted in ANSYS Academic Research Mechanical software package to simulate the c-Si PV model response to the applied loads and boundary conditions. The material properties of

the chosen materials, which include thermal conductivity, electrical conductivity and coefficient of thermal expansion (CTE), constitute part of the Engineering Data input to the ANSYS Academic Research Mechanical software package. For more details on these materials and their respective properties, refer to Table 3.1.

Thermo-mechanical material models used for the investigation include linear elastic, viscoelastic, creep and temperature dependent material models. The Garofalo creep model, is used to determine the maximum creep strain energy which is a measure of PV solder interconnection degradation. The material properties of solder and EVA layers demonstrate temperature dependence and viscoelasticity. Hence, they are modelled using the appropriate material models. Refer to Eqn. 3.1 and Fig. 3.5 for the temperature dependent and viscoelastic models of solder and EVA respectively. More details on constitutive material models can be found in chapter 3 of this thesis.

The conventional solder interconnection under elevated temperature climate conditions was assigned the role of central tendency (CT) in chapter 5 and this denotation will be employed in this present chapter. Utilising single variate experiments, the performance of each of the 84 c-Si PV solder interconnection thickness models will be compared to that of the CT in the elevated temperature operation. Modes 1-4 derived and discussed in chapter 5 of this thesis will be employed for this performance comparison. Mode 1, presented in Eqns. 5.1 & 5.2, and Mode 3, presented in Eqns. 5.5 & 5.6 will be applied to derive the values for normalised degradation, $N_{d_i}$ and normalised degradation deviation, $D_i$ respectively. Mode 2, presented in Eqns. 5.3 & 5.4, and Mode 4, presented in Eqns. 5.7 & 5.8 will be applied to derive the values for normalised fatigue life, $N_{f_i}$ and normalised fatigue life deviation, $F_i$ respectively. Refer to section 5.3.2 for more details on the

modes of performance comparison of conventional PV solder interconnection and proposed thickness models in elevated temperature climate.

## 6.3 SOLDER LAYER THICKNESS MODELLING

This section presents the investigations which examine the thermo-mechanical behaviour of twenty-eight (28) c-Si PV solder interconnection models when the thickness of the solder component layer is varied. The thickness values of the solder layer used for this set of experiments are 31μm, 36μm, 41μm, 46μm, 51μm, 56μm and 61μm. The standard dimension (SD) value is the 46μm and all other thickness models will be compared to the SD model. Table 6.1 presents the c-Si PV module component layer dimensions for the solder thickness investigations.

The performance of each c-Si PV solder thickness model will be compared to that of the CT by employing the performance comparison modes 1-4 derived and discussed in chapter 5. Additionally, any trends between solder thickness and the degradation of c-Si PV solder interconnection under hot climate operations will be identified.

Results for the solder thickness experiments of Silver-Silver, Aluminium-Aluminium, Silver-Aluminium and Aluminium-Silver ribbon-contact material combinations will be discussed in sub-sections 6.3.1, 6.3.2, 6.3.3 and 6.3.4 respectively.

**Table 6.1:** c-Si PV module component dimensions for solder thickness experiments

| **Component Layer** | **Thickness (μm)** |
|---|---|
| Glass | 3000 |
| Top EVA Encapsulant | 179, 174, 169, 164, 159, 154, 149 |
| Ribbon | 200 |
| Solder | 31, 36, 41, 46, 51, 56, 61 |
| Contact | 50 |
| Silicon Wafer | 200 |
| Aluminium Back Contact | 25 |
| Bottom EVA Encapsulant | 229, 224, 219, 214, 209, 204, 199 |
| Tedlar Back Sheet | 190 |

### 6.3.1 Solder thickness modelling for Silver-Silver Combination

For this set of investigations, the ribbon and contact layers are both Silver material while the solder layer is the Sn3.5Ag0.5Cu alloy. The ribbon and contact layer thicknesses are kept constant at the SDs while the solder layer thickness is varied. See Table 6.1 for more details. Table 6.2 presents the solder interconnection degradation for the solder thickness experiments of the Silver-Silver Combination The results show that all the solder thickness models are improvements of the CT with $N_{d_i} < 1$ and negative $D_i$ values. It can also be observed that an increase in the solder thickness value from 46μm (the standard dimension, SD) to 51μm, 56μm and 61μm demonstrates further improvement in performance but decreasing the solder thickness value from 46μm results in the opposite effect. Thickness value of 51μm is the best performing design of the Silver-Silver combination set with $N_{d_{BD}}$= 0.0054 & $D_{BD}$= -99.46%. This means that the solder degradation of the Ag-Ag Combination at solder thickness of 51μm is 0.0054 times that of the CT and has decreased degradation by 99.46%. It can be established that further increase in solder thickness beyond 51μm shows no improvement.

**Table 6.2:** Solder interconnection degradation for solder thickness experiments of the Silver-Silver Combination

| **Solder Thickness (µm)** | **Accumulated Max. Creep Strain Energy Density (E-03 Pa)** | $N_{d_i}$ | $D_i$(%) |
|---|---|---|---|
| 31 | 1.81 | 0.0413 | -95.87 |
| 36 | 1.25 | 0.0287 | -97.13 |
| 41 | 0.883 | 0.0202 | -97.98 |
| 46 | 0.577 | 0.0132 | -98.68 |
| 51 | 0.238 | 0.0054 | -99.46 |
| 56 | 0.432 | 0.0099 | -99.01 |
| 61 | 0.547 | 0.0125 | -98.75 |

Table 6.3 presents the fatigue life for solder thickness experiments of Silver-Silver Combination The best solder thickness design of the Ag-Ag Combination is 51µm with $N_{f_{BD}}$= 183.98 & $F_{BD}$= 18298%. This means that the fatigue life is 183.98 times that of the CT and has increased fatigue life by 18298%.

**Table 6.3:** Fatigue life for solder thickness experiments of Silver-Silver Combination

| **Solder Thickness (µm)** | **Fatigue Life (years)** | $N_{f_i}$ | $F_i$ (%) |
|---|---|---|---|
| 31 | 127.94 | 24.23 | 2323 |
| 36 | 184.50 | 34.94 | 3394 |
| 41 | 261.72 | 49.57 | 4857 |
| 46 | 400.55 | 75.86 | 7486 |
| 51 | 971.42 | 183.98 | 18298 |
| 56 | 534.39 | 101.21 | 10021 |
| 61 | 422.22 | 79.97 | 7897 |

### 6.3.2 Solder thickness modelling for Aluminium-Aluminium Combination

The ribbon and contact layers are both Aluminium material while the solder layer is the Sn3.5Ag0.5Cu alloy. The solder layer thickness is varied while the ribbon and

contact layer thicknesses are kept constant at the SDs. See Table 6.1 for more details. Table 6.4 presents the solder interconnection degradation for the solder thickness experiments of the Aluminium-Aluminium Combination All the solder thickness models possess $N_{d_i} < 1$ and negative $D_i$ values hence are improvements of the CT. Thickness value of 41μm is the best design of the Aluminium-Aluminium Combination with $N_{d_{BD}}$= 0.0081 & $D_{BD}$= -99.19%. This means that the solder degradation of the Al-Al Combination at solder thickness of 41μm is 0.0081 times that of the CT and has decreased degradation by 99.19%. It is observed that a one-step increase and decrease in the solder thickness value from 46μm (SD) to 41μm and 51μm respectively demonstrates further improvement in performance but increasing or decreasing the solder thickness value beyond these values (41μm and 51μm) result in the opposite effect.

Table 6.5 presents the fatigue life for solder thickness experiments of Aluminium-Aluminium Combination The best solder thickness design of the Al-Al Combination is 41μm with $N_{f_{BD}}$= 122.94 & $F_{BD}$= 12194%. This means that the fatigue life is 122.94 times that of the CT and has increased fatigue life by 12194%.

**Table 6.4:** Solder interconnection degradation for solder thickness experiments of Aluminium-Aluminium Combination

| **Solder Thickness (μm)** | **Accumulated Max. Creep Strain Energy Density (E-03 Pa)** | $N_{d_i}$ | $D_i$(%) |
|---|---|---|---|
| 31 | 1.16 | 0.0265 | -97.35 |
| 36 | 0.649 | 0.0148 | -98.52 |
| 41 | 0.356 | 0.0081 | -99.19 |
| 46 | 0.604 | 0.0138 | -98.62 |
| 51 | 0.400 | 0.0092 | -99.08 |
| 56 | 0.622 | 0.0142 | -98.58 |
| 61 | 0.673 | 0.0154 | -98.46 |

**Table 6.5:** Fatigue life for solder thickness experiments of Aluminium-Aluminium Combination

| Solder Thickness (µm) | Fatigue Life (years) | $N_{f_i}$ | $F_i$ (%) |
|---|---|---|---|
| 31 | 199.15 | 37.72 | 3672 |
| 36 | 356.02 | 67.43 | 6643 |
| 41 | 649.13 | 122.94 | 12194 |
| 46 | 382.28 | 72.40 | 7140 |
| 51 | 577.47 | 109.37 | 10837 |
| 56 | 371.54 | 70.37 | 6937 |
| 61 | 343.50 | 65.06 | 6406 |

### 6.3.3 Solder thickness modelling for Silver-Aluminium Combination

For this experiment, the ribbon layer is Silver, the contact layer is Aluminium, and the solder layer is the Sn3.5Ag0.5Cu alloy. The ribbon and contact layer thicknesses are kept constant at the SDs while the solder layer thickness is varied. See table 6.1 for more details. Table 6.6 presents the solder interconnection degradation for the solder thickness experiments of the Silver-Aluminium Combination The results show that all the solder thickness models are improvements of the CT with $N_{d_i} < 1$ and negative $D_i$ values. It can be observed that an increase in the solder thickness value from 46µm (SD) to 51µm and 56µm demonstrates further improvement in performance but decreasing the solder thickness value from 46µm results in the opposite effect. It is also established that further increase in solder thickness beyond 56µm shows no improvement on the SD solder thickness model. Thickness value of 51µm is the best design of the Silver-Aluminium Combination with $N_{d_{BD}}$= 0.007 & $D_{BD}$= -99.3%. This means that the solder degradation of the Ag-Al Combination at solder thickness of 51µm is 0.007 times that of the CT and has decreased degradation by 99.3%.

**Table 6.6:** Solder interconnection degradation for solder thickness experiments of Silver-Aluminium Combination

| **Solder Thickness (µm)** | **Accumulated Max. Creep Strain Energy Density (E-03 Pa)** | $N_{d_i}$ | $D_i$(%) |
|---|---|---|---|
| 31 | 1.96 | 0.0448 | -95.52 |
| 36 | 1.16 | 0.0265 | -97.35 |
| 41 | 0.691 | 0.0158 | -98.42 |
| 46 | 0.608 | 0.0139 | -98.61 |
| 51 | 0.305 | 0.0070 | -99.30 |
| 56 | 0.501 | 0.0115 | -98.85 |
| 61 | 0.625 | 0.0143 | -98.57 |

Table 6.7 presents the fatigue life for solder thickness experiments of Silver-Aluminium Combination The best solder thickness design of the Ag-Al Combination is 51µm with $N_{f_{BD}}$= 143.68 & $F_{BD}$= 14268%. This means that the fatigue life is 143.68 times that of the CT and has increased fatigue life by 14268%.

**Table 6.7:** Fatigue life for solder thickness experiments of Silver-Aluminium Combination

| **Solder Thickness (µm)** | **Fatigue Life (years)** | $N_{f_i}$ | $F_i$ (%) |
|---|---|---|---|
| 31 | 118.06 | 22.36 | 2136 |
| 36 | 199.43 | 37.77 | 3677 |
| 41 | 334.38 | 63.33 | 6233 |
| 46 | 380.22 | 72.01 | 7101 |
| 51 | 758.64 | 143.68 | 14268 |
| 56 | 461.16 | 87.34 | 8634 |
| 61 | 369.82 | 70.04 | 6904 |

### 6.3.4 Solder thickness modelling for Aluminium-Silver Combination

The ribbon layer is Aluminium, the contact layer is Silver, and the solder layer is the Sn3.5Ag0.5Cu alloy. The solder layer thickness is varied while the ribbon and contact layer thicknesses are kept constant at the SDs. See table 6.1 for more details. Table 6.8 presents the solder interconnection degradation for the solder thickness experiments of the Aluminium-Silver Combination All the solder thickness models possess $N_{d_i} < 1$ and negative $D_i$ values hence are improvements of the CT. Thickness value of 41µm is the best design of the Aluminium-Silver Combination with $N_{d_{BD}}$= 0.0067 & $D_{BD}$= -99.33%. This means that the solder degradation of the Al-Ag Combination at solder thickness of 41µm is 0.0067 times that of the CT and has decreased degradation by 99.33%. It is observed that an increase in the solder thickness value from 46µm (SD) to 51µm, 56µm and 61µm and decrease to 41µm, 36µm demonstrate further improvement in performance. It can be established that further decrease in solder thickness beyond 36µm shows no improvement. The Al-Ag Combination is the only ribbon-contact material combination that shows improvement on the SD solder thickness model when solder thickness is reduced to 36µm. This is desirable for miniaturisation purposes. The only other ribbon-contact material combination that showed improvement on the SD solder thickness model when the solder thickness reduced is the Al-Al at 41µm.

**Table 6.8:** Solder interconnection degradation for solder thickness experiments of Aluminium-Silver Combination

| **Solder Thickness (µm)** | **Accumulated Max. Creep Strain Energy Density (E-03 Pa)** | $N_{d_i}$ | $D_i$(%) |
|---|---|---|---|
| 31 | 0.978 | 0.0224 | -97.76 |
| 36 | 0.557 | 0.0127 | -98.73 |
| 41 | 0.293 | 0.0067 | -99.33 |
| 46 | 0.768 | 0.0176 | -98.24 |
| 51 | 0.340 | 0.0078 | -99.22 |
| 56 | 0.515 | 0.0118 | -98.82 |
| 61 | 0.592 | 0.0136 | -98.64 |

**Table 6.9:** Fatigue life for solder thickness experiments of Aluminium-Silver Combination

| **Solder Thickness (µm)** | **Fatigue Life (years)** | $N_{f_i}$ | $F_i$ (%) |
|---|---|---|---|
| 31 | 236.26 | 44.75 | 4375 |
| 36 | 415.13 | 78.62 | 7762 |
| 41 | 789.25 | 149.48 | 14848 |
| 46 | 300.91 | 56.99 | 5599 |
| 51 | 678.77 | 128.55 | 12755 |
| 56 | 448.63 | 84.97 | 8397 |
| 61 | 390.11 | 73.88 | 7288 |

Table 6.9 presents the fatigue life for solder thickness experiments of Aluminium-Silver Combination The best solder thickness design of the Al-Ag Combination is 41µm with $N_{f_{BD}}$ = 149.48 & $F_{BD}$= 14848%. This means that the fatigue life is 149.48 times that of the CT and has increased fatigue life by 14848%.

## 6.4 CONTACT LAYER THICKNESS MODELLING

The experiments which examine the thermo-mechanical behaviour of twenty-eight (28) c-Si PV solder interconnection models by varying the thickness of the contact component layer are presented in this section. The contact layer thickness values are 35μm, 40μm, 45μm, 50μm, 55μm, 60μm and 65μm. The standard dimension (SD) value is the 50μm and all other thickness models will be compared to the SD model. Table 6.10 presents the c-Si PV module component layer dimensions used for the contact thickness investigations.

**Table 6.10:** c-Si PV module component dimensions for contact thickness experiments

| **Component Layer** | **Thickness (μm)** |
|---|---|
| Glass | 3000 |
| Top EVA Encapsulant | 179, 174, 169, 164, 159, 154, 149 |
| Ribbon | 200 |
| Solder | 46 |
| Contact | 35, 40, 45, 50, 55, 60, 65 |
| Silicon Wafer | 200 |
| Aluminium Back Contact | 25 |
| Bottom EVA Encapsulant | 214 |
| Tedlar Back Sheet | 190 |

The performance of each c-Si PV contact thickness model will be compared to that of the CT by employing the performance comparison modes 1-4 derived and discussed in chapter 5. Any trends between contact thickness and the degradation of c-Si PV solder interconnection under hot climate operations will be identified.

Results for the contact thickness experiments of Silver-Silver, Aluminium-Aluminium, Silver-Aluminium and Aluminium-Silver ribbon-contact material

combinations will be discussed in sub-sections 6.4.1, 6.4.2, 6.4.3 and 6.4.4 respectively.

### 6.4.1 Contact thickness modelling for Silver-Silver Combination

For this experiment, the ribbon and contact layers are both Silver material while the solder layer is the Sn3.5Ag0.5Cu alloy. The ribbon and solder layer thicknesses are kept constant at the SDs while the contact layer thickness is varied. See table 6.10 for more details. Table 6.11 presents the solder interconnection degradation for the contact thickness experiments of the Silver-Silver Combination The results show that all the contact thickness models are improvements of the CT with $N_{d_i} < 1$ and negative $D_i$ values. It can also be observed that increasing and decreasing the contact thickness value from 50μm (the standard dimension, SD) demonstrates no further improvement in performance. Therefore, the standard dimension contact thickness value at 50μm is the best design of the Silver-Silver Combination with $N_{d_{BD}}$= 0.0132 & $D_{BD}$= -98.68%. This means that the solder degradation of the Ag-Ag Combination at contact thickness of 50μm is 0.0132 times that of the CT and has decreased degradation by 98.68%.

**Table 6.11:** Solder interconnection degradation for contact thickness experiments of Silver-Silver Combination

| **Contact Thickness (μm)** | **Accumulated Max. Creep Strain Energy Density (E-03 Pa)** | $N_{d_i}$ | $D_i$(%) |
|---|---|---|---|
| 35 | 3.84 | 0.0878 | -91.22 |
| 40 | 4.08 | 0.0935 | -90.65 |
| 45 | 4.00 | 0.0914 | -90.86 |
| 50 | 0.577 | 0.0132 | -98.68 |
| 55 | 3.74 | 0.0855 | -91.45 |
| 60 | 3.74 | 0.0855 | -91.45 |
| 65 | 3.48 | 0.0795 | -92.05 |

Table 6.12 presents the fatigue life for contact thickness experiments of Silver-Silver Combination The best contact thickness design of the Ag-Ag Combination is the SD at 50μm with $N_{f_{BD}}$= 75.86 & $F_{BD}$= 7486%. This means that the fatigue life is 75.86 times that of the CT and has increased fatigue life by 7486%.

**Table 6.12:** Fatigue life for contact thickness experiments of Silver-Silver Combination

| **Contact Thickness (μm)** | **Fatigue Life (years)** | $N_{f_i}$ | $F_i$ **(%)** |
|---|---|---|---|
| 35 | 60.21 | 11.40 | 1040 |
| 40 | 56.56 | 10.71 | 971 |
| 45 | 57.83 | 10.95 | 995 |
| 50 | 400.55 | 75.86 | 7486 |
| 55 | 61.80 | 11.70 | 1070 |
| 60 | 61.83 | 11.71 | 1071 |
| 65 | 66.46 | 12.59 | 1159 |

### 6.4.2 Contact thickness modelling for Aluminium-Aluminium Combination

The ribbon and contact layers are both Aluminium material while the solder layer is the Sn3.5Ag0.5Cu alloy. The ribbon and solder layer thicknesses are kept constant at the SDs while the contact layer thickness is varied. See Table 6.10 for more details. Table 6.13 presents the solder interconnection degradation for the contact thickness experiments of the Aluminium-Aluminium Combination All the contact thickness models possess $N_{d_i} < 1$ and negative $D_i$ values hence are improvements of the CT. Contact thickness value of 50μm, the SD, is the best design of the Aluminium-Aluminium Combination with $N_{d_{BD}}$= 0.0138 & $D_{BD}$= -98.62%. This means that the solder degradation of the Al-Al Combination at contact thickness of 50μm is 0.0138 times that of the CT and has decreased degradation by 98.62%. Consequently, it is

established that increasing and decreasing the contact thickness value from 50μm (the standard dimension, SD) demonstrates no further improvement in performance.

**Table 6.13:** Solder interconnection degradation for contact thickness experiments of Aluminium-Aluminium Combination

| **Contact Thickness (μm)** | **Accumulated Max. Creep Strain Energy Density (E-03 Pa)** | $N_{d_i}$ | $D_i$(%) |
|---|---|---|---|
| 35 | 2.71 | 0.0620 | -93.80 |
| 40 | 2.77 | 0.0634 | -93.66 |
| 45 | 2.44 | 0.0557 | -94.43 |
| 50 | 0.604 | 0.0138 | -98.62 |
| 55 | 2.06 | 0.0472 | -95.28 |
| 60 | 1.86 | 0.0425 | -95.75 |
| 65 | 1.49 | 0.0341 | -96.59 |

**Table 6.14:** Fatigue life for contact thickness experiments of Aluminium-Aluminium Combination

| **Contact Thickness (μm)** | **Fatigue Life (years)** | $N_{f_i}$ | $F_i$ (%) |
|---|---|---|---|
| 35 | 85.27 | 16.15 | 1515 |
| 40 | 83.35 | 15.79 | 1479 |
| 45 | 94.84 | 17.96 | 1696 |
| 50 | 382.28 | 72.40 | 7140 |
| 55 | 111.93 | 21.20 | 2020 |
| 60 | 124.30 | 23.54 | 2254 |
| 65 | 155.14 | 29.38 | 2838 |

Table 6.14 presents the fatigue life for contact thickness experiments of Aluminium-Aluminium Combination The best contact thickness design of the Al-Al Combination is the SD at 50μm with $N_{f_{BD}}$= 72.4 & $F_{BD}$= 7140%. This means that the fatigue life is 72.4 times that of the CT and has increased fatigue life by 7140%.

### 6.4.3 Contact thickness modelling for Silver-Aluminium Combination

For this experiment, the ribbon layer is Silver, the contact layer is Aluminium, and the solder layer is the Sn3.5Ag0.5Cu alloy. The ribbon and solder layer thicknesses are kept constant at the SDs while the contact layer thickness is varied. See Table 6.10 for more details. Table 6.15 presents the solder interconnection degradation for the contact thickness experiments of the Silver-Aluminium Combination The results show that all the contact thickness models are improvements of the CT with $N_{d_i} < 1$ and negative $D_i$ values. It can also be observed that increasing and decreasing the contact thickness value from 50μm (the standard dimension, SD) demonstrates no further improvement in performance. Therefore, the standard dimension contact thickness value at 50μm is the best design of the Silver-Aluminium Combination with $N_{d_{BD}}$= 0.0139 & $D_{BD}$= -98.61%. This means that the solder degradation of the Ag-Al Combination at contact thickness of 50μm is 0.0139 times that of the CT and has decreased degradation by 98.61%.

Table 6.16 presents the fatigue life for contact thickness experiments of Silver-Aluminium Combination The best contact thickness design of the Ag-Al Combination is the SD at 50μm with $N_{f_{BD}}$= 72.01 & $F_{BD}$= 7101%. This means that the fatigue life is 72.01times that of the CT and has increased fatigue life by 7101%.

**Table 6.15:** Solder interconnection degradation for contact thickness experiments of Silver-Aluminium Combination

| **Contact Thickness (µm)** | **Accumulated Max. Creep Strain Energy Density (E-03 Pa)** | $N_{d_i}$ | $D_i$(%) |
|---|---|---|---|
| 35 | 3.74 | 0.0856 | -91.44 |
| 40 | 3.86 | 0.0882 | -91.18 |
| 45 | 3.61 | 0.0825 | -91.75 |
| 50 | 0.608 | 0.0139 | -98.61 |
| 55 | 3.13 | 0.0716 | -92.84 |
| 60 | 3.15 | 0.0720 | -92.80 |
| 65 | 3.07 | 0.0701 | -92.99 |

**Table 6.16:** Fatigue life for contact thickness experiments of Silver-Aluminium Combination

| **Contact Thickness (µm)** | **Fatigue Life (years)** | $N_{f_i}$ | $F_i$ (%) |
|---|---|---|---|
| 35 | 61.78 | 11.70 | 1070 |
| 40 | 59.93 | 11.35 | 1035 |
| 45 | 64.07 | 12.13 | 1113 |
| 50 | 380.22 | 72.01 | 7101 |
| 55 | 73.88 | 13.99 | 1299 |
| 60 | 73.43 | 13.91 | 1291 |
| 65 | 75.37 | 14.27 | 1327 |

### 6.4.4 Contact thickness modelling for Aluminium-Silver Combination

The ribbon layer is Aluminium, the contact layer is Silver, and the solder layer is the Sn3.5Ag0.5Cu alloy. The ribbon and solder layer thicknesses are kept constant at the SDs while the contact layer thickness is varied. See Table 6.10 for more details. Table 6.17 presents the solder interconnection degradation for the contact thickness experiments of the Aluminium-Silver Combination All the contact thickness models

possess $N_{d_i} < 1$ and negative $D_i$ values hence are improvements of the CT. Contact thickness value of 50μm, the SD, is the best design of the Aluminium-Silver Combination with $N_{d_{BD}}$= 0.0176 & $D_{BD}$= -98.24%. This means that the solder degradation of the Al-Ag Combination at contact thickness of 50μm is 0.0176 times that of the CT and has decreased degradation by 98.24%. Consequently, it is established that increasing and decreasing the contact thickness value from 50μm (the standard dimension, SD) demonstrates no further improvement in performance.

**Table 6.17:** Solder interconnection degradation for contact thickness experiments of Aluminium-Silver Combination

| **Contact Thickness (μm)** | **Accumulated Max. Creep Strain Energy Density (E-03 Pa)** | $N_{d_i}$ | $D_i$(%) |
|---|---|---|---|
| 35 | 2.89 | 0.0662 | -93.38 |
| 40 | 3.13 | 0.0715 | -92.85 |
| 45 | 2.99 | 0.0684 | -93.16 |
| 50 | 0.768 | 0.0176 | -98.24 |
| 55 | 2.65 | 0.0606 | -93.94 |
| 60 | 2.42 | 0.0554 | -94.46 |
| 65 | 2.02 | 0.0463 | -95.37 |

**Table 6.18:** Fatigue life for contact thickness experiments of Aluminium-Silver Combination

| **Contact Thickness (μm)** | **Fatigue Life (years)** | $N_{f_i}$ | $F_i$ (%) |
|---|---|---|---|
| 35 | 79.89 | 15.13 | 1413 |
| 40 | 73.89 | 14.00 | 1300 |
| 45 | 77.33 | 14.65 | 1365 |
| 50 | 300.91 | 56.99 | 5599 |
| 55 | 87.28 | 16.53 | 1553 |
| 60 | 95.51 | 18.09 | 1709 |
| 65 | 114.29 | 21.65 | 2065 |

Table 6.18 presents the fatigue life for contact thickness experiments of Aluminium-Silver Combination The best contact thickness design of the Al-Ag Combination is the SD at 50µm with $N_{f_{BD}}$= 56.99 & $F_{BD}$= 5599%. This means that the fatigue life is 56.99 times that of the CT and has increased fatigue life by 5599%.

## 6.5 RIBBON LAYER THICKNESS MODELLING

This section presents the experiments which examine the thermo-mechanical behaviour of twenty-eight (28) c-Si PV solder interconnection models by varying the thickness of the ribbon component layer. The thickness values of the ribbon layer 170µm, 180µm, 190µm, 200µm, 210µm, 220µm and 230µm. The standard dimension (SD) value is the 200µm and all other thickness models will be compared to the SD model. Table 6.19 presents the c-Si PV module component layer dimensions used for the ribbon thickness investigations.

**Table 6.19:** c-Si PV module component dimensions for ribbon thickness experiments

| **Component Layer** | **Thickness (µm)** |
|---|---|
| Glass | 3000 |
| Top EVA Encapsulant | 194, 184, 174, 164, 154, 144, 134 |
| Ribbon | 170, 180, 190, 200, 210, 220, 230 |
| Solder | 46 |
| Contact | 50 |
| Silicon Wafer | 200 |
| Aluminium Back Contact | 25 |
| Bottom EVA Encapsulant | 244, 234, 224, 214, 204, 194, 184 |
| Tedlar Back Sheet | 190 |

The performance of each c-Si PV ribbon thickness model will be compared to that of the CT by employing the performance comparison modes 1-4 derived and discussed in chapter 5. Additionally, any trends between ribbon thickness and the degradation of c-Si PV solder interconnection under hot climate operations will be identified.

Results for the ribbon thickness experiments of Silver-Silver, Aluminium-Aluminium, Silver-Aluminium and Aluminium-Silver ribbon-contact material combinations will be discussed in sub-sections 6.5.1, 6.5.2, 6.5.3 and 6.5.4 respectively.

### 6.5.1 Ribbon thickness modelling for Silver-Silver Combination

For this experiment, the ribbon and contact layers are both Silver material while the solder layer is the Sn3.5Ag0.5Cu alloy. The contact and solder layer thicknesses are kept constant at the SDs while the ribbon layer thickness is varied. See Table 6.19 for more details. Table 6.20 presents the solder interconnection degradation for the ribbon thickness experiments of the Silver-Silver Combination The results show that all the ribbon thickness models are improvements of the CT with $N_{d_i} < 1$ and negative $D_i$ values. It can also be observed that increasing and decreasing the ribbon thickness value from 200μm (the standard dimension, SD) demonstrates no further improvement in performance. Therefore, the standard dimension ribbon thickness value at 200μm is the best design of the Silver-Silver Combination with $N_{d_{BD}}$= 0.0132 & $D_{BD}$= -98.68%. This means that the solder degradation of the Ag-Ag Combination at ribbon thickness of 200μm is 0.0132 times that of the CT and has decreased degradation by 98.68%.

Table 6.21 presents the fatigue life for ribbon thickness experiments of Silver-Silver Combination The best ribbon thickness design of the Ag-Ag Combination is the SD

at 200μm with $N_{f_{BD}}$ = 75.86 & $F_{BD}$= 7486%. This means that the fatigue life is 75.86 times that of the CT and has increased fatigue life by 7486%.

**Table 6.20:** Solder interconnection degradation for ribbon thickness experiments of Silver-Silver Combination

| **Ribbon Thickness (μm)** | **Accumulated Max. Creep Strain Energy Density (E-03 Pa)** | $N_{d_i}$ | $D_i$(%) |
|---|---|---|---|
| 170 | 2.25 | 0.0516 | -94.84 |
| 180 | 1.56 | 0.0357 | -96.43 |
| 190 | 0.916 | 0.0210 | -97.90 |
| 200 | 0.5774 | 0.0132 | -98.68 |
| 210 | 4.30 | 0.0983 | -90.17 |
| 220 | 4.49 | 0.1028 | -89.72 |
| 230 | 4.32 | 0.0988 | -90.12 |

**Table 6.21:** Fatigue life for ribbon thickness experiments of Silver-Silver Combination

| **Ribbon Thickness (μm)** | **Fatigue Life (years)** | $N_{f_i}$ | $F_i$ (%) |
|---|---|---|---|
| 170 | 102.50 | 19.41 | 1841 |
| 180 | 148.29 | 28.08 | 2708 |
| 190 | 252.23 | 47.77 | 4677 |
| 200 | 400.55 | 75.86 | 7486 |
| 210 | 53.76 | 10.18 | 918 |
| 220 | 51.44 | 9.74 | 874 |
| 230 | 53.50 | 10.13 | 913 |

### 6.5.2 Ribbon thickness modelling for Aluminium-Aluminium Combination

The ribbon and contact layers are both Aluminium material while the solder layer is the Sn3.5Ag0.5Cu alloy. The contact and solder layer thicknesses are kept constant at the SDs while the ribbon layer thickness is varied. See Table 6.19 for more details. Table 6.22 presents the solder interconnection degradation for the ribbon thickness

experiments of the Aluminium-Aluminium Combination All the ribbon thickness models possess $N_{d_i} < 1$ and negative $D_i$ values hence are improvements of the CT. Ribbon thickness value of 200μm, the SD, is the best design of the Aluminium-Aluminium Combination with $N_{d_{BD}}$= 0.0138 & $D_{BD}$= -98.62%. This means that the solder degradation of the Al-Al Combination at ribbon thickness of 200μm is 0.0138 times that of the CT and has decreased degradation by 98.62%. Consequently, it is established that increasing and decreasing the ribbon thickness value from 200μm (the standard dimension, SD) demonstrates no further improvement in performance.

**Table 6.22:** Solder interconnection degradation for ribbon thickness experiments of Aluminium-Aluminium Combination

| **Ribbon Thickness (μm)** | **Accumulated Max. Creep Strain Energy Density (E-03 Pa)** | $N_{d_i}$ | $D_i$(%) |
|---|---|---|---|
| 170 | 4.96 | 0.1135 | -88.65 |
| 180 | 2.38 | 0.0544 | -94.56 |
| 190 | 1.32 | 0.0302 | -96.98 |
| 200 | 0.604 | 0.0138 | -98.62 |
| 210 | 2.42 | 0.0554 | -94.46 |
| 220 | 2.53 | 0.0580 | -94.20 |
| 230 | 2.61 | 0.0598 | -94.02 |

**Table 6.23:** Fatigue life for ribbon thickness experiments of Aluminium-Aluminium Combination

| **Ribbon Thickness (μm)** | **Fatigue Life (years)** | $N_{f_i}$ | $F_i$ (%) |
|---|---|---|---|
| 170 | 46.59 | 8.82 | 782 |
| 180 | 97.26 | 18.42 | 1742 |
| 190 | 174.84 | 33.11 | 3211 |
| 200 | 382.28 | 72.40 | 7140 |
| 210 | 95.40 | 18.07 | 1707 |
| 220 | 91.17 | 17.27 | 1627 |
| 230 | 88.44 | 16.75 | 1575 |

Table 6.23 presents the fatigue life for ribbon thickness experiments of Aluminium-Aluminium Combination The best ribbon thickness design of the Al-Al Combination is the SD at 200μm with $N_{f_{BD}}$= 72.4 & $F_{BD}$= 7140%. This means that the fatigue life is 72.4 times that of the CT and has increased fatigue life by 7140%.

### 6.5.3 Ribbon thickness modelling for Silver-Aluminium Combination

For this experiment, the ribbon layer is Silver, the contact layer is Aluminium, and the solder layer is the Sn3.5Ag0.5Cu alloy. The contact and solder layer thicknesses are kept constant at the SDs while the ribbon layer thickness is varied. See Table 6.19 for more details. Table 6.24 presents the solder interconnection degradation for the ribbon thickness experiments of the Silver-Aluminium Combination The results show that all the ribbon thickness models are improvements of the CT with $N_{d_i} < 1$ and negative $D_i$ values. It can also be observed that increasing and decreasing the ribbon thickness value from 200μm (the standard dimension, SD) demonstrates no further improvement in performance. Therefore, the standard dimension ribbon thickness value at 200μm is the best design of the Silver-Aluminium Combination with $N_{d_{BD}}$= 0.0139 & $D_{BD}$= -98.61%. This means that the solder degradation of the Ag-Al Combination at ribbon thickness of 200μm is 0.0139 times that of the CT and has decreased degradation by 98.61%.

Table 6.25 presents the fatigue life for ribbon thickness experiments of Silver-Aluminium Combination The best ribbon thickness design of the Ag-Al Combination is the SD at 200μm with $N_{f_{BD}}$= 72.01 & $F_{BD}$= 7101%. This means that the fatigue life is 72.01times that of the CT and has increased fatigue life by 7101%.

**Table 6.24:** Solder interconnection degradation for ribbon thickness experiments of Silver-Aluminium Combination

| **Ribbon Thickness (µm)** | **Accumulated Max. Creep Strain Energy Density (E-03 Pa)** | $N_{d_i}$ | $D_i$(%) |
|---|---|---|---|
| 170 | 2.41 | 0.0551 | -94.49 |
| 180 | 1.65 | 0.0378 | -96.22 |
| 190 | 0.931 | 0.0213 | -97.87 |
| 200 | 0.608 | 0.0139 | -98.61 |
| 210 | 3.82 | 0.0875 | -91.25 |
| 220 | 4.05 | 0.0928 | -90.72 |
| 230 | 4.26 | 0.0975 | -90.25 |

**Table 6.25:** Fatigue life for ribbon thickness experiments of Silver-Aluminium Combination

| **Ribbon Thickness (µm)** | **Fatigue Life (years)** | $N_{f_i}$ | $F_i$ (%) |
|---|---|---|---|
| 170 | 95.96 | 18.17 | 1717 |
| 180 | 139.80 | 26.48 | 2548 |
| 190 | 248.11 | 46.99 | 4599 |
| 200 | 380.22 | 72.01 | 7101 |
| 210 | 60.43 | 11.45 | 1045 |
| 220 | 56.98 | 10.79 | 979 |
| 230 | 54.22 | 10.27 | 927 |

### 6.5.4 Ribbon thickness modelling for Aluminium-Silver Combination

The ribbon layer is Aluminium, the contact layer is Silver, and the solder layer is the Sn3.5Ag0.5Cu alloy. The contact and solder layer thicknesses are kept constant at the SDs while the ribbon layer thickness is varied. See Table 6.19 for more details. Table 6.26 presents the solder interconnection degradation for the ribbon thickness experiments of the Aluminium-Silver Combination All the ribbon thickness models possess $N_{d_i} < 1$ and negative $D_i$ values hence are improvements of the CT. Ribbon

thickness value of 200μm, the SD, is the best design of the Aluminium-Silver Combination with $N_{d_{BD}}$= 0.0176 & $D_{BD}$= -98.24%. This means that the solder degradation of the Al-Ag Combination at ribbon thickness of 200μm is 0.0176 times that of the CT and has decreased degradation by 98.24%. Consequently, it is established that increasing and decreasing the ribbon thickness value from 200μm (the standard dimension, SD) demonstrates no further improvement in performance.

**Table 6.26:** Solder interconnection degradation for ribbon thickness experiments of Aluminium-Silver Combination

| **Ribbon Thickness (μm)** | **Accumulated Max. Creep Strain Energy Density (E-03 Pa)** | $N_{d_i}$ | $D_i$(%) |
|---|---|---|---|
| 170 | 4.48 | 0.1024 | -89.76 |
| 180 | 2.33 | 0.0532 | -94.68 |
| 190 | 1.36 | 0.0312 | -96.88 |
| 200 | 0.768 | 0.0176 | -98.24 |
| 210 | 3.02 | 0.0692 | -93.08 |
| 220 | 3.11 | 0.0711 | -92.89 |
| 230 | 3.12 | 0.0714 | -92.86 |

**Table 6.27:** Fatigue life for ribbon thickness experiments of Aluminium-Silver Combination

| **Ribbon Thickness (μm)** | **Fatigue Life (years)** | $N_{f_i}$ | $F_i$ (%) |
|---|---|---|---|
| 170 | 51.63 | 9.78 | 878 |
| 180 | 99.29 | 18.80 | 1780 |
| 190 | 169.40 | 32.08 | 3108 |
| 200 | 300.91 | 56.99 | 5599 |
| 210 | 76.43 | 14.47 | 1347 |
| 220 | 74.35 | 14.08 | 1308 |
| 230 | 74.09 | 14.03 | 1303 |

Table 6.27 presents the fatigue life for ribbon thickness experiments of Aluminium-Silver Combination The best ribbon thickness design of the Al-Ag Combination is the SD at 200μm with $N_{f_{BD}}$= 56.99 & $F_{BD}$= 5599%. This means that the fatigue life is 56.99 times that of the CT and has increased fatigue life by 5599%.

## 6.6 CONCLUSIONS

This chapter presented an investigation on the effects of thickness of bonded materials in the solder joint on the degradation of c-Si PV solder interconnections for improved reliability in elevated temperature climate using appropriate thermo-mechanical models in the ANSYS FEM environment. The four (4) best performing ribbon-contact material combinations (Silver-Silver, Aluminium-Aluminium, Silver-Aluminium and Aluminium-Silver), extensively discussed in chapter 5 of this thesis, were used to design eighty-four (84) c-Si PV solder interconnection models where either the ribbon, solder or contact component layer thicknesses were varied from the standard dimensions (SD). Single variate thickness experiments were carried out on each of the eighty-four (84) c-Si solder interconnection models and their respective performances in elevated temperature climate were compared to that of the conventional c-Si PV solder interconnection at SD. This was done to test their suitability to replace the latter in elevated temperature operating conditions. The performance comparison modes 1-4 derived in chapter 5 were applied.

Results show that all eighty-four (84) c-Si PV solder interconnection thickness models are improvements of the CT with $N_{d_i} < 1$ and negative $D_i$ values. They each decreased solder interconnection degradation and increased fatigue life and so, could replace the conventional c-Si PV solder interconnection in elevated

temperature climate conditions. Their individual performance values range $N_{d_i}$= 0.0054 - 0.1135 & $D_i$= -99.46% to -88.65%.

Findings from the single variate solder thickness experiments show that for all four (4) ribbon-contact material combinations, varying the solder thickness (SD ±5μm) improved the performance of the joint with standard dimensions. However, the relationship between solder layer thickness and interconnection degradation for all four (4) material combinations is non-linear. There could be several reasons for this nonlinear relationship observed between solder layer thickness and interconnection degradation. One of which is the nature of IMC layers formed within each of the four (4) different material combinations. Some studies have been carried out on the IMC layer formed in the conventional c-Si PV module interconnection, but further investigation is required on the composition and properties of IMC layers formed within the proposed material combinations. This is necessary to ascertain the effects these new IMCs have on the thermo-mechanical reliability of the c-Si PV modules especially in elevated temperature climates and so formulates one of the recommendations for further study. Also worthy of further investigation is the evolution of microstructures resulting in creep-fatigue resistance. The Al-Ag combination showed desirable miniaturisation characteristics. This is the only combination to show improvement on the SD when the solder thickness was decreased by 10μm down to 36μm. 36μm is the lowest solder thickness to demonstrate such improvement over the SD and so further reduction beyond 36μm shows no performance improvement over the SD model. The best performing solder thickness models are 51μm for the Ag-Ag combination ($N_{d_i}$= 0.0054 & $D_i$= -99.46%), 41μm for the Al-Al combination ($N_{d_i}$= 0.0081 & $D_i$= -99.19%), 51μm for

the Ag-Al combination ($N_{d_i}$= 0.007 & $D_i$= -99.3%), and 41μm for the Al-Ag combination ($N_{d_i}$= 0.0067 & $D_i$= -99.33).

Further findings from the single variate contact and ribbon thickness experiments show that for all four (4) ribbon-contact material combinations, varying their thickness values (lower or higher from SD) does not improve the performance of the joint with standard dimensions. The best performing contact thickness models remained 50μm (SD) for all 4 combs. Similarly, the 200μm (SD) ribbon thickness model was the best.

In the next chapter of this thesis, chapter 7, the optimisation of the c-Si PV module interconnection reliability influencing factors (RIFs) for improved performance in elevated temperature climates will be presented. The component layer materials and thicknesses of the solder interconnection will be varied simultaneously and any interactions between layers will be highlighted. Taguchi L25 orthogonal array will be applied for the experimental design. These sets of experiments will determine the optimal design settings of the c-Si PV solder interconnection for improved performance in elevated temperature climates.

# CHAPTER 7

# TAGUCHI'S ROBUST OPTIMISATION OF RELIABILITY INFLEUNCING FACTORS FOR IMPROVED PEFROMANCE OF PHOTOVOLTAIC (PV) SOLDER INTERCONNECTIONS

## 7.1 INTRODUCTION

Chapters 4, 5 and 6 of this thesis have discussed the effects of non-STC operating temperatures, material combination and thickness of bonded materials in the c-Si PV solder interconnection on its degradation in elevated temperature climates respectively using ANSYS FEM. The conventional c-Si PV solder interconnection has been found to only operate at about 27.5% of its designed performance and fatigue life under elevated temperature climate conditions. This chapter presents an optimisation of these aforementioned reliability influencing factors (RIFs) of the c-Si PV solder interconnection and proposes robust model(s) as suitable substitution(s) to the conventional c-Si module which ensures improved reliability in elevated temperature climates. Unlike in the previous results chapters where single variate experiments were carried out, the ANSYS FEM experiments presented in this chapter are robust in that they determine the effects of multiple RIFs at the same time i.e. multivariate experiments. This ensures that combined effects of RIFs are determined as well as any interactions between RIFs being identified and described. These robust experiments are achieved by applying Taguchi L25 orthogonal array.

The details of the finite element modelling procedure, material properties and models are presented in section 7.2. The robust FEM experiments for the Silver-Silver,

Aluminium-Aluminium, Silver-Aluminium and Aluminium-Silver ribbon-contact material combinations are presented in sections 7.3, 7.4, 7.5, and 7.6 respectively.

## 7.2 FINITE ELEMENT MODELLING

As identified in chapter 5 of this thesis, the four (4) ribbon-contact material combinations chosen as the most suitable alternatives to the conventional c-Si PV solder interconnection in elevated temperature climate conditions are Silver-Silver, Aluminium-Aluminium, Silver-Aluminium and Aluminium-Silver. Employing Taguchi orthogonal array, these material combs. are used to design one hundred (100) different c-Si PV module solder interconnection models in which the effects and interactions of multiple RIFs are investigated. C-Si PV solder interconnection component layer thicknesses and material combinations will be varied simultaneously.

Table 7.1 presents the Taguchi L25 orthogonal array applied for this investigation. Three (3) control factors (i.e. independent variables) at five (5) levels are used. Table 7.2 presents the Taguchi L25 control factors and levels. The control factors are the solder, contact and ribbon layer thicknesses. Solder layer thickness levels are 36μm, 41μm, 46μm, 51μm and 56μm. Contact layer thickness levels are 40μm, 45μm, 50μm, 55μm, and 60μm. Ribbon layer thickness levels are 180μm, 190μm, 200μm, 210μm and 220μm. In the wake of the investigation carried out in chapter 6; the effect of thickness of bonded materials in the solder joint on PV interconnection degradation, these component layer thickness dimensions were chosen for the Taguchi L25 robust experiments. For each of the 100 models, the corresponding dimensions of the other c-Si PV module component layers are set depending on the values of their respective control factors. 1mm by 1mm c-Si PV cell assemblies of

the 100 models are designed using the Solid Works 3D modelling software package and are thereafter converted to the acceptable Parasolid (*.x_t) format for the ANSYS FEM simulations. The degradation response of the designed models to applied loads and boundary conditions are measured. Details of model design procedures, material properties and thermo-mechanical material models of the component layers can be found in chapter 3 of this thesis.

Minitab 18 and Microsoft Excel 365 software are employed as the statistics tools. The performance parameter for this set of Taguchi L25 robust experiments is the accumulated creep strain energy density which is the measure of c-Si PV solder interconnection degradation. To improve reliability of the module and elongate fatigue life in elevated temperature climates, solder interconnection degradation must be reduced. Hence, Eqn. 3.13 is applied to derive the signal to noise (SN) ratio values for minimisation. Combining Eqns. 3.10 and 3.13,

$$SN = -10 \log \omega_{acc}^2 \qquad \text{Equation 7.1}$$

For each design point, the SN ratio is calculated using Eqn. 7.1. The model with the maximum SN ratio, $SN_{MAX}$, is the best design while the model with the lowest SN ratio value, $SN_{MIN}$, is the worst design.

$$SN_{MAX} = best\ design \qquad \text{Equation 7.2}$$

$$SN_{MIN} = worst\ design \qquad \text{Equation 7.3}$$

As established in chapter 5, the conventional c-Si PV solder interconnection under elevated temperature climate conditions retains the role of central tendency (CT). Applying the performance comparison modes 1 – 4, the performance of each of the 100 Taguchi designed solder interconnection models will be compared to that of the CT in elevated temperature operation. Fatigue life of CT under elevated temperature was measured at only 5.28 years which is a 72.5% decrease from 19.2 years at STC.

Refer to Eqns. 5.1 - 5.8 in section 5.3.2 of chapter 5 for more details on the modes of performance comparison of conventional PV solder interconnection with proposed designed models in non STC climates.

**Table 7.1:** Taguchi L25 orthogonal array

| **Model No.** | **Control Factors** | | | **Mean Response Parameter** | **Signal to Noise Ratio** |
|---|---|---|---|---|---|
| | **S** | **C** | **R** | **P** | **SN** |
| 1 | 1 | 1 | 1 | $P_1$ | $SN_1$ |
| 2 | 1 | 2 | 2 | $P_2$ | $SN_2$ |
| 3 | 1 | 3 | 3 | $P_3$ | $SN_3$ |
| 4 | 1 | 4 | 4 | $P_4$ | $SN_4$ |
| 5 | 1 | 5 | 5 | $P_5$ | $SN_5$ |
| 6 | 2 | 1 | 2 | $P_6$ | $SN_6$ |
| 7 | 2 | 2 | 3 | $P_7$ | $SN_7$ |
| 8 | 2 | 3 | 4 | $P_8$ | $SN_8$ |
| 9 | 2 | 4 | 5 | $P_9$ | $SN_9$ |
| 10 | 2 | 5 | 1 | $P_{10}$ | $SN_{10}$ |
| 11 | 3 | 1 | 3 | $P_{11}$ | $SN_{11}$ |
| 12 | 3 | 2 | 4 | $P_{12}$ | $SN_{12}$ |
| 13 | 3 | 3 | 5 | $P_{13}$ | $SN_{13}$ |
| 14 | 3 | 4 | 1 | $P_{14}$ | $SN_{14}$ |
| 15 | 3 | 5 | 2 | $P_{15}$ | $SN_{15}$ |
| 16 | 4 | 1 | 4 | $P_{16}$ | $SN_{16}$ |
| 17 | 4 | 2 | 5 | $P_{17}$ | $SN_{17}$ |
| 18 | 4 | 3 | 1 | $P_{18}$ | $SN_{18}$ |
| 19 | 4 | 4 | 2 | $P_{19}$ | $SN_{19}$ |
| 20 | 4 | 5 | 3 | $P_{20}$ | $SN_{20}$ |
| 21 | 5 | 1 | 5 | $P_{21}$ | $SN_{21}$ |
| 22 | 5 | 2 | 1 | $P_{22}$ | $SN_{22}$ |
| 23 | 5 | 3 | 2 | $P_{23}$ | $SN_{23}$ |
| 24 | 5 | 4 | 3 | $P_{24}$ | $SN_{24}$ |
| 25 | 5 | 5 | 4 | $P_{25}$ | $SN_{25}$ |

**Table 7.2:** Taguchi L25 control factors and levels

| Levels | Control Factors (µm) | | |
|---|---|---|---|
| | **Solder** | **Contact** | **Ribbon** |
| 1 | 36 | 40 | 180 |
| 2 | 41 | 45 | 190 |
| 3 | 46 | 50 | 200 |
| 4 | 51 | 55 | 210 |
| 5 | 56 | 60 | 220 |

### 7.2.1 Estimating the effects of each control factor on predicting optimal design using analysis of means (ANOM)

The optimal design point occurs when the mean SN ratio for each control factor level is at maximum. The effect of each control factor level is given by the deviation of the mean SN ratio at that factor level from the overall mean SN ratio for the experiment.

Overall mean for experiment,

$$SN_{exp} = \frac{1}{N}\left(\sum_{i=1}^{N} SN_i\right) \qquad \text{Equation 7.4}$$

Inputting, $N$ = 25, as required for the Taguchi L25 orthogonal array employed in this study, and referring to Table 7.1, Eqn. 7.4 becomes,

$$SN_{exp} = \frac{1}{25}\left(SN_1 + SN_2 + \cdots + SN_{25}\right) \qquad \text{Equation 7.5}$$

Using Table 7.1 as the reference, the mean SN ratios of each control factor can be derived at each factor level. Table 7.3 presents the control factor effects on the response parameter. For each factor level, the number of experiments, $n$ = 5, as required for the present study.

Mean SN ratio for solder at level 1,

$$SN_{S_1} = \frac{1}{5}\left(SN_1 + SN_2 + SN_3 + SN_4 + SN_5\right) \qquad \text{Equation 7.6}$$

Mean SN ratio for solder at level 2,

$$SN_{S_2} = \frac{1}{5}(SN_6 + SN_7 + SN_8 + SN_9 + SN_{10}) \quad \text{Equation 7.7}$$

Mean SN ratio for solder at level 3,

$$SN_{S_3} = \frac{1}{5}(SN_{11} + SN_{12} + SN_{13} + SN_{14} + SN_{15}) \quad \text{Equation 7.8}$$

Mean SN ratio for solder at level 4,

$$SN_{S_4} = \frac{1}{5}(SN_{16} + SN_{17} + SN_{18} + SN_{19} + SN_{20}) \quad \text{Equation 7.9}$$

Mean SN ratio for solder at level 5,

$$SN_{S_5} = \frac{1}{5}(SN_{21} + SN_{22} + SN_{23} + SN_{24} + SN_{25}) \quad \text{Equation 7.10}$$

Mean SN ratio for contact at level 1,

$$SN_{C_1} = \frac{1}{5}(SN_1 + SN_6 + SN_{11} + SN_{16} + SN_{21}) \quad \text{Equation 7.11}$$

Mean SN ratio for contact at level 2,

$$SN_{C_2} = \frac{1}{5}(SN_2 + SN_7 + SN_{12} + SN_{17} + SN_{22}) \quad \text{Equation 7.12}$$

Mean SN ratio for contact at level 3,

$$SN_{C_3} = \frac{1}{5}(SN_3 + SN_8 + SN_{13} + SN_{18} + SN_{23}) \quad \text{Equation 7.13}$$

Mean SN ratio for contact at level 4,

$$SN_{C_4} = \frac{1}{5}(SN_4 + SN_9 + SN_{14} + SN_{19} + SN_{24}) \quad \text{Equation 7.14}$$

Mean SN ratio for contact at level 5,

$$SN_{C_5} = \frac{1}{5}(SN_5 + SN_{10} + SN_{15} + SN_{20} + SN_{25}) \quad \text{Equation 7.15}$$

Mean SN ratio for ribbon at level 1,

$$SN_{R_1} = \frac{1}{5}(SN_1 + SN_{10} + SN_{14} + SN_{18} + SN_{22}) \quad \text{Equation 7.16}$$

Mean SN ratio for ribbon at level 2,

$$SN_{R_2} = \frac{1}{5}(SN_2 + SN_6 + SN_{15} + SN_{19} + SN_{23}) \quad \text{Equation 7.17}$$

Mean SN ratio for ribbon at level 3,

$$SN_{R_3} = \frac{1}{5}(SN_3 + SN_7 + SN_{11} + SN_{20} + SN_{24}) \quad \text{Equation 7.18}$$

Mean SN ratio for ribbon at level 4,

$$SN_{R_4} = \frac{1}{5}(SN_4 + SN_8 + SN_{12} + SN_{16} + SN_{25}) \quad \text{Equation 7.19}$$

Mean SN ratio for ribbon at level 5,

$$SN_{R_5} = \frac{1}{5}(SN_5 + SN_9 + SN_{13} + SN_{17} + SN_{21}) \quad \text{Equation 7.20}$$

The delta effect of each factor (F) at a level (L) is calculated by,

$$\Delta F_L = SN_{F_L} - SN_{exp} \quad \text{Equation 7.21}$$

The SN ratio of the optimum design point can be predicted using Eqn. 7.22. Where $SN_{S_{max}}$, $SN_{C_{max}}$, and $SN_{R_{max}}$ are the maximum mean SN ratios for solder, contact and ribbon. The predicted SN ratio for optimum design point will be compared to the value obtained from the verification experiments.

$$SN_{opt} = SN_{exp} + \left(SN_{S_{max}} - SN_{exp}\right) + \left(SN_{C_{max}} - SN_{exp}\right) + \left(SN_{R_{max}} - SN_{exp}\right)$$

Equation 7.22

Equations 7.5 – 7.22 will be applied to obtain the optimum design points for each of the four different c-Si PV module material combinations discussed in sections 7.3, 7.4, 7.5 and 7.6. These Taguchi L25 orthogonal array experiments are carried out for the robust optimisation of reliability influencing factors (RIFs) for the improved performance of c-Si PV solder interconnections in elevated temperature climates.

**Table 7.3:** Control factor effects on response parameter

| Control Factor | Level | SN Ratio |
|---|---|---|
| Solder (S) | 1 | $SN_{S1}$ |
| | 2 | $SN_{S2}$ |
| | 3 | $SN_{S3}$ |
| | 4 | $SN_{S4}$ |
| | 5 | $SN_{S5}$ |
| Contact (C) | 1 | $SN_{C1}$ |
| | 2 | $SN_{C2}$ |
| | 3 | $SN_{C3}$ |
| | 4 | $SN_{C4}$ |
| | 5 | $SN_{C5}$ |
| Ribbon (R) | 1 | $SN_{R1}$ |
| | 2 | $SN_{R2}$ |
| | 3 | $SN_{R3}$ |
| | 4 | $SN_{R4}$ |
| | 5 | $SN_{R5}$ |

### 7.2.2 Contribution of each control factor to the response parameter using analysis of variance (ANOVA)

The sum of squares (SS) technique of ANOVA is applied to determine the contribution of each control factor on the response parameter. The total SS is derived in Eqn. 7.23.

$$SS_T = \sum_{i=1}^{N} \left(SN_i - SN_{exp}\right)^2 \qquad \text{Equation 7.23}$$

Inputting, $N$ = 25, as required for the Taguchi L25 orthogonal array employed in this study, and referring to Table 7.1, Eqn. 7.23 becomes,

$$SS_T = \left(SN_1 - SN_{exp}\right)^2 + \left(SN_2 - SN_{exp}\right)^2 + \cdots + \left(SN_{25} - SN_{exp}\right)^2$$

Equation 7.24

The sum of squares due to variation for solder (S),

$$SS_S = 5\left(\left(SN_{S_1} - SN_{exp}\right)^2 + \left(SN_{S_2} - SN_{exp}\right)^2 + \cdots + \left(SN_{S_5} - SN_{exp}\right)^2\right)$$

Equation 7.25

Percentage contribution of solder (S), $= \frac{SS_S}{SS_T} \times 100$ Equation 7.26

The sum of squares due to variation for contact (C),

$$SS_C = 5\left(\left(SN_{C_1} - SN_{exp}\right)^2 + \left(SN_{C_2} - SN_{exp}\right)^2 + \cdots + \left(SN_{C_5} - SN_{exp}\right)^2\right)$$

Equation 7.27

Percentage contribution of contact (C), $= \frac{SS_C}{SS_T} \times 100$ Equation 7.28

The sum of squares due to variation for ribbon (R),

$$SS_R = 5\left(\left(SN_{R_1} - SN_{exp}\right)^2 + \left(SN_{R_2} - SN_{exp}\right)^2 + \cdots + \left(SN_{R_5} - SN_{exp}\right)^2\right)$$

Equation 7.29

Percentage contribution of ribbon (R), $= \frac{SS_R}{SS_T} \times 100$ Equation 7.30

$SS_T = SS_S + SS_C + SS_R$ Equation 7.31

The additive Taguchi design model has been employed and so the focus of the robust experiments is on mean control factor effects hence they are free of any major interactions. Co-dependency between control factors is absent and any interactions are minimised.

## 7.3 TAGUCHI DESIGN FOR SILVER-SILVER COMBINATION

In this set of Taguchi L25 orthogonal array experiments, each c-Si PV solder interconnection model is designed such that both the ribbon and contact layers are Silver material while the solder layer is the Sn3.5Ag0.5Cu alloy. All the other component layer materials remain the same as in the conventional c-Si PV module. Table 3.3 presents the component layer materials and their respective properties

which form the Engineering Data Input into the ANSYS FEM environment. Accumulated creep strain energy density values are calculated and using Eqn. 3.6, fatigue life can be derived.

Table 7.4 presents the Taguchi experiment results for the Silver-Silver combination. Model 1 is identified as the worst design with the minimum SN ratio value of 33.85 dB while Model 22 is the best design with the maximum SN ratio of 47.83 dB.

Applying Eqns. 7.6-7.21, the mean SN ratios for solder, contact and ribbon control factors are calculated and presented in Table 7.5. Mean SN for experiments from Eqn. 7.5, $SN_{exp}$ = 41.305 dB.

Applying Eqns. 7.25-7.31, the contribution of each control factor derived as follows:

$$SS_S = 5((35.41 - 41.305)^2 + (39.28 - 41.305)^2 + (41.72 - 41.305)^2 + (44.20 - 41.305)^2 + (45.91 - 41.305)^2)$$

$$SS_S = 343.05\ (dB)^2$$

$$SS_C = 5((40.89 - 41.305)^2 + (40.97 - 41.305)^2 + (41.89 - 41.305)^2 + (41.60 - 41.305)^2 + (41.17 - 41.305)^2)$$

$$SS_C = 3.66\ (dB)^2$$

$$SS_R = 5((42.34 - 41.305)^2 + (41.64 - 41.305)^2 + (41.02 - 41.305)^2 + (40.79 - 41.305)^2 + (40.73 - 41.305)^2)$$

$$SS_R = 9.30\ (dB)^2$$

$$SS_T = 356.02\ (dB)^2$$

Percentage contribution of solder (S), $= \frac{343.05}{356.02} \times 100$

$$= 96.36\%$$

Percentage contribution of contact (C), $= \frac{3.66}{356.02} \times 100$

$$= 1.03\%$$

Percentage contribution of ribbon (R), $= \frac{9.30}{356.02} \times 100$

$= 2.61\%$

**Table 7.4:** Taguchi experiment results of Silver-Silver Combination

| Model No. | Control Factors | | | Mean Response Parameter | SN Ratio (dB) |
|---|---|---|---|---|---|
| | Solder | Contact | Ribbon | Accumulated Creep Strain Energy Density (Pa) | |
| 1 | $1_{(36)}$ | $1_{(40)}$ | $1_{(180)}$ | 0.020290 | 33.8544 |
| 2 | $1_{(36)}$ | $2_{(45)}$ | $2_{(190)}$ | 0.019797 | 34.0679 |
| 3 | $1_{(36)}$ | $3_{(50)}$ | $3_{(200)}$ | 0.014862 | 36.5587 |
| 4 | $1_{(36)}$ | $4_{(55)}$ | $4_{(210)}$ | 0.015342 | 36.2823 |
| 5 | $1_{(36)}$ | $5_{(60)}$ | $5_{(220)}$ | 0.015296 | 36.3083 |
| 6 | $2_{(41)}$ | $1_{(40)}$ | $2_{(190)}$ | 0.009930 | 40.0609 |
| 7 | $2_{(41)}$ | $2_{(45)}$ | $3_{(200)}$ | 0.011202 | 39.0141 |
| 8 | $2_{(41)}$ | $3_{(50)}$ | $4_{(210)}$ | 0.011890 | 38.4963 |
| 9 | $2_{(41)}$ | $4_{(55)}$ | $5_{(220)}$ | 0.011809 | 38.5560 |
| 10 | $2_{(41)}$ | $5_{(60)}$ | $1_{(180)}$ | 0.009714 | 40.2524 |
| 11 | $3_{(46)}$ | $1_{(40)}$ | $3_{(200)}$ | 0.008080 | 41.8522 |
| 12 | $3_{(46)}$ | $2_{(45)}$ | $4_{(210)}$ | 0.008796 | 41.1144 |
| 13 | $3_{(46)}$ | $3_{(50)}$ | $5_{(220)}$ | 0.009202 | 40.7227 |
| 14 | $3_{(46)}$ | $4_{(55)}$ | $1_{(180)}$ | 0.007096 | 42.9793 |
| 15 | $3_{(46)}$ | $5_{(60)}$ | $2_{(190)}$ | 0.007998 | 41.9407 |
| 16 | $4_{(51)}$ | $1_{(40)}$ | $4_{(210)}$ | 0.006725 | 43.4466 |
| 17 | $4_{(51)}$ | $2_{(45)}$ | $5_{(220)}$ | 0.007238 | 42.8080 |
| 18 | $4_{(51)}$ | $3_{(50)}$ | $1_{(180)}$ | 0.004574 | 46.7933 |
| 19 | $4_{(51)}$ | $4_{(55)}$ | $2_{(190)}$ | 0.005472 | 45.2370 |
| 20 | $4_{(51)}$ | $5_{(60)}$ | $3_{(200)}$ | 0.007302 | 42.7309 |
| 21 | $5_{(56)}$ | $1_{(40)}$ | $5_{(220)}$ | 0.005459 | 45.2583 |
| 22 | $5_{(56)}$ | $2_{(45)}$ | $1_{(180)}$ | 0.004059 | 47.8323 |
| 23 | $5_{(56)}$ | $3_{(50)}$ | $2_{(190)}$ | 0.004518 | 46.9012 |
| 24 | $5_{(56)}$ | $4_{(55)}$ | $3_{(200)}$ | 0.005665 | 44.9357 |
| 25 | $5_{(56)}$ | $5_{(60)}$ | $4_{(210)}$ | 0.005874 | 44.6208 |

With 96.36%, solder layer has the greatest contribution to the response parameter hence it is given the rank 1. Ribbon gets rank 2 and contact gets rank 3.

Figure 7.1 presents the control factors main effects plots. The predicted optimum design points occur when the SN ratio is maximum for each control factor level. This occurs at solder level 5, contact level 3 and ribbon level 1. Applying Eqn. 7.22, the predicted optimum SN ratio,

$$SN_{opt} = 41.305 + (45.91 - 41.305) + (41.89 - 41.305) + (42.34 - 41.305)$$

$$= 47.53\ dB$$

**Table 7.5:** Control factor effects on response parameter for Silver-Silver Combination

| **Control Factor** | **Level** | **SN Ratio (dB)** | **Rank** |
|---|---|---|---|
| Solder (S) | 1 | 35.41 | 1 |
| | 2 | 39.28 | |
| | 3 | 41.72 | |
| | 4 | 44.20 | |
| | 5 | 45.91 | |
| | Delta effect | 10.50 | |
| Contact (C) | 1 | 40.89 | 3 |
| | 2 | 40.97 | |
| | 3 | 41.89 | |
| | 4 | 41.60 | |
| | 5 | 41.17 | |
| | Delta effect | 1.00 | |
| Ribbon (R) | 1 | 42.34 | 2 |
| | 2 | 41.64 | |
| | 3 | 41.02 | |
| | 4 | 40.79 | |
| | 5 | 40.73 | |
| | Delta effect | 1.61 | |

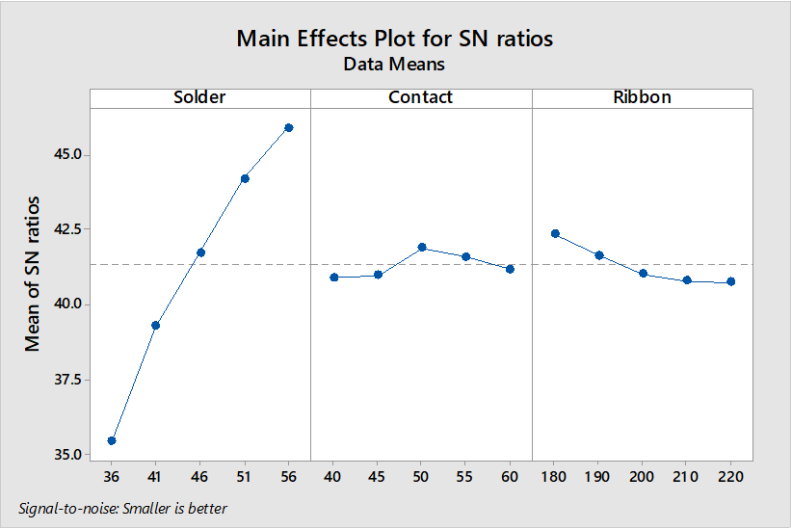


**Figure 7.1:** Control factors main effects plot for Silver-Silver Combination

### 7.3.1 Control factor interactions for Taguchi experiments of Silver-Silver Combination

The interactions between the c-Si PV solder interconnection layers are presented in Figs. 7.2-7.4. The solder layer demonstrates negligible interaction with the contact and ribbon layers. This is evident by no intersections amongst the plot lines in Figs. 7.2 and 7.3 respectively. However, there is a strong interaction between the contact and ribbon layers evident by several plot line interactions in Fig. 7.4.

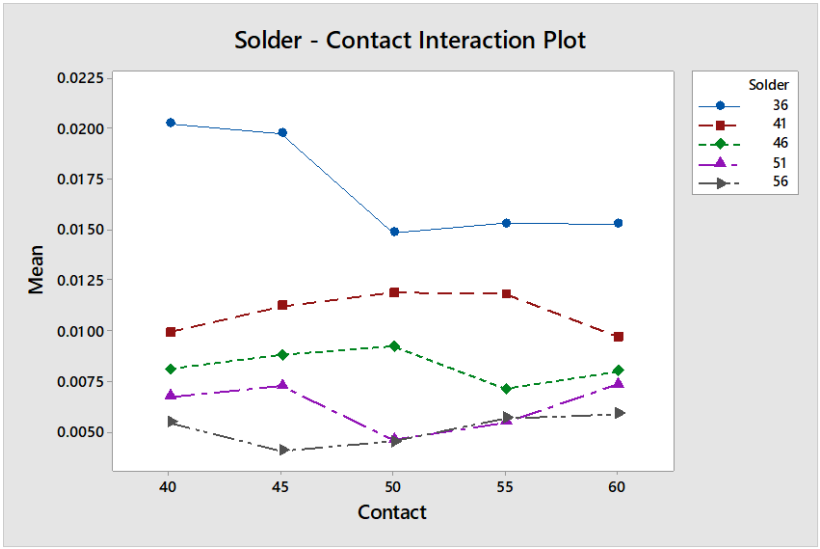


**Figure 7.2:** Solder-Contact interaction plot for Silver-Silver Combination

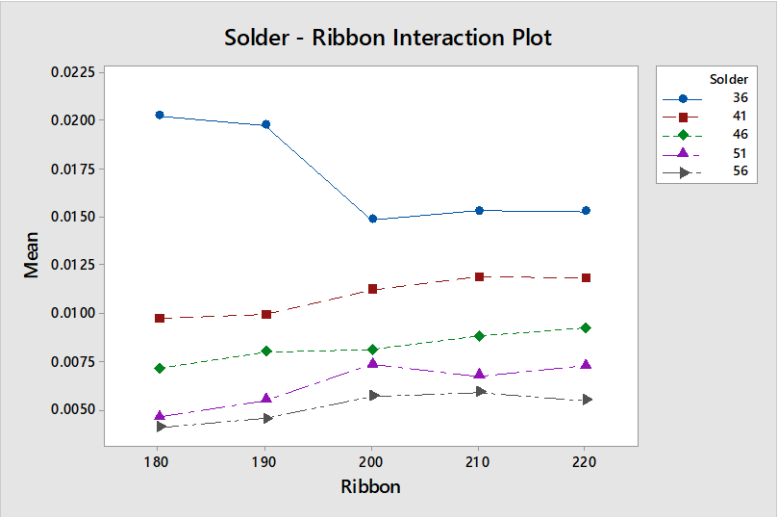


**Figure 7.3:** Solder-Ribbon interaction plot for Silver-Silver Combination

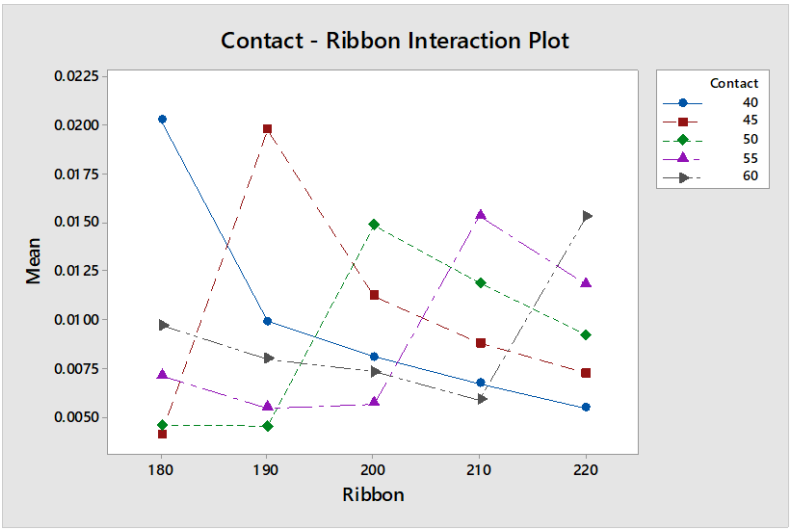


**Figure 7.4:** Contact-Ribbon interaction plot for Silver-Silver Combination

### 7.3.2 Performance comparison for Taguchi experiments of Silver-Silver Combination

Applying modes 1-4 derived in chapter 5, the performance of all twenty-five (25) design models are compared to the conventional c-Si PV solder interconnection (CT) under elevated temperature climate conditions. This performance comparison is presented in Table 7.6. The results show that all 25 design models show improvements over the CT with $N_{d_i} < 1$ and negative $D_i$ values. With fatigue life of 11.39 years, Model 1, which is the worst design outperforms the CT under the elevated temperature operating conditions. Several of the models demonstrated better

fatigue lives than the CT even at STC. The best design, Model 22, reduced solder interconnection degradation by 90.71%.

**Table 7.6:** Performance comparison for Taguchi experiments of Silver-Silver Combination

| **Model No.** | **Accumulated Max. Creep Strain Energy Density (Pa)** | $N_{d_i}$ | $D_i$(%) | **Fatigue Life (years)** | $N_{f_i}$ | $F_i$(%) |
|---|---|---|---|---|---|---|
| 1 | 0.020290 | 0.4643 | -53.57 | 11.39 | 2.16 | 116 |
| 2 | 0.019797 | 0.4530 | -54.70 | 11.67 | 2.21 | 121 |
| 3 | 0.014862 | 0.3401 | -65.99 | 15.55 | 2.94 | 194 |
| 4 | 0.015342 | 0.3511 | -64.89 | 15.06 | 2.85 | 185 |
| 5 | 0.015296 | 0.3500 | -65.00 | 15.10 | 2.86 | 186 |
| 6 | 0.009930 | 0.2272 | -77.28 | 23.27 | 4.41 | 341 |
| 7 | 0.011202 | 0.2563 | -74.37 | 20.62 | 3.91 | 291 |
| 8 | 0.011890 | 0.2721 | -72.79 | 19.43 | 3.68 | 268 |
| 9 | 0.011809 | 0.2702 | -72.98 | 19.56 | 3.71 | 271 |
| 10 | 0.009714 | 0.2223 | -77.77 | 23.78 | 4.50 | 350 |
| 11 | 0.008080 | 0.1849 | -81.51 | 28.59 | 5.42 | 442 |
| 12 | 0.008796 | 0.2013 | -79.87 | 26.27 | 4.97 | 397 |
| 13 | 0.009202 | 0.2106 | -78.94 | 25.11 | 4.76 | 376 |
| 14 | 0.007096 | 0.1624 | -83.76 | 32.56 | 6.17 | 517 |
| 15 | 0.007998 | 0.1830 | -81.70 | 28.89 | 5.47 | 447 |
| 16 | 0.006725 | 0.1539 | -84.61 | 34.36 | 6.51 | 551 |
| 17 | 0.007238 | 0.1656 | -83.44 | 31.92 | 6.05 | 505 |
| 18 | 0.004574 | 0.1047 | -89.53 | 50.50 | 9.57 | 857 |
| 19 | 0.005472 | 0.1252 | -87.48 | 42.22 | 8.00 | 700 |
| 20 | 0.007302 | 0.1671 | -83.29 | 31.64 | 5.99 | 499 |
| 21 | 0.005459 | 0.1249 | -87.51 | 42.32 | 8.02 | 702 |
| 22 | 0.004059 | 0.0929 | -90.71 | 56.92 | 10.78 | 978 |
| 23 | 0.004518 | 0.1034 | -89.66 | 51.14 | 9.68 | 868 |
| 24 | 0.005665 | 0.1296 | -87.04 | 40.78 | 7.72 | 672 |
| 25 | 0.005874 | 0.1344 | -86.56 | 39.33 | 7.45 | 645 |

### 7.3.3 Optimal design verification for Taguchi experiments of Silver-Silver Combination

The predicted optimum design points occur at solder level 5, contact level 3 and ribbon level 1. A c-Si PV solder interconnection model is designed at these optimum level settings and verification experiments are carried out. The SN ratio of the optimal design from the verification results is 49.69 dB. Comparing this verified optimal design to the predicted optimum of 47.53 dB, there is a good correlation of 95.66%.

Table 7.7 and Fig. 7.5 present the performance comparison of the worst, best and optimal designs of the Silver-Silver material combination. The optimal design is a significant improvement on the conventional c-Si PV module under elevated temperature conditions. The optimal design reduced solder interconnection degradation by 92.5%. Figures 7.6, 7.8 and 7.10 show the creep strain energy, equivalent stress and equivalent strain of the Silver-Silver material combination best design in the ANSYS FEM environment respectively while Figures 7.7, 7.9 and 7.11 show those of the optimal design. The optimal design performs better than the best design and demonstrates lower degradation.

**Table 7.7:** Performance comparison of worst, best and optimal designs of the Silver-Silver Combination

| **Taguchi Design** | **Accumulated Max. Creep Strain Energy Density (E-04 Pa)** | **Fatigue Life (E+03 Cycles)** | **Fatigue Life (years)** |
|---|---|---|---|
| Worst Design | 203 | 35 | 11.4 |
| Best Design | 41 | 176 | 56.9 |
| Optimal Design | 33 | 218 | 70.5 |

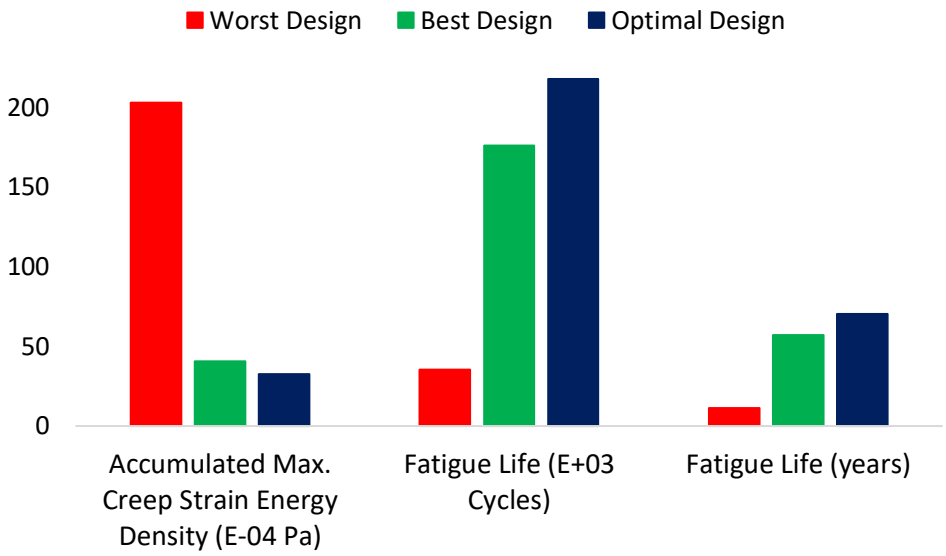


**Figure 7.5:** Performance comparison of worst, best and optimal designs of the Silver-Silver combination

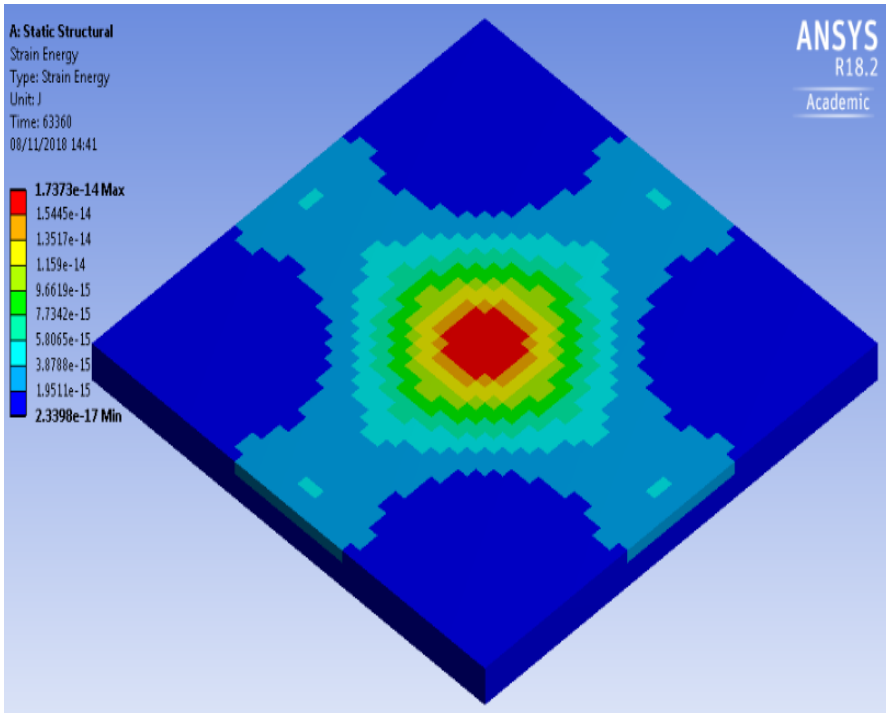


**Figure 7.6:** Creep strain energy of Silver-Silver combination best design

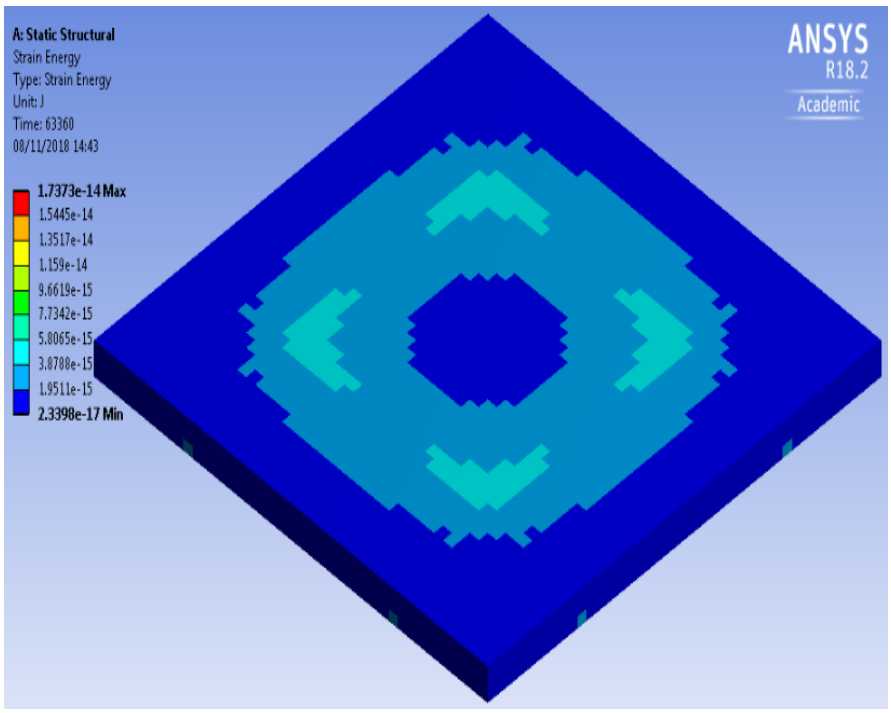


**Figure 7.7:** Creep strain energy of Silver-Silver combination optimal design

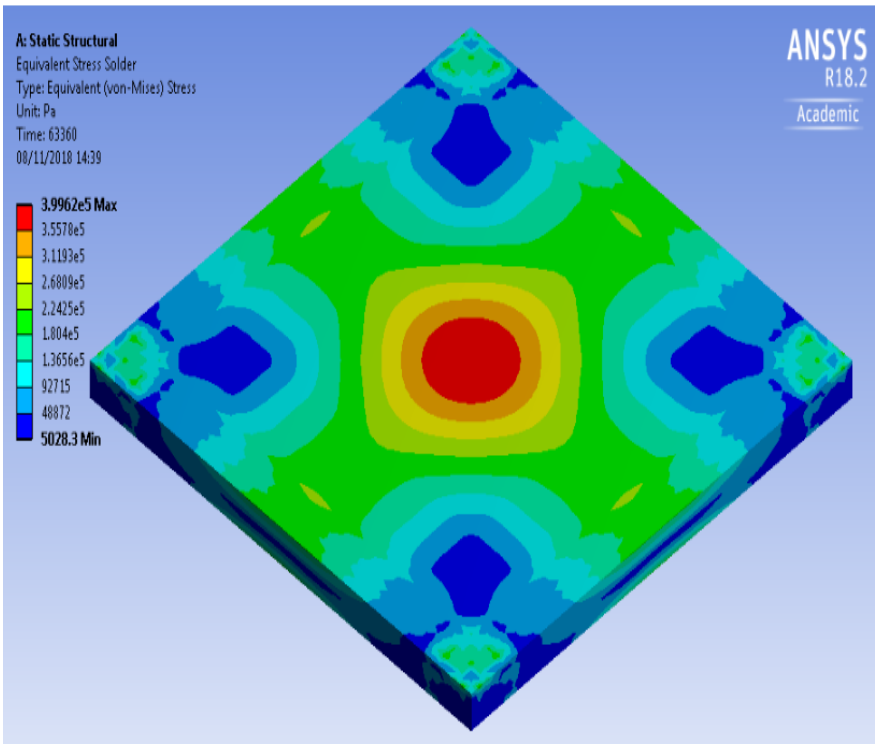


**Figure 7.8:** Equivalent stress of Silver-Silver combination best design

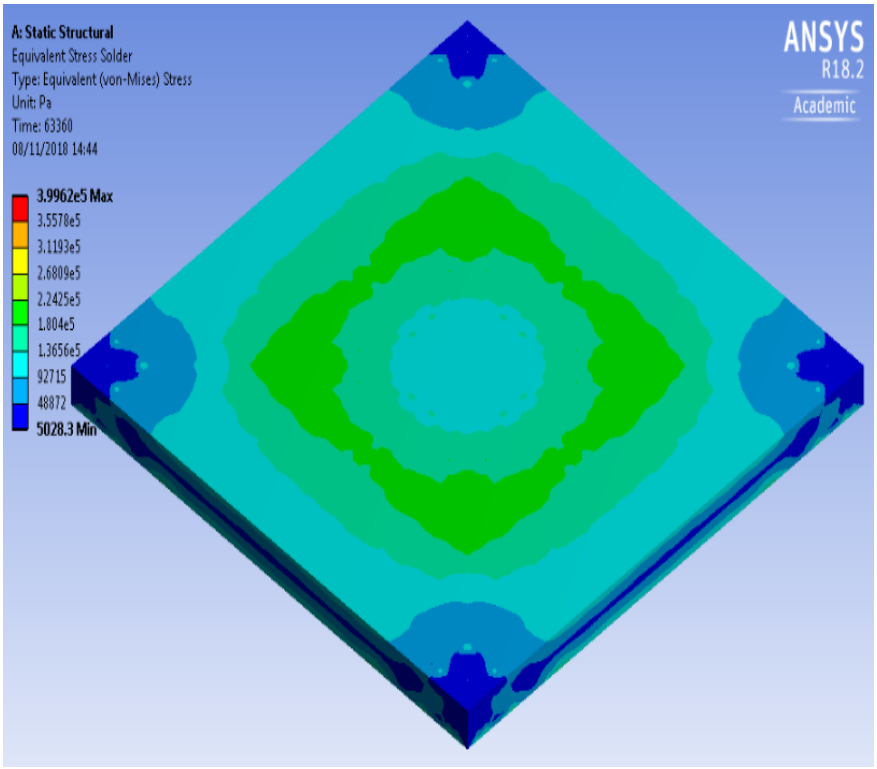


**Figure 7.9:** Equivalent stress of Silver-Silver combination optimal design

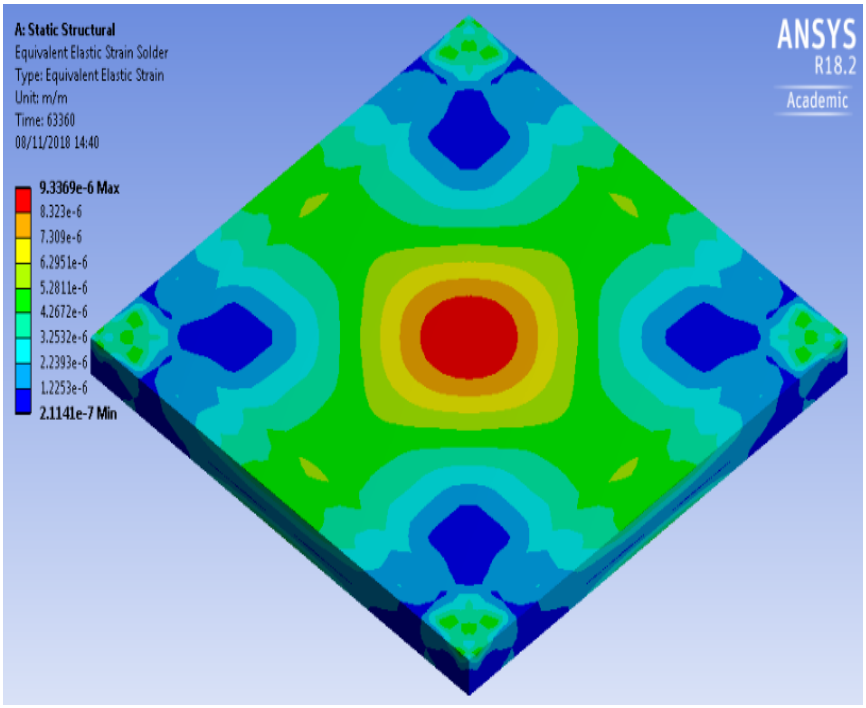


**Figure 7.10:** Equivalent strain of Silver-Silver combination best design

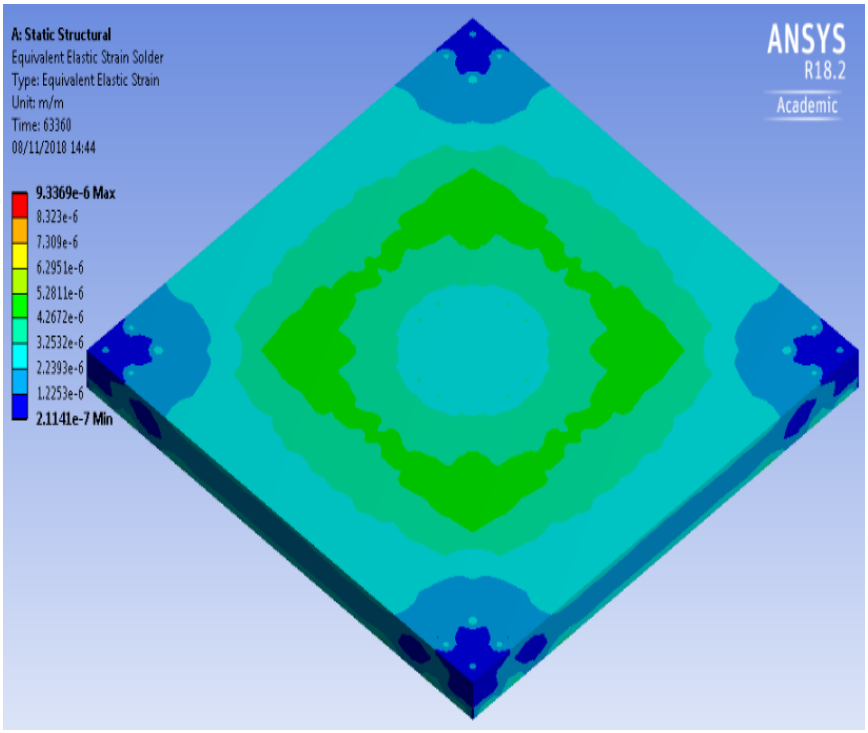


**Figure 7.11:** Equivalent strain of Silver-Silver combination optimal design

## 7.4 TAGUCHI DESIGN FOR ALUMINIUM-ALUMINIUM COMBINATION

Each c-Si PV solder interconnection model is designed such that both the ribbon and contact layers are Aluminium material while the solder layer is the Sn3.5Ag0.5Cu alloy. All the other component layer materials remain the same as in the conventional c-Si PV module. Table 3.3 presents the component layer materials and their respective properties which form the Engineering Data Input into the ANSYS FEM environment. Accumulated creep strain energy density values are calculated and using Eqn. 3.6, fatigue life can be derived. The results from the Taguchi L25 experiments for the Aluminium-Aluminium material combination is presented in Table 7.8. The best design is Model 22 with the maximum SN ratio of 50.02 dB while the worst design is Model 2 with the minimum SN ration of 35.66 dB.

**Table 7.8:** Taguchi experiment results of Aluminium-Aluminium Combination

| Model No. | Control Factors | | | Mean Response Parameter | SN Ratio (dB) |
|---|---|---|---|---|---|
| | Solder | Contact | Ribbon | Accumulated Creep Strain Energy Density (Pa) | |
| 1 | $1_{(36)}$ | $1_{(40)}$ | $1_{(180)}$ | 0.014279 | 36.9059 |
| 2 | $1_{(36)}$ | $2_{(45)}$ | $2_{(190)}$ | 0.016488 | 35.6567 |
| 3 | $1_{(36)}$ | $3_{(50)}$ | $3_{(200)}$ | 0.010882 | 39.2655 |
| 4 | $1_{(36)}$ | $4_{(55)}$ | $4_{(210)}$ | 0.012334 | 38.1777 |
| 5 | $1_{(36)}$ | $5_{(60)}$ | $5_{(220)}$ | 0.011501 | 38.7850 |
| 6 | $2_{(41)}$ | $1_{(40)}$ | $2_{(190)}$ | 0.008050 | 41.8845 |
| 7 | $2_{(41)}$ | $2_{(45)}$ | $3_{(200)}$ | 0.007680 | 42.2922 |
| 8 | $2_{(41)}$ | $3_{(50)}$ | $4_{(210)}$ | 0.008696 | 41.2137 |
| 9 | $2_{(41)}$ | $4_{(55)}$ | $5_{(220)}$ | 0.008382 | 41.5328 |
| 10 | $2_{(41)}$ | $5_{(60)}$ | $1_{(180)}$ | 0.008444 | 41.4695 |
| 11 | $3_{(46)}$ | $1_{(40)}$ | $3_{(200)}$ | 0.005649 | 44.9611 |
| 12 | $3_{(46)}$ | $2_{(45)}$ | $4_{(210)}$ | 0.006123 | 44.2601 |
| 13 | $3_{(46)}$ | $3_{(50)}$ | $5_{(220)}$ | 0.006809 | 43.3379 |
| 14 | $3_{(46)}$ | $4_{(55)}$ | $1_{(180)}$ | 0.005608 | 45.0236 |
| 15 | $3_{(46)}$ | $5_{(60)}$ | $2_{(190)}$ | 0.006019 | 44.4102 |
| 16 | $4_{(51)}$ | $1_{(40)}$ | $4_{(210)}$ | 0.005392 | 45.3655 |
| 17 | $4_{(51)}$ | $2_{(45)}$ | $5_{(220)}$ | 0.005776 | 44.7677 |
| 18 | $4_{(51)}$ | $3_{(50)}$ | $1_{(180)}$ | 0.003911 | 48.1533 |
| 19 | $4_{(51)}$ | $4_{(55)}$ | $2_{(190)}$ | 0.004348 | 47.2344 |
| 20 | $4_{(51)}$ | $5_{(60)}$ | $3_{(200)}$ | 0.005107 | 45.8361 |
| 21 | $5_{(56)}$ | $1_{(40)}$ | $5_{(220)}$ | 0.004279 | 47.3728 |
| 22 | $5_{(56)}$ | $2_{(45)}$ | $1_{(180)}$ | 0.003156 | 50.0170 |
| 23 | $5_{(56)}$ | $3_{(50)}$ | $2_{(190)}$ | 0.003449 | 49.2459 |
| 24 | $5_{(56)}$ | $4_{(55)}$ | $3_{(200)}$ | 0.003988 | 47.9850 |
| 25 | $5_{(56)}$ | $5_{(60)}$ | $4_{(210)}$ | 0.003862 | 48.2641 |

The mean SN ratios for the control factors are derived using Eqns. 7.6-7.21 and presented in Table 7.9. The mean SN for the experiments, $SN_{exp}$ = 43.737 dB.

Applying Eqns. 7.25-7.31, the contribution of each control factor derived as follows:

$$SS_S = 5((37.76 - 43.737)^2 + (41.68 - 43.737)^2 + (44.40 - 43.737)^2 + (46.27 - 43.737)^2 + (48.58 - 43.737)^2)$$

$$SS_S = 351.33\ (dB)^2$$

$$SS_C = 5((43.30 - 43.737)^2 + (43.40 - 43.737)^2 + (44.24 - 43.737)^2 + (43.99 - 43.737)^2 + (43.75 - 43.737)^2)$$

$$SS_C = 3.11\ (dB)^2$$

$$SS_R = 5((44.31 - 43.737)^2 + (43.69 - 43.737)^2 + (44.07 - 43.737)^2 + (43.46 - 43.737)^2 + (43.16 - 43.737)^2)$$

$$SS_R = 4.26\ (dB)^2$$

$$SS_T = 358.69\ (dB)^2$$

Percentage contribution of solder (S), $= \frac{351.33}{358.69} \times 100$

$$= 97.95\%$$

Percentage contribution of contact (C), $= \frac{3.11}{358.69} \times 100$

$$= 0.87\%$$

Percentage contribution of ribbon (R), $= \frac{4.26}{358.69} \times 100$

$$= 1.19\%$$

Solder layer has the greatest contribution of 97.95% and it is given the rank 1. Ribbon gets rank 2 and contact gets rank 3.

Figure 7.12 presents the control factors main effects plots. The predicted optimum design points occur where the SN ratio is maximum for each control factor level.

This occurs at solder level 5, contact level 3 and ribbon level 1. Applying Eqn. 7.22, the predicted optimal SN ratio,

$$SN_{opt} = 43.737 + (48.58 - 43.737) + (44.24 - 43.737) + (44.31 - 43.737)$$

$$= 49.66\ dB$$

**Table 7.9:** Control factor effects on response parameter for Aluminium-Aluminium Combination

| **Control Factor** | **Level** | **SN Ratio (dB)** | **Rank** |
|---|---|---|---|
| Solder (S) | 1 | 37.76 | 1 |
| | 2 | 41.68 | |
| | 3 | 44.40 | |
| | 4 | 46.27 | |
| | 5 | 48.58 | |
| | Delta effect | 10.82 | |
| Contact (C) | 1 | 43.30 | 3 |
| | 2 | 43.40 | |
| | 3 | 44.24 | |
| | 4 | 43.99 | |
| | 5 | 43.75 | |
| | Delta effect | 0.95 | |
| Ribbon (R) | 1 | 44.31 | 2 |
| | 2 | 43.69 | |
| | 3 | 44.07 | |
| | 4 | 43.46 | |
| | 5 | 43.16 | |
| | Delta effect | 1.15 | |

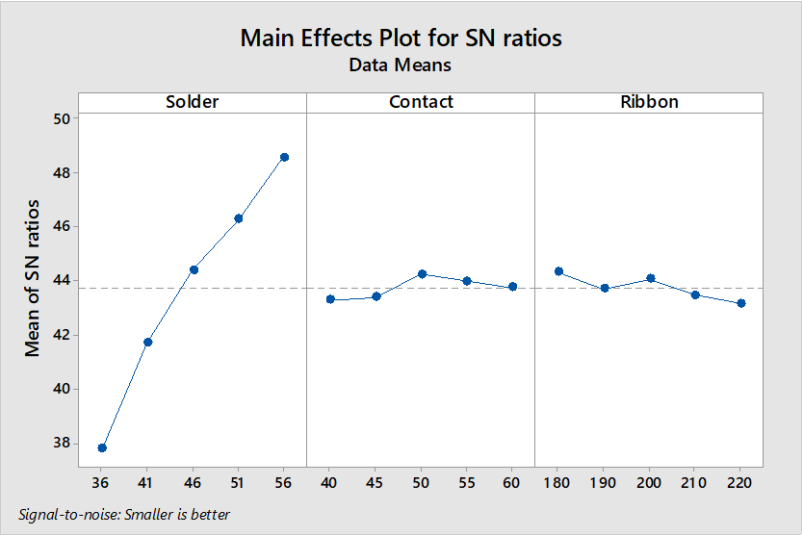


**Figure 7.12:** Control factors main effects plot for Aluminium-Aluminium Combination

### 7.4.1 Control factor interactions for Taguchi experiments of Aluminium-Aluminium Combination

The interactions between the solder and contact component layers can be assumed to be negligible. This is because there are no plot line intersections as seen in Fig. 7.13. The same case of no interactions is observed between the solder and ribbon layers as seen in Fig. 7.14. In Fig. 7.15, a strong interaction is observed between the contact and ribbon layers evident by several plot line interactions.

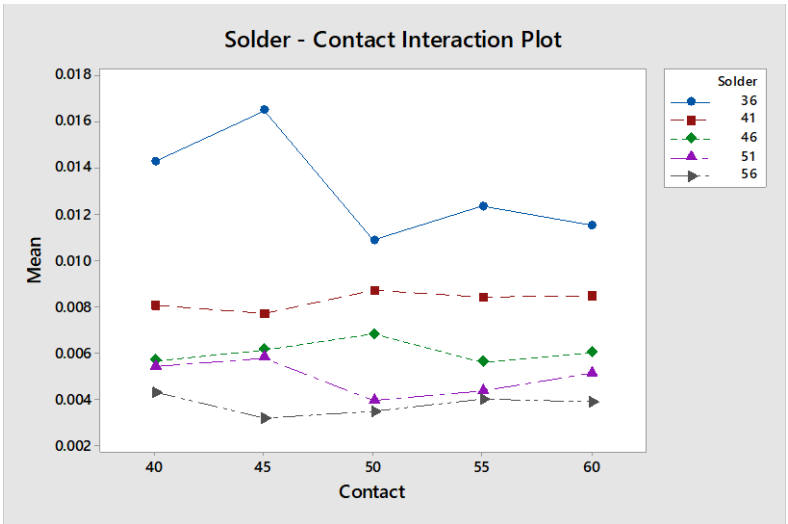


**Figure 7.13:** Solder-Contact interaction plot for Aluminium-Aluminium Combination

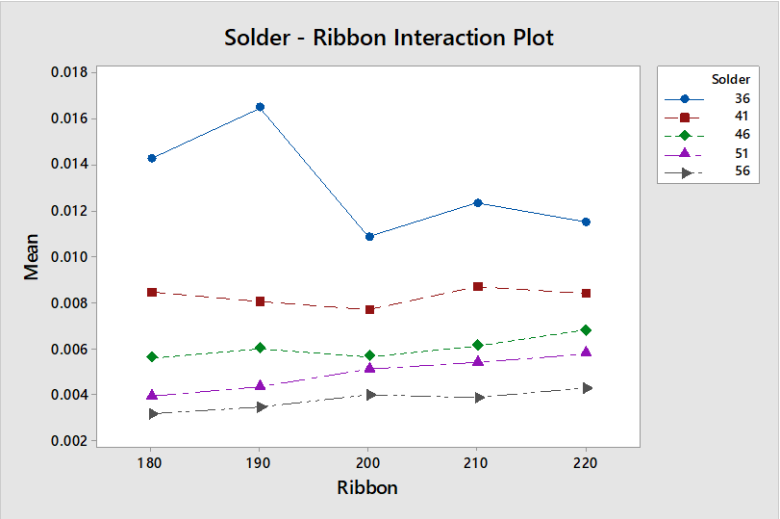


**Figure 7.14:** Solder-Ribbon interaction plot for Aluminium-Aluminium Combination

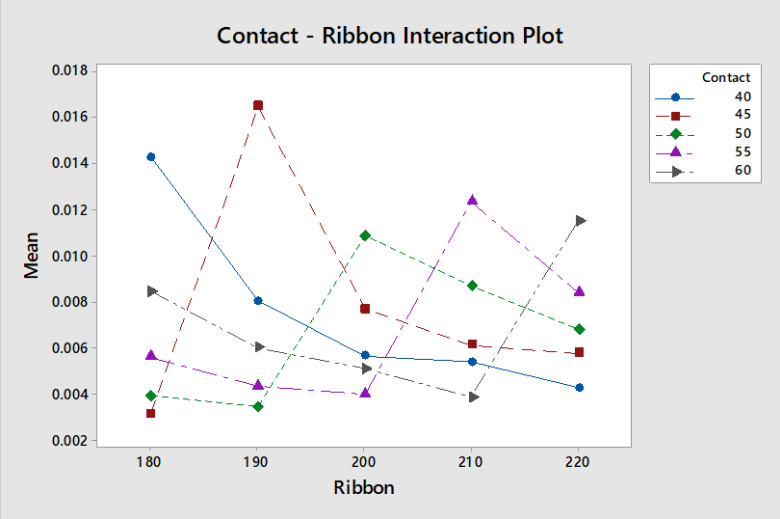


**Figure 7.15:** Contact-Ribbon interaction plot for Aluminium-Aluminium Combination

### 7.4.2 Performance comparison for Taguchi experiments of Aluminium-Aluminium Combination

The performance of all twenty-five (25) design models are compared to the conventional c-Si PV solder interconnection (CT) under elevated temperature climate conditions. This is done by applying modes 1-4 derived in chapter 5. This performance comparison is presented in Table 7.10. The results show that all 25 design models show improvements over the CT with $N_{d_i} < 1$ and negative $D_i$ values.

**Table 7.10:** Performance comparison for Taguchi experiments of Aluminium-Aluminium Combination

| **Model No.** | **Accumulated Max. Creep Strain Energy Density (Pa)** | $N_{d_i}$ | $D_i$(%) | **Fatigue Life (years)** | $N_{f_i}$ | $F_i$(%) |
|---|---|---|---|---|---|---|
| 1 | 0.014279 | 0.3268 | -67.32 | 16.18 | 3.06 | 206 |
| 2 | 0.016488 | 0.3773 | -62.27 | 14.01 | 2.65 | 165 |
| 3 | 0.010882 | 0.2490 | -75.10 | 21.23 | 4.02 | 302 |
| 4 | 0.012334 | 0.2822 | -71.78 | 18.73 | 3.55 | 255 |
| 5 | 0.011501 | 0.2632 | -73.68 | 20.09 | 3.80 | 280 |
| 6 | 0.008050 | 0.1842 | -81.58 | 28.70 | 5.44 | 444 |
| 7 | 0.007680 | 0.1758 | -82.42 | 30.08 | 5.70 | 470 |
| 8 | 0.008696 | 0.1990 | -80.10 | 26.57 | 5.03 | 403 |
| 9 | 0.008382 | 0.1918 | -80.82 | 27.56 | 5.22 | 422 |
| 10 | 0.008444 | 0.1932 | -80.68 | 27.36 | 5.18 | 418 |
| 11 | 0.005649 | 0.1293 | -87.07 | 40.90 | 7.75 | 675 |
| 12 | 0.006123 | 0.1401 | -85.99 | 37.73 | 7.15 | 615 |
| 13 | 0.006809 | 0.1558 | -84.42 | 33.93 | 6.43 | 543 |
| 14 | 0.005608 | 0.1283 | -87.17 | 41.20 | 7.80 | 680 |
| 15 | 0.006019 | 0.1377 | -86.23 | 38.39 | 7.27 | 627 |
| 16 | 0.005392 | 0.1234 | -87.66 | 42.85 | 8.12 | 712 |
| 17 | 0.005776 | 0.1322 | -86.78 | 40.00 | 7.58 | 658 |
| 18 | 0.003911 | 0.0895 | -91.05 | 59.06 | 11.19 | 1019 |
| 19 | 0.004348 | 0.0995 | -90.05 | 53.14 | 10.06 | 906 |
| 20 | 0.005107 | 0.1169 | -88.31 | 45.23 | 8.57 | 757 |
| 21 | 0.004279 | 0.0979 | -90.21 | 53.99 | 10.23 | 923 |
| 22 | 0.003156 | 0.0722 | -92.78 | 73.20 | 13.86 | 1286 |
| 23 | 0.003449 | 0.0789 | -92.11 | 66.98 | 12.69 | 1169 |
| 24 | 0.003988 | 0.0913 | -90.87 | 57.93 | 10.97 | 997 |
| 25 | 0.003862 | 0.0884 | -91.16 | 59.82 | 11.33 | 1033 |

The worst design, Model 2, outperforms the CT under the elevated temperature operating conditions with fatigue life of 14.01 years. Over 20 of the models demonstrated better fatigue lives than the CT even at STC. The best design, Model 22, reduced solder interconnection degradation by 92.11%.

### 7.4.3 Optimal design verification for Taguchi experiments of Aluminium-Aluminium Combination

As seen in Fig. 7.12, the predicted optimum design points occur at solder level 5, contact level 3 and ribbon level 1. The c-Si PV solder interconnection model designed at these optimum level settings is tested and compared with the predicted optimum design in verification experiments. The SN ratio of the optimal design from the verification results is 51.77 dB. Comparing this verified optimal design to the predicted optimum of 49.66 dB, there is a good correlation of 95.91%.

The performance comparison of the worst, best and optimal designs of the Aluminium-Aluminium material combination is presented in Table 7.11 and Fig. 7.16. The optimal design is a significant improvement on the conventional c-Si PV module under elevated temperature conditions. The optimal design reduced solder interconnection degradation by 94.1%. The creep strain energy, equivalent stress and equivalent strain of the Aluminium-Aluminium material combination best design in the ANSYS FEM environment are presented in Figs. 7.17, 7.19 and 7.21 respectively while parameters of the optimal design are presented in Figs. 7.18, 7.20 and 7.22. The highest degradation levels are represented by red on the coloured key while lowest degradation is royal blue. The optimal design performs better than the best design and demonstrates lower degradation.

**Table 7.11:** Performance comparison of worst, best and optimal designs of the Aluminium-Aluminium Combination

| Taguchi Design | Accumulated Max. Creep Strain Energy Density (E-04 Pa) | Fatigue Life (E+03 Cycles) | Fatigue Life (years) |
|---|---|---|---|
| Worst Design | 165 | 43 | 14.0 |
| Best Design | 32 | 226 | 73.2 |
| Optimal Design | 26 | 277 | 89.6 |

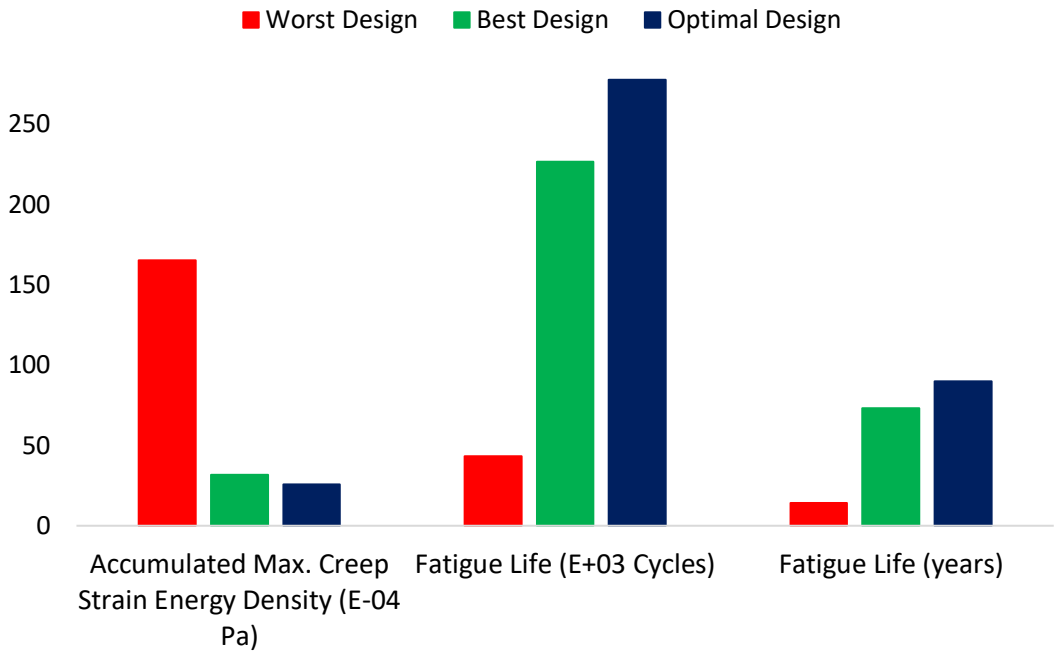


**Figure 7.16:** Performance comparison of worst, best and optimal designs of the Aluminium-Aluminium Combination

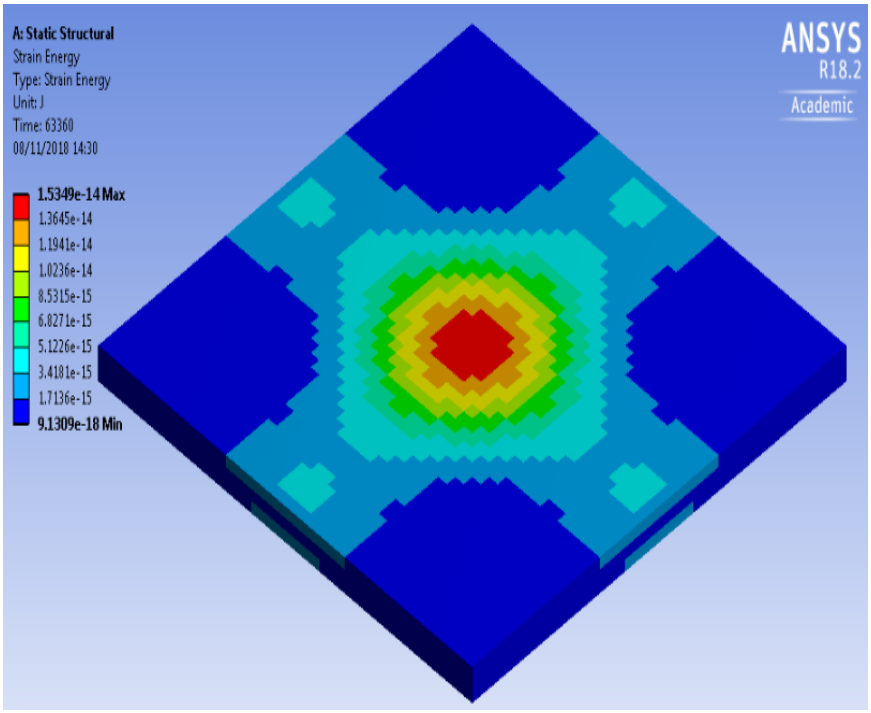


**Figure 7.17:** Creep strain energy of Aluminium-Aluminium combination best design

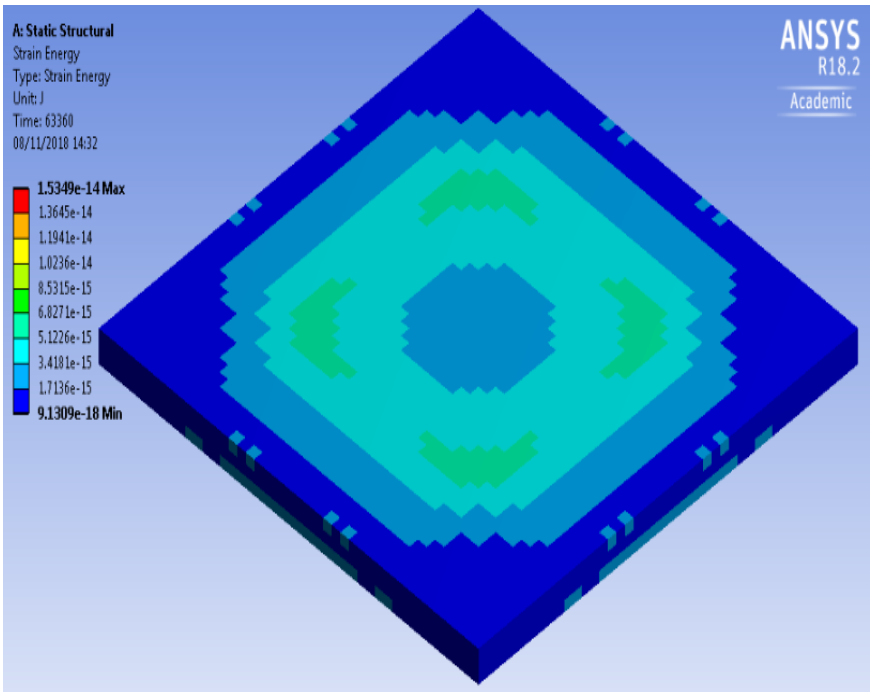


**Figure 7.18:** Creep strain energy of Aluminium-Aluminium combination optimal design

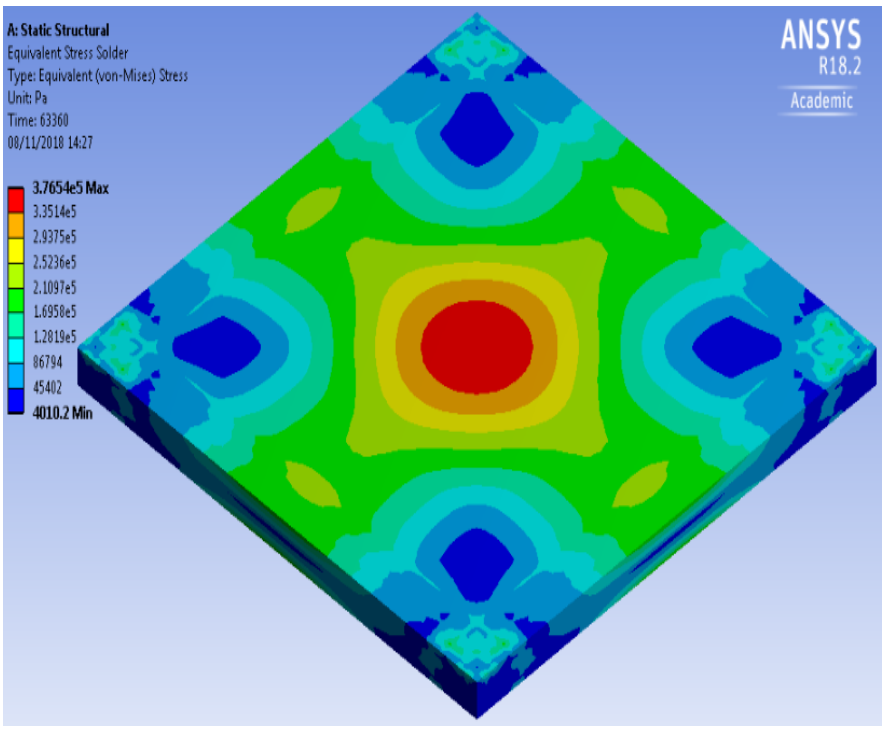


**Figure 7.19:** Equivalent stress of Aluminium-Aluminium combination best design

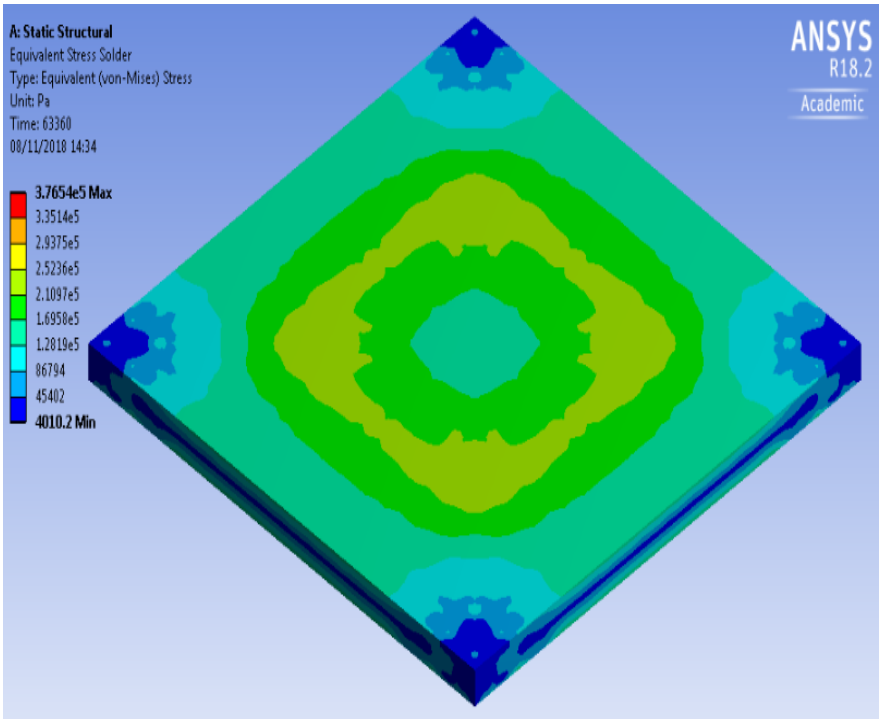


**Figure 7.20:** Equivalent stress of Aluminium-Aluminium combination optimal design

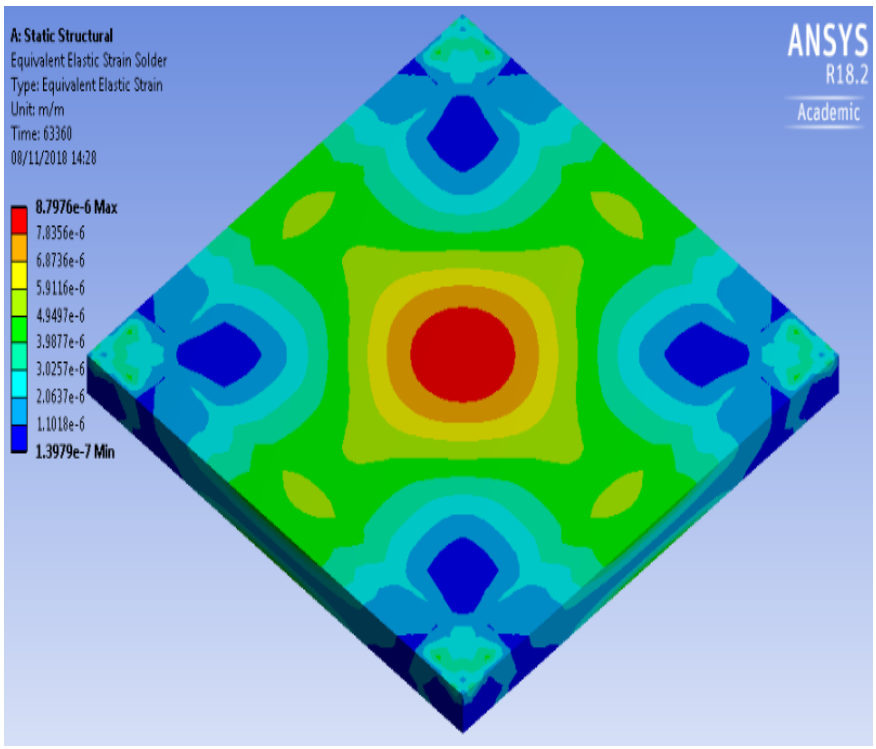


**Figure 7.21:** Equivalent strain of Aluminium-Aluminium combination best design

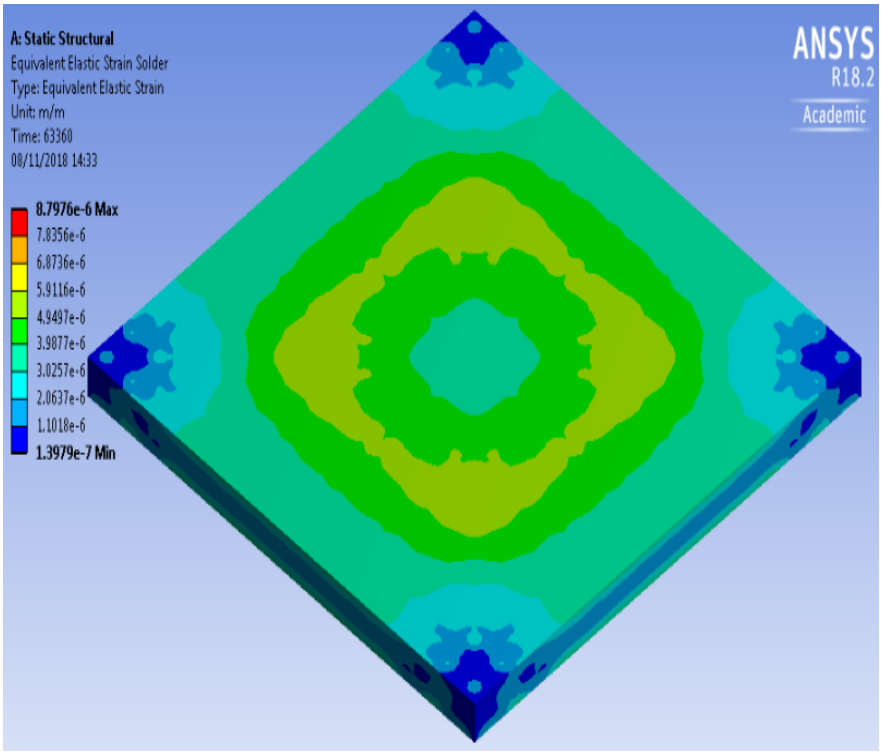


**Figure 7.22:** Equivalent strain of Aluminium-Aluminium combination optimal design

## 7.5 TAGUCHI DESIGN FOR SILVER-ALUMINIUM COMBINATION

For this set of Taguchi L25 orthogonal array experiments, each c-Si PV solder interconnection model is designed such that the ribbon layer is Silver material, the contact layer is Aluminium material and the solder layer is the Sn3.5Ag0.5Cu alloy. All the other component layer materials remain the same as in the conventional c-Si PV module. Table 3.3 presents the component layer materials and their respective properties which form the Engineering Data Input into the ANSYS FEM environment. Accumulated creep strain energy density values are calculated and using Eqn. 3.6, fatigue life can be derived.

Table 7.12 presents the Taguchi experiment results for the Silver-Aluminium material combination. Model 1 is the worst design with the minimum SN ratio value of 34.36 dB while Model 22 is the best design with the maximum SN ratio of 47.51 dB. The mean SN ratios for solder, contact and ribbon control factors are calculated and presented in Table 7.13. Mean SN for experiments, $SN_{exp}$ = 40.909 dB. The contribution of each control factor is derived as follows:

$$SS_S = 5((35.38 - 40.909)^2 + (38.93 - 40.909)^2 + (41.28 - 40.909)^2 + (43.52 - 40.909)^2 + (45.44 - 40.909)^2)$$

$$SS_S = 309.86\ (dB)^2$$

$$SS_C = 5((40.36 - 40.909)^2 + (40.63 - 40.909)^2 + (41.05 - 40.909)^2 + (41.36 - 40.909)^2 + (41.15 - 40.909)^2)$$

$$SS_C = 3.30\ (dB)^2$$

$$SS_R = 5((42.21 - 40.909)^2 + (41.45 - 40.909)^2 + (40.61 - 40.909)^2 + (40.11 - 40.909)^2 + (40.17 - 40.909)^2)$$

$$SS_R = 16.30\ (dB)^2$$

$$SS_T = 329.46\ (dB)^2$$

**Table 7.12:** Taguchi experiment results of Silver-Aluminium Combination

| Model No. | Control Factors | | | Mean Response Parameter | SN Ratio (dB) |
|---|---|---|---|---|---|
| | Solder | Contact | Ribbon | Accumulated Creep Strain Energy Density (Pa) | |
| 1 | $1_{(36)}$ | $1_{(40)}$ | $1_{(180)}$ | 0.019144 | 34.3596 |
| 2 | $1_{(36)}$ | $2_{(45)}$ | $2_{(190)}$ | 0.017922 | 34.9324 |
| 3 | $1_{(36)}$ | $3_{(50)}$ | $3_{(200)}$ | 0.016157 | 35.8328 |
| 4 | $1_{(36)}$ | $4_{(55)}$ | $4_{(210)}$ | 0.016761 | 35.5142 |
| 5 | $1_{(36)}$ | $5_{(60)}$ | $5_{(220)}$ | 0.015400 | 36.2495 |
| 6 | $2_{(41)}$ | $1_{(40)}$ | $2_{(190)}$ | 0.010605 | 39.4901 |
| 7 | $2_{(41)}$ | $2_{(45)}$ | $3_{(200)}$ | 0.011935 | 38.4638 |
| 8 | $2_{(41)}$ | $3_{(50)}$ | $4_{(210)}$ | 0.012867 | 37.8101 |
| 9 | $2_{(41)}$ | $4_{(55)}$ | $5_{(220)}$ | 0.011910 | 38.4819 |
| 10 | $2_{(41)}$ | $5_{(60)}$ | $1_{(180)}$ | 0.009553 | 40.3970 |
| 11 | $3_{(46)}$ | $1_{(40)}$ | $3_{(200)}$ | 0.008729 | 41.1803 |
| 12 | $3_{(46)}$ | $2_{(45)}$ | $4_{(210)}$ | 0.009610 | 40.3452 |
| 13 | $3_{(46)}$ | $3_{(50)}$ | $5_{(220)}$ | 0.010143 | 39.8763 |
| 14 | $3_{(46)}$ | $4_{(55)}$ | $1_{(180)}$ | 0.007020 | 43.0733 |
| 15 | $3_{(46)}$ | $5_{(60)}$ | $2_{(190)}$ | 0.008023 | 41.9135 |
| 16 | $4_{(51)}$ | $1_{(40)}$ | $4_{(210)}$ | 0.007563 | 42.4260 |
| 17 | $4_{(51)}$ | $2_{(45)}$ | $5_{(220)}$ | 0.008039 | 41.8960 |
| 18 | $4_{(51)}$ | $3_{(50)}$ | $1_{(180)}$ | 0.005190 | 45.6970 |
| 19 | $4_{(51)}$ | $4_{(55)}$ | $2_{(190)}$ | 0.005703 | 44.8776 |
| 20 | $4_{(51)}$ | $5_{(60)}$ | $3_{(200)}$ | 0.007327 | 42.7014 |
| 21 | $5_{(56)}$ | $1_{(40)}$ | $5_{(220)}$ | 0.006075 | 44.3284 |
| 22 | $5_{(56)}$ | $2_{(45)}$ | $1_{(180)}$ | 0.004212 | 47.5102 |
| 23 | $5_{(56)}$ | $3_{(50)}$ | $2_{(190)}$ | 0.004995 | 46.0287 |
| 24 | $5_{(56)}$ | $4_{(55)}$ | $3_{(200)}$ | 0.005711 | 44.8655 |
| 25 | $5_{(56)}$ | $5_{(60)}$ | $4_{(210)}$ | 0.005979 | 44.4677 |

Percentage contribution of solder (S), $= \frac{309.86}{329.46} \times 100$

$= 94.05\%$

Percentage contribution of contact (C), $= \frac{3.30}{329.46} \times 100$

$= 1.00\%$

Percentage contribution of ribbon (R), $= \frac{16.30}{329.46} \times 100$

$= 4.95\%$

**Table 7.13:** Control factor effects on response parameter for Silver-Aluminium Combination

| **Control Factor** | **Level** | **SN Ratio (dB)** | **Rank** |
|---|---|---|---|
| Solder (S) | 1 | 35.38 | 1 |
| | 2 | 38.93 | |
| | 3 | 41.28 | |
| | 4 | 43.52 | |
| | 5 | 45.44 | |
| | Delta effect | 10.06 | |
| Contact (C) | 1 | 40.36 | 3 |
| | 2 | 40.63 | |
| | 3 | 41.05 | |
| | 4 | 41.36 | |
| | 5 | 41.15 | |
| | Delta effect | 1.01 | |
| Ribbon (R) | 1 | 42.21 | 2 |
| | 2 | 41.45 | |
| | 3 | 40.61 | |
| | 4 | 40.11 | |
| | 5 | 40.17 | |
| | Delta effect | 2.09 | |

With 94.05%, the solder layer demonstrates the greatest contribution to the response parameter hence it is given the rank 1. Ribbon gets rank 2 and contact gets rank 3.

Figure 7.23 presents the control factors main effects plots for the Silver-Aluminium material combination. The predicted optimum design points occur at solder level 5, contact level 4 and ribbon level 1. Applying Eqn. 7.22, the predicted optimal SN ratio,

$$SN_{opt} = 40.909 + (45.44 - 40.909) + (41.36 - 40.909) + (42.21 - 40.909)$$

$$= 47.19\ dB$$

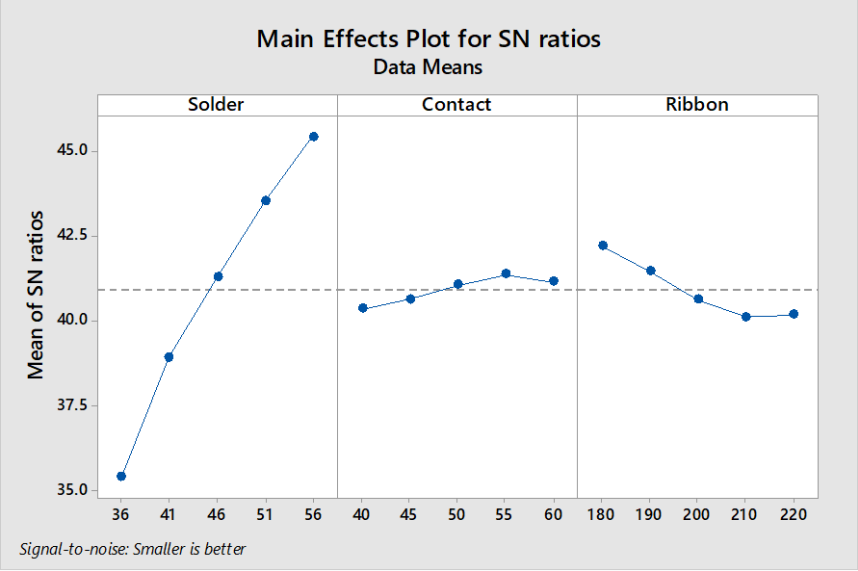


**Figure 7.23:** Control factors main effects plot for Silver-Aluminium Combination

### 7.5.1 Control factor interactions for Taguchi experiments of Silver-Aluminium Combination

With no clear plot lines intersections, the solder-contact and solder-ribbon interactions are assumed to be negligible. This is shown in Figs. 7.24 and 7.25 respectively. However, there is a strong interaction between the contact and ribbon layers evident by several plot line interactions in Fig. 7.26.

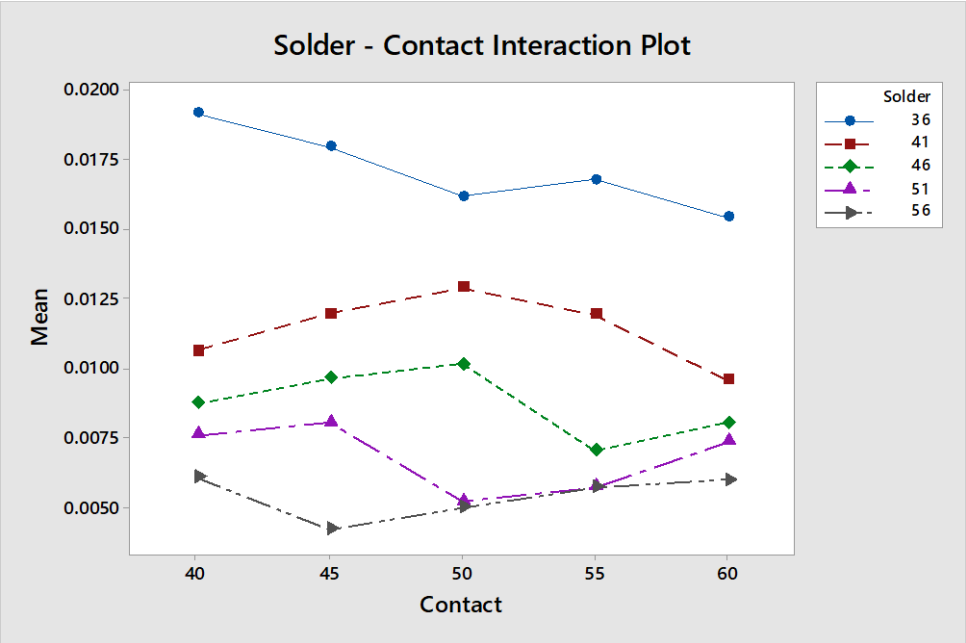


**Figure 7.24:** Solder-Contact interaction plot for Silver-Aluminium Combination

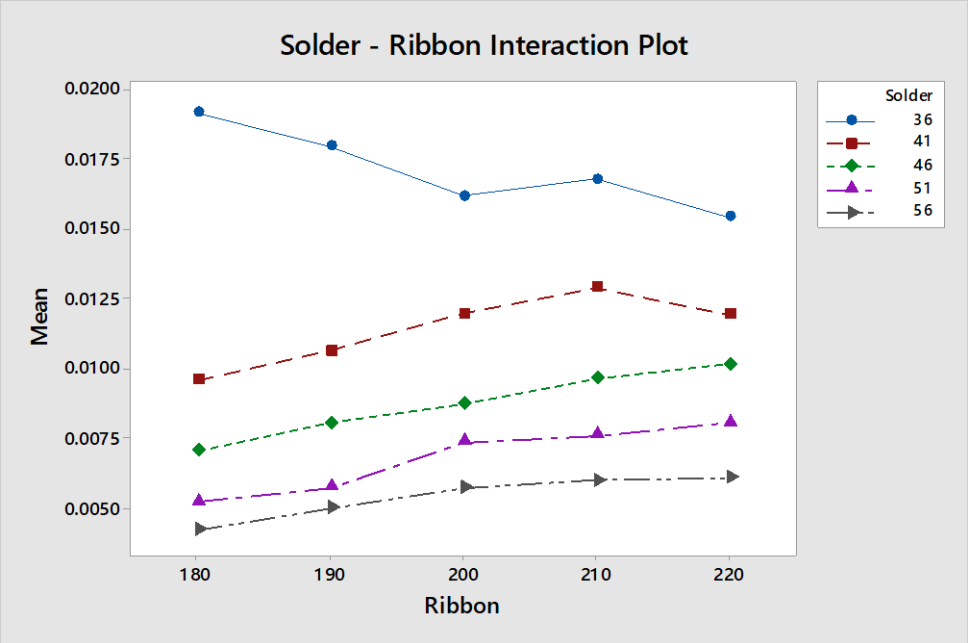


**Figure 7.25:** Solder-Ribbon interaction plot for Silver-Aluminium Combination

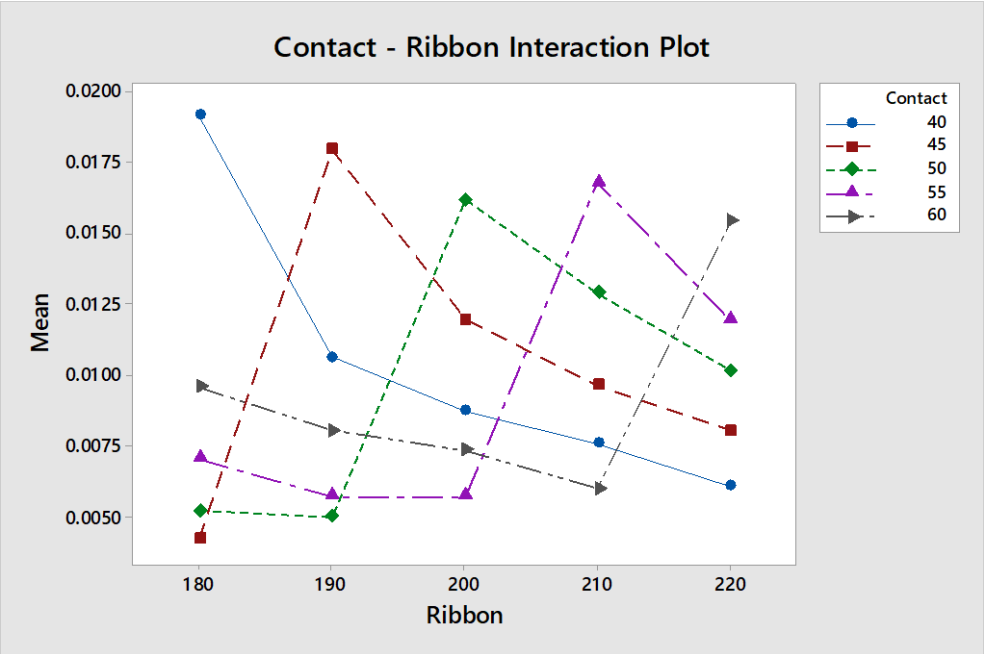


**Figure 7.26:** Contact-Ribbon interaction plot for Silver-Aluminium Combination

### 7.5.2 Performance comparison for Taguchi experiments of Silver-Aluminium Combination

Modes 1-4 derived in chapter 5 are applied for the performance comparison of all twenty-five (25) design models to the conventional c-Si PV solder interconnection (CT) under elevated temperature climate conditions. This performance comparison is presented in Table 7.14.

All 25 design models show improvements over the CT with $N_{d_i} < 1$ and negative $D_i$ values. With fatigue life of 12.07 years, the worst design (Model 1) outperforms the CT under the elevated temperature operating conditions. Several Models demonstrated better fatigue lives than the CT even at STC. The best design, Model 22, reduced solder interconnection degradation by 90.36%.

**Table 7.14:** Performance comparison for Taguchi experiments of Silver-Aluminium Combination

| Model No. | Accumulated Max. Creep Strain Energy Density (Pa) | $N_{d_i}$ | $D_i$(%) | Fatigue Life (years) | $N_{f_i}$ | $F_i$(%) |
|---|---|---|---|---|---|---|
| 1 | 0.019144 | 0.4381 | -56.19 | 12.07 | 2.29 | 129 |
| 2 | 0.017922 | 0.4101 | -58.99 | 12.89 | 2.44 | 144 |
| 3 | 0.016157 | 0.3697 | -63.03 | 14.30 | 2.71 | 171 |
| 4 | 0.016761 | 0.3835 | -61.65 | 13.78 | 2.61 | 161 |
| 5 | 0.015400 | 0.3524 | -64.76 | 15.00 | 2.84 | 184 |
| 6 | 0.010605 | 0.2427 | -75.73 | 21.79 | 4.13 | 313 |
| 7 | 0.011935 | 0.2731 | -72.69 | 19.36 | 3.67 | 267 |
| 8 | 0.012867 | 0.2945 | -70.55 | 17.95 | 3.40 | 240 |
| 9 | 0.011910 | 0.2725 | -72.75 | 19.40 | 3.67 | 267 |
| 10 | 0.009553 | 0.2186 | -78.14 | 24.18 | 4.58 | 358 |
| 11 | 0.008729 | 0.1998 | -80.02 | 26.47 | 5.01 | 401 |
| 12 | 0.009610 | 0.2199 | -78.01 | 24.04 | 4.55 | 355 |
| 13 | 0.010143 | 0.2321 | -76.79 | 22.78 | 4.31 | 331 |
| 14 | 0.007020 | 0.1606 | -83.94 | 32.91 | 6.23 | 523 |
| 15 | 0.008023 | 0.1836 | -81.64 | 28.80 | 5.45 | 445 |
| 16 | 0.007563 | 0.1731 | -82.69 | 30.55 | 5.79 | 479 |
| 17 | 0.008039 | 0.1840 | -81.60 | 28.74 | 5.44 | 444 |
| 18 | 0.005190 | 0.1188 | -88.12 | 44.52 | 8.43 | 743 |
| 19 | 0.005703 | 0.1305 | -86.95 | 40.51 | 7.67 | 667 |
| 20 | 0.007327 | 0.1677 | -83.23 | 31.53 | 5.97 | 497 |
| 21 | 0.006075 | 0.1390 | -86.10 | 38.03 | 7.20 | 620 |
| 22 | 0.004212 | 0.0964 | -90.36 | 54.85 | 10.39 | 939 |
| 23 | 0.004995 | 0.1143 | -88.57 | 46.25 | 8.76 | 776 |
| 24 | 0.005711 | 0.1307 | -86.93 | 40.45 | 7.66 | 666 |
| 25 | 0.005979 | 0.1368 | -86.32 | 38.64 | 7.32 | 632 |

### 7.5.3 Optimal design verification for Taguchi experiments of Silver-Aluminium Combination

The predicted optimum design points occur at solder level 5, contact level 4 and ribbon level 1. To perform the verification experiments, a c-Si PV solder interconnection model is designed at these optimum level settings. The SN ratio of the optimal design from the verification results is 48.52 dB. Comparing this verified optimal design to the predicted optimum of 47.19 dB, there is a good correlation of 97.26%.

Table 7.15 and Fig. 7.27 present the performance comparison of the worst, best and optimal designs of the Silver-Aluminium material combination. The optimal design is a significant improvement on the conventional c-Si PV module under elevated temperature conditions. The optimal design reduced solder interconnection degradation by 91.42%. Figures 7.28, 7.30 and 7.32 show the creep strain energy, equivalent stress and equivalent strain of the Silver-Aluminium material combination best design in the ANSYS FEM environment respectively while Figs. 7.29, 7.31 and 7.33 show the optimal design. The optimal design performs better than the best design and demonstrates lower degradation. On the coloured key, red signifies highest degradation levels while lowest degradation is royal blue.

**Table 7.15:** Performance comparison of worst, best and optimal designs of the Silver-Aluminium Combination

| **Taguchi Design** | **Accumulated Max. Creep Strain Energy Density (E-04 Pa)** | **Fatigue Life (E+03 Cycles)** | **Fatigue Life (years)** |
|---|---|---|---|
| Worst Design | 191 | 37 | 12.1 |
| Best Design | 42 | 170 | 54.8 |
| Optimal Design | 37 | 190 | 61.6 |

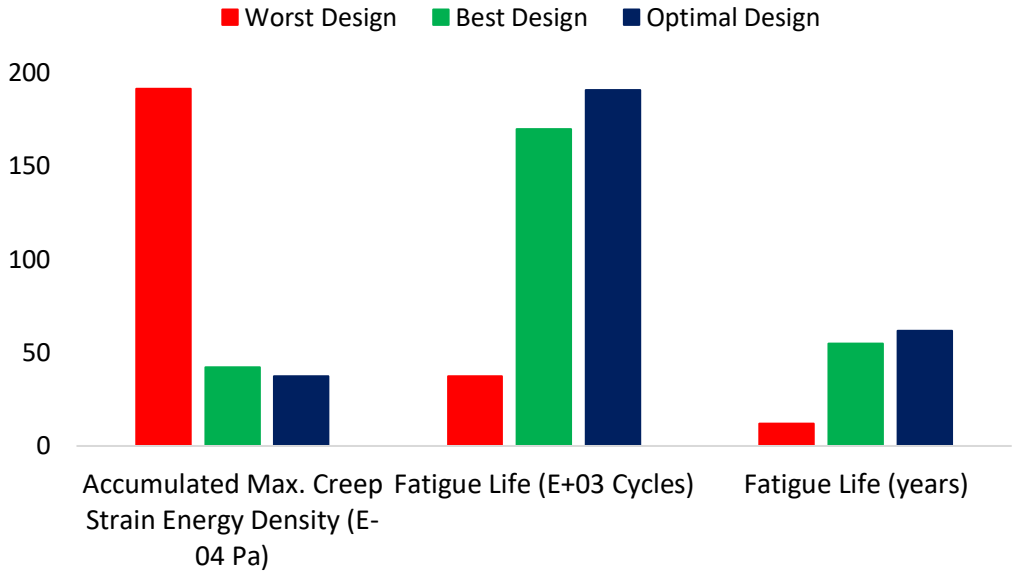


**Figure 7.27:** Performance comparison of worst, best and optimal designs of the Silver-Aluminium combination

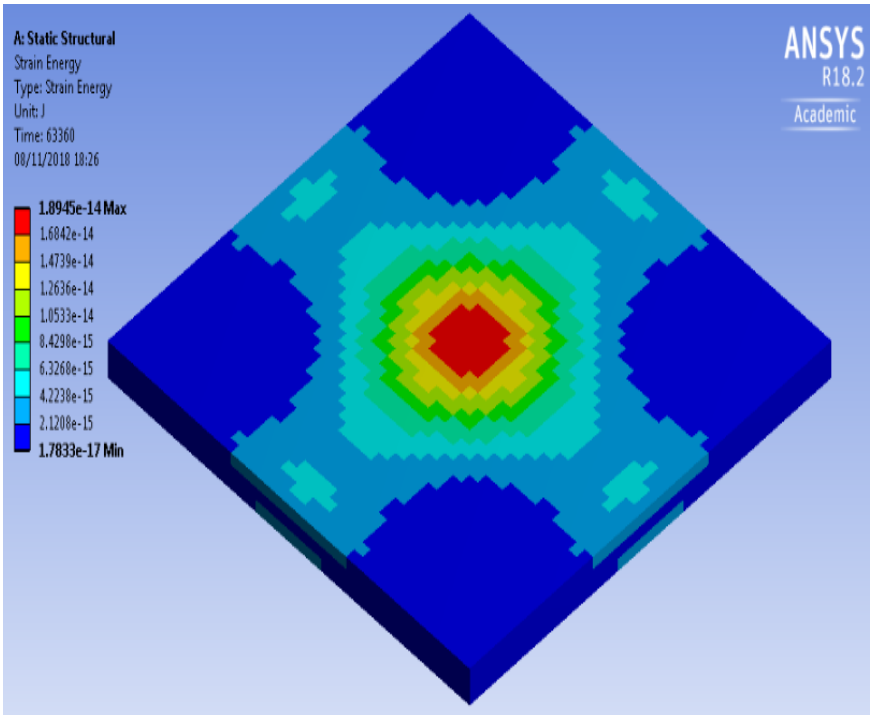


**Figure 7.28:** Creep strain energy of Silver-Aluminium combination best design

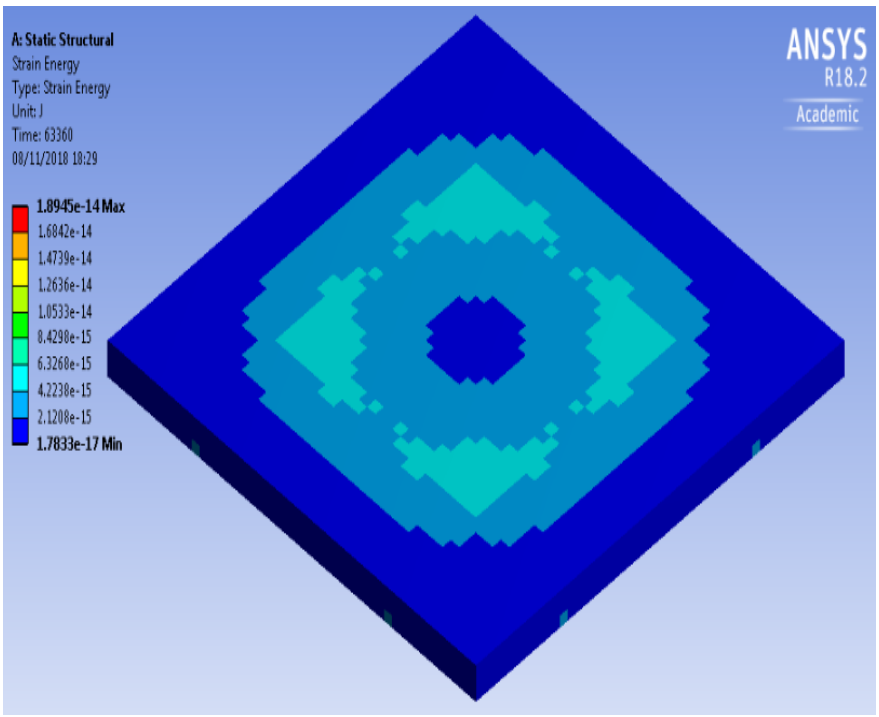


**Figure 7.29:** Creep strain energy of Silver-Aluminium combination optimal design

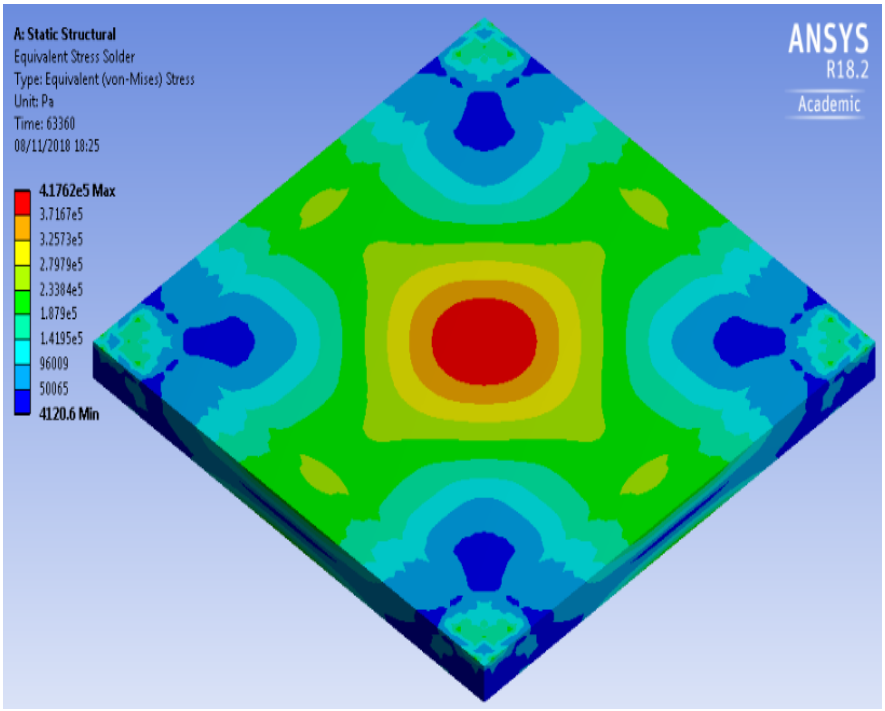


**Figure 7.30:** Equivalent stress of Silver-Aluminium combination best design

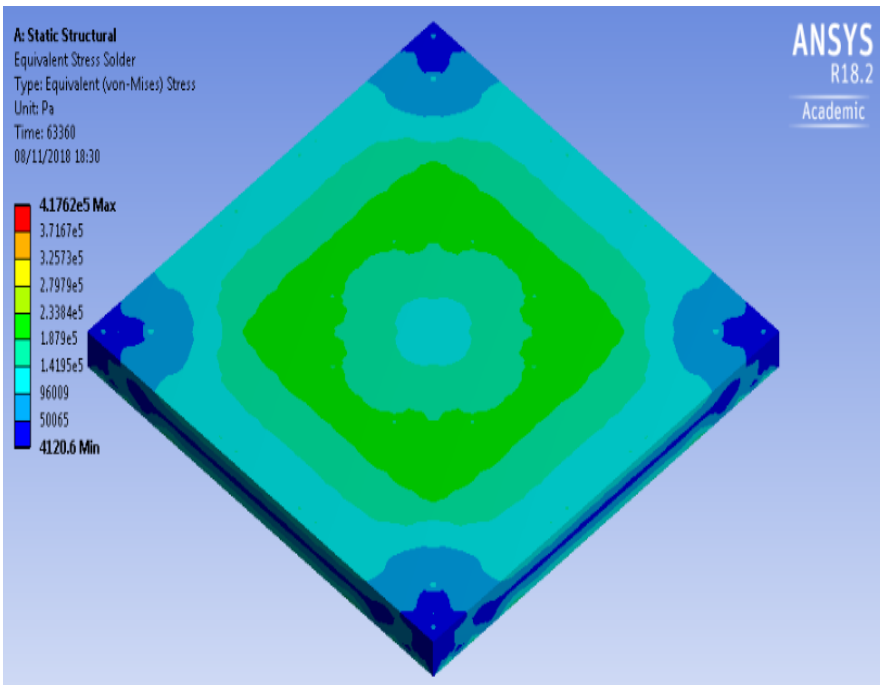


**Figure 7.31:** Equivalent stress of Silver-Aluminium combination optimal design

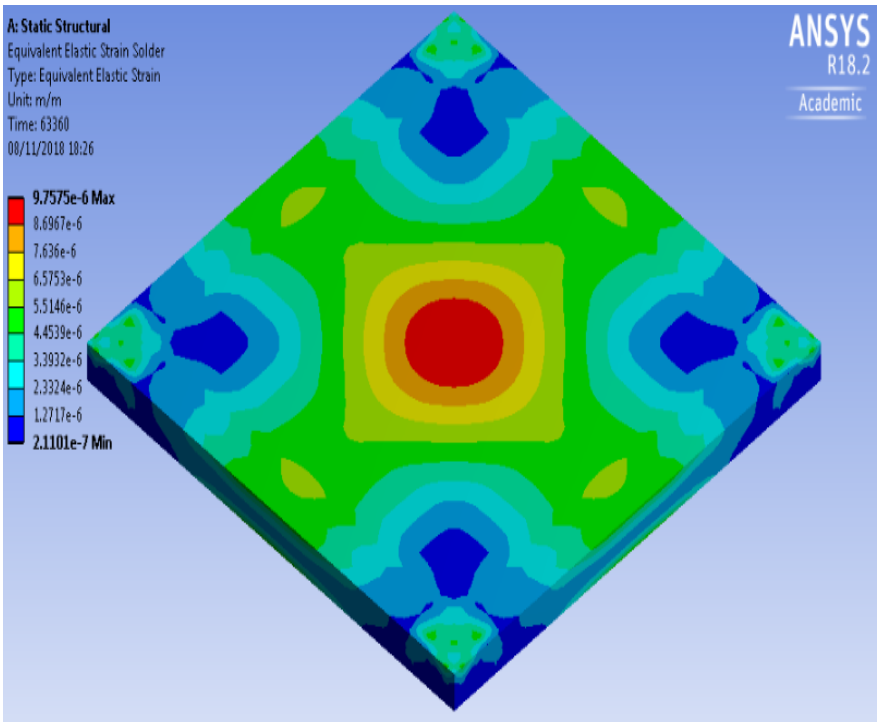


**Figure 7.32:** Equivalent strain of Silver-Aluminium combination best design

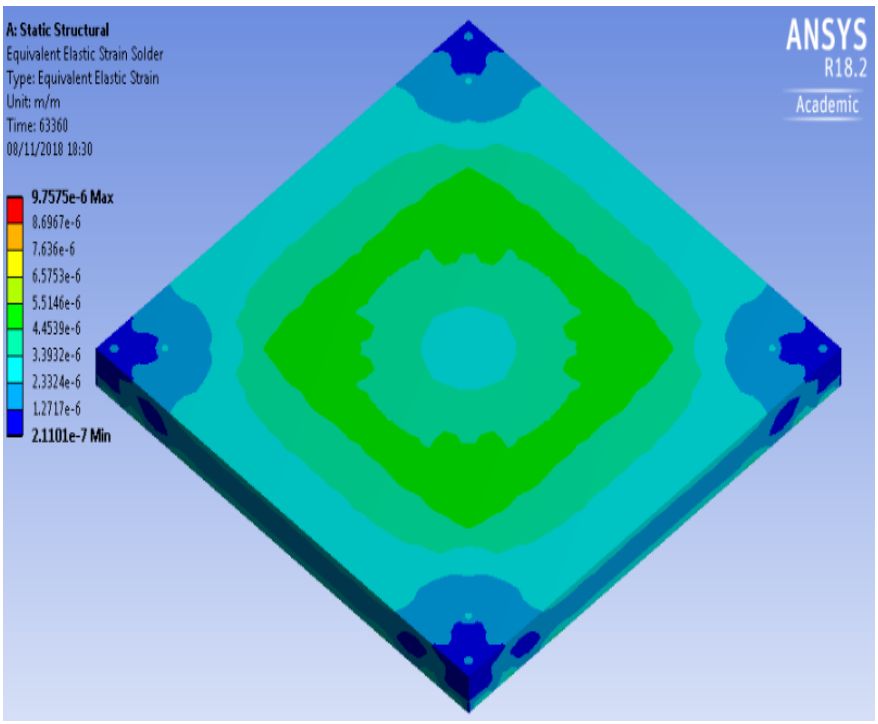


**Figure 7.33:** Equivalent strain of Silver-Aluminium combination optimal design

## 7.6 TAGUCHI DESIGN FOR ALUMINIUM-SILVER COMBINATION

The twenty-five (25) c-Si PV solder interconnection models used for this set of investigations are designed with Aluminium ribbon, Silver contact and Sn3.5Ag0.5Cu solder alloy. All the other component layer materials remain the same as in the conventional c-Si PV module. Table 3.3 presents the component layer materials and their respective properties which form the Engineering Data Input into the ANSYS FEM environment. Accumulated creep strain energy density values are calculated and using Eqn. 3.6, fatigue life can be derived.

Table 7.16 presents the Taguchi L25 robust experiment results for the Aluminium-Silver combination. Model 2 and Model 22 are identified as the worst and best designs with minimum SN ratio value of 34.90 dB and maximum SN ratio of 52.74 dB respectively.

**Table 7.16:** Taguchi experiment results of Aluminium-Silver Combination

| Model No. | Control Factors | | | Mean Response Parameter | SN Ratio (dB) |
|---|---|---|---|---|---|
| | Solder | Contact | Ribbon | Accumulated Creep Strain Energy Density (Pa) | |
| 1 | $1_{(36)}$ | $1_{(40)}$ | $1_{(180)}$ | 0.016163 | 35.8296 |
| 2 | $1_{(36)}$ | $2_{(45)}$ | $2_{(190)}$ | 0.017996 | 34.8966 |
| 3 | $1_{(36)}$ | $3_{(50)}$ | $3_{(200)}$ | 0.010259 | 39.7781 |
| 4 | $1_{(36)}$ | $4_{(55)}$ | $4_{(210)}$ | 0.011451 | 38.8228 |
| 5 | $1_{(36)}$ | $5_{(60)}$ | $5_{(220)}$ | 0.011696 | 38.6391 |
| 6 | $2_{(41)}$ | $1_{(40)}$ | $2_{(190)}$ | 0.007466 | 42.5383 |
| 7 | $2_{(41)}$ | $2_{(45)}$ | $3_{(200)}$ | 0.007159 | 42.9028 |
| 8 | $2_{(41)}$ | $3_{(50)}$ | $4_{(210)}$ | 0.008031 | 41.9046 |
| 9 | $2_{(41)}$ | $4_{(55)}$ | $5_{(220)}$ | 0.008504 | 41.4079 |
| 10 | $2_{(41)}$ | $5_{(60)}$ | $1_{(180)}$ | 0.008599 | 41.3115 |
| 11 | $3_{(46)}$ | $1_{(40)}$ | $3_{(200)}$ | 0.005168 | 45.7337 |
| 12 | $3_{(46)}$ | $2_{(45)}$ | $4_{(210)}$ | 0.005517 | 45.1660 |
| 13 | $3_{(46)}$ | $3_{(50)}$ | $5_{(220)}$ | 0.006172 | 44.1908 |
| 14 | $3_{(46)}$ | $4_{(55)}$ | $1_{(180)}$ | 0.005656 | 44.9503 |
| 15 | $3_{(46)}$ | $5_{(60)}$ | $2_{(190)}$ | 0.005946 | 44.5162 |
| 16 | $4_{(51)}$ | $1_{(40)}$ | $4_{(210)}$ | 0.004773 | 46.4242 |
| 17 | $4_{(51)}$ | $2_{(45)}$ | $5_{(220)}$ | 0.005198 | 45.6825 |
| 18 | $4_{(51)}$ | $3_{(50)}$ | $1_{(180)}$ | 0.003516 | 49.0802 |
| 19 | $4_{(51)}$ | $4_{(55)}$ | $2_{(190)}$ | 0.004545 | 46.8496 |
| 20 | $4_{(51)}$ | $5_{(60)}$ | $3_{(200)}$ | 0.005210 | 45.6637 |
| 21 | $5_{(56)}$ | $1_{(40)}$ | $5_{(220)}$ | 0.003820 | 48.3579 |
| 22 | $5_{(56)}$ | $2_{(45)}$ | $1_{(180)}$ | 0.002308 | 52.7354 |
| 23 | $5_{(56)}$ | $3_{(50)}$ | $2_{(190)}$ | 0.003147 | 50.0418 |
| 24 | $5_{(56)}$ | $4_{(55)}$ | $3_{(200)}$ | 0.004003 | 47.9525 |
| 25 | $5_{(56)}$ | $5_{(60)}$ | $4_{(210)}$ | 0.003808 | 48.3856 |

The mean SN ratios for the control factors are calculated and presented in Table 7.17. Mean SN for experiments from Eqn. 7.5, $SN_{exp}$ = 44.151 dB. The contribution of each control factor derived as follows:

$$SS_S = 5((37.59 - 44.151)^2 + (42.01 - 44.151)^2 + (44.91 - 44.151)^2 + (46.74 - 44.151)^2 + (49.49 - 44.151)^2)$$

$$SS_S = 417.07\ (dB)^2$$

$$SS_C = 5((43.78 - 44.151)^2 + (44.28 - 44.151)^2 + (45.00 - 44.151)^2 + (44.00 - 44.151)^2 + (43.70 - 44.151)^2)$$

$$SS_C = 5.51\ (dB)^2$$

$$SS_R = 5((44.78 - 44.151)^2 + (43.77 - 44.151)^2 + (44.41 - 44.151)^2 + (44.14 - 44.151)^2 + (43.66 - 44.151)^2)$$

$$SS_R = 4.25\ (dB)^2$$

$$SS_T = 426.82\ (dB)^2$$

Percentage contribution of solder (S), $= \frac{417.07}{426.82} \times 100$

$$= 97.72\%$$

Percentage contribution of contact (C), $= \frac{5.51}{426.82} \times 100$

$$= 1.29\%$$

Percentage contribution of ribbon (R), $= \frac{4.25}{426.82} \times 100$

$$= 0.99\%$$

Solder layer has the greatest contribution to the response parameter hence it is given the rank 1 while contact and ribbon layers are ranked 2 and 3 respectively.

**Table 7.17:** Control factor effects on response parameter for Aluminium-Silver Combination

| Control Factor | Level | SN Ratio (dB) | Rank |
|---|---|---|---|
| Solder (S) | 1 | 37.59 | 1 |
| | 2 | 42.01 | |
| | 3 | 44.91 | |
| | 4 | 46.74 | |
| | 5 | 49.49 | |
| | Delta effect | 11.90 | |
| Contact (C) | 1 | 43.78 | 2 |
| | 2 | 44.28 | |
| | 3 | 45.00 | |
| | 4 | 44.00 | |
| | 5 | 43.70 | |
| | Delta effect | 1.30 | |
| Ribbon (R) | 1 | 44.78 | 3 |
| | 2 | 43.77 | |
| | 3 | 44.41 | |
| | 4 | 44.14 | |
| | 5 | 43.66 | |
| | Delta effect | 1.13 | |

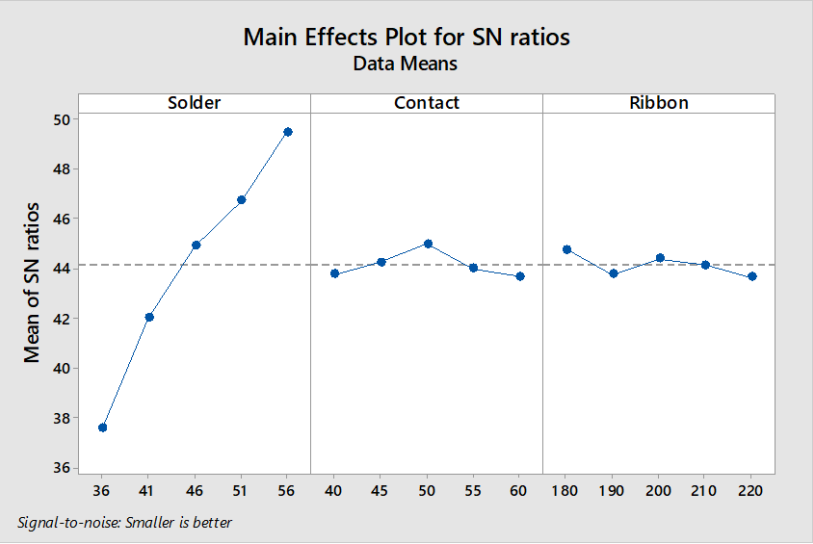


**Figure 7.34:** Control factors main effects plot for Aluminium-Silver Combination

As shown in Fig. 7.34 of the control factors main effects plots for Aluminium-Silver material combination, the predicted optimum design points occur at solder level 5, contact level 3 and ribbon level 1. Applying Eqn. 7.22, the predicted optimal SN ratio,

$$SN_{opt} = 44.151 + (49.49 - 44.151) + (45.00 - 44.151) + (44.78 - 44.151)$$

$$= 50.97\ dB$$

### 7.6.1 Control factor interactions for Taguchi experiments of Aluminium-Silver Combination

The solder-contact and solder-ribbon interactions are presented in Figs. 7.35 and 7.36 respectively. Both plots show no clear intersections between plot lines and so there is negligible interaction. However, in Fig. 7.37, there is a strong interaction between the contact and ribbon layers evident by several plot line interactions.

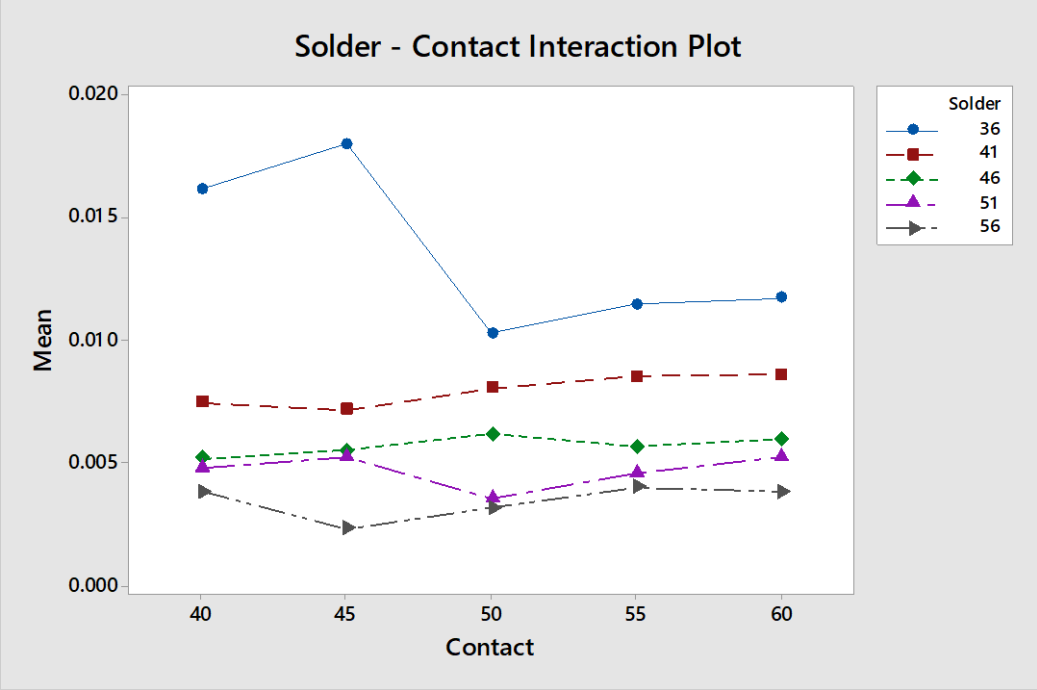


**Figure 7.35:** Solder-Contact interaction plot for Aluminium-Silver Combination

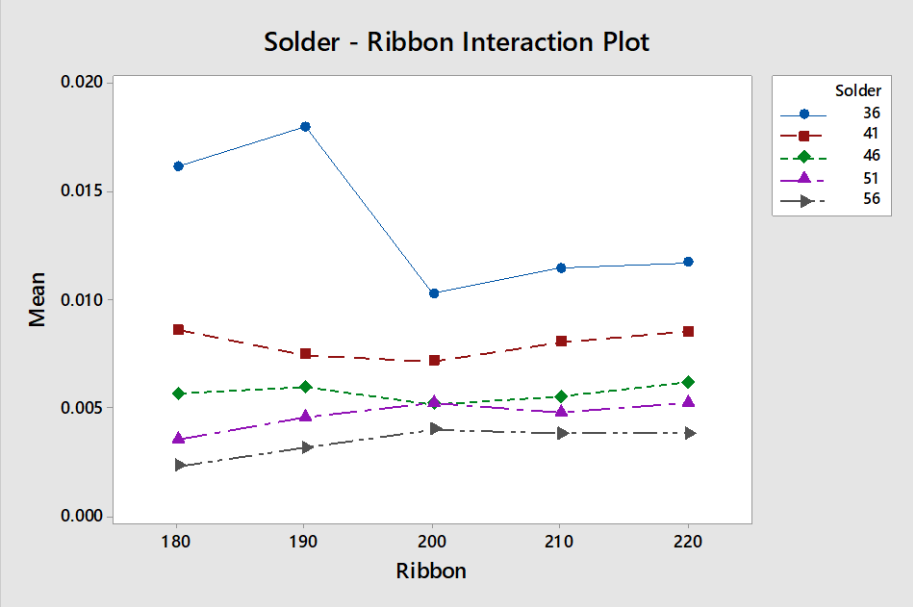


**Figure 7.36:** Solder-Ribbon interaction plot for Aluminium-Silver Combination

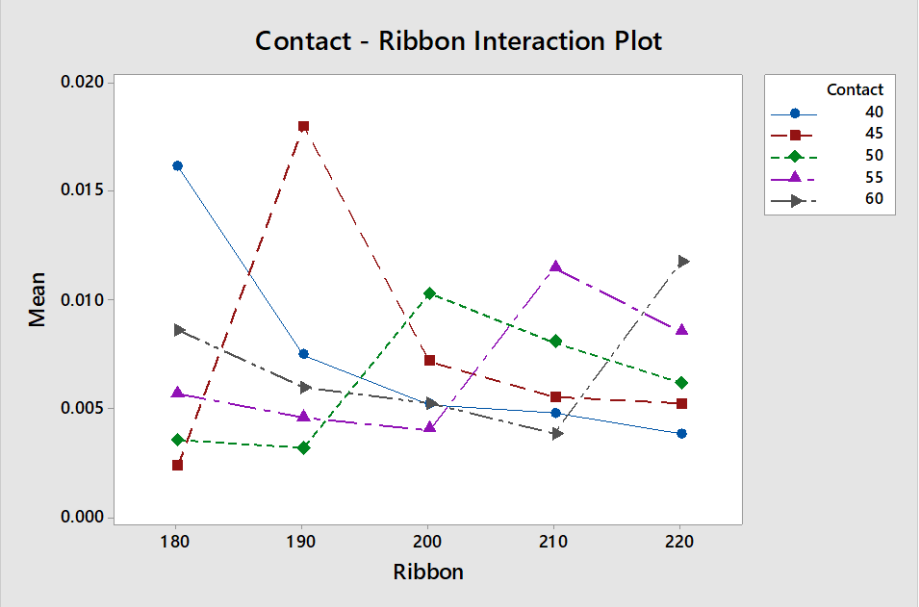


**Figure 7.37:** Contact-Ribbon interaction plot for Aluminium-Silver Combination

### 7.6.2 Performance comparison for Taguchi experiments of Aluminium-Silver Combination

As derived in chapter 5, modes 1-4 are applied to compare the performance of all twenty-five (25) design models to the conventional c-Si PV solder interconnection (CT) under elevated temperature climate conditions. This performance comparison is

presented in Table 7.18. The results show that all 25 design models show significant improvements over the CT with $N_{d_i} < 1$ and negative $D_i$ values.

**Table 7.18:** Performance comparison for Taguchi experiments of Aluminium-Silver Combination

| **Model No.** | **Accumulated Max. Creep Strain Energy Density (Pa)** | $N_{d_i}$ | $D_i$(%) | **Fatigue Life (years)** | $N_{f_i}$ | $F_i$(%) |
|---|---|---|---|---|---|---|
| 1 | 0.016163 | 0.3699 | -63.01 | 14.29 | 2.71 | 171 |
| 2 | 0.017996 | 0.4118 | -58.82 | 12.84 | 2.43 | 143 |
| 3 | 0.010259 | 0.2348 | -76.52 | 22.52 | 4.27 | 327 |
| 4 | 0.011451 | 0.2620 | -73.80 | 20.17 | 3.82 | 282 |
| 5 | 0.011696 | 0.2676 | -73.24 | 19.75 | 3.74 | 274 |
| 6 | 0.007466 | 0.1708 | -82.92 | 30.94 | 5.86 | 486 |
| 7 | 0.007159 | 0.1638 | -83.62 | 32.27 | 6.11 | 511 |
| 8 | 0.008031 | 0.1838 | -81.62 | 28.77 | 5.45 | 445 |
| 9 | 0.008504 | 0.1946 | -80.54 | 27.17 | 5.15 | 415 |
| 10 | 0.008599 | 0.1968 | -80.32 | 26.87 | 5.09 | 409 |
| 11 | 0.005168 | 0.1183 | -88.17 | 44.70 | 8.47 | 747 |
| 12 | 0.005517 | 0.1262 | -87.38 | 41.88 | 7.93 | 693 |
| 13 | 0.006172 | 0.1412 | -85.88 | 37.43 | 7.09 | 609 |
| 14 | 0.005656 | 0.1294 | -87.06 | 40.85 | 7.74 | 674 |
| 15 | 0.005946 | 0.1361 | -86.39 | 38.86 | 7.36 | 636 |
| 16 | 0.004773 | 0.1092 | -89.08 | 48.40 | 9.17 | 817 |
| 17 | 0.005198 | 0.1190 | -88.10 | 44.44 | 8.42 | 742 |
| 18 | 0.003516 | 0.0804 | -91.96 | 65.72 | 12.45 | 1145 |
| 19 | 0.004545 | 0.1040 | -89.60 | 50.83 | 9.63 | 863 |
| 20 | 0.005210 | 0.1192 | -88.08 | 44.35 | 8.40 | 740 |
| 21 | 0.003820 | 0.0874 | -91.26 | 60.47 | 11.45 | 1045 |
| 22 | 0.002308 | 0.0528 | -94.72 | 100.10 | 18.96 | 1796 |
| 23 | 0.003147 | 0.0720 | -92.80 | 73.41 | 13.90 | 1290 |
| 24 | 0.004003 | 0.0916 | -90.84 | 57.72 | 10.93 | 993 |
| 25 | 0.003808 | 0.0871 | -91.29 | 60.67 | 11.49 | 1049 |

Model 2, with fatigue life of 14.29 years, is the worst design but outperforms the CT under the elevated temperature operating conditions. The best design, Model 22, reduced solder interconnection degradation by 94.72%.

### 7.6.3 Optimal design verification for Taguchi experiments of Aluminium-Silver Combination

Verification experiments are carried out on the c-Si PV solder interconnection model is designed at optimum level settings of solder level 5, contact level 3 and ribbon level 1. The SN ratio of the verified optimal design is 53.40 dB while the SN ratio of the predicted optimum design 50.97 dB. There is a good correlation of 95.45%.

Table 7.19 and Fig. 7.38 present the performance comparison of the worst, best and optimal designs of the Aluminium-Silver material combination. The optimal design is a significant improvement on the conventional c-Si PV module under elevated temperature conditions. The optimal design reduced solder interconnection degradation by 95.11%. Figures 7.39, 7.41 and 7.43 show the creep strain energy, equivalent stress and equivalent strain of the Aluminium-Silver material combination best design in the ANSYS FEM environment respectively while parameters of the optimal design are presented in Figs. 7.40, 7.42 and 7.44. The optimal design performs better than the best design and demonstrates lower degradation. Red represents the highest degradation levels on the coloured keys while royal blue signifies the lowest degradation.

**Table 7.19:** Performance comparison of worst, best and optimal designs of the Aluminium-Silver Combination

| Taguchi Design | Accumulated Max. Creep Strain Energy Density (E-04 Pa) | Fatigue Life (E+03 Cycles) | Fatigue Life (years) |
|---|---|---|---|
| Worst Design | 180 | 40 | 12.8 |
| Best Design | 23 | 309 | 100.1 |
| Optimal Design | 21 | 334 | 108.1 |

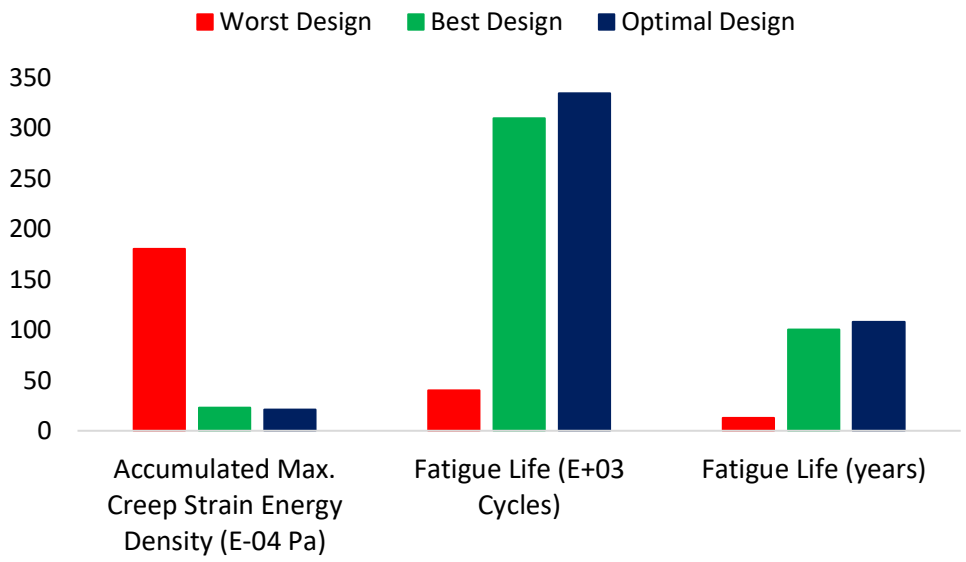


**Figure 7.38:** Performance comparison of worst, best and optimal designs of the Aluminium-Silver Combination

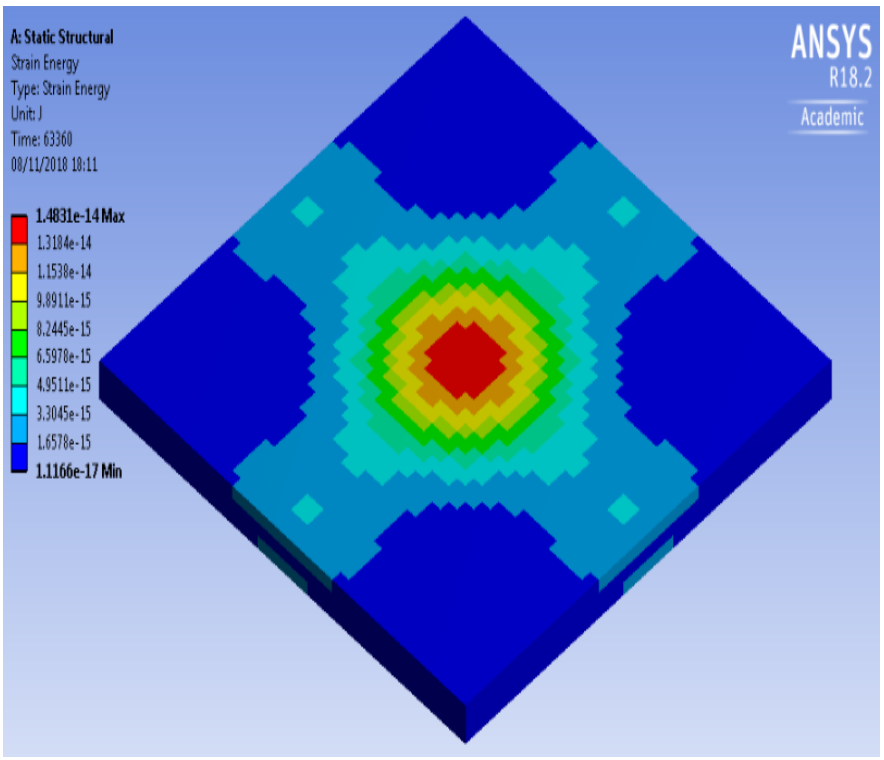


**Figure 7.39:** Creep strain energy of Aluminium-Silver combination best design

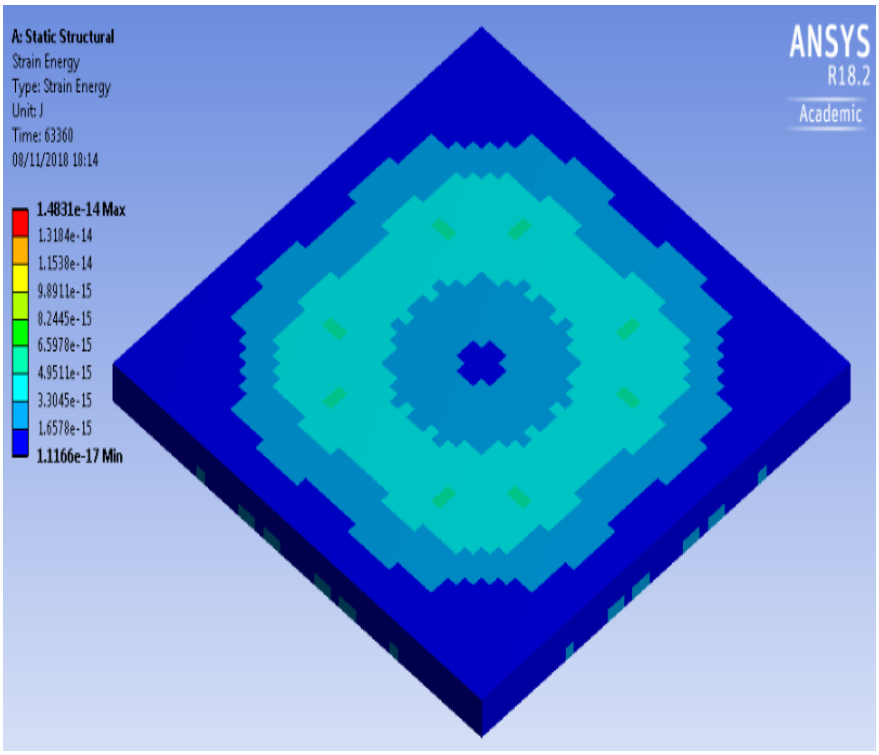


**Figure 7.40:** Creep strain energy of Aluminium-Silver combination optimal design

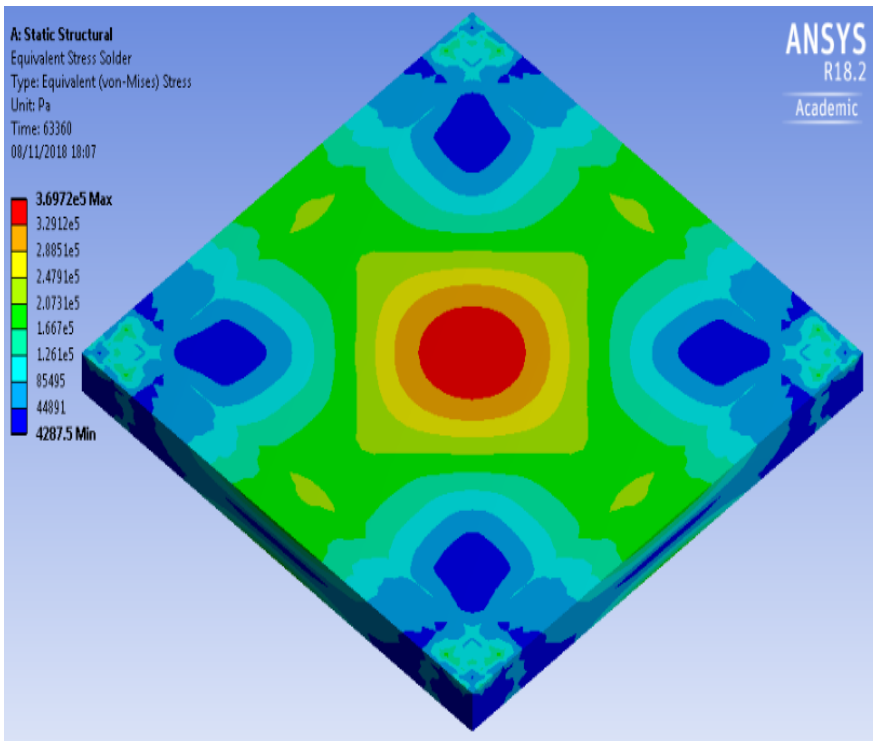


**Figure 7.41:** Equivalent stress of Aluminium-Silver combination best design

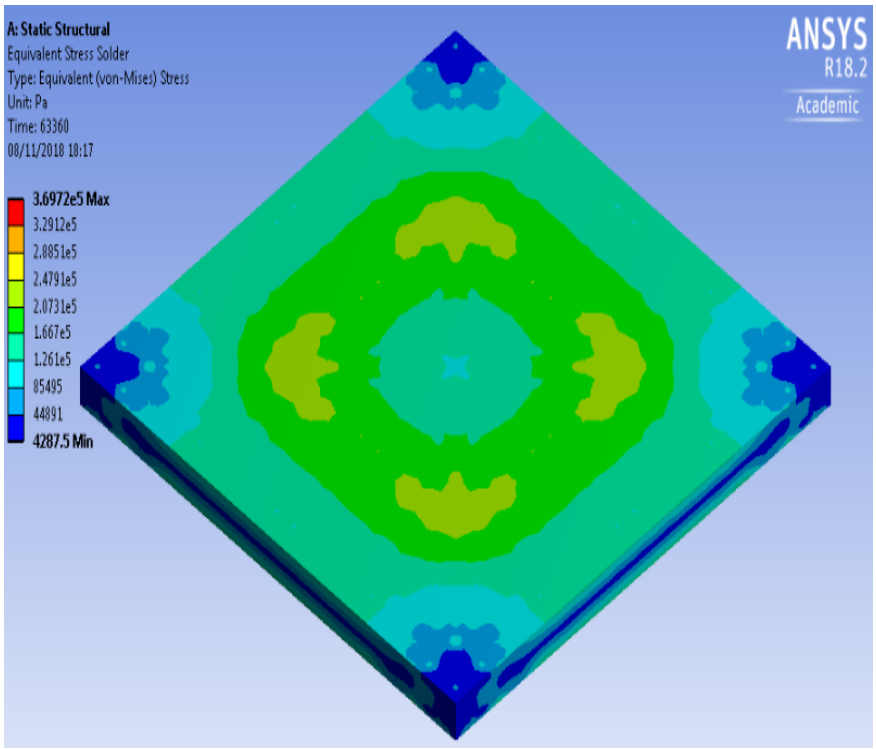


**Figure 7.42:** Equivalent stress of Aluminium-Silver combination optimal design

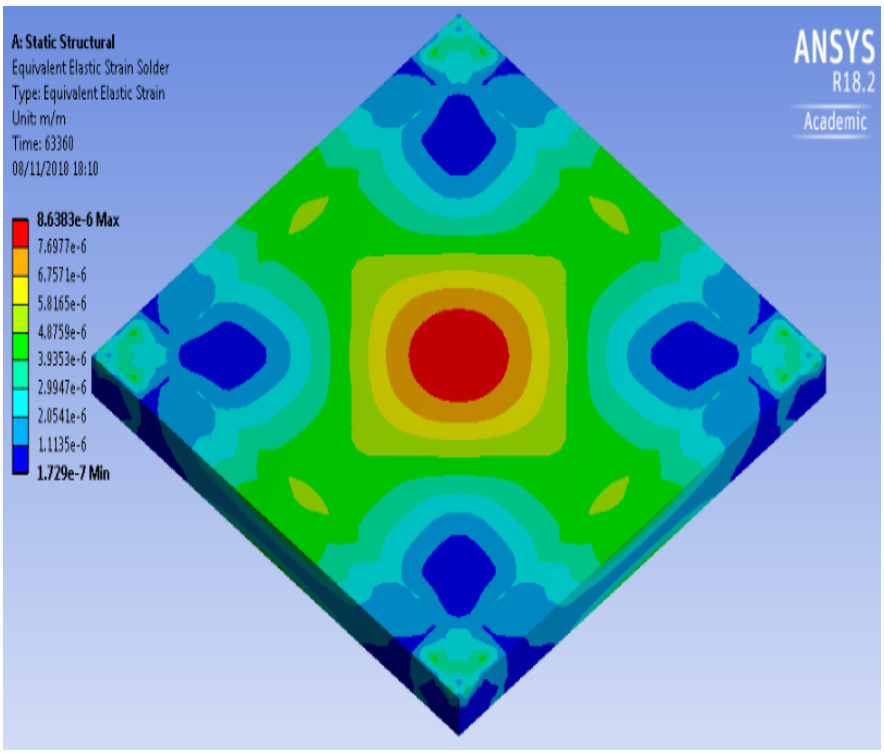


**Figure 7.43:** Equivalent strain of Aluminium-Silver combination best design

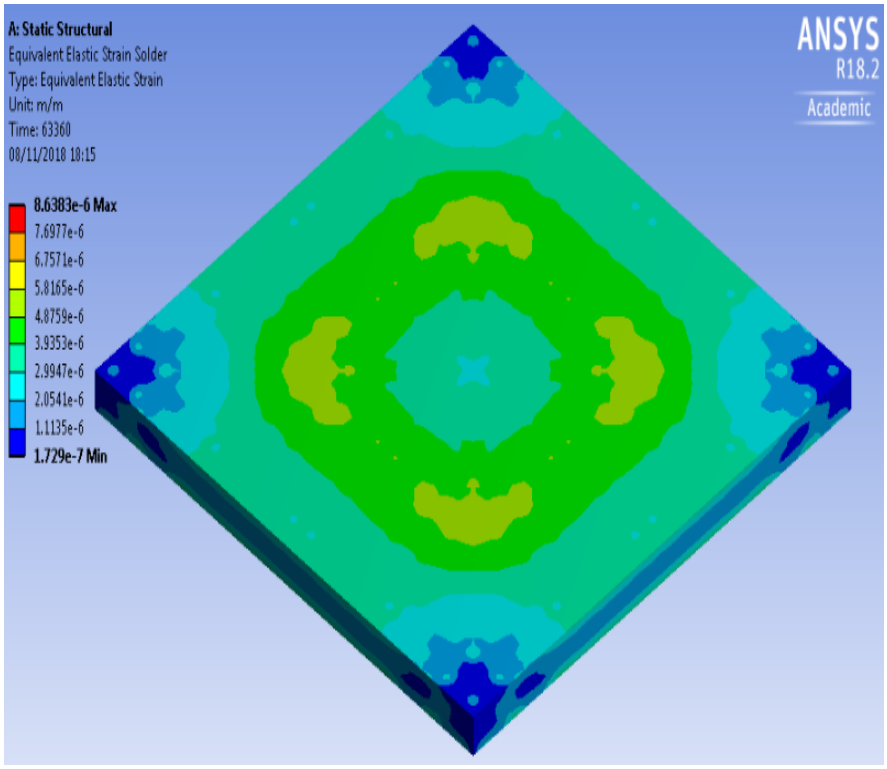


**Figure 7.44:** Equivalent strain of Aluminium-Silver combination optimal design

## 7.7 CONCLUSIONS

This chapter presented the robust optimisation of reliability influencing factors (RIFs) of c-Si PV solder interconnections for improved performance in elevated temperature climates using Taguchi L25 orthogonal array experiments in ANSYS FEM environment. The four ribbon-contact material combinations (Silver-Silver, Aluminium-Aluminium, Silver-Aluminium and Aluminium-Silver) established as best performing from chapter 5 were used for this optimisation investigation. One hundred (100) different c-Si PV solder interconnection models, twenty-five (25) models to each of the four (4) material combinations, were designed and tested for their suitability as substitutes to the conventional c-Si PV module (denoted as CT) in the region.

Applying the performance comparison modes derived in chapter 5, results show that all one hundred (100) tested c-Si PV solder interconnection models demonstrated significant improvements over the CT with $N_{d_i} < 1$ and negative $D_i$ values. Employing SN ratios and control factor main effects plots, the optimum design settings were identified, and verification experiments were carried out. All verification experiments were successful and indicated good correlation at >95%. Fatigue life was elongated, and solder interconnection degradation was reduced by 92.5%, 94.1%, 91.4% and 95.1% for the optimal models of Silver-Silver, Aluminium-Aluminium, Silver-Aluminium and Aluminium-Silver material combinations respectively.

Utilising the ANOVA sum of squares technique, the percentage contributions of each control factor to the response parameter were calculated. The solder layer control factor demonstrated the highest percentage contribution to the response parameter and was ranked 1$^{st}$ for all four (4) material combinations. The contact and ribbon

layer control factors varied between 2nd and 3rd ranks. This agrees with findings from chapter 6 of this thesis where varying the contact and ribbon layer thickness values (lower or higher from the standard dimensions) did not improve the performance of the solder interconnection for all four (4) material combinations. Changes to the solder layer, however, showed performance improvement.

# CHAPTER 8

# CONCLUSIONS AND RECOMMENDATIONS

## 8.1 INTRODUCTION

This research has presented the robust optimisation of c-Si PV module solder interconnections for improved reliability in elevated temperature climates. Elevated temperature was defined as PV cell temperature (25 °C ≤ T ≤ 120 °C) and/or ambient temperature (25 °C ≤ T ≤ 45 °C). This was achieved by employing a combination of ANSYS finite element modelling, Taguchi L25 orthogonal array design of experiment and analytical techniques while aligning the results with published experimental values. Four (4) solder interconnection models were proposed as the most suitable and best performing substitutes to the conventional c-Si PV module solder interconnection in the investigated climatic region. These four (4) optimal design models significantly reduced solder degradation and improved fatigue life. This chapter presents conclusions from the research in section 8.2, limitations of the research and recommendations for future work in section 8.3.

## 8.2 CONCLUSIONS

In the investigation to improve the thermo-mechanical reliability of c-Si PV modules in elevated temperature climates, the conventional solder interconnection was redesigned to develop models with varying material combinations and geometrical settings. The performances of these models were evaluated, and the conclusions drawn are presented under four headings in sections 8.2.1, 8.2.2, 8.2.3 and 8.2.4. In the race to combat climate change, reduce greenhouse gas emissions and global warming, improving the efficiency and reliability of c-Si PV modules cannot be

overemphasised. These findings presented are invaluable to experts and designers in the c-Si PV module manufacturing industry.

### 8.2.1 Effects of operating temperature on c-Si PV module degradation

The following conclusions can be made from the investigations on the effects of operating temperature (cell temperature and ambient temperature) on the performance of c-Si PV modules in elevated temperature climates. Points 1-3 particularly address the first research objective of this study.

- Solder interconnection degradation significantly increased with each 1°C cell temperature rise from STC. Three damage regions were observed which correspond to distinct cell temperature ranges, degradation rates and numerical relationships between solder interconnection degradation and cell temperature.
- Of the three damage regions, region 2 was established as critical. C-Si PV modules operating within this cell temperature range (43 °C to 63 °C) are prone to rapid degradation so this region should either be avoided, or the system redesigned to withstand the effects of the region.
- A power function model $L = 721.48T^{-1.343}$, was derived by the author to predict the fatigue life (years) of the system within the ambient temperature range 25 °C ≤ T ≤ 45 °C. Fatigue life was found to decay with increase in ambient temperature loads. This power function model is a handy toolkit which can be used by consumers to determine the lifetime of their modules in any climatic region.
- The inclusion of the intermetallic compound (IMC) layer influenced c-Si PV solder interconnection degradation for all the investigated ambient

temperature load. The set of models with IMC layer demonstrated greater solder degradation than the models with no IMC. This implies that IMC layer is important for the accurate modelling of c-Si PV modules in ANSYS FEM environment.

- The adequate number of thermal cycles influences the accurate modelling of c-Si PV modules in the ANSYS FEM environment. For both investigations on equivalent stress and strain in the solder interconnection, a turning point was observed after cycle number 3. Hence, it is advised that FE modelling should not employ less than three thermal cycles to ensure accurate representation and results.
- Modelling the EVA and solder layers using viscoelastic and temperature dependent material models significantly influenced the ANSYS FEM results. These layers have been previously modelled by researchers as simply linear elastic, but this investigation took a substantial step further. By employing temperature dependent and viscoelastic material models, the unique properties of EVA and solder were better described and inaccuracies due to nonlinearities were minimised in the FEM simulations. Although, there have been some previous studies where nonlinear modelling EVA and solder component layers were carried out, none has combined viscoelastic and temperature dependent models to investigate the degradation of c-Si PV module solder interconnections in the manner presented in this research by the author.

### 8.2.2 Effects of material combination on c-Si PV module degradation

Having established the poor thermo-mechanical performance of the conventional c-Si PV module under elevated temperature conditions, thirty-six (36) different ribbon-contact combinations formed from six (Aluminium (A), Brass (B), Copper (C), Silver (S), Tin (T) and Zinc (Z)) materials were proposed and investigated as suitable replacements. Five (5) analytical models were derived to compare the performance of the conventional c-Si PV module to the proposed ribbon-contact material combinations. Results derived from the analytical models supported those obtained from FEM environment. The following conclusions can be made to address the second research objective of this study:

- Brass was found to form the most unsuitable replacements. C-Si PV module solder interconnections formed from both Brass ribbons (B-Al, B-Cu, B-Ag, B-Sn, B-Zn) and Brass contacts (Al-B, Cu-B, Ag-B, Sn-B, Zn-B) performed worse than the conventional c-Si PV module. Other unsuitable material combinations were those formed from copper contacts (Al-Cu, B-Cu, Ag-Cu, Sn-Cu, Zn-Cu) and zinc contacts (Al-Zn, B-Zn, Cu-Zn, Ag-Zn, Sn-Zn). These material combinations increased solder degradation and reduced fatigue life in the investigation climatic region. The Brass, Zinc and Copper materials contributed majorly to the stiffness of the composite laminate beam model resulting in increased stress and degradation of the solder interconnection. These combinations possessed high deformation ratios, $\delta_R$ and normalised degradation values, $N_{d_i} > 1$, and positive normalised degradation deviation, $D_i$ values. These unsuitable models showed poor fatigue life with normalised fatigue life, $N_{f_i} < 1$ and negative normalised fatigue life deviation, $F_i$ values.

- From the zero CTE mismatch investigations carried out, only Al-Al and Ag-Ag material combinations were suitable replacements with the lowest deformation ratios, $\delta_R$. They decreased solder interconnection degradation by 99% with solder deformation 0.01 times that of the CT. Also, fatigue life was significantly elongated with $N_{f_i} > 1$ and positive $F_i$. The other zero CTE mismatch combinations (B-B, Cu-Cu, Sn-Sn, Zn-Zn) were found to be unsuitable substitutions.
- Four (4) ribbon-contact material combinations were chosen as best substitutes to the CT in elevated temperature conditions. They are Silver-Silver, Aluminium-Aluminium, Silver-Aluminium, and Aluminium-Silver. They have been chosen because each possesses the four (4) most desirable performance indicators values which fall within a narrow margin of $N_{d_i}$= 0.01-0.02 & $D_i$= -99% to -98% hence any of the four could replace the conventional c-Si PV solder interconnection in elevated temperature climate conditions.

### 8.2.3 Effects of thickness of bonded materials in the solder joint on c-Si PV module degradation

In order to further improve the reliability of the conventional c-Si PV module in elevated temperature conditions, the four (4) best performing material combinations chosen as suitable substitutions to the conventional c-Si PV module were used to design eighty-four (84) different c-Si PV module solder interconnection models in which the thicknesses of either the ribbon, solder or contact component layers were varied from the standard dimensions (SD) to carry out single variate experiments in

the ANSYS FEM environment. The following conclusions can be made to address the third research objective of this study:

- C-Si PV module solder interconnection models formed by varying solder layer thickness (SD ±5μm) demonstrated improved performance for all four (4) material combinations. The best performing solder thickness models were 51μm for the Ag-Ag combination ($N_{d_i}$= 0.0054 & $D_i$= -99.46%), 41μm for the Al-Al combination ($N_{d_i}$= 0.0081 & $D_i$= -99.19%), 51μm for the Ag-Al combination ($N_{d_i}$= 0.007 & $D_i$= -99.3%), and 41μm for the Al-Ag combination ($N_{d_i}$= 0.0067 & $D_i$= -99.33).
- Al-Ag showed more desirable miniaturisation properties because it showed improvement over the conventional c-Si PV module at SD when the solder thickness was decreased by 10μm down to 36μm. This was the lowest solder thickness value to show any improvement over the conventional PV module under elevated temperature conditions.
- Varying the ribbon and contact layer thicknesses from SD did not improve the performance of the c-Si PV module solder interconnection models formed from the four (4) material combinations. The SD remained the best performing design setting for both ribbon and contact single variate experiments.

### 8.2.4 Proposed optimised model(s) of c-Si PV module for elevated temperature climate applications

To address the fourth research objective of this study, Taguchi L25 orthogonal arrays were employed for the robust optimisation of the reliability influencing factors (RIFs) of c-Si PV modules operating in elevated temperature climates. One hundred

(100) different c-Si PV solder interconnection models were designed, twenty-five (25) models to each of the four (4) chosen material combinations, tested and verified for their suitability as substitutes to the conventional c-Si PV module. The following conclusions can be made:

- The optimal design models for all four (4) investigated material combinations reduced solder interconnection degradation however, the Aluminium-Silver ribbon-contact material combination model (ribbon = 180μm, solder = 56μm, contact = 50μm) demonstrated the best performance, reduced solder degradation by 95.1% and was the most suitable substitute to the conventional c-Si PV module solder interconnection in elevated temperature climate conditions – in terms of thermo-mechanical degradation.
- All the verification experiments carried out at the optimum design settings were successful and indicated good correlation of >95%. This high correlation indicates that the experiments and statistical models were performed correctly and accurately.
- ANOVA sum of squares technique was utilised to calculate the percentage contributions of each control factor to the response parameter. The solder layer control factor demonstrated the highest percentage contribution to the response parameter and was ranked 1$^{st}$ for all four (4) investigated material combinations. The contact and ribbon layer control factors varied between 2$^{nd}$ and 3$^{rd}$ ranks.

## 8.3 LIMITATIONS OF RESEARCH AND RECOMMENDATIONS FOR FUTURE WORK

The findings presented throughout this thesis, however, ground-breaking still leave room for improvement. Some of the limitations of the research are presented in section 8.3.1 and the recommendations for future work in section 8.3.2.

### 8.3.1 Limitations of research

The following are some of the limitations of the research:

- A macroscopic finite element modelling approach was considered in the study. This meant that emphasis was placed on the degradation occurring in the solder interconnection region of the c-Si PV model for creep failure and fatigue life prediction. Although temperature dependent and viscoelastic material models were applied to ensure more realistic simulations in the solder and EVA layers, there could have been a numerical evaluation of any effects the behaviour and interaction of these layers had on the solder interconnection degradation.
- The choice of control factors for the Taguchi L25 orthogonal array experiments were based on the material combination and geometry of the solder interconnection layers (i.e. solder, ribbon and contact) while the noise factor was the ambient temperature. There are some other factors worthy of investigation that could have been included such as silicon layer material and geometry, encapsulant composition, humidity, solar irradiation and heat transfer.
- In the process of reducing experimental runs, simulation runtime and cost, the intervals between dimension points of component layers especially for the thickness experiments and optimisation investigations were large. There may

be more trends and numerical relationships observed if the dimension intervals had been smaller.

### 8.3.2 Recommendations for future work

The following are recommendations for future work:

- From the ANSYS FEM investigations, the four (4) optimal designs have demonstrated significant improvement on the conventional c-Si PV module. However, prototypes of the four (4) optimal designs should be constructed, and laboratory and field life tests carried out on their thermo-mechanical reliability under elevated temperature climates. This will further validate acquired results.
- Although the proposed optimal designs for all four (4) material combinations reduced solder interconnection degradation by over 91% and elongated fatigue life in elevated temperature climates, further research must be done to ascertain their suitability based on other performance parameters such as solder bond adhesion, electrical conductivity and resistivity, electrical power output, thermal conductivity, cost and availability of materials, and manufacturing process compatibility.
- The available library of data on the IMC layer is based on the conventional c-Si PV module hence, further investigation is required on the composition and properties of IMC layers formed from the proposed four (4) solder interconnection models. This is necessary to ascertain the effects these new IMCs have on the thermo-mechanical reliability of the c-Si PV modules especially in elevated temperature climates. Dynamic mechanical analysis

(DMA) machine and scanning electron microscope (SEM) should be employed to study mechanical properties and microstructures.

- In the current study, the interactions between component layers of the c-Si PV module have been assumed as negligible. This was to simplify the FE models, minimise nonlinearities and reduce disc storage and simulation time. For future work, more robust and advanced modelling could be employed for investigations. These models should consider, amongst others, the interface interactions, imperfect bonding, heat dissipation between component layers and externally to the environs.

# REFERENCES


Adcock, T. and Henckens, A. (2011) *Lower cost, greater efficiency, drive development of back-contact solar modules, Renewable Energy World*. Available at: https://www.renewableenergyworld.com/articles/2011/05/lower-cost-greater-efficiency-drive-development-of-back-contact-solar-modules.html (Accessed: 5 August 2019).

Ahmad Dar, A. and Anuradha, N. (2018) 'Use of orthogonal arrays and design of experiment via Taguchi L9 method in probability of default', *Accounting*, 4(3), pp. 113–122. doi: 10.5267/j.ac.2017.11.001.

Aliyu, A. S., Ramli, A. T. and Saleh, A. (2013) 'Nigeria electricity crisis: Power generation capacity expansion and environmental ramifications', *Energy*, 61, pp. 354–367. doi: 10.1016/j.energy.2013.09.011.

Amalu, E. H. *et al.* (2011) 'A study of SnAgCu solder paste transfer efficiency and effects of optimal reflow profile on solder deposits', *Microelectronic Engineering*, 88(7), pp. 1610–1617. doi: 10.1016/j.mee.2011.02.104.

Amalu, E. H. *et al.* (2018) 'Thermo-mechanical deformation degradation of crystalline silicon photovoltaic (c-Si PV) module in operation', *Engineering Failure Analysis*. Pergamon, 84, pp. 229–246. doi: 10.1016/J.ENGFAILANAL.2017.11.009.

Amalu, E. H. and Ekere, N. N. (2012a) 'Damage of lead-free solder joints in flip chip assemblies subjected to high-temperature thermal cycling', *Computational Materials Science*, 65, pp. 470–484. doi: 10.1016/j.commatsci.2012.08.005.

Amalu, E. H. and Ekere, N. N. (2012b) 'Prediction of damage and fatigue life of high-temperature flip chip assembly interconnections at operations', *Microelectronics Reliability*, 52, pp. 2731–2743. doi: 10.1016/j.microrel.2012.04.004.

Arndt, R. and Puto, R. I. (2010) 'Basic Understanding of IEC Standard Testing For Photovoltaic Panels', *TÜV SÜD Product Service*. Available at: www.TUVamerica.com.

Aste, N., Pero, C. Del and Leonforte, F. (2014) 'PV technologies performance comparison in temperate climates', *Solar Energy*, 109, pp. 1–10. doi: 10.1016/j.solener.2014.08.015.

Athreya, S. and Venkatesh, Y. D. (2012) *Application Of Taguchi Method For Optimization Of Process Parameters In Improving The Surface Roughness Of Lathe Facing Operation, International Refereed Journal of Engineering and Science*. Available at: www.irjes.comwww.irjes.com (Accessed: 23 April 2019).

Balato, M., Costanzo, L. and Vitelli, M. (2015) 'Optimization of both the energetic efficiency and the duration of life of PV arrays by means of the dynamical reconfiguration of PV modules connections', in *10th International Conference on Ecological Vehicles and Renewable Energies (EVER)*. IEEE, pp. 1–6. doi: 10.1109/EVER.2015.7112922.

Bastidas-Rodriguez, J. D. *et al.* (2017) 'Quantification of photovoltaic module degradation using model based indicators', *Mathematics and Computers in Simulation*, 131, pp. 101–113. doi: 10.1016/j.matcom.2015.04.003.

Basu, J. B. (2015) 'Failure Modes and Effects Analysis (FMEA) of a Rooftop PV System', *International Journal of Scientific Engineering and Research (IJSER)* , 3(9), pp. 51–55. Available at: www.ijser.in (Accessed: 31 January 2019).

Belmont, J. (2013) *26+ Year Old Photovoltaic Power Plant: Degradation and Reliability Evaluation of Crystalline Silicon Modules – North Array*. Department of Technology, Arizona State University.

Borri, C., Gagliardi, M. and Paggi, M. (2018) 'Fatigue crack growth in Silicon solar cells and hysteretic behaviour of busbars', *Solar Energy Materials and Solar Cells*. doi: 10.1016/j.solmat.2018.02.016.

Bosco, N., Silverman, T. J. and Kurtz, S. (2016) 'Climate specific thermomechanical fatigue of flat plate photovoltaic module solder joints', *Microelectronics Reliability*, 62, pp. 124–129. doi: 10.1016/j.microrel.2016.03.024.

Carr, A. J. and Pryor, T. L. (2004) 'A comparison of the performance of different PV module types in temperate climates', *Solar Energy*, 76, pp. 285–294. doi: 10.1016/j.solener.2003.07.026.

Catelani, M. *et al.* (2011) 'FMECA technique on photovoltaic module', in *IEEE Instrumentation and Measurement Technology Conference*. IEEE, pp. 1717–1722. doi: 10.1109/IMTC.2011.5944245.

Chandel, S. S. *et al.* (2015) 'Degradation analysis of 28 year field exposed mono-c-Si

photovoltaic modules of a direct coupled solar water pumping system in western Himalayan region of India', *Renewable Energy*. Elsevier Ltd, 78, pp. 193–202. doi: 10.1016/j.renene.2015.01.015.

Chantana, J., Kamei, A. and Minemoto, T. (2017) 'Influences of environmental factors on Si-based photovoltaic modules after longtime outdoor exposure by multiple regression analysis', *Renewable Energy*, 101, pp. 10–15. doi: 10.1016/j.renene.2016.08.037.

Chao, W. *et al.* (2016) 'Low Cycle Fatigue Behavior of SnAgCu Solder Joints', *Rare Metal Materials and Engineering*, 45, pp. 829–835. doi: 10.1016/S1875-5372(16)30083-2.

Chattopadhyay, S. *et al.* (2015) 'All India Survey of Photovoltaic Module Degradation 2014: Survey methodology and statistics', *2015 IEEE 42nd Photovoltaic Specialist Conference, PVSC 2015*, pp. 1–6. doi: 10.1109/PVSC.2015.7355712.

Chung, D. D. L. (2001) 'Thermal interface materials', *Journal of Materials Engineering and Performance*. Springer-Verlag, 10(1), pp. 56–59. doi: 10.1361/105994901770345358.

Czanderna, A. W. and Pern, F. J. (1996) *Encapsulation of PV modules using ethylene vinyl acetate copolymer as a pottant: A critical review, Solar Energy Materials and Solar Cells*. Available at: https://ac-els-cdn-com.ezproxy.wlv.ac.uk/0927024895001506/1-s2.0-0927024895001506-main.pdf?_tid=47e54f54-5d8a-4025-ab7b-47e63d89c7d3&acdnat=1550234938_6f45e0f4e9018008cbc6342ece4573c6 (Accessed: 15 February 2019).

Djordjevic, S., Parlevliet, D. and Jennings, P. (2014) 'Detectable faults on recently installed solar modules in Western Australia', *Renewable Energy*, 67, pp. 215–221. doi: 10.1016/j.renene.2013.11.036.

Dubey, S., Sarvaiya, J. N. and Seshadri, B. (2013) 'Temperature Dependent Photovoltaic (PV) Efficiency and Its Effect on PV Production in the World – A Review', *Energy Procedia*. Elsevier, 33, pp. 311–321. doi: 10.1016/J.EGYPRO.2013.05.072.

Van Dyk, E. E. and Meyer, E. L. (2004) 'Analysis of the effect of parasitic

resistances on the performance of photovoltaic modules', *Renewable Energy*, 29, pp. 333–344. doi: 10.1016/S0960-1481(03)00250-7.

Eitner, U. *et al.* (2011) 'Thermomechanics of PV Modules Including the Viscoelasticity of EVA', in *26th European Photovoltaic Solar Energy Conference and Exhibition*. Hamburg, Germany, pp. 3267–3269. Available at: file:///C:/Users/GRO/Downloads/4EO.3.1_paper.pdf (Accessed: 19 September 2017).

Elibol, E. *et al.* (2016) 'Outdoor performance analysis of different PV panel types', *Renewable and Sustainable Energy Reviews*, 67, pp. 651–661. doi: 10.1016/j.rser.2016.09.051.

Fowlkes, W. Y. and Creveling, C. M. (1995) *Engineering methods for robust product design : using Taguchi methods in technology and product development*. Edited by Addison-Wesley Pub. Co. Reading , MA: Addison-Wesley Pub. Co. Available at: https://librarysearch.wlv.ac.uk/discovery/fulldisplay?vid=44UOWO_INST:MAIN&id=991000721479704901&inst=44UOWO_INST&context=L (Accessed: 2 January 2019).

Francis, R. and Colli, A. (2014) 'Information-based reliability weighting for failure mode prioritization in photovoltaic (PV) module design', in *Probabilistic Safety Assessment and Management PSAM*. Honolulu, pp. 1–12. Available at: http://psam12.org/proceedings/paper/paper_215_1.pdf (Accessed: 31 January 2019).

FSEC (2010) *Test Method for Photovoltaic Module Power Rating*. Florida. Available at: http://www.fsec.ucf.edu/en/publications/pdf/standards/FSECstd_202-10.pdf (Accessed: 23 January 2019).

Gagliardi, M., Lenarda, P. and Paggi, M. (2017) 'A reaction-diffusion formulation to simulate EVA polymer degradation in environmental and accelerated ageing conditions', *Solar Energy Materials and Solar Cells*, 164, pp. 93–106. doi: 10.1016/j.solmat.2017.02.014.

Gallardo-Saavedra, S. *et al.* (2017) 'Failure rate determination and Failure Mode, Effect and Criticality Analysis (FMECA) based on historical data for photovoltaic plants', in *IEA SHC International Conference on Solar Heating and Cooling for Buildings and Industry*, pp. 1–8. doi: 10.18086/swc.2017.20.04.

George, E. (2010) ‘THERMAL CYCLING RELIABILITY OF LEAD- FREE SOLDERS (SAC305 AND SN3.5AG) FOR HIGH TEMPERATURE APPLICATIONS’, *University of Maryland*, XXXIII(2), pp. 81–87. doi: 10.1007/s13398-014-0173-7.2.

Ghaffarian, R. (2000) ‘Accelerated Thermal Cycling and Failure Mechanisms for BGA and CSP Assemblies’, *Journal of Electronic Packaging*, 122(4), p. 335. doi: 10.1115/1.1289627.

Ghani, F. *et al.* (2015) ‘On the influence of temperature on crystalline silicon solar cell characterisation parameters’, *Solar Energy*, 112, pp. 437–445. doi: 10.1016/j.solener.2014.12.018.

Giurgiu, T., Ciortan, F. and Pupaza, C. (2013) ‘Static and Transient Analysis of Radial Tires Using ANSYS’, in *Recent advances in industrial and manufacturing technologies: proceedings of the 1st international conference on industrial and manufacturing technologies (INMAT’13)*. Vouliagmeni, Athens, Greece, pp. 148–152.

Green, M. A. (1981) ‘Solar cell fill factors: General graph and empirical expressions’, *Solid-State Electronics*, 24(8), pp. 788–789. doi: 10.1016/0038-1101(81)90062-9.

Gujba, H., Mulugetta, Y. and Azapagic, A. (2011) ‘Power generation scenarios for Nigeria: An environmental and cost assessment’, *Energy Policy*, 39(2), pp. 968–980. doi: 10.1016/j.enpol.2010.11.024.

Guyenot, M. *et al.* (2011) ‘Enhancing the lifetime prediction methodology for photovoltaic modules based on electronic packaging experience’, in *2011 12th Intl. Conf. on Thermal, Mechanical & Multi-Physics Simulation and Experiments in Microelectronics and Microsystems. IEEE*. IEEE, pp. 1–4. doi: 10.1109/ESIME.2011.5765781.

Harrington, R. (2015) *This incredible fact will get you psyched about solar*, *Tech News, Business Insider UK*. Available at: http://uk.businessinsider.com/this-is-the-potential-of-solar-power-2015-9?r=US&IR=T (Accessed: 4 September 2017).

Hasselbrink, E. *et al.* (2013) ‘Validation of the PVLife model using 3 million module-years of live site data’, in *2013 IEEE 39th Photovoltaic Specialists Conference (PVSC)*. IEEE, pp. 0007–0012. doi: 10.1109/PVSC.2013.6744087.

Herrmann, W. (2010) 'How temperature cycling degrades photovoltaic-module performance', *International Society Advancing an Interdisciplinary Approach to the Science and Application of Light (SPIE)*. doi: 10.1117/2.1201007.003177.

Hren, R. (2011) *Understanding PV Module Specifications*, *Home Power Magazine*. Available at: https://www.homepower.com/articles/solar-electricity/equipment-products/understanding-pv-module-specifications (Accessed: 7 September 2017).

Hui, X. *et al.* (2013) 'Damage Behavior of SnAgCu Solder under Thermal Cycling', *Rare Metal Materials and Engineering*, 42(2), pp. 221–226. doi: 10.1016/S1875-5372(13)60035-1.

Huld, T. *et al.* (2010) 'Mapping the performance of PV modules, effects of module type and data averaging', *Solar Energy*, 84(2), pp. 324–338. doi: 10.1016/j.solener.2009.12.002.

Hussein, H. M. S., Ahmad, G. E. and El-Ghetany, H. H. (2004) 'Performance evaluation of photovoltaic modules at different tilt angles and orientations', *Energy Conversion and Management*, 45(15–16), pp. 2441–2452. doi: 10.1016/j.enconman.2003.11.013.

IEC (2006a) *Analysis techniques for dependability-Reliability block diagram and boolean methods*. Geneva, International Electrotehnical Commission (IEC). Available at: www.iec.ch/online_news/justpub (Accessed: 7 February 2019).

IEC (2006b) *Analysis techniques for system reliability-Procedure for failure mode and effects analysis (FMEA)*. Geneva, International Electrotehnical Commission (IEC). Available at: www.iec.ch/searchpub (Accessed: 5 February 2019).

IEC (2006c) *Fault tree analysis (FTA)*. Geneva, International Electrotehnical Commission (IEC). Available at: www.iec.ch/searchpub/cur_fut-f.htm (Accessed: 7 February 2019).

IMCA (2002) *Guidance on Failure Modes & Effects Analyses (FMEAs)*. Wavespec, The International Marine Contractors Association (IMCA). Available at: www.imca-int.com (Accessed: 5 February 2019).

Janakeeraman, S. V. (2013) *Angle of Incidence And Power Degradation Analysis of Photovoltaic Modules*. Arizona State University.

Jeong, J.-S., Park, N. and Han, C. (2012) 'Field failure mechanism study of solder

interconnection for crystalline silicon photovoltaic module', *Microelectronics Reliability*, 52(9–10), pp. 2326–2330. doi: 10.1016/j.microrel.2012.06.027.

Jiang, Y. and Lu, L. (2015) 'A Study of Dust Accumulating Process on Solar Photovoltaic Modules with Different Surface Temperatures', *Energy Procedia*. Elsevier, 75, pp. 337–342. doi: 10.1016/J.EGYPRO.2015.07.378.

Jordan, D. C. *et al.* (2010) 'Outdoor PV degradation comparison', in *Conference Record of the IEEE Photovoltaic Specialists Conference*. doi: 10.1109/PVSC.2010.5616925.

Jordan, D. C. *et al.* (2015) 'Performance and Aging of a 20-Year-Old Silicon PV System', *IEEE Journal of Photovoltaics*, 5(3), pp. 744–751. doi: 10.1109/JPHOTOV.2015.2396360.

Jordan, D. C. *et al.* (2017) 'Photovoltaic failure and degradation modes', *Progress in Photovoltaics: Research and Applications*, 25(4), pp. 318–326. doi: 10.1002/pip.2866.

Jordan, D. C. and Kurtz, S. R. (2013) 'Photovoltaic degradation rates - An Analytical Review', *Progress in Photovoltaics: Research and Applications*. doi: 10.1002/pip.1182.

Kato, K. (2012) 'PV module failures observed in the field - solder bond and bypass diode failures -', *International Energy Agency*.

Kim, N. *et al.* (2016) 'Analysis and reproduction of snail trails on silver grid lines in crystalline silicon photovoltaic modules'. doi: 10.1016/j.solener.2015.11.040.

King, D. L., Boyson, W. E. and Kratochvil, J. A. (2002) 'Analysis of Factors Influencing the Annual Energy Production of Photovoltaic Systems', in *Photovoltaic Specialists Conference, Conference Record of the 29th IEEE*, pp. 1356–1361.

Köntges, M. *et al.* (2014) 'Review of Failures of Photovoltaic Modules', *Photvoltaic Power Systems Programme (PVPS)*, 13, pp. 1–132.

Köntges, M. *et al.* (2017) 'Assessment of Photovoltaic Module Failures in the Field', *International Energy Agency Photovoltaic Power Systems Programme (IEA PVPS)*, 13, pp. 12–57.

Kraemer, F. and Wiese, S. (2014) 'FEM Stress Analysis of Various Solar Module Concepts under Temperature Cycling Load', in *Thermal, mechanical and multi-*

*physics simulation and experiments in microelectronics and microsystems (eurosime), 15th iIEEE*, pp. 1–8.

Kuitche, J. M. (2014) *A Statistical Approach to Solar Photovoltaic Module Lifetime Prediction*. Arizona State University. Available at: https://repository.asu.edu/attachments/143310/content/Kuitche_asu_0010E_14456.pdf (Accessed: 1 February 2019).

Kuitche, J. M., Pan, R. and Tamizhmani, G. (2014) 'Investigation of dominant failure mode(s) for field-aged crystalline silicon PV modules under desert climatic conditions', *IEEE Journal of Photovoltaics*, 4(3), pp. 814–826. doi: 10.1109/JPHOTOV.2014.2308720.

Kuitche, J. M., Tamizhmani, G. and Pan, R. (2011) 'Failure modes effects and criticality analysis (FMECA) approach to the crystalline silicon photovoltaic module reliability assessment', in *Reliability of Photovoltaic Cells, Modules, Components, and Systems IV*. San Diego, California, United States: International society for optics and photonics, p. 81120L. Available at: file:///C:/Users/GRO/Downloads/PSI81120L.pdf (Accessed: 4 February 2019).

Kurnik, J. *et al.* (2011) 'Outdoor testing of PV module temperature and performance under different mounting and operational conditions', *Solar Energy Materials and Solar Cells*, 95(1), pp. 373–376. doi: 10.1016/j.solmat.2010.04.022.

Lenarda, P. and Paggi, · M (2016) 'A geometrical multi-scale numerical method for coupled hygro-thermo-mechanical problems in photovoltaic laminates', *Computational Mechanics*, 57(6), pp. 947–963. doi: 10.1007/s00466-016-1271-5.

Lindeman, T. (2015) *Without electricity, 1.3 billion are living in the dark*, *Washington Post*. Available at: https://www.washingtonpost.com/graphics/world/world-without-power/ (Accessed: 24 February 2016).

Liu, M., Johnston, M. B. and Snaith, H. J. (2013) 'Efficient planar heterojunction perovskite solar cells by vapour deposition.', *Nature*. Nature Publishing Group, 501(7467), pp. 395–8. doi: 10.1038/nature12509.

Mallineni, J. K. (2013) *Failure and Degradation Modes of PV modules in a Hot Dry Climate: Results after 4 and 12 years of field exposure*. Arizona State University.

Matsunaga, S. *et al.* (2011) 'Viscoelastic Study of PV Module Encapsulant for the Prediction of Thermal Durability', in *26th European Photovoltaic Solar Energy Conference and Exhibition*. Hamburg, Germany, pp. 3295–3297. Available at: file:///C:/Users/GRO/Downloads/4AV.1.1_paper.pdf (Accessed: 19 September 2017).

McEwan, W., Belavendram, N. and Abou-Ali, M. (1992) 'Taguchi methods and expert systems in fabrication design', *International Journal of Pressure Vessels and Piping*. Elsevier, 53(1), pp. 47–61. doi: 10.1016/0308-0161(93)90103-Z.

Meydbray, J. and Dross, F. (2016) *PV Module Reliability Scorecard Report 2016*. Oslo, Norway, DNV GL. Available at: file:///C:/Users/GRO/Downloads/solar-pv-module-reliability-scorecard-2016-2-1473940821.pdf (Accessed: 1 February 2019).

Meyer, E. L. and Van Dyk, E. E. (2004) 'Assessing the reliability and degradation of photovoltaic module performance parameters', *IEEE Transactions on Reliability*. doi: 10.1109/TR.2004.824831.

Miller, D. C. *et al.* (2010) 'Creep in Photovoltaic Modules: Examining the Stability of Polymeric Materials and Components', *National Renewable Energy Laboratory (NREL)*. Available at: http://www.osti.gov/bridge (Accessed: 26 September 2017).

Mohammed, S., Boumediene, B. and Miloud, B. (2016) 'Assessment of PV Modules Degradation based on Performances and Visual Inspection in Algerian Sahara', *INTERNATIONAL JOURNAL of RENEWABLE ENERGY RESEARCH B. Boumediene et al*, 6(1), pp. 106–116.

Morris, J. W., Song, H. G. and Hua, F. (2003) 'Creep properties of Sn-rich solder joints', in *53rd Electronic Components and Technology Conference, 2003. Proceedings*. IEEE, pp. 54–57.

Mussard, M. (2017) 'Solar energy under cold climatic conditions: A review', *Renewable and Sustainable Energy Reviews*. Pergamon, 74, pp. 733–745. doi: 10.1016/J.RSER.2017.03.009.

Mustafa, M. *et al.* (2011) 'The effects of aging on the cyclic stress-strain behavior and hysteresis loop evolution of lead free solders', in *61st Electronic Components and Technology Conference*, pp. 927–939. Available at: file:///C:/Users/GRO/Downloads/Uniaxial Cyclic Behavior with Aging-IEEE2011.pdf (Accessed: 6 September 2017).

Nadimpalli, S. P. V. and Spelt, J. K. (2010) 'Fracture load prediction of lead-free solder joints', *Engineering Fracture Mechanics*, 77(17), pp. 3446–3461. doi: 10.1016/j.engfracmech.2010.09.012.

Nadimpalli, S. P. V. and Spelt, J. K. (2011) 'Effect of geometry on the fracture behavior of lead-free solder joints', *Engineering Fracture Mechanics*, 78(6), pp. 1169–1181. doi: 10.1016/j.engfracmech.2011.01.026.

Ndiaye, A. *et al.* (2013) 'Degradations of silicon photovoltaic modules: A literature review', *Solar Energy*. Pergamon, 96, pp. 140–151. doi: 10.1016/J.SOLENER.2013.07.005.

Obinata, K. *et al.* (2010) 'Geometrical Optimization of Arrangement of Solar Cells in Photovoltaic Modules', *Forma*, (25), pp. 31–35.

Ogbomo, O. O. *et al.* (2017) 'A review of photovoltaic module technologies for increased performance in tropical climate', *Renewable and Sustainable Energy Reviews*, 75, pp. 1225–1238. doi: 10.1016/j.rser.2016.11.109.

Ogbomo, O. O. *et al.* (2018) 'Effect of operating temperature on degradation of solder joints in crystalline silicon photovoltaic modules for improved reliability in hot climates', *Solar Energy*, 170, pp. 682–693. doi: 10.1016/j.solener.2018.06.007.

Ojo, S. O. and Paggi, M. (2016a) 'A 3D coupled thermo-visco-elastic shear-lag formulation for the prediction of residual stresses in photovoltaic modules after lamination', *Composite Structures*, (157), pp. 348–359. doi: 10.1016/j.compstruct.2016.08.036.

Ojo, S. O. and Paggi, M. (2016b) 'A thermo-visco-elastic shear-lag model for the prediction of residual stresses in photovoltaic modules after lamination', *Composite Structures*, (136), pp. 481–492. doi: 10.1016/j.compstruct.2015.10.023.

Olaniyan, K. *et al.* (2018) 'Estimating Residential Electricity Consumption in Nigeria to Support Energy Transitions', *Sustainability*, 10(1440), pp. 1–22. Available at: file:///C:/Users/GRO/Downloads/sustainability-10-01440.pdf (Accessed: 21 August 2019).

OpenAIS (2015) *FMEA and Hazard analysis report (Deliverable D4.2)*. Open Architectures for Intelligent Solid State Lighting Systems. Available at: http://www.openais.eu/user/file/openais_fmea_and_hazard_analysis_report_(d4.2)_v

1.0-pub.pdf (Accessed: 5 February 2019).

Otiaba, K. C. *et al.* (2013) 'Finite element analysis of the effect of silver content for Sn-Ag-Cu alloy compositions on thermal cycling reliability of solder die attach', *Engineering Failure Analysis*. Elsevier Ltd, 28, pp. 192–207. doi: 10.1016/j.engfailanal.2012.10.008.

Pacca, S., Sivaraman, D. and Keoleian, G. a. (2007) 'Parameters affecting the life cycle performance of PV technologies and systems', *Energy Policy*, 35(6), pp. 3316–3326. doi: 10.1016/j.enpol.2006.10.003.

Packard, C. E. *et al.* (2012) 'Field PV Module Condition', *27th EU PVSEC and IEA PVPS Task 13 Subtask 3.2 Meeting*.

Packard, C. E., Wohlgemuth, J. H. and Kurtz, S. R. (2012) *Development of a Visual Inspection Data Collection Tool for Evaluation of Fielded PV Module Condition*. National Renewable Energy Laboratory (NREL). Available at: http://www.osti.gov/bridge (Accessed: 2 February 2019).

Paggi, M. *et al.* (2014) 'Fatigue degradation and electric recovery in Silicon solar cells embedded in photovoltaic modules', *Scientific Reports*, (4), p. 4506. doi: 10.1038/srep04506.

Paggi, M., Corrado, M. and Rodriguez, M. A. (2013) 'A multi-physics and multi-scale numerical approach to microcracking and power-loss in photovoltaic modules', *Composite Structures*, (95), pp. 630–638. doi: 10.1016/j.compstruct.2012.08.014.

Paggi, M., Kajari-Schröder, S. and Eitner, U. (2011) 'Thermomechanical deformations in photovoltaic laminates', *The Journal of Strain Analysis for Engineering Design*. SAGE PublicationsSage UK: London, England, 46(8), pp. 772–782. doi: 10.1177/0309324711421722.

Paggi, M. and Sapora, A. (2015) 'An Accurate Thermoviscoelastic Rheological Model for Ethylene Vinyl Acetate Based on Fractional Calculus', *International Journal of Photoenergy*. Hindawi, 2015, pp. 1–7. doi: 10.1155/2015/252740.

Pantic, L. S. *et al.* (2016) 'The assessment of different models to predict solar module temperature, output power and efficiency for Nis, Serbia', *Energy*. Pergamon, 109, pp. 38–48. doi: 10.1016/J.ENERGY.2016.04.090.

Patil, H. and Jeyakarthikeyan, P. V (2018) 'Mesh convergence study and estimation

of discretization error of hub in clutch disc with integration of ANSYS', *IOP Conference Series: Materials Science and Engineering*, 402, pp. 1–11. doi: 10.1088/1757-899X/402/1/012065.

Pern, F. J. (1996) 'Factors that affect the EVA encapsulant discoloration rate upon accelerated exposure', *Solar Energy Materials and Solar Cells*, 41, pp. 587–615. Available at: https://ac-els-cdn-com.ezproxy.wlv.ac.uk/092702489500128X/1-s2.0-092702489500128X-main.pdf?_tid=270e7a77-ba7b-4b39-89a6-15594a0544fe&acdnat=1531182031_461043b99d350aafb421948640a9ca1d (Accessed: 10 July 2018).

Petrana, S., Setiawan, E. A. and Januardi, A. (2018) 'Solar panel performance analysis under indonesian tropic climate using sandia PV array performance model and five parameter performance model', *EDP Sciences*, 67(02048), pp. 1–11. doi: 10.1051/e3sconf/20186702048.

Phadke, M. S. (1989) 'Quality Engineering using Design of Experiments', in *Quality Control, Robust Design, and the Taguchi Method*. Boston, MA: Springer US, pp. 31–50. doi: 10.1007/978-1-4684-1472-1_3.

Phinikarides, A. *et al.* (2014) 'Review of photovoltaic degradation rate methodologies', *Renewable and Sustainable Energy Reviews*, (40), pp. 143–152. doi: 10.1016/j.rser.2014.07.155.

Pignatiello, J. J. and Ramberg, J. S. (1991) 'Top Ten Triumphs and Tragedies of Genichi Taguchi', *Quality Engineering*, 4(2), pp. 211–225. doi: 10.1080/08982119108918907.

Polverini, D. *et al.* (2013) 'Polycrystalline silicon PV modules performance and degradation over 20years', *Progress in Photovoltaics: Research and Applications*, 21, pp. 1004–1015. doi: 10.1002/pip.

*PV cell contacts* (no date). Available at: https://www.google.co.uk/search?q=PV+cell+contacts&source=lnms&tbm=isch&sa=X&ved=0CAkQ_AUoAmoVChMIy-y5v96YyQIVCTkaCh1C8g1w&biw=1366&bih=633#imgrc=Yoh1Zm3MGmNhQM%3A (Accessed: 18 November 2015).

Qin, H. B. *et al.* (2014) 'Low cycle fatigue performance of ball grid array structure Cu/Sn–3.0Ag–0.5Cu/Cu solder joints', *Microelectronics Reliability*. Pergamon,

54(12), pp. 2911–2921. doi: 10.1016/J.MICROREL.2014.07.052.

Qin, H. B. *et al.* (2015) 'Geometry effect on mechanical performance and fracture behavior of micro-scale ball grid array structure Cu/Sn-3.0Ag0.5Cu/Cu solder joints', *Microelectronics Reliability*, 55, pp. 1214–1225. doi: 10.1016/j.microrel.2015.05.013.

Quintana, M. A. and Kurtz, S. R. (2008) *Reliability R&D: DOE Program Review*. Solar Energy Technologies Program (SETP) Annual Program Review Meeting. Austin, Texas. Available at: https://www.nrel.gov/docs/fy08osti/43214.pdf (Accessed: 2 February 2019).

Rajput, P. *et al.* (2016) 'Degradation of mono-crystalline photovoltaic modules after 22 years of outdoor exposure in the composite climate of India', *Solar Energy*, 135. doi: 10.1016/j.solener.2016.06.047.

Rajput, P., Sastry, O. S. and Tiwari, G. N. (2017) 'Effect of irradiance, temperature exposure and an Arrhenius approach to estimating weathering acceleration factor of Glass, EVA and Tedlar in a composite climate of India', *Solar Energy*, 144, pp. 267–277. doi: 10.1016/j.solener.2017.01.027.

Ramberg, J. S. *et al.* (1991) 'Designing simulation experiments: Taguchi methods and response surface metamodels', in *1991 Winter Simulation Conference Proceedings.* Phoenix, AZ, USA: IEEE, pp. 167–176. doi: 10.1109/WSC.1991.185612.

Ramli, M. A. M. *et al.* (2016) 'On the investigation of photovoltaic output power reduction due to dust accumulation and weather conditions', *Renewable Energy*, 99, pp. 836–844. Available at: https://ac-els-cdn-com.ezproxy.wlv.ac.uk/S0960148116306784/1-s2.0-S0960148116306784-main.pdf?_tid=spdf-08af52b4-06a1-41ce-a131-76b536f1d0c5&acdnat=1519745752_70a7266adbd187ad853238f7a6239a95 (Accessed: 27 February 2018).

Rust, W. and Schweizerhof, K. (2003) 'Finite element limit load analysis of thin-walled structures by ANSYS (implicit), LS-DYNA (explicit) and in combination', in *Thin-Walled Structures*. doi: 10.1016/S0263-8231(02)00089-7.

Ryan, T. P. (2011) *Statistical Methods for Quality Improvement*. Edited by John Wiley & Sons. John Wiley & Sons.

Ryan, T. P. and Morgan, J. P. (2007) *Modern Experimental Design, Journal of Statistical Theory and Practice*. Edited by J. Wiley. New Jersey, USA: John Wiley & Sons. doi: 10.1080/15598608.2007.10411855.

Sander, M. *et al.* (2010) 'PV module defect detection by combination of mechanical and electrical analysis methods', in *35th IEEE Photovoltaic Specialists Conference*. IEEE, pp. 001765–001769. doi: 10.1109/PVSC.2010.5615878.

Sarr, O. N. *et al.* (2017) 'Analysis of Failure Modes Effect and Criticality Analysis (FMECA): A Stand-Alone Photovoltaic System', *Science Journal of Energy Engineering*, 5(2), pp. 40–47. doi: 10.11648/j.sjee.20170502.11.

Sastry, O. S. *et al.* (2010) 'Performance analysis of field exposed single crystalline silicon modules', *Solar Energy Materials and Solar Cells*, 94, pp. 1463–1468. doi: 10.1016/j.solmat.2010.03.035.

Schmitt, P. *et al.* (2012) 'Intermetallic Phase Growth and Reliability of Sn-Ag-Soldered Solar Cell Joints', *Energy Procedia*, 27, pp. 664–669. doi: 10.1016/j.egypro.2012.07.126.

Schubert, A. *et al.* (2001) 'Thermo-mechanical properties and creep deformation of lead-containing and lead-free solders', in *Proceedings International Symposium on Advanced Packaging Materials Processes, Properties and Interfaces (IEEE Cat. No.01TH8562)*. Braselton, GA, USA: IEEE, pp. 129–134.

Schubert, A. *et al.* (2003) 'Fatigue life models for SnAgCu and SnPb solder joints evaluated by experiments and simulation', in *53rd Electronic Components and Technology Conference, 2003. Proceedings.* New Orleans, Louisiana, USA: IEEE, pp. 603–610. doi: 10.1109/ECTC.2003.1216343.

SEAI (2014) 'Best Practice Guide Photovoltaics (PV)', *Sustainable Energy Authority of Ireland*. Available at: http://irishsolarenergy.org/wp-content/uploads/2014/12/Best_Practice_Guide_Photovoltaics.pdf (Accessed: 7 September 2017).

Shrestha, S. (2014) *Determination of Dominant Failure Modes Using Combined Experimental and Statistical Methods and Selection of Best Method to Calculate Degradation Rates*. Arizona State University.

Sinha, A., Sastry, O. S. and Gupta, R. (2016) 'Nondestructive characterization of

encapsulant discoloration effects in crystalline-silicon PV modules', *Solar Energy Materials & Solar Cells*, 155, pp. 234–242. doi: 10.1016/j.solmat.2016.06.019.

Sitthiphol, N. *et al.* (2016) 'Insulation Resistance and Leakage Current in PV Modules and Strings with Different Grounding Configurations', *Applied Mechanics and Materials*, 839, pp. 114–118. doi: 10.4028/www.scientific.net/AMM.839.114.

Skoplaki, E., Boudouvis, A. G. and Palyvos, J. A. (2008) 'A simple correlation for the operating temperature of photovoltaic modules of arbitrary mounting', *Solar Energy Materials and Solar Cells*, 92(11), pp. 1393–1402. doi: 10.1016/j.solmat.2008.05.016.

Smith, D. R. and Madeni, J. C. (2002) 'Properties of Lead-Free Solders', *Electronics*.

Smith, K. (2016) *Degradation Effects in Photovoltaic Modules*. Murdoch University.

Steinberg, D. M. and Bursztyn, D. (1998) 'NOISE FACTORS, DISPERSION EFFECTS, AND ROBUST DESIGN', *Statistica Sinica*, 8, pp. 67–85. Available at: https://pdfs.semanticscholar.org/dd97/d6d8fe7de48d123bea56a0cc278d93647652.pdf (Accessed: 2 January 2019).

SUNPOWER (2013) *SunPower® Module 40-year Useful Life*. SunPower Corporation, San Jose, California.

Syed, A. (2004) 'Accumulated creep strain and energy density based thermal fatigue life prediction models for SnAgCu solder joints', in *2004 Proceedings. 54th Electronic Components and Technology Conference (IEEE Cat. No.04CH37546)*. Las Vegas, NV, USA: IEEE, pp. 737–746. doi: 10.1109/ECTC.2004.1319419.

Taylor, N. (2010) 'Guidelines for PV Power Measurement in Industry', *JRC Scientific and Technical Reports*, JRC57794(EUR 24359 EN). Available at: http://publications.europa.eu/others/agents/index_en.htm (Accessed: 2 October 2018).

Tossa, A. K. *et al.* (2016) 'Energy performance of different silicon photovoltaic technologies under hot and harsh climate', *Energy*. Pergamon, 103, pp. 261–270. doi: 10.1016/J.ENERGY.2016.02.133.

Triki-Lahiani, A., Bennani-Ben Abdelghani, A. and Slama-Belkhodja, I. (2017) 'Fault detection and monitoring systems for photovoltaic installations: A review', *Renewable and Sustainable Energy Reviews*, 82, pp. 2680–2692. doi:

10.1016/j.rser.2017.09.101.

Tsui, K.-L. (1996) ‘A critical look at Taguchi’s modelling approach for robust design’, *Journal of Applied Statistics*, 23(1), pp. 81–95. Available at: file:///C:/Users/GRO/Downloads/A critical look at Taguchi’s modelling approach for robust design.pdf (Accessed: 13 December 2018).

Vandevelde, B. *et al.* (2007) ‘Thermal cycling reliability of SnAgCu and SnPb solder joints: A comparison for several IC-packages’, *Microelectronics Reliability*, 47(2–3), pp. 259–265. doi: 10.1016/j.microrel.2006.09.034.

Walsh, T. M. *et al.* (2012) ‘Singapore Modules - Optimised PV Modules for the Tropics’, *Energy Procedia*, 15, pp. 388–395. doi: 10.1016/j.egypro.2012.02.047.

Wiese, S., Schubert, A., Walter, H., Dukek, R., *et al.* (2001) ‘Constitutive behaviour of lead-free solders vs. lead-containing solders-experiments on bulk specimens and flip-chip joints’, in *2001 Proceedings. 51st Electronic Components and Technology Conference (Cat. No.01CH37220)*. IEEE, pp. 890–902. doi: 10.1109/ECTC.2001.927900.

Wiese, S., Schubert, A., Walter, H., Dudek, R., *et al.* (2001) ‘Constitutive behaviour of lead-free solders vs. lead-containing solders-experiments on bulk specimens and flip-chip joints’, in *2001 Proceedings 51st Electronic Components and Technology Conference (IEEE Cat. No. 01CH37220)*. Orlando, FL, USA,: IEEE, pp. 890–902. doi: 10.1109/ectc.2001.927900.

Wohlgemuth, J. H. and Kempe, M. D. (2013) ‘Equating Damp Heat Testing with Field Failures of PV Modules’, *IEEE 39th Photovoltaic Specialists Conference*, pp. 0126–0131. doi: 10.1109/PVSC.2013.6744113.

Wong, E. H. *et al.* (2016) ‘Creep fatigue models of solder joints: A critical review’, *Microelectronics Reliability*, 59, pp. 1–12. doi: 10.1016/j.microrel.2016.01.013.

World Bank (2018) *Tracking SDG7: The Energy Progress Report*. Available at: https://trackingsdg7.esmap.org/data/files/download-documents/chapter_2_electrification.pdf (Accessed: 21 August 2019).

World Energy Council (2016) *World Energy Resources Solar*. Available at: https://www.worldenergy.org/wp-content/uploads/2017/03/WEResources_Solar_2016.pdf (Accessed: 19 March 2018).

Woyte, A. *et al.* (2013) 'Monitoring of Photovoltaic Systems: Good Practices and Systematic Analysis', *28th European PV Solar Energy Conference and Exhibition*.

Wysk, R. A. *et al.* (2000) *Manufacturing processes: Integrated product and process design*. New York: McGraw Hill. Available at: https://www.mne.psu.edu/simpson/courses/ie466/ie466.robust.handout.PDF (Accessed: 2 January 2019).

Xiao, H. *et al.* (2013) 'Damage behavior of SnAgCu/Cu solder joints subjected to thermomechanical cycling', *Journal of Alloys and Compounds*, 578, pp. 110–117. doi: 10.1016/j.jallcom.2013.05.026.

Ye, J. Y. *et al.* (2014) 'Performance degradation of various PV module technologies in tropical Singapore', *IEEE Journal of Photovoltaics*, 4(5). doi: 10.1109/JPHOTOV.2014.2338051.

Zaoui, F. *et al.* (2015) 'A combined experimental and simulation study on the effects of irradiance and temperature on photovoltaic modules', *Energy Procedia*, 75, pp. 373–380. doi: 10.1016/j.egypro.2015.07.393.

Zarmai, M. T. *et al.* (2015a) 'A review of interconnection technologies for improved crystalline silicon solar cell photovoltaic module assembly', *Applied Energy*, 154(SEPTEMBER), pp. 173–182. doi: 10.1016/j.apenergy.2015.04.120.

Zarmai, M. T. *et al.* (2015b) 'EFFECT OF INTERMETALLIC COMPOUNDS ON THERMO-MECHANICAL RELIABILITY OF LEAD-FREE SOLDER JOINTS IN SOLAR CELL ASSEMBLY', *International Journal of Mechanical Engineering (IJME)*, 4(6), pp. 29–38. Available at: www.iaset.us (Accessed: 29 January 2019).

Zarmai, M. T. (2016) *MODELLING OF SOLDER INTERCONNECTION'S PERFORMANCE IN PHOTOVOLTAIC MODULES FOR RELIABILITY PREDICTION*. School of Engineering, Faculty of Science and Engineering, University of Wolverhampton.

Zhang, Q., Dasgupta, A. and Haswell, P. (2003) 'Viscoplastic constitutive properties and energy-partitioning model of lead-free Sn3. 9Ag0. 6Cu solder alloy', in *53rd Electronic Components and Technology Conference, 2003. Proceedings*. IEEE, pp. 1862–1868.

# APPENDICES

**Documentation of module condition**

Date _____ Name of data recorder_____

Location _____

**1. System Data**

**System design:** ☐ single module ☐ multiple modules ☐ unknown

***BEGIN INSPECTION AT BACK SIDE OF MODULE***

**2. Module Data**

**Technology:** ☐ mono Si ☐ multi Si ☐ a--Si ☐ CdTe ☐ CIGS/CIS
☐ other: _____

Estimated deployment date _____

Manufacturer _____

Model # _____

Serial # _____

**3. Rear-side Glass**: ☐ **not applicable** ☐ **applicable**

**Damage:** ☐ no damage ☐ small, localized ☐ extensive

Damage Type (mark all that apply):

☐ crazing or other non--crack damage

☐ shattered (tempered ) ☐ shattered (non-tempered ) ☐ Cracked ☐ Chipped

**4. Backsheet:** ☐ **not applicable** ☐ **applicable**

**Appearance:** ☐ like new ☐ minor discoloration ☐ major discoloration

**Texture:** ☐ like new ☐ wavy (not delaminated) ☐ wavy (delaminated) ☐ dented

**Material quality --chalking:** ☐ none ☐ slight ☐ substantial

**Damage:** ☐ no damage ☐ small, localized ☐ extensive

Damage Type (mark all that apply):

☐ burn marks ☐ bubbles ☐ delamination ☐ cracks/scratches

**5. Wires/Connectors:**

**Wires:** ☐ not applicable ☐ like new ☐ pliable, but degraded ☐ embrittled

(mark all that apply): ☐ cracked/disintegrated insulation ☐ burnt

☐ corroded ☐ animal bites/marks

**Connectors:** ☐ not applicable ☐ like new ☐ pliable, but degraded ☐ embrittled

**Type:** ☐ unsure ☐ MC3 or MC4 ☐ Tyco Solarlok ☐ other

(mark all that apply): ☐ cracked/disintegrated insulation ☐ burnt ☐ corroded

**Figure A.1:** Visual Inspection Sheet I

Source: (Packard, Wohlgemuth and Kurtz, 2012)

**6. Junction Box:**

**Junction box itself: ☐ not applicable/observable ☐ applicable**
Physical state: ☐ intact ☐ unsound structure
(mark all that apply): ☐ weathered ☐ cracked ☐ burnt ☐ warped
Lid: ☐ intact/potted ☐ loose ☐ fell off ☐ cracked
**Junction box adhesive: ☐ not applicable/observable ☐ applicable**
Attachment: ☐ well attached ☐ loose/brittle ☐ fell off
Pliability: ☐ like new ☐ pliable, but degraded ☐ embrittled
**Junction box wire attachments: ☐ not applicable/observable ☐ applicable**
Attachment: ☐ well attached ☐ loose ☐ fell off
Seal: ☐ good seal ☐ seal will leak
other: ☐ arced/started a fire

**(7. Frame Grounding: Null)**

***CONTINUE INSPECTION ON FRONT SIDE OF MODULE***

**8. Frame: ☐ not applicable ☐ applicable**

**Appearance:** ☐ like new ☐ damaged ☐ missing
**Frame Adhesive:** ☐ like new/not visible ☐ degraded

**9. Frameless Edge Seal: ☐ not applicable ☐ applicable**

**Appearance:** ☐ like new ☐ discoloration ☐ visibly degraded
Material problems:
☐ squeezed/pinched out ☐ shows signs of moisture penetration
Delamination: ☐ none ☐ area(s) delaminated

**10. Glass/Polymer (front):**

**Material:** ☐ glass ☐ polymer ☐ glass/polymer composite ☐ unknown
**Appearance:** ☐ clean ☐ lightly soiled ☐ heavily soiled
**Damage:** ☐ no damage ☐ small, localized ☐ extensive
Damage Type (mark all that apply):
☐ crazing or other non--crack damage ☐ shattered (tempered)
☐ shattered (non--tempered) ☐ Cracked ☐ Chipped ☐ milky discoloration

**11. Metallization:**

**Appearance:** ☐ like new ☐ light discoloration ☐ dark discoloration

**Figure A.2:** Visual Inspection Sheet II

Source: (Packard, Wohlgemuth and Kurtz, 2012)

Worksheet

```
      EPTH        ALL
      EPCR        ALL


 SOLUTION MONITORING INFO IS WRITTEN TO FILE=
file.mntr

 MAXIMUM NUMBER OF EQUILIBRIUM ITERATIONS HAS BEEN MODIFIED
  TO BE, NEQIT = 25, BY SOLUTION CONTROL LOGIC.

     FORCE CONVERGENCE VALUE  =   273.4      CRITERION=   1.395
     DISP CONVERGENCE VALUE   =  0.1215E-04  CRITERION=  0.8670E-06
    EQUIL ITER   1 COMPLETED.  NEW TRIANG MATRIX.  MAX DOF INC= -0.1215E-04
     DISP CONVERGENCE VALUE   =  0.1215E-04  CRITERION=  0.8847E-06
     LINE SEARCH PARAMETER =   1.000     SCALED MAX DOF INC = -0.1215E-04
     FORCE CONVERGENCE VALUE  =  0.4957      CRITERION=  0.5206E-04
    EQUIL ITER   2 COMPLETED.  NEW TRIANG MATRIX.  MAX DOF INC=  0.8965E-06
     DISP CONVERGENCE VALUE   =  0.8965E-06  CRITERION=  0.9028E-06 <<< CONVERGED
     LINE SEARCH PARAMETER =   1.000     SCALED MAX DOF INC =  0.8965E-06
     FORCE CONVERGENCE VALUE  =  0.3450E-01  CRITERION=  0.5312E-04
    EQUIL ITER   3 COMPLETED.  NEW TRIANG MATRIX.  MAX DOF INC= -0.6699E-06
     DISP CONVERGENCE VALUE   =  0.6699E-06  CRITERION=  0.9212E-06 <<< CONVERGED
     LINE SEARCH PARAMETER =   1.000     SCALED MAX DOF INC = -0.6699E-06
     FORCE CONVERGENCE VALUE  =  0.6518E-02  CRITERION=  0.5421E-04
    EQUIL ITER   4 COMPLETED.  NEW TRIANG MATRIX.  MAX DOF INC=  0.1756E-06
     DISP CONVERGENCE VALUE   =  0.1584E-06  CRITERION=  0.9400E-06 <<< CONVERGED
     LINE SEARCH PARAMETER =  0.9021     SCALED MAX DOF INC =  0.1584E-06
     FORCE CONVERGENCE VALUE  =  0.1445E-01  CRITERION=  0.5531E-04
    EQUIL ITER   5 COMPLETED.  NEW TRIANG MATRIX.  MAX DOF INC= -0.2507E-06
     DISP CONVERGENCE VALUE   =  0.2507E-06  CRITERION=  0.9592E-06 <<< CONVERGED
     LINE SEARCH PARAMETER =   1.000     SCALED MAX DOF INC = -0.2507E-06
     FORCE CONVERGENCE VALUE  =  0.2123E-02  CRITERION=  0.5644E-04
    EQUIL ITER   6 COMPLETED.  NEW TRIANG MATRIX.  MAX DOF INC=  0.2738E-07
     DISP CONVERGENCE VALUE   =  0.9891E-08  CRITERION=  0.9787E-06 <<< CONVERGED
     LINE SEARCH PARAMETER =  0.3612     SCALED MAX DOF INC =  0.9891E-08
     FORCE CONVERGENCE VALUE  =  0.1391E-02  CRITERION=  0.5760E-04
    EQUIL ITER   7 COMPLETED.  NEW TRIANG MATRIX.  MAX DOF INC=  0.2184E-07
     DISP CONVERGENCE VALUE   =  0.2184E-07  CRITERION=  0.9987E-06 <<< CONVERGED
     LINE SEARCH PARAMETER =   1.000     SCALED MAX DOF INC =  0.2184E-07
     FORCE CONVERGENCE VALUE  =  0.3266E-02  CRITERION=  0.5877E-04
    EQUIL ITER   8 COMPLETED.  NEW TRIANG MATRIX.  MAX DOF INC= -0.5934E-07
     DISP CONVERGENCE VALUE   =  0.5630E-07  CRITERION=  0.1019E-05 <<< CONVERGED
     LINE SEARCH PARAMETER =  0.9489     SCALED MAX DOF INC = -0.5630E-07
     FORCE CONVERGENCE VALUE  =  0.3674E-03  CRITERION=  0.5997E-04
    EQUIL ITER   9 COMPLETED.  NEW TRIANG MATRIX.  MAX DOF INC= -0.3650E-08
     DISP CONVERGENCE VALUE   =  0.3650E-08  CRITERION=  0.1040E-05 <<< CONVERGED
     LINE SEARCH PARAMETER =   1.000     SCALED MAX DOF INC = -0.3650E-08
     FORCE CONVERGENCE VALUE  =  0.1193E-02  CRITERION=  0.1224E-03
    EQUIL ITER  10 COMPLETED.  NEW TRIANG MATRIX.  MAX DOF INC=  0.2134E-07
     DISP CONVERGENCE VALUE   =  0.2134E-07  CRITERION=  0.1061E-05 <<< CONVERGED
     LINE SEARCH PARAMETER =   1.000     SCALED MAX DOF INC =  0.2134E-07
     FORCE CONVERGENCE VALUE  =  0.1305E-03  CRITERION=  0.1249E-03
    EQUIL ITER  11 COMPLETED.  NEW TRIANG MATRIX.  MAX DOF INC=  0.1013E-08
     DISP CONVERGENCE VALUE   =  0.5640E-09  CRITERION=  0.1083E-05 <<< CONVERGED
     LINE SEARCH PARAMETER =  0.5566     SCALED MAX DOF INC =  0.5640E-09
```

**Figure A.3:** ANSYS FEM solution codes I

```
    FORCE CONVERGENCE VALUE  =  0.2507E-03  CRITERION=  0.1274E-03
   EQUIL ITER  12 COMPLETED.  NEW TRIANG MATRIX.  MAX DOF INC=  0.4768E-08
    DISP CONVERGENCE VALUE   =  0.4768E-08  CRITERION=  0.1105E-05 <<< CONVERGED
    LINE SEARCH PARAMETER =   1.000     SCALED MAX DOF INC =  0.4768E-08
    FORCE CONVERGENCE VALUE  =  0.1979E-03  CRITERION=  0.1300E-03
   EQUIL ITER  13 COMPLETED.  NEW TRIANG MATRIX.  MAX DOF INC= -0.3387E-08
    DISP CONVERGENCE VALUE   =  0.2426E-08  CRITERION=  0.1127E-05 <<< CONVERGED
    LINE SEARCH PARAMETER =  0.7164     SCALED MAX DOF INC = -0.2426E-08
    FORCE CONVERGENCE VALUE  =  0.2391E-04  CRITERION=  0.1327E-03 <<< CONVERGED

*** WARNING ***                         CP =    8200.926   TIME= 16:38:27
A reference force value times the tolerance is used by the
Newton-Raphson method for checking convergence.  The calculated
reference FORCE CONVERGENCE VALUE = 1.148075876E-03 is less than a
threshold.  This threshold defaults to 1.0-2 or is specified as MINREF
on the CNVTOL command.  Check results carefully.
   >>> SOLUTION CONVERGED AFTER EQUILIBRIUM ITERATION  13
*** LOAD STEP    26   SUBSTEP     1  COMPLETED.    CUM ITER =    385
*** TIME =   59760.0         TIME INC =   900.000
*** CREEP RATIO = 0.3628E-03   CRITERION FOR CREEP RATIO CONTROL =  8.000
*** AUTO STEP TIME:  NEXT TIME INC =  900.00      UNCHANGED

    FORCE CONVERGENCE VALUE  =   1.195      CRITERION=  0.7012
    DISP CONVERGENCE VALUE   =  0.1094E-04  CRITERION=  0.8670E-06
   EQUIL ITER   1 COMPLETED.  NEW TRIANG MATRIX.  MAX DOF INC=  0.1094E-04
    DISP CONVERGENCE VALUE   =  0.1079E-04  CRITERION=  0.8847E-06
    LINE SEARCH PARAMETER =  0.9857     SCALED MAX DOF INC =  0.1079E-04
    FORCE CONVERGENCE VALUE  =   1.197      CRITERION=  0.5206E-04
   EQUIL ITER   2 COMPLETED.  NEW TRIANG MATRIX.  MAX DOF INC= -0.6238E-06
    DISP CONVERGENCE VALUE   =  0.6238E-06  CRITERION=  0.9028E-06 <<< CONVERGED
    LINE SEARCH PARAMETER =   1.000     SCALED MAX DOF INC = -0.6238E-06
    FORCE CONVERGENCE VALUE  =  0.2434E-01  CRITERION=  0.5312E-04
   EQUIL ITER   3 COMPLETED.  NEW TRIANG MATRIX.  MAX DOF INC=  0.3532E-06
    DISP CONVERGENCE VALUE   =  0.2559E-06  CRITERION=  0.9212E-06 <<< CONVERGED
    LINE SEARCH PARAMETER =  0.7246     SCALED MAX DOF INC =  0.2559E-06
    FORCE CONVERGENCE VALUE  =  0.1020E-01  CRITERION=  0.5421E-04
   EQUIL ITER   4 COMPLETED.  NEW TRIANG MATRIX.  MAX DOF INC= -0.1818E-06
    DISP CONVERGENCE VALUE   =  0.1818E-06  CRITERION=  0.9400E-06 <<< CONVERGED
    LINE SEARCH PARAMETER =   1.000     SCALED MAX DOF INC = -0.1818E-06
    FORCE CONVERGENCE VALUE  =  0.1968E-02  CRITERION=  0.5531E-04
   EQUIL ITER   5 COMPLETED.  NEW TRIANG MATRIX.  MAX DOF INC=  0.2899E-07
    DISP CONVERGENCE VALUE   =  0.2899E-07  CRITERION=  0.9592E-06 <<< CONVERGED
    LINE SEARCH PARAMETER =   1.000     SCALED MAX DOF INC =  0.2899E-07
    FORCE CONVERGENCE VALUE  =  0.1610E-03  CRITERION=  0.5644E-04
   EQUIL ITER   6 COMPLETED.  NEW TRIANG MATRIX.  MAX DOF INC= -0.2076E-08
    DISP CONVERGENCE VALUE   =  0.2076E-08  CRITERION=  0.9787E-06 <<< CONVERGED
    LINE SEARCH PARAMETER =   1.000     SCALED MAX DOF INC = -0.2076E-08
    FORCE CONVERGENCE VALUE  =  0.5502E-04  CRITERION=  0.5760E-04 <<< CONVERGED
   >>> SOLUTION CONVERGED AFTER EQUILIBRIUM ITERATION   6
*** LOAD STEP    26   SUBSTEP     2  COMPLETED.    CUM ITER =    391
```

**Figure A.4:** ANSYS FEM solution codes II

```
*** LOAD STEP    26   SUBSTEP     2  COMPLETED.    CUM ITER =    391
*** TIME =   60660.0         TIME INC =   900.000
*** CREEP RATIO = 0.1497E-02   CRITERION FOR CREEP RATIO CONTROL =  8.000
*** AUTO TIME STEP:  NEXT TIME INC =  1350.0      INCREASED (FACTOR = 1.5000)

    FORCE CONVERGENCE VALUE  =  0.4022      CRITERION=  0.2272
    DISP CONVERGENCE VALUE   =  0.3832E-05  CRITERION=  0.8670E-06
   EQUIL ITER   1 COMPLETED.  NEW TRIANG MATRIX.  MAX DOF INC=  0.3832E-05
    DISP CONVERGENCE VALUE   =  0.3615E-05  CRITERION=  0.8847E-06
    LINE SEARCH PARAMETER =  0.9432     SCALED MAX DOF INC =  0.3615E-05
    FORCE CONVERGENCE VALUE  =  0.1843      CRITERION=  0.5206E-04
   EQUIL ITER   2 COMPLETED.  NEW TRIANG MATRIX.  MAX DOF INC= -0.2932E-05
    DISP CONVERGENCE VALUE   =  0.2624E-05  CRITERION=  0.9028E-06
    LINE SEARCH PARAMETER =  0.8949     SCALED MAX DOF INC = -0.2624E-05
    FORCE CONVERGENCE VALUE  =  0.2591E-01  CRITERION=  0.5312E-04
   EQUIL ITER   3 COMPLETED.  NEW TRIANG MATRIX.  MAX DOF INC=  0.6588E-06
    DISP CONVERGENCE VALUE   =  0.4543E-06  CRITERION=  0.9212E-06 <<< CONVERGED
    LINE SEARCH PARAMETER =  0.6895     SCALED MAX DOF INC =  0.4543E-06
    FORCE CONVERGENCE VALUE  =  0.2227E-01  CRITERION=  0.5421E-04
   EQUIL ITER   4 COMPLETED.  NEW TRIANG MATRIX.  MAX DOF INC= -0.1180E-05
    DISP CONVERGENCE VALUE   =  0.1150E-05  CRITERION=  0.9400E-06
    LINE SEARCH PARAMETER =  0.9744     SCALED MAX DOF INC = -0.1150E-05
    FORCE CONVERGENCE VALUE  =  0.3068E-02  CRITERION=  0.5531E-04
   EQUIL ITER   5 COMPLETED.  NEW TRIANG MATRIX.  MAX DOF INC=  0.7294E-07
    DISP CONVERGENCE VALUE   =  0.6464E-07  CRITERION=  0.9592E-06 <<< CONVERGED
    LINE SEARCH PARAMETER =  0.8862     SCALED MAX DOF INC =  0.6464E-07
    FORCE CONVERGENCE VALUE  =  0.2558E-02  CRITERION=  0.5644E-04
   EQUIL ITER   6 COMPLETED.  NEW TRIANG MATRIX.  MAX DOF INC=  0.1143E-06
    DISP CONVERGENCE VALUE   =  0.9843E-07  CRITERION=  0.9787E-06 <<< CONVERGED
    LINE SEARCH PARAMETER =  0.8612     SCALED MAX DOF INC =  0.9843E-07
    FORCE CONVERGENCE VALUE  =  0.3705E-03  CRITERION=  0.5760E-04
   EQUIL ITER   7 COMPLETED.  NEW TRIANG MATRIX.  MAX DOF INC=  0.1191E-07
    DISP CONVERGENCE VALUE   =  0.1037E-07  CRITERION=  0.9987E-06 <<< CONVERGED
    LINE SEARCH PARAMETER =  0.8707     SCALED MAX DOF INC =  0.1037E-07
    FORCE CONVERGENCE VALUE  =  0.2954E-03  CRITERION=  0.5877E-04
   EQUIL ITER   8 COMPLETED.  NEW TRIANG MATRIX.  MAX DOF INC=  0.1306E-07
    DISP CONVERGENCE VALUE   =  0.1148E-07  CRITERION=  0.1019E-05 <<< CONVERGED
    LINE SEARCH PARAMETER =  0.8796     SCALED MAX DOF INC =  0.1148E-07
    FORCE CONVERGENCE VALUE  =  0.4584E-04  CRITERION=  0.5997E-04 <<< CONVERGED
   >>> SOLUTION CONVERGED AFTER EQUILIBRIUM ITERATION   8
*** LOAD STEP    26   SUBSTEP     3  COMPLETED.    CUM ITER =    399
*** TIME =   62010.0         TIME INC =   1350.00
*** CREEP RATIO = 0.1662       CRITERION FOR CREEP RATIO CONTROL =  8.000
*** AUTO STEP TIME:  NEXT TIME INC =  1350.0      UNCHANGED

    FORCE CONVERGENCE VALUE  =  0.2136      CRITERION=  0.1293
    DISP CONVERGENCE VALUE   =  0.2938E-05  CRITERION=  0.8670E-06
   EQUIL ITER   1 COMPLETED.  NEW TRIANG MATRIX.  MAX DOF INC=  0.2938E-05
    DISP CONVERGENCE VALUE   =  0.2730E-05  CRITERION=  0.8847E-06
    LINE SEARCH PARAMETER =  0.9294     SCALED MAX DOF INC =  0.2730E-05
```

**Figure A.5:** ANSYS FEM solution codes III

```
   EQUIL ITER   2 COMPLETED.  NEW TRIANG MATRIX.  MAX DOF INC= -0.2870E-05
    DISP CONVERGENCE VALUE    =  0.2180E-05  CRITERION=  0.9028E-06
    LINE SEARCH PARAMETER =  0.7594     SCALED MAX DOF INC = -0.2180E-05
    FORCE CONVERGENCE VALUE  =  0.1251E-01  CRITERION=  0.5312E-04
   EQUIL ITER   3 COMPLETED.  NEW TRIANG MATRIX.  MAX DOF INC=  0.5863E-06
    DISP CONVERGENCE VALUE    =  0.5863E-06  CRITERION=  0.9212E-06 <<< CONVERGED
    LINE SEARCH PARAMETER =   1.000     SCALED MAX DOF INC =  0.5863E-06
    FORCE CONVERGENCE VALUE  =  0.6278E-02  CRITERION=  0.5421E-04
   EQUIL ITER   4 COMPLETED.  NEW TRIANG MATRIX.  MAX DOF INC= -0.7137E-06
    DISP CONVERGENCE VALUE    =  0.5592E-06  CRITERION=  0.9400E-06 <<< CONVERGED
    LINE SEARCH PARAMETER =  0.7835     SCALED MAX DOF INC = -0.5592E-06
    FORCE CONVERGENCE VALUE  =  0.9477E-03  CRITERION=  0.5531E-04
   EQUIL ITER   5 COMPLETED.  NEW TRIANG MATRIX.  MAX DOF INC=  0.3005E-07
    DISP CONVERGENCE VALUE    =  0.2500E-07  CRITERION=  0.9592E-06 <<< CONVERGED
    LINE SEARCH PARAMETER =  0.8320     SCALED MAX DOF INC =  0.2500E-07
    FORCE CONVERGENCE VALUE  =  0.2074E-03  CRITERION=  0.5644E-04
   EQUIL ITER   6 COMPLETED.  NEW TRIANG MATRIX.  MAX DOF INC= -0.2613E-07
    DISP CONVERGENCE VALUE    =  0.2248E-07  CRITERION=  0.9787E-06 <<< CONVERGED
    LINE SEARCH PARAMETER =  0.8605     SCALED MAX DOF INC = -0.2248E-07
    FORCE CONVERGENCE VALUE  =  0.4606E-04  CRITERION=  0.5760E-04 <<< CONVERGED
   >>> SOLUTION CONVERGED AFTER EQUILIBRIUM ITERATION   6
*** LOAD STEP    26   SUBSTEP     4  COMPLETED.    CUM ITER =    405
*** TIME =   63360.0         TIME INC =   1350.00
*** CREEP RATIO = 0.3036       CRITERION FOR CREEP RATIO CONTROL =  8.000
**************************************************
*************** FINISHED SOLVE FOR LS 26 **************

*GET  _WALLASOL  FROM  ACTI  ITEM=TIME WALL  VALUE=  16.7575000

PRINTOUT RESUMED BY /GOP

FINISH SOLUTION PROCESSING


***** ROUTINE COMPLETED *****  CP =      8629.258


*** ANSYS - ENGINEERING ANALYSIS SYSTEM  RELEASE Release 18.2     18.2     ***
DISTRIBUTED ANSYS Academic Research
```

**Figure A.6:** ANSYS FEM solution codes IV

**Table A.1:** Fatigue life (years) master table of ribbon-contact material combination models at STC

| Materials | | Ribbon Interconnect | | | | | |
|---|---|---|---|---|---|---|---|
| | | Aluminium | Brass | Copper | Silver | Tin | Zinc |
| Contact | Aluminium | 130.50 | 6.55 | 11.96 | 128.76 | 50.83 | 7.29 |
| | Brass | 6.69 | 0.32 | 0.69 | 5.98 | 1.76 | 0.33 |
| | Copper | 7.18 | 0.39 | 0.85 | 6.51 | 2.12 | 0.38 |
| | Silver | 144.29 | 6.13 | 19.20 | 138.69 | 46.72 | 10.72 |
| | Tin | 9.86 | 0.69 | 1.54 | 9.19 | 3.55 | 0.56 |
| | Zinc | 7.31 | 0.35 | 0.81 | 6.59 | 2.10 | 0.35 |

**Table A.2:** Fatigue life (years) master table of ribbon-contact material combination models in elevated temperature climate

| Materials | | Ribbon Interconnect | | | | | |
|---|---|---|---|---|---|---|---|
| | | Aluminium | Brass | Copper | Silver | Tin | Zinc |
| Contact | Aluminium | 382.28 | 1.79 | 6.49 | 380.22 | 6.37 | 2.25 |
| | Brass | 4.22 | 0.23 | 0.35 | 3.78 | 0.94 | 0.20 |
| | Copper | 4.75 | 0.32 | 0.43 | 4.24 | 1.07 | 0.24 |
| | Silver | 300.91 | 1.74 | 5.28 | 400.55 | 5.84 | 5.71 |
| | Tin | 6.51 | 0.59 | 0.71 | 5.78 | 1.46 | 0.35 |
| | Zinc | 4.53 | 0.24 | 0.38 | 4.07 | 1.03 | 0.21 |

**Table A.3:** Fatigue life (years) from solder thickness experiments in elevated temperature climate

| Solder Thickness(μm) | Ribbon-Contact Material Combination | | | |
|---|---|---|---|---|
| | Ag-Ag | Al-Al | Ag-Al | Al-Ag |
| 31 | 127.94 | 199.15 | 118.06 | 236.26 |
| 36 | 184.50 | 356.02 | 199.43 | 415.13 |
| 41 | 261.72 | 649.13 | 334.38 | 789.25 |
| 46 | 400.55 | 382.28 | 380.22 | 300.91 |
| 51 | 971.42 | 577.47 | 758.64 | 678.77 |
| 56 | 534.39 | 371.54 | 461.16 | 448.63 |
| 61 | 422.22 | 343.50 | 369.82 | 390.11 |

**Table A.4:** Fatigue life (years) from contact thickness experiments in elevated temperature climate

| Contact Thickness(μm) | Ribbon-Contact Material Combination | | | |
|---|---|---|---|---|
| | Ag-Ag | Al-Al | Ag-Al | Al-Ag |
| 35 | 60.21 | 85.27 | 61.78 | 79.89 |
| 40 | 56.56 | 83.35 | 59.93 | 73.89 |
| 45 | 57.83 | 94.84 | 64.07 | 77.33 |
| 50 | 400.55 | 382.28 | 380.22 | 300.91 |
| 55 | 61.80 | 111.93 | 73.88 | 87.28 |
| 60 | 61.83 | 124.30 | 73.43 | 95.51 |
| 65 | 66.46 | 155.14 | 75.37 | 114.29 |

**Table A.5:** Fatigue life (years) from ribbon thickness experiments in elevated temperature climate

| Ribbon Thickness(μm) | Ribbon-Contact Material Combination | | | |
|---|---|---|---|---|
| | Ag-Ag | Al-Al | Ag-Al | Al-Ag |
| 170 | 102.50 | 46.59 | 95.96 | 51.63 |
| 180 | 148.29 | 97.26 | 139.80 | 99.29 |
| 190 | 252.23 | 174.84 | 248.11 | 169.40 |
| 200 | 400.55 | 382.28 | 380.22 | 300.91 |
| 210 | 53.76 | 95.40 | 60.43 | 76.43 |
| 220 | 51.44 | 91.17 | 56.98 | 74.35 |
| 230 | 53.50 | 88.44 | 54.22 | 74.09 |